TU Clausthal

Microkinetic Investigation of the Transient Methanation of Carbon Dioxide on Ni Catalysts

Doctoral Thesis

(Cumulative Dissertation)

to be awarded the degree

Doctor of Engineering (Dr.-Ing.)

submitted by

Bjarne Kreitz, M. Sc.

from Gillersheim

approved by the

Faculty of Mathematics/Computer Science and

Mechanical Engineering,

Clausthal University of Technology

Date of oral examination

01 October 2021

Dean:

Prof. Dr. rer. nat. Jörg P. Müller

Chairperson of the Board of Examiners:

Prof. Dr. rer. nat. Alfred P. Weber

Supervising tutor:

Prof. Dr.-Ing. Thomas Turek

Reviewer:

Prof. Dr. C. Franklin Goldsmith

Prof. Dr.-Ing. Robert Güttel

“Kühner,
als das Unbekannte zu erforschen,
kann es sein,
das Bekannte zu bezweifeln."

ALEXANDER VON HUMBOLDT

Abstract

Production of CH_4 in the Power-to-Gas (PtG) process offers the chance to store renewable energies while producing sustainable natural gas. In the PtG process, the renewable energies are used to produce H_2 via water electrolysis, which is subsequently converted with CO_2 to CH_4 over a Ni catalyst. The fluctuating nature of the renewable energy source imposes a transient operation, requiring the design of tolerant catalysts and reactors that can efficiently function under these conditions. CO_2 methanation reactors are designed with reactor models, where closed-form rate expressions are used, which lump all elementary steps of a mechanism into an analytical equation. The simulation of the periodic operation of a microstructured reactor with such kinetics predicts ample variation in the temperature profile and productivity. This highlights the necessity for accurate and predictive kinetic approaches to describe the transient behavior of the methanation catalyst. Transient phenomena on the catalyst surface can only be quantified by detailed microkinetic models, where each elementary step of the methanation mechanism is considered.

The investigation of the microkinetics for the CO_2 methanation on Ni is accomplished with a combination of ab-initio electronic structure calculations and experimental methods. First, Ni/SiO_2 and Ni/γ-Al_2O_3 catalysts were produced and screened for activity in transient methanation experiments to determine suitable catalysts for the development of the microkinetics. The interaction of CO_2 with supported catalysts is challenging and was investigated with temperature-programmed desorption (TPD) experiments. These TPD experiments show that the Ni/SiO_2 catalyst needs to be used because CO_2 interacts with basic sites on the γ-Al_2O_3 support, overshadowing the interaction of CO_2 with the Ni crystal.

The Ni crystals on the support consist of a variety of exposed crystal facets, whereas microkinetic models are usually derived for a single crystal facet. This gap was bridged by comparing CO_2-TPD experiment with a first-principles-based microkinetic model considering the combination of the four most important Ni facets via a Wulff construction of the crystal. Energetic properties of the microkinetic model were derived with state-of-the-art density functional theory (DFT) methods. Propagation of the uncertainty in the DFT-derived parameters to the output of the model in a global uncertainty analysis revealed feasible sets with reasonable agreement with the data. This combination of experiments and multiscale modeling reveals that the multiple desorption peaks can be attributed to desorption from different Ni facets. Ni(111) contributes considerably to the desorption profile and is further considered in the development of a full microkinetic model for the CO_2 methanation.

Microkinetic models are not created by hand with DFT, but by using the Reaction Mechanism Generator (RMG), a software for the automated construction of reaction networks. Therefore, it is ensured that all the possible methanation chemistry is considered and the discovered reaction mechanism is not biased. Uncertainty quantification is directly included in the mechanism generation procedure because of the considerable uncertainty in DFT-derived parameters. 5,000 possible mechanisms within the uncertainty range were generated and analyzed. All generated microkinetics were compared to transient methanation experiments from a differential fixed-bed and a Berty reactor in a multiscale modeling approach. Feasible sets of ab-initio model parameters exists, which can describe the experiments with remarkable accuracy. This approach identifies the limitations of current DFT methods in elucidating the mechanism. The combination of uncertainty quantification in automated mechanism generation and multiscale modeling provides deep insights into the CO_2 methanation mechanism on Ni(111).

Kurzfassung

Der Power-to-Gas (PtG) Prozess bietet die Chance erneuerbare Energien in Form von synthetischem Erdgas zu speichern. Im PtG-Prozess wird zunächst H_2 mittels Wasserelektrolyse erzeugt, welches anschließend mit CO_2 an einem Ni-Katalysator zu CH_4 umgesetzt wird. Die fluktuierend anfallenden erneuerbaren Energien erzwingen einen dynamischen Betrieb, was die Entwicklung von toleranten Katalysatoren und Reaktoren erfordert, welche effizient unter den Bedingungen arbeiten. Reaktoren für die CO_2-Methanisierung werden mithilfe geeigneter Reaktormodelle ausgelegt, wobei stationäre kinetische Ansätze verwendet werden, bei denen alle Schritte eines Mechanismus in einer analytischen Gleichung zusammengefasst werden. Die Simulation des periodischen Betriebs eines mikrostrukturierten Reaktors auf der Grundlage einer solchen Kinetik zeigt eine starke Variation des Temperaturprofils und der Produktivität. Um die transienten Phänomene auf der Katalysatoroberfläche korrekt zu beschreiben ist es erforderlich Mikrokinetiken zu verwenden, wobei jeder Schritt des Reaktionsmechanismus berücksichtigt wird.

Die Entwicklung einer Mikrokinetik für die CO_2-Methanisierung auf Ni-Katalysatoren erfolgt mit einer Kombination aus ab-initio Berechnungen und experimentellen Methoden. Zunächst werden verschiedene Ni/SiO_2 und $Ni/\gamma\text{-}Al_2O_3$ Katalysatoren hergestellt und in dynamischen Methanisierungsexperimenten auf ihre Aktivität untersucht. CO_2 zeigt vielfältige Wechselwirkungen mit den Ni-Katalysatoren, welche durch temperaturprogrammierten Desorptionsexperimenten (TPD) untersucht wurden. Diese TPD-Experimente zeigen, dass das Ni/SiO_2 System für weitere kinetische Untersuchungen verwendet werden muss, da CO_2 an basischen Zentren auf dem $\gamma\text{-}Al_2O_3$ Träger adsorbiert.

Die Ni-Kristalle auf dem Katalysator bestehen aus einer Vielzahl an Kristallflächen, wohingegen mikrokinetische Modelle üblicherweise nur für eine einzelne Ebene ermittelt werden. Das Desorptionsspektrum von CO_2 wurde mit einem mikrokinetischen Modell, basierend auf ab-initio Parametern und unter Berücksichtigung der Form eines realen Ni-Kristalls, reproduziert. Die Zusammensetzung des Ni-Kristalls aus den vier wichtigsten Ebenen wurde anhand einer Wulff-Konstruktion bestimmt. Kinetischen und thermodynamische Parameter des Models wurden mit Dichtefunktionaltheorie (DFT) Methoden berechnet. Die Unsicherheiten in den ab-initio Parametern werden in einer globalen Unsicherheitsanalyse bis zu den Simulationsergebnissen fortgepflanzt. Kombinationen an Parametern werden identifiziert, welche die Experimente mit guter Genauigkeit wiedergeben können. Diese Untersuchung zeigt, dass sich das TPD-Profil aus den einzelnen Kristallflächen zusammensetzt. Ni(111) trägt signifikant zum Desorptionsprofil bei und wird für die Entwicklung einer Mikrokinetik der CO_2-Methanisierung verwendet.

Mikrokinetiken werden nicht von Hand mit DFT-Berechnungen erstellt, sondern mithilfe des "Reaction Mechanism Generator (RMG)", einer Software zur automatischen Konstruktion von Reaktionsnetzwerken. Dadurch werden alle möglichen Reaktionspfade berücksichtigt und der Mechanismus ist frei von den Erwartungen des Forschenden. Aufgrund der beträchtlichen Unsicherheit in den DFT-basierten Parametern wird diese direkt in der Generierung der Mechanismen berücksichtigt. 5000 mögliche Methanisierungsmechanismen werden in dem Bereich der Unsicherheiten generiert und analysiert. Alle erzeugten Mechanismen werden mit dynamischen Experimenten aus einem differentiellen Festbettreaktor und Berty-Reaktor in einem multiskalen Modell verglichen. Es existierten Kombinationen von ab-intio Modellparametern, welche die dynamischen Experimente mit bemerkenswerter Genauigkeit beschreiben können. Die Einbindung von Unsicherheiten in die automatische Generierung von Mechanismen und der multiskalen Modellierung liefert tiefgreifende Einblicke in den Reaktionsmechanismus der CO_2-Methanisierung auf Ni(111).

Acknowledgements

"Chemistry without catalysis would be a sword without a handle, a light without brilliance, a bell without sound."

(Alwin Mittasch)

The long and sometimes strenuous process of doing a PhD comes now to an end with this document. It was a great adventure with many hours of work in the laboratory or behind the desk, lots of encounters with many colleagues who became good friends later on, and an awesome research stay in the US. What Alwin Mittasch thinks about the role of catalysis in chemistry fits very well into this context. Many people *catalyzed* my research and work. Without their contribution and support, the whole adventure would not have been possible and the thesis would be without *brilliance*.

First of all, my biggest thanks go to my supervisor Thomas for giving me the opportunity to do a PhD at the ICVT and providing the best possible working environment I could imagine. I really appreciate the freedom that I had during this time. I could always drive my research in the directions that were most interesting to me, even when it went from chemical engineering very deep into the field of catalysis. Thanks for the continuous support, guidance, and feedback so that I could become an actual researcher. Most of all, I'm very grateful for the possibility and the encouragement to go abroad.

Special thanks go to Franklin. I'm grateful that you allowed me to visit your group at Brown University and introduced me to the "rabbit hole" of computational catalysis. I cherish the time I spent in Providence and I'm very much looking forward to continue working with you. Our weekly chats on all topics, from good barbecue to beekeeping and sometimes work, were a source of continuous advice and joy. Your feedback and support helped me to advance my research to the next level.

I like to thank Robert for reviewing the thesis. Also, I'm grateful for our many discussions at conferences and the fruitful exchange of ideas on the transient operation of reactors from Ulm to Clausthal.

Many thanks to all my colleagues at the ICVT, who provided an excellent and supportive working environment, enjoyable coffee breaks, and various activities besides work. I like to thank some in particular. Frank, for many fun hours, and maybe twice the amount of beer, outside the institute. Gregor, thanks for the help with lots of drafts, presentations, and discussions. Jörn, for being a great office and lab buddy and for always providing help with Latex and Python. Philipp, for starting this whole procedure as a great supervisor for my master thesis. Jens, for the continuous exchange of ideas on methanation and chemical engineering in general. Aurina, thank you for contributing to this work, especially the production and characterization of the silica catalysts, as well as some funny evenings. Jan, for providing a second pair of eyes on the methanation stuff. Matthias, for many discussions and also for finally pronouncing my name correctly. Mauritio, for his advice on the "real reaction engineering" and also for always knowing where everything is in the institute.

Thanks to Franklins' group at Brown University, who made the research stay so enjoyable. It truly was an amazing time. Katrín, thank you for teaching me how to do DFT calculations and for all the help with various software issues. Thanks, Jongyoon and Shubham, for lots of funny lunch breaks and other activities in Providence. Also, many thanks to Emily, Chris, and Richard for the tips, tricks, and help on RMG.

I like to thank all my Bachelor (Hanqi, Lasse, Christoph) and Master students (Marco, Jan, David), who contributed to my research and this thesis in many ways.

Another big thanks go to Malte for being the best roommate (for 10 years!) and friend. From the start of the first courses at the university to the work in the institute on the PhD, we were not able to escape Clausthal. It wouldn't have been possible and so much fun without you.

Last but foremost, I would like to highlight the great support from my family, who enabled me to pursue my study and always supported me through this long process. Thanks, Mama, Papa, Finn, and Eike!

With gratitude,

Bjarne

Contents

CHAPTER 1

"If you give a man an answer, all he gains is a little fact. But give him a question and he'll look for his own answers."

(Kvothe, The Wise Mans Fear, Patrick Rothfuss)

Introduction

Global warming requires us to reduce our CO_2 emissions to prevent a temperature increase beyond 2 K, which imposes that the current fossil fuel reserves must remain unused to some extent [1]. In contrast, the energy demand is steadily increasing in all sectors ranging from industry to transportation [2]. Thus an increase in the share of renewable energies like wind and solar power for electricity generation is necessary. However, increasing the share of renewable energies in the electricity mix leads to concerns about the stability of the electricity grid due to the volatile nature of the renewable energies, which requests sufficient energy storage capacities [3, 4]. Large amounts of energy can only be stored for a long time in the form of a chemical compound [5]. Still, a complete and quick adjustment of all sectors to be powered by renewable electricity is not possible because of constraints from energy-technology deployment [6, 7]. Carbon-based fuels will be required for a foreseeable time and oil or natural gas remain a major feedstock for the chemical industry [4, 7–9]. A very promising reaction that addresses all of the points described above is the production of synthetic methane by hydrogenation of CO_2 in the Power-to-Gas process (PtG) [10–13]. The PtG process is depicted in Figure 1.1.

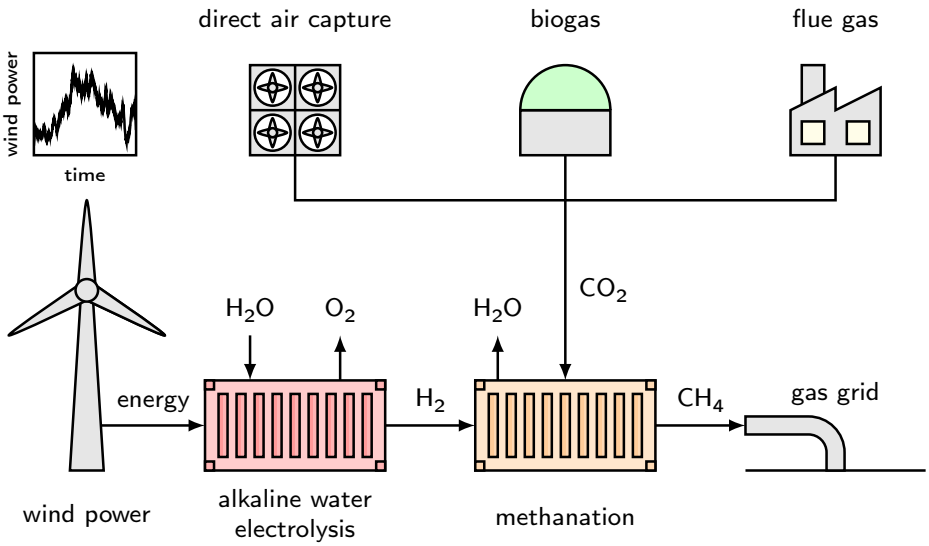

Figure 1.1.: Schematic of the Power-to-Gas process with the main sources for CO_2 and a typical wind power signal (adapted from Ref. 14).

In the PtG process, H_2 is first produced via electrochemical water splitting, usually in an alkaline water electrolyzer [15], using excess renewable energy. H_2 and CO_2 react further to CH_4 and H_2O in a catalytic reactor. The CO_2 can be used from industrial processes, where it is emitted in large quantities such as cement production, biogas, or even via direct-air capture [9]. In that way, CO_2 is converted to a C_1 building block for the industry or a clean-burning synthetic fuel with a neutral CO_2 balance. Moreover, this provides an excellent potential for seasonal energy storage for renewable energy [4, 8–10]. The

PtG process directly couples the renewable energy source with the natural gas grid, which has extensive storage capacities [10].

Next to its importance for the transition to a sustainable carbon economy, methanation is also very interesting from a fundamental point of view. It is the simplest conversion of CO_2 to a C_1 alkane over a transition metal catalyst. Thereby, it offers fundamental insights into the activation of the relatively inert CO_2 molecule on the supported metal catalyst. Furthermore, the CO_2 methanation is also a perfect example to address fundamental questions in multiscale modeling in the field of chemical engineering and heterogeneous catalysis [16–19]. The volatility of renewable energy sources imposes various challenges on the reactor operation and how to describe the behavior of the catalyst and the reactor in transient scenarios [19]. Whether the aim is to gain insights in the activation of CO_2 on the catalyst or to describe the reaction progress in the transient operation, the usage and thus the development of the microkinetics for the CO_2 methanation is required.

1.1. Methanation of CO_2

The methanation of CO_2 is a heterogeneously catalyzed reaction, which proceeds in the presence of a transition metal catalyst via the overall reaction equation

$$CO_2 + 4\,H_2 \rightleftharpoons CH_4 + 2\,H_2O\,(g) \qquad \{1\}$$

Nearly all the transition metals exhibit methanation activity, and the order of active materials is defined as follows: Ru>Fe>Ni>Co>Rh [11, 12, 20, 21]. Ru is the most active metal, but it is also very rare and consequently expensive. Although Fe has a high hydrogenation activity, the selectivity to CH_4 is low. Thus, the catalytic metal of choice is Ni because it is abundant, has a reasonable activity at moderate costs, and has a high selectivity to CH_4 [10, 12, 21]. Promoters can be added to the catalyst to increase the stability against sintering (e.g. MgO) [21] or to adjust the selectivity (e.g. K) [22]. A promising system is the bimetallic NiFe catalyst, which was unraveled by first-principles-based catalyst screening studies and proven in experiments to be superior in activity compared to the pure metals [23, 24].

The active metal is usually distributed on a porous ceramic support with a high surface area to prepare small metal crystals and a high metal surface area. Common support materials are γ-Al_2O_3, SiO_2, and CeO_2 [12, 21]. In addition to the dispersion of the active metal, the support can play a crucial role in the methanation mechanism [25]. CO_2 adsorbs on basic adsorption sites on the support, which are present on γ-Al_2O_3 or CeO_2 and forms various carbonates and bicarbonates [26–29]. The CO_2 methanation over Ni catalysts with basic sites on the support usually exhibits a higher activity compared to the similar catalyst on an acidic support, which indicates that the support or the metal/support interface participates in the mechanism [25, 30, 31].

The CO_2 methanation is a strongly exothermic reaction, with a standard reaction enthalpy of $\Delta_R H^\ominus = -164.7\,\mathrm{kJ\,mol^{-1}}$. It is constrained by limits from the thermodynamic equilibrium, which requires low temperatures to achieve high conversion and high selectivity to CH_4 [32]. Side reactions include (reverse) water-gas-shift reaction (reaction $\{2\}$), CO methanation (reaction $\{3\}$), Boudouard reaction

(reaction {4}), and n-alkane chain growth (reaction {5}), with mainly C_2H_6 and C_3H_8 [12, 32]. The typical operation window for the CO_2 methanation is between 573 to 823 K and 1 to 100 bar [11–13].

$$CO_2 + H_2 \rightleftharpoons CO + H_2O \quad \{2\}$$

$$CO + 3\,H_2 \rightleftharpoons CH_4 + H_2O \quad \{3\}$$

$$2\,CO \rightleftharpoons C + CO_2 \quad \{4\}$$

$$nCO_2 + (3\,n + 1)\,H_2 \rightleftharpoons C_nH_{2n+2} + 4\,nH_2O \quad \{5\}$$

Several reactor concepts are available: fixed-bed (adiabatic, polytropic), fluidized-bed, and three-phase [11–13, 33–35]. All reactor concepts (except the adiabatic reactor) focus on the removal of the released reaction heat to avoid the formation of hot-spots. Hot-spots must be avoided for two reasons. First, the catalyst starts to deactivate at temperatures beyond 823 K due to coke formation [36] and sintering of the metal crystals [12]. Second, high temperatures reduce the possible conversion and favor the formation of CO due to the thermodynamic equilibrium [32]. Nearly isothermal conditions can be achieved in the fluidized-bed and three-phase reactor, but they face other issues like catalyst attrition in the fluidized-bed and the stability of the liquid phase [12]. Most often used in the industry are fixed-bed reactors in tube bundle arrangement, which are cooled by thermal oil or molten salt [13]. A polytropic profile is usually obtained with a distinct hot-spot at the reactor entry in the fixed-bed reactors [37, 38]. Very promising are microstructured fixed-bed reactors, which intensify the heat and mass transfer because of the reduced characteristic length [39–41]. These microstructured reactors are best suited for decentralized applications and the most likely to be operated in a transient way [42].

1.2. Transient Methanation

All reactors for heterogeneously catalyzed reactions are usually designed for and operated in a steady-state. In contrast, the processes on the catalyst surface are never in a steady-state when the local environment on the atomic scale is considered [43, 44]. It is a dynamic system by nature with the cycle of adsorption-reaction-desorption on the active site, but even transformation of the active site via islands formation, reconstruction, and oxidation during the reaction [19, 44–46]. Usually, the only transient operation of the reactor occurs during the start-up/shut-down of the reactor or to regenerate the catalyst. For most of the lifetime of the reactor, the input concentrations, temperatures, and pressures will remain constant. Exceptions from this are catalytic reactors for emission control, e.g. of the automotive exhaust gas, which are always operated in a fully transient mode [47]. As shown in the wind signal in Figure 1.1, large variations in wind speed can occur already in the range of seconds to minutes that will lead to a dynamic operation of the alkaline water electrolyzer and a fluctuating production of H_2 [14]. Thus, transient operation of methanation reactors becomes necessary in the PtG setup. It is possible to consider scenarios for the PtG process where the operation occurs in the steady-state when large storage vessels are included for H_2 or CO_2, but this is not viable for economic reasons, especially for decentralized applications [11, 19].

The transient operation of reactors is not a new topic and has been around for a few decades [48], but it gained a revived interest because of processes to convert renewable energy, exemplified by the PtG concept [19]. So far, most of the applications of dynamic operation have focused on the periodic modulation of the inlet concentrations to achieve production rates superior to the steady-state [48].

Recently, new ideas on the dynamic operation of catalytic reactions with the aim of rate enhancement have been proposed [49–52]. Imposing dynamic stimuli to the catalyst to force an oscillation in the binding energy of adsorbates or the transition state with frequencies in the range of the turnover frequency can cause catalytic resonance behavior and enhance the rates by up to 4 orders of magnitude compared to the steady-state [50]. Tools for such a forced operation of the catalyst include, among others, strain, electrical fields, photocatalysis [52]. The concentration modulation is the most relevant and also the realistic scenario for methanation reactors regarding the PtG application on an industrial scale. The input for the PtG process is a highly chaotic signal, but this can be approximated by an ordered periodic concentration forcing. A form of such a continuous periodic operation is the so-called "bang-bang" operation, where the reactor inlet concentration is alternated between two different gas mixtures, usually the pure reactants, which is achieved by switching between two gas supply lines [48]. Consequently, periodically repeating step changes are applied to the system. In some catalytic processes, one of the reactants has an inhibiting effect on the reaction rate because of too strong adsorption, resulting in low steady-state reaction rates. When the concentrations are modulated between the reactants, the catalyst surface is periodically cleaned, allowing other reactants to adsorb. Thus, the reaction rate is higher compared to the steady-state operation. Examples for the beneficial effect of the bang-bang operation on the reaction rate are ammonia [53] and methanol synthesis [54]. This operation mode has also been applied for the CO [55–58] and CO_2 methanation [59–62]. During the steady-state CO methanation, the surface is covered by CO preventing H_2 from adsorbing, which results in low methanation rates. When the inlet concentration is switched between feeds of pure CO and H_2 it is possible to clean the surface from CO enabling the adsorption of H_2, which results in an improvement of the average reaction rates [56, 57]. However, no process improvement was observed for the CO_2 methanation during periodic concentration forcing [59–61].

A transient operation is also a valuable tool in kinetic investigations because the dynamic experiments provide further insights into the processes on the catalyst surface, which cannot be obtained from steady-state experiments. The adsorption/desorption steps become visible during the transients and the evolution of intermediates on the catalyst surface can be observed. When coupled to spectroscopic methods, it is even possible to track the intermediates on the surface [63, 64]. There are many concentration modulation techniques available, such as the temporal analysis of products (TAP) [65–67], the chemical transient kinetics (CTK) approach [68–70], the periodic transient kinetic approach [71], and the steady-state isotopic transient kinetic analysis (SSITKA) [72, 73]. Next to concentration changes, it is also possible to apply a transient operation via the modulation of the temperature, which results in temperature-programmed techniques like temperature-programmed desorption (TPD) and temperature-programmed surface reaction (TPSR) [48, 74]. These tools enable the direct measurement of elementary kinetic parameters, e.g. the activation energy of the desorption.

The transient CO_2 methanation on the reactor scale was solely studied by reactor modeling to investigate start-up/shut-down behavior [75–78], process control [79] and step changes [80–83]. All these simulation studies have in common that macrokinetic reaction kinetics are used, which were obtained from steady-state experiments to describe the transient behavior of the methanation reactor. However, these steady-state kinetic approaches fail to describe the observed transient behavior, which is clearly illustrated in the study of Marwood et al. [60] for the CO_2 methanation on Ru/TiO_2. For a correct prediction of the reactor behavior and design of the system, it is, therefore, necessary to implement kinetic approaches suitable for the dynamic operation, i.e. microkinetics.

1.3. Kinetics of the Methanation

In the design of the reactor or the field of chemical engineering in general, closed-form kinetic approaches are used to predict the performance of a reactor [17]. The simplest kinetic expression is the power-law approach, which for the methane production rate r_{CH_4} is

$$r_{CH_4} = k\, c_{H_2}^{\alpha}\, c_{CO_2}^{\beta} \tag{1.1}$$

where the rate constant k and exponents α and β are regressed to match experimental data from steady-state kinetic measurements. Examples for this approach for the CO_2 methanation are summarized by Weatherbee and Bartholomew [84]. A physically more sound method is the usage of a Langmuir-Hinshelwood-Hougen-Watson (LHHW) rate expression, which is derived from an underlying mechanism. The LHHW approach is determined from one possible path for CH_4 formation with the assumption of most abundant surface intermediates (MASIs) as well as equilibrated and rate-determining steps (RDS). Equation (1.2) is the LHHW ansatz developed by Koschany et al. [85] for the CO_2 methanation

$$r_{CH_4} = \frac{k\, p_{H_2}^{0.5}\, p_{CO_2}^{0.5} \left(1 - \frac{p_{CH_4}\, p_{H_2O}^2}{p_{CO_2}\, p_{H_2}^4\, K_{eq}}\right)}{\left(1 + K_{OH} \frac{p_{H_2O}}{p_{H_2}^{0.5}} + K_{H_2}\, p_{H_2}^{0.5} + K_{mix}\, p_{CO_2}^{0.5}\right)^2} \tag{1.2}$$

where a term in the nominator is included for the equilibrium and the denominator contains adsorption terms. The general procedure is to develop several of these LHHW expressions by assuming different mechanisms, MASIs or RDSs [17, 85–87]. All of these generated expressions are then regressed by fitting the rate constants and their temperature dependence to steady-state data. The approach which describes the experiments the best is considered to contain the correct mechanism. There are many studies deriving these LHHW approaches for CO_2 methanation [84–86, 88] and co-methanation of CO and CO_2 [89, 90]. Usually, several LHHW kinetics based on different mechanisms and assumptions (MASI, RDS) can describe the same set of data with equal accuracy. Therefore, no differentiation between the underlying mechanisms is possible [17]. Power-law and LHHW approaches can be classified as postdictive kinetics and they are often not well suited to make predictions for other setups or provide insights on the true mechanism [91]. Still, reaction kinetics based on the LHHW approach are most frequently used in transient reactor simulation studies [75–83] or to design optimized catalysts for dynamic operation [92]. However, extrapolation of these closed-form rate expressions beyond their range of regression can be erroneous [91, 93, 94]. This can be particularly problematic during transient operation, where large concentration gradients can be expected, with total dropouts of a single reactant. Moreover, coverage of adsorbates changes significantly during the transients, which challenges the assumption of a single MASI or RDS for all possible operating conditions. In addition, as clearly shown by numerous experimental studies for CO as well as CO_2 methanation, there is a storage of adsorbates on the catalyst surface [55–57, 59–61, 95] and on basic sites of the support for CO_2 [26–29]. Closed-form rate expressions fail to describe this reservoir and consequently, they are not suited to describe the transient behavior of the catalyst [60]. For a correct description of the behavior of the catalyst and the reactor during transient operation, it is necessary to apply a multiscale modeling approach and use microkinetic models, which account for all elementary steps of a mechanism [17, 94, 96, 97]. Therefore, it is first necessary to know the mechanism of the CO_2 methanation. The mechanism of a reaction can be derived by first-principles methods using density functional theory (DFT) calculations to access the

binding energy of adsorbates or the saddle point of transition states on a metal surface [17, 96, 97] or by surface science techniques in combination with operando methods [63, 64]. The methanation has already been investigated using DFT methods to investigate the mechanism [30, 31, 98–103]. Still, the mechanism for the methanation of CO_2 is not resolved and three possible pathways are discussed in the literature, which can be grouped into the formate, the carboxyl, and the redox/carbide pathway [10, 12, 73, 98, 100, 104]. These pathways differ in the activation of the CO_2 molecule (see Figure 1.2a). In the formate pathway, CO_2 is activated at the C atom, whereas the activation in the carboxyl pathway occurs on the O atom. An unassisted dissociation of CO_2^* to CO^* occurs in the redox/carbide pathway. The various pathways are not separate mechanisms and there are many possible connections among the different paths, which makes it challenging to unravel the methanation mechanism.

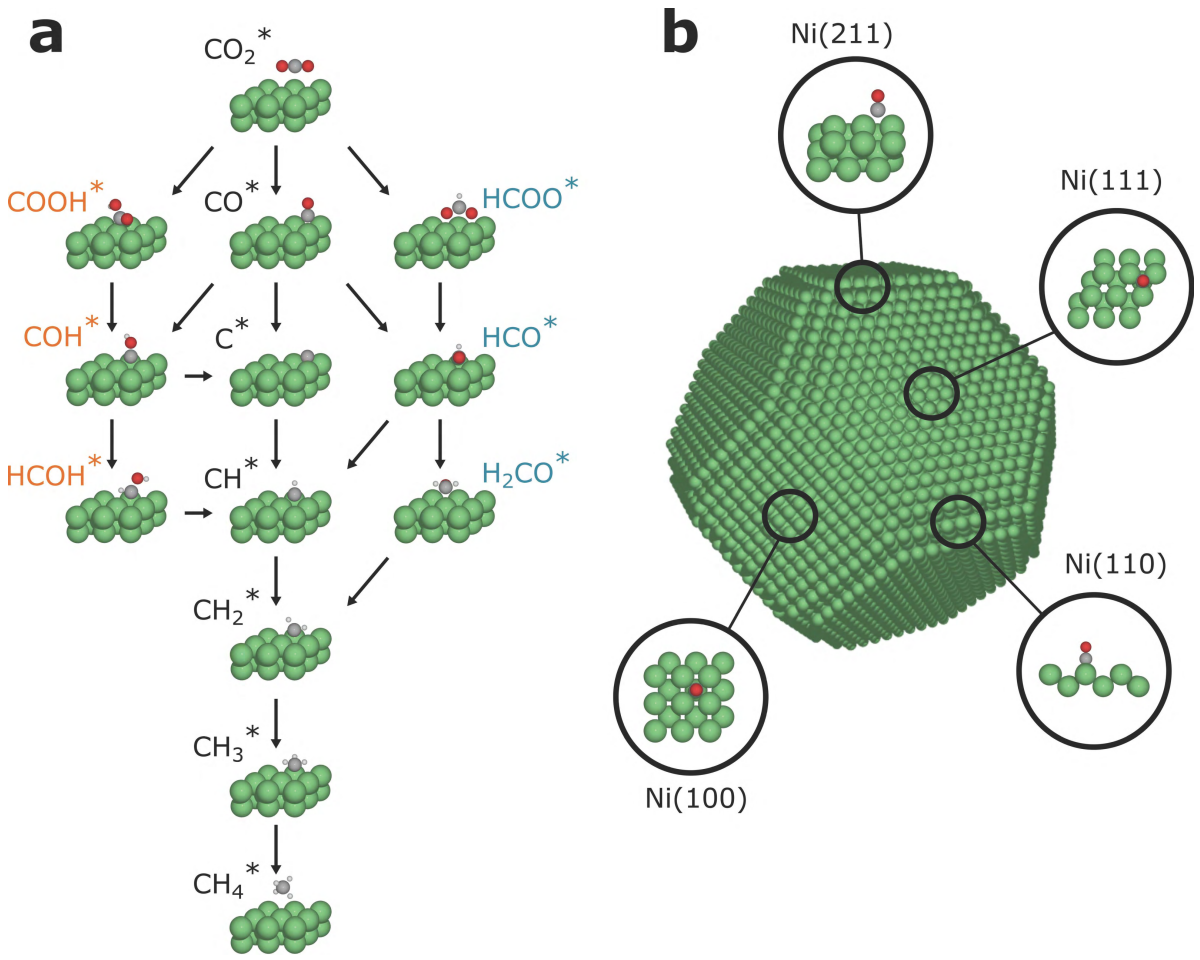

Figure 1.2.: (a) Schematic drawing of the discussed reaction network for the CO_2 methanation: the formate path (orange, left), the redox path (black, center), and the carboxyl path (blue, right). All adsorbates are shown in their most stable position on the Ni(111) surface. Adapted from Vogt et al. [100] (b). Equilibrium shape of a Ni crystal with 16,000 atoms and a size of 6.8 nm consisting of the Ni(111), Ni(100), Ni(110), and Ni(211) facet created via Wulff construction (see Chapter 5).

Another source of discussion is the active site for the methanation. The four most important facets of a Ni crystal are the (111), (100), (110) and the (211) facet (see Figure 1.2b) and their catalytic activity is controversially discussed. (111) and (100) are close-packed terrace sites, which have the highest share of the equilibrium shape. The terrace sites are separated by (211) steps and the open (110) facet [105]. From CO_2 methanation experiments on Ni/γ-Al_2O_3 catalysts, Beierlein et al. [106] conclude that it is

a structure insensitive reaction and should proceed on the terrace sites. In contrast, Vogt et al. [107] report a structure-sensitivity for the Ni/SiO_2 system. The similar CO methanation proceeds mainly on Ni(211) step sites [99].

There are published microkinetic models available in the literature for the CO_2 methanation on Ni catalysts [73, 98, 100, 108, 109]. Delgado et al. [108], Aparicio [73], and Blaylock et al. [110, 111] developed microkinetic models for the steam-reforming of methane, which also contain sub-mechanisms for the CO_2 methanation. In a very recent study, Schmider et al. [109] adjusted and appended the microkinetic model derived by Delgado et al. [108] to describe CO and CO_2 methanation on $Ni/\gamma\text{-}Al_2O_3$ catalysts. These three models are not derived from first-principles calculations but fitted to match experimental data. The regression of microkinetic models to experimental data with many kinetic parameters that are also strongly correlated due to the Arrhenius approach is challenging and can lead to ambiguous solutions [91]. Moreover, a $Ni/\gamma\text{-}Al_2O_3$ catalyst was used, which can alter the mechanism due to the activation of CO_2 on the support [30, 31]. Although the microkinetic model can describe the experimental results adequately, the microkinetic model does not represent the actual methanation mechanism because of the usage of a $Ni/\gamma\text{-}Al_2O_3$ catalyst. The omission of these support effects on the microkinetics is called structural uncertainty [112]. Furthermore, the regression of parameters of a microkinetic model to a set of experimental data can lead to physically unrealistic rate constants and activation barriers, especially with respect to the structural uncertainty of these models. This can run into problems when extrapolating the kinetics to predict the chemistry outside of the regressed parameter space. Physically correct rate constants and activation barriers of the elementary reactions as well as the thermochemistry of intermediates can be derived from first-principles using electronic structure calculations, mainly DFT, and statistical mechanics [17, 18]. Vogt et al. [100] and Lozano-Reis et al. [98] reported microkinetic models for the CO_2 methanation based on first-principles calculations. Lozano-Reis et al. [98] investigated the Ni(111) facet and Vogt et al. [100] derived microkinetic models for all four important Ni facets. Both studies consider all the three discussed pathways, but they come to different conclusions on the rate-determining steps, the important chemistry and even the general activity of the Ni facets. This is a consequence of the parametric uncertainty in the DFT methods, which is on the order of 20 to 30 $kJ\,mol^{-1}$ for the activation barriers and heats of formation of adsorbates [16, 97, 113]. Developing mechanisms by hand requires that the researcher knows all the relevant chemistry for a certain system, metal, and facet at the start of the mechanism generation procedure. Consequently, the developed mechanism is biased by the researcher's experience and expectations [18]. Another challenge with using electronic structure calculations is the high computational costs, which prohibit an exploration of all the possible chemistry. Screening methods like linear scaling [114] and Brønsted-Evans-Polanyi relations can significantly accelerate this procedure. However, the mechanism is still biased because the researcher needs to predict intermediates and elementary reactions. These screening techniques have been applied for the methanation reaction to determine superior catalyst materials like the NiFe system, but the results are based on a simple methanation mechanism with only a single rate-determining step [24, 115, 116]. Furthermore, the present microkinetic models violate the definition of elementary reaction [73, 108, 109], are thermodynamically inconsistent [108], the reaction networks are not complete, biased because they are developed by hand and the effect of parametric uncertainty is not considered [24, 73, 98, 100, 108, 109, 115, 116].

For a truly exhaustive and completely unbiased exploration of the CO_2 methanation mechanism, it is necessary to use automated reaction mechanism generation software like the Reaction Mechanism

Generator (RMG) [117–119]. RMG can predict all possible species and reactions using chemical graph theory and reaction templates. Kinetics of elementary reactions and thermochemistry of species is estimated via approximate routines based on DFT-derived databases. Upon the automated construction of these models, only the kinetically significant pathways are included in the final mechanism based on a rate-based algorithm. RMG was successfully used to discover mechanisms for combustion [120, 121], pyrolysis [122] and also for heterogeneously catalyzed reactions [118, 123, 124].

1.4. Objective of the Thesis

The CO_2 methanation shows great potential as an energy storage solution and for the production of sustainable natural gas. Its use in the Power-to-Gas process can require a transient operation of the system, which possesses many challenges. The fluctuating gas inlets can cause a product stream with ample variation in the composition that affects the temperature control of the exothermic reaction and productivity. Therefore, it is necessary to predict how such a reactor will behave in dynamic operation scenarios. One of the biggest assumptions in these process models is the reaction rate expression, which is a strongly simplified version of the true kinetics that govern the actual progress on the catalyst surface. The overall aim of this thesis is to derive microkinetics for the CO_2 methanation on Ni catalysts that can be used to describe the transient methanation. Experimental and theoretical methods are combined to develop such a microkinetic model.

In order to compare microkinetics for a Ni facet with experiments, it is necessary to ensure that the reaction proceeds only on the Ni surface. Although this seems obvious, it is a challenge for the CO_2 methanation because CO_2 adsorbs and can be activated on basic sites of the support, which can offer pathways with lower activation barriers compared to the mechanism on the Ni surface [30, 31, 125]. Consequently, an active Ni catalyst with acidic support needs to be produced. When deriving microkinetics with ab-initio methods, a Ni facet needs to be assumed. However, as shown in Figure 1.2b, the equilibrium shape of the Ni crystal consists of four facets and all can interact with CO_2. For the produced catalyst, it is necessary to investigate which of the facets is the most important for the activation of CO_2. When the important facet has been elucidated, microkinetic models can be developed. Instead of assuming/guessing the mechanism, the approach taken in this study relies on the automated generation of the reaction network to consider all the possible methanation chemistry. The thesis is structured into five main parts, where Chapter 3 to Chapter 6 are each a publication that addresses one part of the main research objective. Unpublished results are presented and discussed in Chapter 7. In the following, an overview of the Chapters is given. A graphical summary of the chapters is provided in Figure 1.3.

- **Chapter 3** presents a detailed dynamic one-dimensional heterogeneous model of a microstructured fixed-bed reactor with a state-of-the-art LHHW kinetic approach. The dynamic behavior of the reactor is investigated at various frequencies using forced periodic operation. This reveals strong temperature and concentration gradients.
- **Chapter 4** describes a spray-drying method for the production of highly active Ni/SiO_2 catalysts. The produced catalysts are characterized with various chemical and physical methods. A new transient screening technique for methanation catalysts is developed. The study reveals that the

catalysts can be tailored in the production process and used to produce optimal methanation catalysts, where the support does not interact with CO_2.

- **Chapter 5** combines microkinetic modeling with temperature-programmed desorption experiments to determine the active site for CO_2 activation. Thermodynamic parameters for the microkinetic model are determined from ab-initio electronic structure calculations. The study shows that the recorded TPD spectra can be attributed to various Ni facets, highlighting the possible contribution of each facet to the methanation mechanism. It is shown that the Ni(111) facet contributes significantly to the CO_2 desorption.
- **Chapter 6** contains the development of a microkinetic mechanism for the CO_2 methanation on the Ni(111) facet using an automated mechanism generator. Instead of assuming just one mechanism, all possible mechanisms within the uncertainty range of the parameters were created, evaluated and compared to experiments. A feasible mechanism is determined, which describes the experimental data from Chapter 4 without any fitting procedure. The study reveals strong limitations for the analysis of a single mechanism, given the current uncertainty of the exchange-correlation functionals in the DFT methods. The factors that govern the activity of the Ni(111) facet are unraveled by performing global uncertainty analyses.
- **Chapter 7** provides unpublished experimental results of the transient CO_2 methanation in a Berty reactor using the Ni/SiO_2 catalyst from Chapter 6. In this chapter, the experimental setup of the process unit is described and the residence time behavior of the Berty reactor is investigated first. The microkinetic models developed in Chapter 6 are then applied in a transient reactor model and compared to the experimental results. Feasible sets of parameters exist that can describe the transient experiments. Although the parameters between Chapter 6 and 7 of the feasible sets deviate, the dominant path for methane formation remains the same. This chapter highlights the complexity of the microkinetic model and further needs of research.

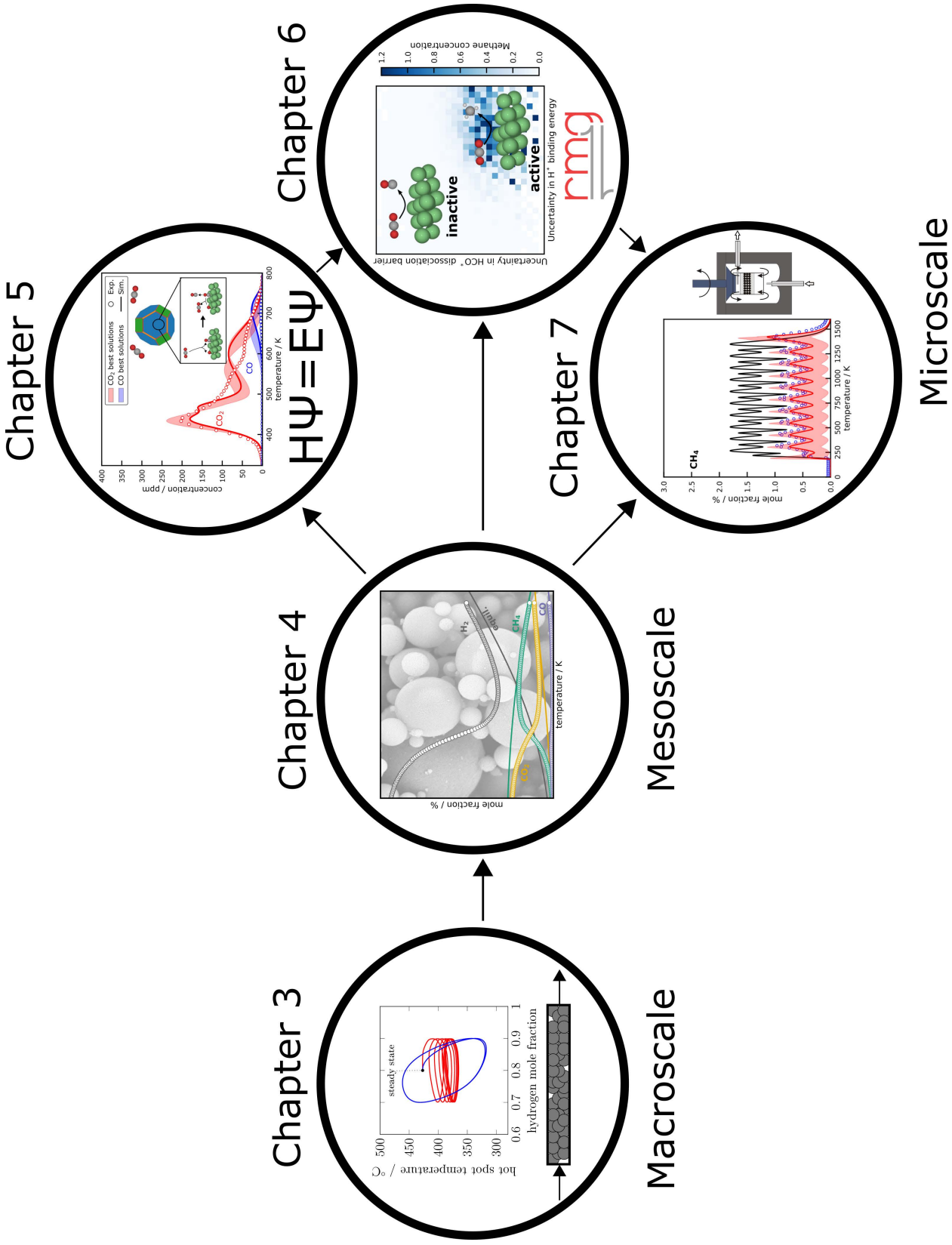

Figure 1.3.: Graphical overview of the chapters and their connection in this doctoral thesis.

CHAPTER 2

"There is nothing more exciting than science. You get all the fun of sitting still, being quiet, write down numbers, paying attention. Science has it all."

(Seymour Skinner, The Simpsons)

Publication Overview

The following publications were submitted and published in *peer-reviewed* scientific journals and are an integral part of this doctoral thesis.

1. **B. Kreitz**, G. D. Wehinger, T. Turek. Dynamic Simulation of the CO_2 Methanation in a Micro-Structured Fixed-Bed Reactor. *Chem. Eng. Sci.* **2019**, 195, 541-552

   The actual impact factor of *Chemcial Engineering Science* is **4.311 (2020)**. B. Kreitz conceptualized the idea, developed the reactor model, performed the dynamic simulation and wrote the manuscript. G. D. Wehinger assisted in editing of the manuscript. T. Turek conceptualized the idea, supervised, wrote and edited the manuscript. This publication is reprinted in Chapter 3 and contains the dynamic simulation study of a microstructured reactor with a LHHW reaction-rate expression and is an example for the state-of-the-art transient reactor modeling. Concentration forcing was applied to investigate the variation in temperature and productivity. Periodic forcing at very high frequencies reveals a relaxed steady-state of the reactor.

2. **B. Kreitz**, A. Martínez Arias, J. Martin, A. P. Weber, T. Turek. Spray-Dried Ni Catalysts with Tailored Properties for CO_2 Methanation. *Catalysts* **2020**, 10, 1410

   The actual impact factor of *Catalysts* is **4.146 (2020)**. B. Kreitz and A. Martínez Arias contributed equally to this work. B. Kreitz performed the chemical characterization of the catalysts and the experiments, developed the screening technique, conceptualized the work and wrote the manuscript. A. Martínez Arias produced the catalysts, performed the physical characterization, conceptualized the work and wrote the manuscript. J. Martin assisted with the experiments, writing and editing of the manuscript. A.P. Weber and T. Turek conceptualized the work, supervised and contributed to writing and editing of the manuscript. Chapter 4 is the reprint of this publication. The publication contains the production method of the Ni/SiO_2 catalysts and the screening procedure, along with a detailed description of the experimental results.

3. **B. Kreitz**, G.D. Wehinger, C. F. Goldsmith, T. Turek. Microkinetic Modeling of the CO_2 Desorption from Supported Multifaceted Ni Catalysts. *J. Phys. Chem. C* **2021**, 125, 2984-3000

   The actual impact factor of the *Journal of Physical Chemistry C* is **4.126 (2020)**. B. Kreitz conceptualized the idea, conducted the TPD experiments, the DFT calculations, performed the microkinetic simulations and wrote the manuscript. G. D. Wehinger assisted in editing of the manuscript. C. F. Goldsmith conceptualized the idea, supervised and contributed to writing and editing of the manuscript. T. Turek conceptualized the idea, supervised and contributed to writing and editing of the manuscript. The publication is reprinted in Chapter 5. This publication deals with the microkinetic modeling of the temperature-programmed desorption experiments assuming a composition of four Ni facets via a Wulff construction. Global uncertainty analysis is applied to investigate the effect of parametric uncertainty.

4. **B. Kreitz**, K. Sargsyan, K. Blöndal, E. J. Mazeau, R. H. West, G.D. Wehinger, T. Turek, C. F. Goldsmith. Quantifying the Impact of Parametric Uncertainty on Automatic Mechanism Generation for CO_2 Hydrogenation on Ni(111). *J. Am. Chem. Soc. Au* **2021**

   The actual impact factor of the *Journal of the American Chemical Society Au* is not defined yet, because it is a new journal. *Journal of the American Chemical Society Au* is an open access version of the *Journal of the American Chemical Society*, which has an impact factor of **15.419 (2020)**. B. Kreitz generated and evaluated the mechanism, performed the electronic structure calculations and experiments, conceptualized the idea and wrote the manuscript. K. Sargsyan provided support with the global sensitivity analysis. K. Blöndal assisted with the DFT calculations and the calculations of the thermodynamic properties. E. J. Mazeau and R. H. West contributed to the improvement of RMG. G. D. Wehinger assisted in editing of the manuscript. T. Turek supervised, assisted in conceptualization of the work and editing of the manuscript. C.F Goldsmith conceptualized the work, wrote and edited the manuscript and supervised. This publication is reprinted in Chapter 6. In this publication, RMG is used to construct 5,000 possible methanation mechanisms within the uncertainty of the database parameters. The model predictions are compared to experimental methanation results of a Ni/SiO_2 catalyst, which shows that within the uncertainty, feasible sets of mechanisms are available. A thorough analysis of all mechanisms is performed using local and global sensitivity analyses to unravel the factors controlling the methanation activity of the Ni(111) facet.

"To start press any key.
Homer: 'Where is the ANY key?'"

(Homer Simpsons, The Simpsons)

CHAPTER 3

Dynamic Simulation of the CO_2 Methanation in a Micro-Structured Fixed-Bed Reactor

Reprinted with permission from Elsevier

B. Kreitz, G. D. Wehinger, T. Turek.
Chem. Eng. Sci. **2019**, 195, 541-552
https://doi.org/10.1016/j.ces.2018.09.053

Abstract

The dynamic operation of methanation reactors is under discussion due to the increasing interest in power-to-gas technology. Here, hydrogen is supplied via a water electrolyzer which is powered by fluctuating renewable energy sources. With dynamic process modeling and simulation, the methanation reactor can be designed. Since the methanation reaction proceeds fast in the presence of an active catalyst and releases a large amount of reaction heat, the model has to account for the pellet phase in terms of energy, species mass and reaction. In this work, a dynamic 1D heterogeneous model is presented. The model describes a micro-structured fixed-bed reactor for the methanation of carbon dioxide under industrially relevant operating conditions with periodic oscillations of the inlet feed composition. The simulation shows that the hot spot temperature changes significantly during the periodic operation, both in position and magnitude. For high frequency changes the reactor behavior moves towards a thermally relaxed steady state. The outlet methane concentration in the dynamic operation does not reach the steady-state value. However, the model reveals interesting insights of the dynamic CO_2 methanation, which will be accompanied with experiments in the future.

Keywords: Dynamic simulation, Methanation, Micro-structured reactor, Carbon dioxide, Reactor modeling, Periodic operation

Supporting information for this publication is reprinted in Appendix A.

3.1. Introduction

The dynamic hydrogenation of carbon oxides towards methane becomes increasingly important, since methane is discussed as an energy storage molecule. Besides hydrogen, synthetic methane offers the possibility to store large amounts of energy from renewable sources for long time scales in an already existing storage system, the natural gas grid [1]. Carbon dioxide captured from the atmosphere, biogas plants, or flue gas emitted by large scale power plants can be converted with hydrogen from renewable energies via water electrolysis in the Sabatier reaction:

$$CO_2 + 4\,H_2 \rightleftharpoons CH_4 + 2\,H_2O \qquad \Delta_R H^{\ominus} = -164.70\,\mathrm{kJ\,mol^{-1}}$$

This overall process is usually denoted as power-to-gas technology [2]. The fluctuating and intermittent nature of renewable energy sources, e.g. wind or solar, results in fluctuations of the hydrogen outlet flow from an electrolyzer [3]. If the electrolyzer is directly coupled with a methanation reactor without a storage vessel for hydrogen, the reactor will be operated in a dynamic mode, too. There are various methanation reactor concepts available on the market, but most frequently fixed-bed reactors are used in power-to-gas plants [4].

The causes for the dynamic operation of the fixed-bed methanation can be changes in the inlet flow rate [5], variations in inlet temperature [6, 7] and fluctuations in the inlet composition [6, 7], where the latter is of particular importance. Variations in the inlet composition are not only the result of unintended fluctuations during the operation of a chemical reactor. Defined concentration forcing of the inlet composition (periodic, transients) can on one hand be used to study the reaction mechanism of the hydrogenation of carbon monoxide [8, 9] and carbon dioxide [10, 11]. On the other hand, this operation of a chemical reactor can lead to an improved performance compared to the steady-state behavior. When the inlet composition is cycled between pure carbon monoxide/carbon dioxide and hydrogen, the adsorption capacity for hydrogen can increase compared to steady-state operation, which results in a higher methane formation rate [12–16]. To determine the design of the methanation reactor in the power-to-gas process, the tool of process modeling is used. Dynamic reactor models in particular, are used to study the start and stop behavior or to conduct research on control strategies. Despite of growing interest in the dynamic operation of the carbon dioxide methanation in fixed-bed reactors, only a few of these dynamic models can be found in the literature, which differ in the regarded phases and dimensions of the reactor. 1D pseudo-homogeneous models were used for the simulation of the periodic isothermal operation [17], transient behavior [6, 7, 18] and the optimization of the reactor [19]. The work of Li et al. [20] covers a completely different aspect of the dynamic modeling of the methanation reaction. These authors solved a linearized version of a homogeneous plug flow model of a fixed-bed reactor, to investigate the thermal behavior for changes in the carbon monoxide inlet concentration and temperature. It was reported that the fast concentration response of the system is followed by a slow temperature response. In a further study the model was extended with mass transfer from the gas to the catalyst pellet and the calculation of an effective reaction rate, via a catalyst efficiency factor [21]. A different dynamic modeling approach was published by Currie et al. [22]. In this work the nonlinear frequency response analysis was applied on a pseudo-homogeneous isothermal flow reactor model to investigate the effect of periodic fluctuations in the inlet carbon dioxide concentration. This approach revealed an increase in carbon dioxide conversion for high frequency changes. The numerical simulation of the model also predicted an improved conversion depending on the amplitude and frequency. Further

published 2D pseudo-homogeneous models studied the start-up [23] and start-and-stop operation [24] of the methanation reactor. These model resolved axial and radial gradients, but did not account for temperature differences between the gas and solid phase.

A dynamic 1D heterogeneous model for the CO and CO_2 methanation in a structured catalytic reactor was proposed by Sudiro et al. [25] to calculate the temperature and concentration profile across the reactor. Despite simulating the dynamic behavior of the reactor, solely steady-state results were reported. Moreover, the balance equations of the pellet were not solved directly but rather a catalyst efficiency-factor was used, which was defined similar to Li et al. [21]. Other heterogeneous models did only regard the thermal behavior of the methanation reactor without the solution of mass balances [26, 27].

It can be seen from the reviewed literature that the current research mostly concentrates on the thermal behavior during the dynamic operation of the methanation reactor. That is why only pseudo-homogeneous models are used to describe the reactors or processes. Due to the nature of the methanation process with its fast reaction rate and large heat of reaction, gradients at the interface between the catalyst pellet and the gaseous phase will arise [28]. Also, diffusion limitations in the catalyst can occur and with the complex rate expressions an a priori estimation of the catalyst effectiveness factor can not be conducted. This demands for a dynamic model to account for the solid phase such as in the published 1D heterogeneous steady-state models by e.g. Schlereth et al. [28] and Ducamp et al. [29].

The development and solution of such a detailed dynamic 1D heterogeneous fixed-bed reactor model for the methanation of carbon dioxide is the aim of this paper. The model is formulated for a micro-structured fixed-bed reactor, since this reactor type can help to overcome the drawbacks of conventional fixed-bed reactors for the methanation [2]. Moreover, this reactor type is in discussion for small scale decentralized power-to-gas plants due to its good heat and mass transfer characteristics as well as its compact design [30]. Especially for this application, the dynamic operation of the reactor is of interest because of the high costs for hydrogen storage [2]. To study the dynamic behavior of the reactor under fluctuating inlet concentrations the forced periodic operation is used with different frequencies and amplitudes at a constant inlet velocity. This operation reveals a strong effect on the hot spot temperature and the main influencing factors on the thermal behavior can be explored.

3.2. Methods

3.2.1. Reactor Type and Dimensions

For this simulation study it is assumed, that the reaction is conducted in a microstructured fixed-bed reactor based on the rippled plate heat-exchanger design [31], which is depicted in Figure 3.1. From this reactor setup, only one channel is investigated in the simulation and therefore designed to reach certain criteria. It is assumed that the geometry of the reactor is a square channel with an edge length of 2 mm [31]. The reactor is filled with spherical catalyst particles with a diameter of 0.4 mm as a compromise between pressure drop and sufficient catalyst inventory. The inlet pressure of the reactor is set to 8 bar, since this is in the range of industrial relevant operating pressure for methanation reactors in power-to-gas plants [1]. The maximum allowed pressure drop is set to 400 mbar m^{-1}. If it is assumed that the methanation reactor should be suitable to operate in a power-to-gas plant, it would be of great advantage, if the reactor could achieve a conversion which allows for a direct supply in the natural gas

grid. For the case of Germany the synthetic natural gas must have a methane content above 90 % for the L-Gas quality and above 95 % to be classified as H-Gas [1]. This corresponds to a target conversion of the reactor for the L-Gas of 97.8 % and 98.98 % for the H-Gas, which is difficult to achieve in a single-stage reactor. In this study it is assumed that the L-gas quality shall be reached in the reactor. Due to the large reaction heat and the high activity of the catalyst towards methane a hot spot occurs at the entrance of the reactor. This hot spot must be kept below 500 °C to avoid degradation of the catalyst [4]. The assumed constraints are summarized in Table 3.1.

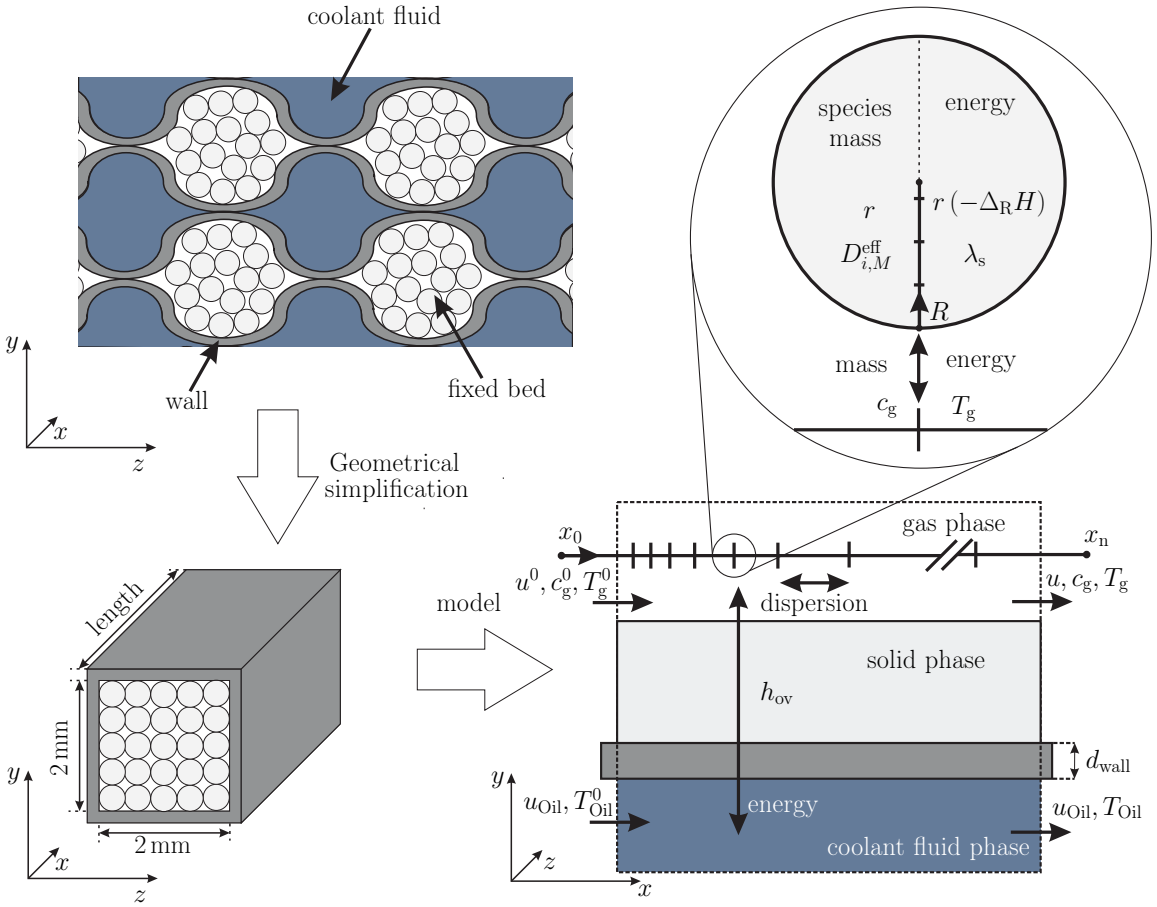

Figure 3.1.: Sketch of the microstructured fixed-bed reactor filled with spherical catalyst particles adapted from Gruber et al. [31] (upper left). Geometrical simplification of the setup to one squared channel (lower left) and abstraction of the channel with the 1D heterogeneous model (lower right). At each grid point the inter- and intraparticular gradients are evaluated to account for mass and heat transfer (upper right).

3.2.2. Governing Equations of the Microstructured Fixed-Bed Reactor Model

The steady-state and dynamic behavior is investigated with a 1D heterogeneous model. The mass and energy balance of the gas phase include an expression for the exchange of energy and mass with the catalyst surface [32]. A list of the used symbols can be found in the nomenclature. All the correlations are listed in the supplementary material. The axial dispersion of heat and mass is also accounted for.

The gas phase mass balance reads:

$$\varepsilon_{\text{bed}} \cdot \frac{\partial c_{\text{g,i}}}{\partial t} = -\frac{\partial (u \cdot c_{\text{g,i}})}{\partial x} + \varepsilon_{\text{bed}} \cdot D_{\text{ax,i}} \cdot \frac{\partial^2 c_{\text{g,i}}}{\partial x^2} - \beta_{\text{GS,i}} \cdot a_{\text{V}} \cdot (c_{\text{g,i}} - c^{\text{s}}_{\text{s,i}}) \tag{3.1}$$

The gas phase energy balance can be written as follows with an additional exchange term with the cooling fluid:

$$\begin{aligned} \varepsilon_{\text{bed}} \cdot \rho_{\text{g}} \cdot c_{p,\text{g}} \cdot \frac{\partial T_{\text{g}}}{\partial t} = &-\frac{\partial (u \cdot \rho_{\text{g}} \cdot c_{p,\text{g}} \cdot T_{\text{g}})}{\partial x} + \lambda_{\text{ax}} \cdot \frac{\partial^2 T_{\text{g}}}{\partial x^2} \\ &- h_{\text{GS}} \cdot a_{\text{V}} \cdot (T_{\text{g}} - T^{\text{s}}_{\text{s}}) - \frac{4}{d_{\text{h}}} \cdot h_{\text{ov}} \cdot (T_{\text{g}} - T_{\text{oil}}) \end{aligned} \tag{3.2}$$

At the entrance of the reactor the Danckwert's boundary conditions for the mass and energy balance are used due to the consideration of axial dispersion.

$$-\varepsilon_{\text{bed}} \cdot D_{\text{ax,i}} \cdot \frac{\partial c_{\text{g,i}}}{\partial x} = u \cdot (c^0_{\text{g,i}} - c_{\text{g,i}}) \tag{3.3a}$$

$$-\lambda_{\text{ax}} \cdot \frac{\partial T_{\text{g}}}{\partial x} = u \cdot \rho_{\text{g}} \cdot c_{p,\text{g}} \cdot (T^0_{\text{g}} - T_{\text{g}}) \tag{3.3b}$$

At the reactor exit it is assumed that the change in concentration and temperature can be linear, hence the second order derivative is set to zero. This can be valid in the dynamic simulation when a sufficient reaction rate at the reactor exit is still present. Moreover, this assumption improves the numerical stability of the model and the simulation is more likely to converge. The difference in the gas phase temperature at the outlet of the reactor between this and the Danckwert's boundary condition is in the range of $2{\times}10^{-3}$ K.

$$0 = \frac{\partial^2 c_{\text{g,i}}}{\partial x^2} \tag{3.4a}$$

$$0 = \frac{\partial^2 T_{\text{g}}}{\partial x^2} \tag{3.4b}$$

For the momentum balance the equation of Eisfeld and Schnitzlein [33] is applied to account for the effect of the confining reactor walls. The definition of the coefficients A and B can be found in the supplementary information.

$$\frac{\partial p}{\partial x} = -154 \cdot A^2 \cdot \frac{(1-\varepsilon_{\text{bed}})^2}{\varepsilon^3_{\text{bed}}} \cdot \frac{\mu_{\text{g}} \cdot u}{d^2_{\text{s}}} - \frac{A}{B} \cdot \frac{1-\varepsilon_{\text{bed}}}{\varepsilon^3_{\text{bed}}} \cdot \frac{\rho_{\text{g}} u^2}{d_{\text{s}}} \tag{3.5}$$

The volume reduction of the reaction causes a change in the gas velocity, which is accounted for by the overall mass conservation (Equation (3.6)). It is assumed, that the mass does not change over time, since there is no mass accumulation on the catalyst surface based on adsorption. This was also assumed in the dynamic model of Güttel [17].

$$u = u^0 \cdot \frac{\rho^0_{\text{g}}}{\rho_{\text{g}}} \tag{3.6}$$

Due to the strongly exothermic reaction, the temperature gradient inside the pellet cannot be neglected. Therefore, the mass and energy balances are formulated based on a spherical geometry as:

$$\varepsilon_{\text{s}} \cdot \frac{\partial c_{\text{s,i}}}{\partial t} = D^{\text{eff}}_{\text{i,M}} \cdot \left(\frac{\partial^2 c_{\text{s,i}}}{\partial R^2} + \frac{2}{R} \frac{\partial c_{\text{s,i}}}{\partial R} \right) + \rho_{\text{s}} \cdot \nu_{\text{i}} \cdot r \tag{3.7}$$

$$\varepsilon_{\text{s}} \cdot \rho_{\text{s}} \cdot c_{p,\text{s}} \cdot \frac{\partial T_{\text{s}}}{\partial t} = \lambda_{\text{s}} \cdot \left(\frac{\partial^2 T_{\text{s}}}{\partial R^2} + \frac{2}{R} \frac{\partial T_{\text{s}}}{\partial R} \right) + \rho_{\text{s}} \cdot (-\Delta_{\text{R}} H) \cdot r \tag{3.8}$$

The solid phase and the gaseous phase are coupled with a boundary condition at the catalyst surface. On the surface, the mass flux from the gas phase via convection and the transport inside the pellet via diffusion have to be equal in a steady-state. Since the stagnant film on the catalyst particle is small, it is further assumed that the accumulation of mass in the film can be neglected for the dynamic operation.

$$-D_{\mathrm{i,M}}^{\mathrm{eff}} \cdot \frac{\partial c_{\mathrm{s,i}}^{\mathrm{s}}}{\partial R} = \beta_{\mathrm{GS,i}} \cdot (c_{\mathrm{s,i}}^{\mathrm{s}} - c_{\mathrm{g,i}}) \tag{3.9a}$$

$$-\lambda_{\mathrm{s}} \cdot \frac{\partial T_{\mathrm{s}}^{\mathrm{s}}}{\partial R} = h_{\mathrm{GS}} \cdot (T_{\mathrm{s}}^{\mathrm{s}} - T_{\mathrm{g}}) \tag{3.9b}$$

In the center of the pellet symmetry is assumed.

$$0 = \frac{\partial c_{\mathrm{s,i}}^{\mathrm{c}}}{\partial R} \tag{3.10a}$$

$$0 = \frac{\partial T_{\mathrm{s}}^{\mathrm{c}}}{\partial R} \tag{3.10b}$$

The cooling medium is coupled with the reactor to account for heat transfer resistances and to regard the heating of the coolant along the reactor. The energy balance for the coolant is expressed by the following equation:

$$\rho_{\mathrm{oil}} \cdot c_{p,\mathrm{oil}} \cdot \frac{\partial T_{\mathrm{oil}}}{\partial t} = -\frac{\partial (u_{\mathrm{oil}} \cdot \rho_{\mathrm{oil}} \cdot c_{p,\mathrm{oil}} \cdot T_{\mathrm{oil}})}{\partial x} + \frac{4}{d_{\mathrm{h}}} \cdot h_{\mathrm{ov}} \cdot (T_{\mathrm{g}} - T_{\mathrm{oil}}) \tag{3.11}$$

The coolant flows parallel with the reactant gas and thus the inlet temperatures are identical.

3.2.3. Kinetics

The available reaction kinetics for the methanation of CO_2 were recently reviewed by Rönsch et al. [27]. The kinetic approach of the CO_2 methanation can be described via an indirect route - a linear combination of the CO methanation and the water gas shift reaction - or a direct route. Kinetic rate equations for the first approach can be found in the works of Kopyscinski et al. [34] and Xu and Froment [35]. These are the mostly used reaction kinetics for simulation studies concerning either the CO methanation or the CO_2 methanation. It is pointed out by Rönsch et al. [27] that the kinetic experiments from which the rate expressions were derived, were not perfromed under typical methanation conditions. To use the rate expression for the CO_2 methanation they have to be modified as shown by Witte et al. [36]. A different kinetic approach can be found in the study of Koschany et al. [37], which describes the CO_2 methanation for temperatures of 200 to 340 °C and pressures between 5 and 15 bar. Here, it was shown that a Langmuir-Hinshelwood-Hougan-Watson (LHHW) based reaction rate (Equation (3.12)) is suitable to describe experimental results. Moreover, only traces of carbon monoxide were detected, which leads to the negligence of side reactions. The investigated concentration ranges of carbon dioxide and hydrogen in the feed are between H_2/CO_2 ratios of 0.25 to 8. This allows concentration forcing in the feed with a high amplitude, while staying in the valid range of the kinetic approach. For details on the reaction kinetic see Ref. 37.

$$r = \frac{k \cdot p_{\mathrm{H_2}}^{0.5} \cdot p_{\mathrm{CO_2}}^{0.5} \cdot \left(1 - \frac{p_{\mathrm{CH_4}} \cdot p_{\mathrm{H_2O}}^2}{p_{\mathrm{CO_2}} \cdot p_{\mathrm{H_2}}^4 \cdot K_{\mathrm{eq}}}\right)}{\left(1 + K_{\mathrm{OH}} \frac{p_{\mathrm{H_2O}}}{p_{\mathrm{H_2}}^{0.5}} + K_{\mathrm{H_2}} \cdot p_{\mathrm{H_2}}^{0.5} + K_{\mathrm{mix}} \cdot p_{\mathrm{CO_2}}^{0.5}\right)^2} \tag{3.12}$$

The use of a kinetic expression for only the CO_2 methanation and negligence of the side reactions can be supported by the work of Ducamp et al. [29]. For a stoichiometric composition and in the investigated

temperature range of 200 to 275 °C at pressures of 4 to 8 bar bar neither the experiments nor the simulation with the rate expression from Xu and Froment showed any formation of carbon monoxide, although a hot spot with temperatures of approximately 500 to 550 °C was observed. Steady-state reaction rate expressions of this type are often used in dynamic simulation studies for the methanation of carbon monoxide [6, 7, 17, 18, 20, 21, 25, 38] and carbon dioxide [6, 7, 18, 22–25, 38]. Therefore, the LHHW reaction rate type is also used in this study. To the best of our knowledge, no dynamic reaction rate expression for the methanation of CO_2 over a Ni/Al_2O_3 catalyst is currently available.

3.2.4. Properties and Correlations

All properties are computed at each grid point in dependence of temperature, pressure and the mixture composition. The equations and the parameters for the calculation are listed in the ESI. The viscosity of the single components is calculated with a polynomial expression [39]. The viscosity of the mixture can be calculated according to the Wilke approach [40]. Strongly coupled with the viscosity is the thermal conductivity of the gas mixture. The correlation for the calculation of the thermal conductivities of the pure components can be found in the work of Elnashaie and Elshishini [41]. The thermal conductivity of the gas mixture is calculated via the Wassiljewa approach and the Lindsay-Bromley method. For the thermodynamic properties the Shomate equations can be applied which can be found on the NIST Chemistry Webbook [42]. As cooling medium, a thermal oil from the type Marlotherm® LH [43] (Sasol) is assumed. With linear regression a function is created which describes the temperature dependence of the properties (see ESI). The velocity of the cooling agent u_{oil} is set to $1\,\mathrm{m\,s^{-1}}$.

The porosity of the packed bed can be calculated from the following equation which is valid for a mono-disperse package of spheres [44].

$$\varepsilon_{\mathrm{bed}} = 0.4 + (1 - 0.4) \cdot \frac{0.562}{\frac{d_{\mathrm{h}}}{d_{\mathrm{s}}}} \tag{3.13}$$

The density of the gas can be calculated with the ideal gas law.

$$\rho_{\mathrm{g}} = \frac{p \cdot \sum_{i=1}^{n} M_{\mathrm{i}} \cdot y_{\mathrm{g,i}}}{R_{\mathrm{g}} \cdot T_{\mathrm{g}}} \tag{3.14}$$

For the determination of the diffusion coefficients for the diffusion pairs, the equation of Fuller-Schettler-Giddings is used [45].

$$D_{\mathrm{i,j}} = \frac{T_{\mathrm{g}}^{1.75} \cdot \left(\frac{1}{M_{\mathrm{i}}} + \frac{1}{M_{\mathrm{j}}}\right)}{p \cdot \left(\nu_{\mathrm{Diff,i}}^{\frac{1}{3}} + \nu_{\mathrm{Diff,j}}^{\frac{1}{3}}\right)^2} \tag{3.15}$$

The parameter $\nu_{\mathrm{Diff,i}}$ is the diffusion volume of the species i. The values are taken from Perry and Green [46] and listed in the ESI. As diffusion model for the catalyst pellet the Wilke model is chosen. This model takes into account the diffusion of the components in the gaseous mixture [47, 48].

$$D_{\mathrm{i,M}} = \frac{1 - y_{\mathrm{g,i}}}{\sum_{j=1, j\neq i}^{n} \frac{y_{\mathrm{g,j}}}{D_{\mathrm{i,j}}}} \tag{3.16}$$

The effect of Knudsen diffusion inside the pellets is considered via the Bosanquet equation.

$$\frac{1}{D_{\mathrm{i,M}}^{\mathrm{eff}}} = \frac{\tau}{\varepsilon_{\mathrm{s}} \cdot D_{\mathrm{i,M}}} + \frac{1}{D_{\mathrm{Kn}}} \tag{3.17}$$

The use of the Wilke-Bosanquet model makes a proper description of the multicomponent diffusion possible without using the complete dusty-gas-model [41, 47, 48]. In the ESI a comparison between the Dusty-Gas model and the Wilke-Bosanquet model is performed which justifies the aforementioned assumption. For the calculation of the transport properties state-of-the art correlations are used. The correlations and the references are summarized in Table 3.1 and the corresponding equations are listed in the ESI.

The catalyst for which the rate expression is valid is a $Ni/Al(O)_x$ catalyst prepared via coprecipitation and having a high nickel loading of 50 % [37]. The catalyst density is reported with 2,350 $kg\,m^{-3}$. The thermal conductivity of the catalyst is an important property for the thermal management of the reactor since the conductivity of the packed bed has the highest thermal resistance. In this simulation a value of 0.67 $W\,m^{-1}\,K^{-1}$ is assumed [29]. Despite the significance of this parameter, the values for Ni/Al_2O_3 catalyst reported in the literature differ by two orders of magnitude. In a few simulation studies the thermal conductivity is assumed to be 3 to 5 $W\,m^{-1}\,K^{-1}$ [18, 49] or even 13.8 $W\,m^{-1}\,K^{-1}$ [50, 51] whereas other works assume a value around 0.15 to 0.2 $W\,m^{-1}\,K^{-1}$ [52]. Soomro and Hughes [53] measured the thermal conductivity of Ni/Al_2O_3 catalysts prepared via impregnation and coprecipitation. Their results show that the thermal conductivity increases with nickel loading and is between 0.215 $W\,m^{-1}\,K^{-1}$ (0.5 % Nickel content) and 0.448 $W\,m^{-1}\,K^{-1}$ (72 % Nickel content). Results from Sharma et al. [54] for $Ni/SiO_2/Al_2O_3$ are in the same order of magnitude. These authors obtained a slightly lower conductivity which can be explained with the lower thermal conductivity of the SiO_2 [55]. Catalyst prepared with the coprecipitation method show an even higher thermal conductivity compared to the impregnated catalyst for the same nickel loading [53, 54]. Therefore the selected thermal conductivity of the catalyst from Ducamp et al. [29] stands to reason.

3.2.5. Boundary Conditions

Steady-State Operation

The inlet composition of the feed is a stoichiometric mixture without any dilution. The mole fractions of CH_4 and H_2O at the inlet are set to 1×10^{-5} which improves the robustness of the model. The gas velocity is obtained by the solution of the pressure drop equation from Eisfeld and Schnitzlein [33] which results in a value of 0.349 $m\,s^{-1}$. The GHSV of this reactor is then 3,143 h^{-1}. This GHSV is close to the range of reported values for a multitubular methanation reactor of an operating power-to-gas plant which is 2,000 to 5,000 h^{-1} [1].

Dynamic Operation

One way of applying a periodic operation to the chemical reactor is to change the volume flow of the two components while keeping the overall gas velocity constant. This means, that the amplitude of the hydrogen and the carbon dioxide signal have a phase shift of 180°. The periodic operation is applied to the reactor with a sinusoidal oscillation of the feed composition at the reactor inlet. The mathematical expression for this oscillation is shown in equation Equation (3.18a) and Equation (3.18b):

$$y_{H_2}(t) = \bar{y}_{H_2} + \Delta y \cdot \sin\left(2\pi \cdot f \cdot t\right) \tag{3.18a}$$

$$y_{CO_2}(t) = \bar{y}_{CO_2} - \Delta y \cdot \sin\left(2\pi \cdot f \cdot t\right) \tag{3.18b}$$

Table 3.1.: Summary of the constraints, properties, assumptions and correlations used in the model.

Constraint	Value	Reference
T_{max} / °C	< 500	[4]
x^{dry}_{g,CH_4} / %	> 90	[1]
Δp / bar m^{-1}	< 0.4	Assumption
Property	**Value**	**Reference**
ρ_s / kg m^{-3}	2350	[37]
λ_s / W m^{-1} K^{-1}	0.67	[29]
$c_{p,s}$ / J kg^{-1} K^{-1}	880	[24]
λ_{wall} / W m^{-1} K^{-1}	18	[24]
τ / 1	4	[28]
d_{pore} / m	20×10^{-9}	[28]
d / m	2×10^{-3}	[31]
d_{wall} / m	1×10^{-3}	Assumption
u_{oil} / m s^{-1}	1	Assumption
d_s / m	400×10^{-6}	Assumption
p / bar	8	Assumption
ε_s	0.5	Assumption
Property	**Model**	**Reference**
$D_{i,j}$	Fuller-Schettler-Giddings	[46]
λ_i	polynomial	[41]
λ_g	Wassiljewa	[41]
μ_i	polynomial	[39]
μ_g	Wilke	[41]
$c_{p,g}$	Shomate equations	[42]
r	LHHW	[37]
Correlations	**Model**	**Previous use***
λ_{bed}	Zehner-Bauer-Schlünder [56]	Schlereth et al. [28]
h_{GS}, k_{GS}	Gnielinski [57]	Güttel and Turek [17]
h_{ov}	α_{wall} model [44]	Schlereth et al. [28]
D_{ax}, λ_{ax}	Tsotsas [44]	
h_{oil}	Gnielinski [58]	
$D^{eff}_{i,M}$	Wilke-Bosanquet	Kiewidt and Thöming [59]

*Some of the correlations are already used in the referenced simulation studies concerning microreactors or the CO_2 methanation in fixed-bed reactors.

In this paper the influence of amplitude Δy and frequency f on the reactor behavior is investigated. The amplitude is set to 25 %, 50 % and 75 % of the mole fraction of carbon dioxide. This means that the mole fraction of hydrogen and carbon dioxide is disturbed with a Δy of 0.05, 0.1 and 0.15. The studied frequencies are 2 s^{-1}, 1 s^{-1}, 0.1 s^{-1}, 0.05 s^{-1} and 0.033 s^{-1}. The low frequencies correspond to periods which are far longer than the residence time of the reactor of 2.1 s. To account for high-frequency changes in the signal two shorter periods are used. The frequencies and amplitudes are arbitrarily chosen. The inlet gas composition for the sinusoidal signal is depicted in Figure 3.2.

3.2.6. Numerical Solver

For the solution of the partial differential equations (PDEs) the gPROMS ModelBuilder [60] is used, which has already been applied for the simulation of the methanation reaction [25]. As axial discretization method the first order backwards finite difference method (BFDM) is applied. The discretization is accomplished with a logarithmic grid, to get a good resolution of the hot spot. This discretization method can handle these stiff PDEs, since it offers good numerical stability owing to the implicit nature [18, 24]. The discretization inside the pellet is conducted with a second order central difference

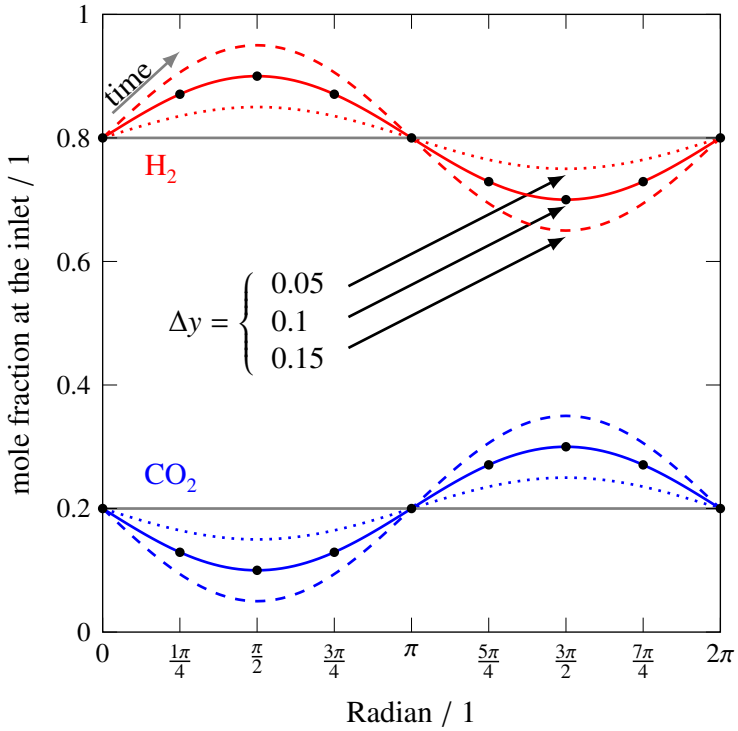

Figure 3.2.: Inlet gas composition with the sinusoidal oscillation for the amplitudes of $\Delta y = 0.05$ (dotted), $\Delta y = 0.1$ (solid) and $\Delta y = 0.15$ (dashed).

method (CFDM). Due to the detailed model and the high degree of complexity between the PDEs and the correlations, a solution for the steady-state cannot be obtained by a direct solution. In order to get good starting values, the problem is initialized with the solution of less detailed and less complex models (i.e. isothermal pseudo-homogeneous, polytropic pseudo-homogeneous, ..., polytropic detailed heterogeneous). The complexity is increased stepwise to ensure a steady-state solution at a rather low operation temperature of 220 °C. After obtaining the initial solution, the temperature of the reactor is raised with a small ramp of $2\,\mathrm{K\,min^{-1}}$ to the operating temperature, in correspondence to the start-up of a reactor. This strategy greatly improves the robustness of the model and a steady-state solution for the detailed model at a high temperature can be found. For the integration of the PDEs the SRADAU Solver is used. The solver is a 4^{th} order Runge-Kutta-method with variable time step adaption. The influence of the number of discretization points on the results for the steady-state is checked. The usage of 400 axial discretization points and 10 points in the pellet is found to be a suitable compromise between accuracy and computation time. The number of axial discretization points must be sufficiently high to decrease the effect of numerical diffusion which is caused by the implicit difference method.

3.3. Results and Discussion

3.3.1. Steady-State Behavior

In Figure 3.3 the steady-state performance of the microreactor is shown. For an inlet temperature of 280 °C the performance of the reactor meets all aforementioned criteria. In this case, a reactor length of 40 cm is required to reach the conversion of 97.8 % which is sufficient for the L-gas quality. The conversion curve shows a steep increase at the entrance of the reactor. This is caused by the

temperature increase due to the large reaction heat and the corresponding fast reaction rate. The gas phase temperature shows a maximum temperature rise of 150 K. The main reason for the occurrence of the hot spot is the limiting heat transfer in the packed bed. The mean thermal resistance on the coolant side ($0.34\,m^2\,K\,kW^{-1}$) is smaller than the mean convective heat transfer resistance on the inside ($0.5\,m^2\,K\,kW^{-1}$) and the mean resistance of the bed ($0.88\,m^2\,K\,kW^{-1}$).

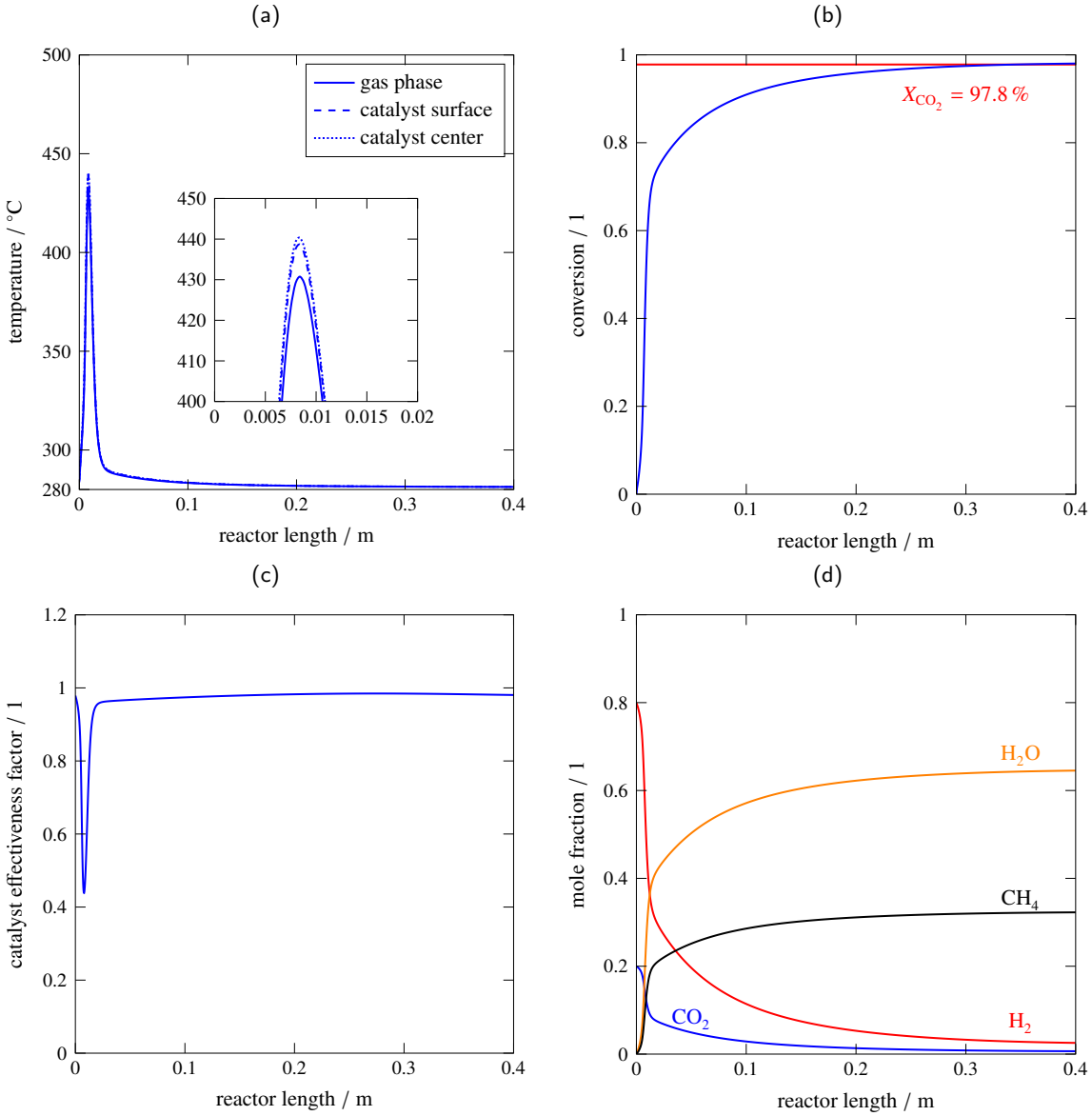

Figure 3.3.: Results for the steady-state simulation of the microstructured fixed bed reactor. (a) Axial temperature profile of the gas phase (T_g), the catalyst surface (T_s^s) and the catalyst center (T_s^c). (b) Conversion profile over the reactor length. (c) Catalyst effectiveness factor over the reactor length calculated for a spherical particle according to Güttel and Turek [61]. (d) Profile of the gas phase composition. *Conditions:* $T_g^0 = 280\,°C$, $d = 2\,mm$, $d_s = 400\,\mu m$, $p = 8\,bar$, $GHSV = 3{,}143\,h^{-1}$.

Having a closer look at the thermal conductivity of the gas phase, it can be seen, that this parameter is particularly high at the entrance of the reactor with $\lambda_g = 0.178\,W\,m^{-1}\,K^{-1}$ caused by the good thermal conductivity of hydrogen. This value decreases to the end of the reactor to almost $\lambda_g = 0.061\,W\,m^{-1}\,K^{-1}$. Therefore, the temperature increase is amplified. A counteracting effect on the hot spot formation is the diffusion resistance inside the catalyst pellet. Due to the rising temperature the

reaction rate is greatly enhanced caused by the exponential dependence. At the hot spot the diffusion inside the pellet is too slow to utilize the entire catalyst [29]. The diagram of the effectiveness factor shows that the value drops to nearly 0.5. Neglecting the diffusion inside the catalyst pellet, which is the case in a pseudo-homogeneous model, would predict a far higher hot spot temperature. The study of Schlereth et al. [28] reveals the same thermal behavior in a cooled fixed-bed reactor. As can be seen in Figure 3.3, a gradient of 8.7 K occurs between gas phase and the catalyst surface. Main reason for this strong difference is the low gas velocity which results in a low gas solid heat transfer coefficient. The temperature rise inside the catalyst pellet due to the exothermic reaction is nearly 2 K. Given these results it appears that intraparticle gradients must be taken into account for a proper description of the reactor behavior.

3.3.2. Periodic Operation

In the periodic operation the oscillation at the inlet causes numerous parameters to change over the length of the reactor and time. The gas phase temperature of the reactor, which is the main parameter of interest besides the conversion, under dynamic operation for $f = 0.1\,\mathrm{s}^{-1}$ and $\Delta y = 0.1$ is shown in Figure 3.4. Only the first 5 cm are regarded, since the steady-state simulation reveals that the hot spot is formed very close to the inlet. The axial position of the hot spot does not change significantly under periodic operation, as a consequence of the constant GHSV. The solid black line corresponds to the temperature profile obtained in the steady-state. The developing temperature profiles in the hydrogen rich part of the cycle (0 to π, see Figure 3.2) are presented in dashed lines whereas those in the hydrogen lean part of the cycle (π to 2π) are dotted. It can be obtained from the profiles, that the temperature of the hot spot is strongly decreasing. When the hydrogen concentration surpasses a maximum ($\pi/2$), the temperature at the hot spot is only 340 °C. In the hydrogen lean part of the cycle, the temperature of the gas phase rises beyond the steady-state value for the hot spot.

The illustration of the dynamic behavior of the reactor can be far better explored in a phase plane diagram (Figure 3.5). In these diagrams the maximum temperature is plotted against the mole fraction of hydrogen in the inlet (Figure 3.5 (a)) to show the thermal effects during the oscillation. The phase plane diagram reveals the same information, as axial temperature profiles at different times of the oscillation (Figure 3.4). The Figure 3.5 (b) and the additional Fig. 1 in the ESI show the reasons for the changes in the temperature profile. In the hydrogen rich part of the cycle the mean thermal conductivity of the gaseous mixture is enhanced because hydrogen has a high thermal conductivity. This directly improves the conductivity of the packed bed and as a result the overall heat transfer coefficient is enlarged. The effect is also amplified by an increase in the mean velocity because of the decreasing density of the gas mixture. The evaluation of the reaction rate over the reactor in the periodic operation at a certain time is achieved with the definition of an mean effective reaction rate. This rate accounts for the entire behavior of the reactor. Due to the 1D heterogeneous model this includes intraparticle mass and heat transfer. The mean effective reaction rate is defined via the following equation:

$$\bar{r} = \sum \frac{r^{\mathrm{s}} \cdot \eta}{\text{Number of discretization points}} \tag{3.19}$$

The reaction rate affects and is affected by the temperature in the reactor. To separate these coupled effects an isothermal simulation is performed (see Figure 3.5 (b)). The simulation points out, that the mean effective reaction rate is decreasing with increasing hydrogen content and has a higher value in

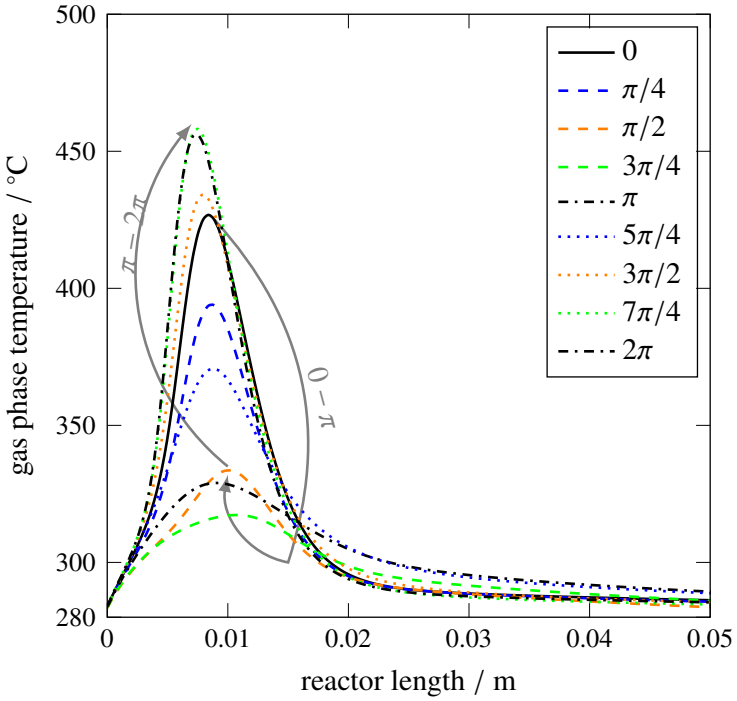

Figure 3.4.: Axial gas phase temperature profile under sinusoidal oscillation for an amplitude of $\Delta y = 0.1$ and a frequency of $f = 0.1\,\mathrm{s}^{-1}$. Only the first 5 cm of the reactor are of interest, where the hot spot occurs. The composition of the feed at the different radians is marked in Figure 3.2 with dots. *Conditions:* $T_g^0 = 280\,°\mathrm{C}$, $d = 2\,\mathrm{mm}$, $d_s = 400\,\mu\mathrm{m}$, $p = 8\,\mathrm{bar}$, $GHSV = 3{,}143\,\mathrm{h}^{-1}$.

the hydrogen lean atmosphere. The behavior of the reaction rate in the polytropic simulation is similar to the isothermal operation, but the absolute values are higher because of the hot spot. The high carbon dioxide concentration deteriorates the conductivity of the mixture caused by its poor thermal conductivity. It would be expected from the steady-state simulation that the higher temperatures cause a decrease of the catalyst effectiveness factor, but the contrary is the case. The mean efficiency is significantly higher, since the higher concentration decreases the diffusion limitations of carbon dioxide which are present in the steady-state. Therefore the higher reaction rates are obtained in hydrogen lean atmosphere and the temperature of the steady-state is exceeded. For this particular frequency, further oscillations do not lead to a different thermal behavior. The reason for this is the much longer time scale of the period in comparison to residence time of the reactor. The difference between bulk and surface in the steady-state is 8.7 K. This difference decreases with increasing hydrogen content whereas the difference is increased in the carbon dioxide rich part of the cycle.

Influence of Frequency

The influence of the frequency is of interest because the energy output of the renewable energy source is subjected to fluctuations on different time scales. Since the microreactor is capable of performing fast dynamic operations, only short periods are of interest which are in the range of seconds. Figure 3.6 (a) shows the effect of different frequencies on the gas-phase temperature. For a period longer than the mean residence time of the reactor, the profiles for T_g reach a stationary pattern after the first cycle, where the steady-state value is enclosed by the phase plan.

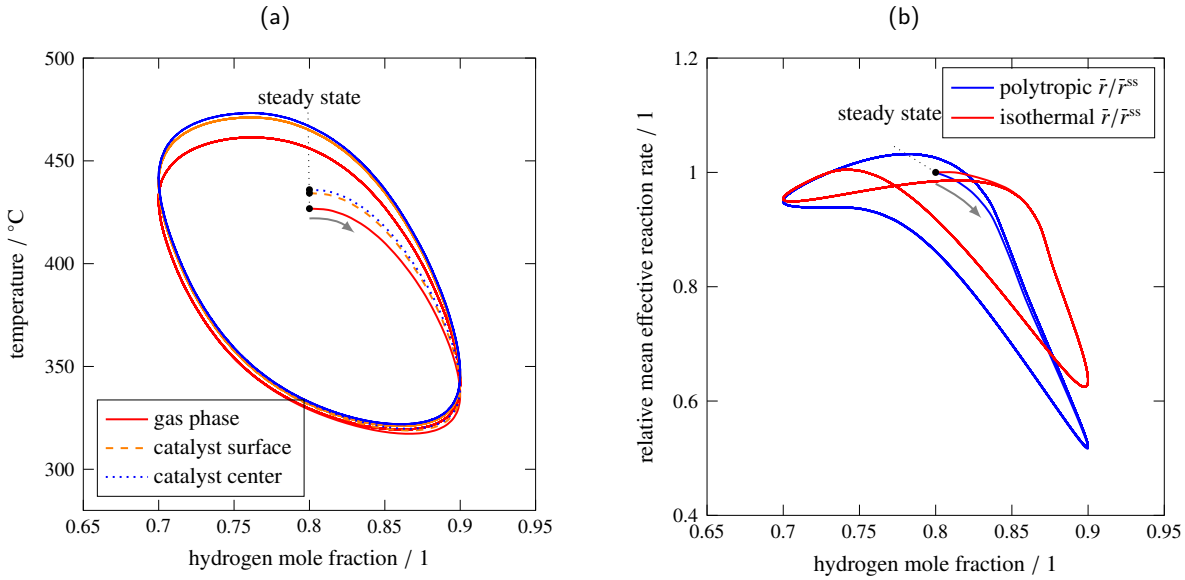

Figure 3.5.: Results for the dynamic simulation of the micro-structured fixed-bed reactor. The gray arrows indicate the direction of progressing time. (a) Phase plane of the maximum temperatures of the gas phase (T_g), the catalyst surface (T_s^s) and the catalyst center (T_s^c) for an amplitude of $\Delta y = 0.1$ and a frequency of $f = 0.1\,s^{-1}$. The black dot in the center represents the maximum of the steady-state profile. (b) Relative mean effective reaction rate, calculated with equation Equation (3.19) for the polytropic operation (blue) and an isothermal operation (red). *Conditions:* $T_g^0 = 280\,°C$, $d = 2\,mm$, $d_s = 400\,\mu m$, $p = 8\,bar$, $GHSV = 3{,}143\,h^{-1}$.

For a frequency of $f = 0.05\,s^{-1}$ the temperature decreases to 311 °C when hydrogen reaches its maximum concentration. At the minimum hydrogen concentration the temperature amounts to 472 °C. A temperature difference of 162 K at the hot spot occurs in 20 s. During the low frequency changes the reactor is supplied with higher carbon dioxide concentrations for a longer time. As a result of the reduced diffusion limitation of carbon dioxide the reaction proceeds fast and thus higher temperatures can be achieved. The opposite is true for the high hydrogen concentrations and the low reaction rates. The maximum temperature difference decreases with increasing frequency (see Table 3.2), with a large distinction among $f = 0.1\,s^{-1}$ and $f = 1\,s^{-1}$. For the case of high frequency, the corresponding periods are shorter than the mean residence time of the reactor. The thermal response pattern changes. Instead of the previously discussed behavior, the hot spot temperature decreases continuously for the first cycles in a helix-like pattern. A thermal quasi-steady-state profile with lower temperatures than the steady-state value is reached after some cycles. Moreover, the temperature difference is only 22 K and it is no longer reached at the concentration extrema but around $y_{H_2} = 0.85$. At the begin of the oscillations the catalyst has still some energy stored from the steady-state operation. Then the temperature decreases because of the aforementioned reasons. The released heat during the fast oscillation is not sufficient to raise the catalyst temperature to or beyond the steady-state temperature and the stored amount of energy is now less compared to the starting point. This continues until a quasi-steady-state is reached. During the high-frequency oscillations, the reactor is not capable of following the input changes as a consequence of its thermal inertia. The reactor moves towards a relaxed steady-state.

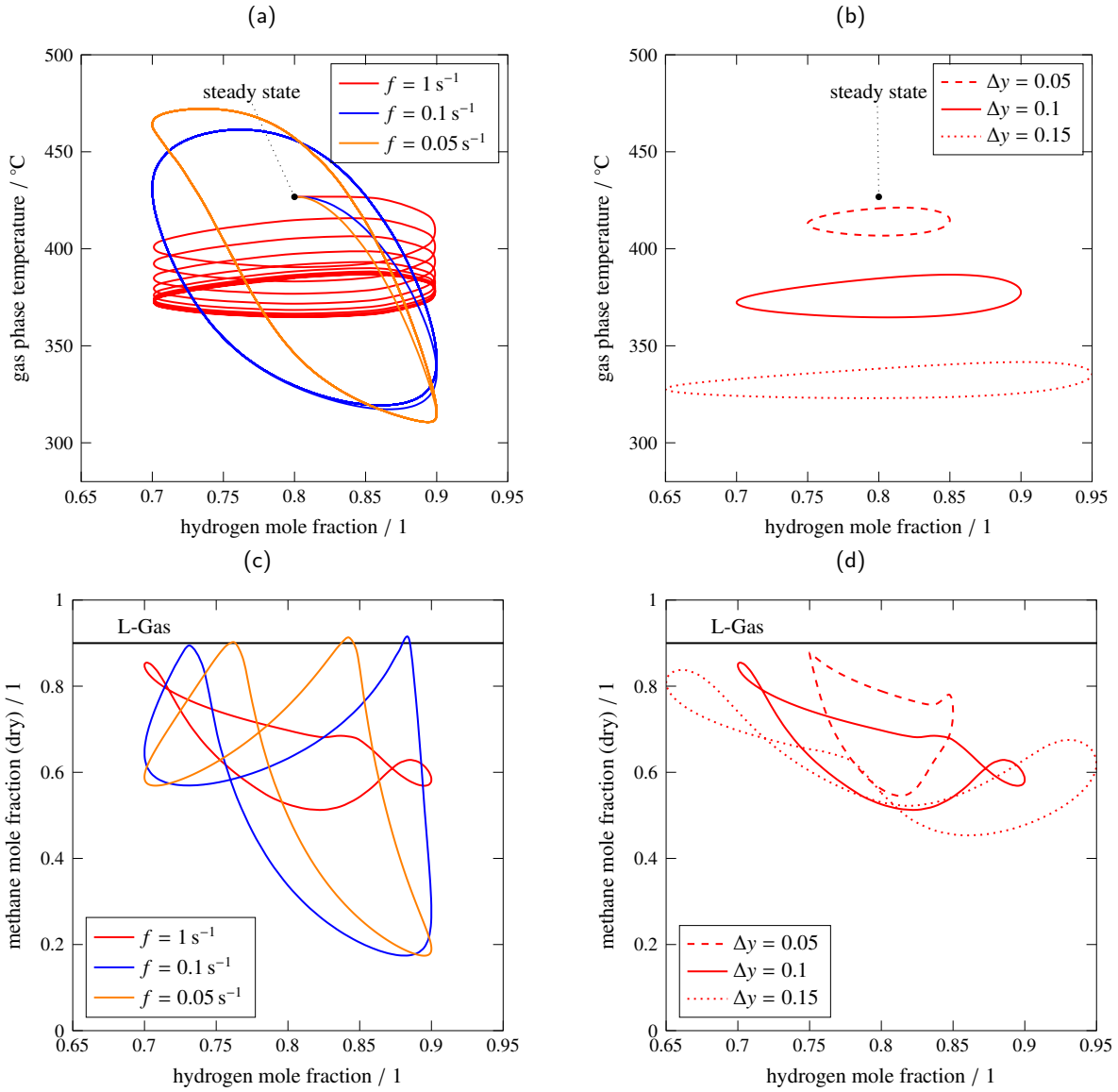

Figure 3.6.: (a) Maximum gas phase temperature for variations of the frequency for an amplitude of $\Delta y = 0.1$. (b) Variation of the amplitude for $f = 1\,s^{-1}$. Only the quasi steady-state profile is depicted. (c) Influence of the frequency on the dry methane content in the outlet for an amplitude of $\Delta y = 0.1$. (d) Dry methane content in the outlet for a frequency of $f = 1\,s^{-1}$ and the investigated amplitudes. Additional phase plane diagrams regarding the dependence of frequency and amplitude of the oscillation on the temperature and methane quality are provided in the ESI. *Conditions:* $T_g^0 = 280\,°C$, $d = 2\,mm$, $d_s = 400\,\mu m$, $p = 8\,bar$, $GHSV = 3{,}143\,h^{-1}$.

The questions arises whether the methane content at the outlet still reaches the designed L-gas quality. Figure 3.6 (c) reveals that the gas quality is not maintained during the periodic operation. This can be explained by the lower reaction rate compared to the steady-state operation and the dilution of the reaction mixture with excess hydrogen and carbon dioxide. The mean methane mole fraction in the outlet increases with increasing frequency. The catalyst is more efficiently used during the high frequency periodic operation, resulting in a higher mean reaction rate despite the lower hot spot temperature.

Influence of Amplitude

The influence of the amplitude on the maximum temperature is shown in Figure 3.6 (b) for $f = 1\,\mathrm{s}^{-1}$ and $f = 0.1\,\mathrm{s}^{-1}$ in the ESI. For the low frequency changes, the temperature difference between minimum and maximum temperature in the gas phase increases from $\Delta T = 76\,\mathrm{K}$ at $\Delta y = 0.05$ to $\Delta T = 165\,\mathrm{K}$ at $\Delta y = 0.15$ (see Table 3.2). This trend is not caused by a symmetrical change. The temperature decrease in the hydrogen rich half cycle is enlarged, whereas the temperature increase during the hydrogen lean half cycle does not change distinctly. When the amplitude is raised from $\Delta y = 0.1$ to $\Delta y = 0.15$ the difference between both maxima is just 2 K while the difference between the minima is 20 K. The temperature differences between the different amplitudes at changes with high frequencies are ΔT =14 K, 22 K and 19 K. Also, the position of the maximal difference changes. For long periods the lowest temperature is obtained near the highest hydrogen concentration, whereas the highest temperature is reached near the stoichiometric composition. For the fluctuations with the short periods, the shape of the phase plane diagram does not change.

The reactor reaches a relaxed steady-state, with a maximum temperature, which decreases continuously with increasing amplitude. While the temperature difference between gas and solid phase increases with increasing amplitude for $f = 0.1\,\mathrm{s}^{-1}$, it decreases with higher amplitudes for $f = 1\,\mathrm{s}^{-1}$. The conversion and thus the methane content at the outlet of the reactor decreases with increasing amplitude (see Figure 3.6 (d) and Table 3.2). This is mainly caused by the dilution of the feed with excess reactants. Also, the reaction rate decreases with increasing amplitude due to diffusion limitations inside the catalyst particle in the low concentration regimes.

Table 3.2.: Summary of the results for the dynamic simulation with different frequencies and amplitudes. Values for the mean carbon dioxide conversion ($\overline{X}_{CO_2}$), mean dry methane mole fraction ($\bar{y}^{dry}_{CH_4}$) at the reactor exit, the maximum hot spot gas temperature during the dynamic operation (T_g^{max}) and the maximum temperature difference at the hot spot (ΔT) are given in the table. The corresponding results for the steady-state profile are $X_{CO_2} = 98.02\,\%$, $y^{dry}_{CH_4} = 90.97$, $T_g^{max} = 431\,°C$, $T_s^{max} = 440\,°C$. *Conditions:* $T_g^0 = 280\,°C$, $d = 2\,mm$, $d_s = 400\,\mu m$, $p = 8\,bar$, $GHSV = 3{,}143\,h^{-1}$.

	$\Delta y = 0.05$				$\Delta y = 0.1$				$\Delta y = 0.15$			
f/s^{-1}	$\overline{X}_{CO_2}/\%$	$\bar{y}^{dry}_{CH_4}/\%$	$T_g^{max}/°C$	$\Delta T/K$	$\overline{X}_{CO_2}/\%$	$\bar{y}^{dry}_{CH_4}/\%$	$T_g^{max}/°C$	$\Delta T/K$	$\overline{X}_{CO_2}/\%$	$\bar{y}^{dry}_{CH_4}/\%$	$T_g^{max}/°C$	$\Delta T/K$
2	95.1	82.2	419	8	92.8	79.5	384	13	87.7	77.1	340	12
1	90.8	73.8	421	14	82.6	67.2	387	22	76.3	63.7	342	19
0.1	90.5	68.1	451	76	83.0	54.3	461	142	75.4	46.2	463	165
0.05	91.2	67.6	462	109	85.3	53.0	472	162	81.0	43.6	473	177
0.033	91.3	67.3	464	118	85.7	52.6	474	164	81.8	43.1	474	178

3.4. Conclusions

A dynamic 1D heterogeneous model is presented to investigate the periodic methanation of CO_2 in a micro-structured fixed-bed reactor. The reactor is designed for the steady-state operation at industrially relevant conditions with the target to produce methane in L-gas quality. The steady-state simulation of the reactor shows, that a heterogeneous model is necessary to describe the reactor behavior properly. Different amplitudes and frequencies are applied to the inlet composition during the dynamic operation and the response of the reactor is analyzed in a phase plane at a constant GHSV.

The results show that a dynamic temperature profile is established with large temperature gradients ($\Delta T \approx 150\,\mathrm{K}$) for low-frequency changes. This can lead to a deactivation of the catalyst through thermal degradation, decrease the selectivity towards methane and induce thermal stress to the reactor. The high-frequency oscillations reveal that the hot spot temperature is reduced to values far lower than the value obtained in steady-state operation. Also, the change of hot spot temperature is reduced to approximately 20 K. The results show, that the reactor behavior moves towards a thermally relaxed steady-state, when high-frequency changes are assigned. The methane production rate for the investigated single channel decreases, which leads to the assumption, that a periodic operation is not beneficial under the investigated conditions. Therefore, it is necessary to change the setup, e.g. longer reactor, buffer tank or second reactor, to ensure a gas quality during dynamic operation, which is sufficient for an injection into the natural gas grid. In a following simulation scenario the dynamic operation of the methanation reactor will be studied under varying inlet composition and inlet flow rate. This operation mode is more realistic since the hydrogen volume flow of the electrolyzer will change fast if it is directly powered by a renewable energy source, whereas the volume flow of carbon dioxide (e.g. from biogas plant) remains nearly constant.

It must be further noted that the application of a reaction rate expression of the LHHW type obtained by steady-state experiments for the investigation of periodic operation can in some cases be insufficient to describe certain phenomena. This is caused by the lack of adsorption and desorption parameters which describe the occupancy of the active sites on the catalyst. Therefore, dynamic experiments of the CO_2 methanation will be conducted in a test unit to validate the kinetic approach or, if necessary, adjust the rate expression.

Acknowledgements

The authors want to thank Prof. Dr. Olaf Ippisch from the department of Scientific Computing from the Institute of Mathematics at the Clausthal University of Technology for the helpful discussion on the numerical solution of complex models.

Nomenclature

Symbol	unit	description
$A_{i,j}$	1	parameter for the calculation of thermal conductivity
A	1	parameter for the calculation of the momentum balance
a_V	$m^2\,m^{-3}$	specific surface area $a_V = \frac{6(1-\varepsilon_{bed})}{d_s}$
B	1	parameter for the calculation of the momentum balance
c	$mol\,m^{-3}$	concentration
c_p	$J\,K^{-1}\,mol^{-1}$	heat capacity
d	m	diameter
D	$m^2\,s^{-1}$	diffusion coefficient
D_{ax}	$m^2\,s^{-1}$	axial dispersion coefficient for the mass
f	s^{-1}	frequency
h	$W\,m^{-2}\,K^{-1}$	heat transfer coefficient
K_R	1	parameter for the calculation of λ_r^{eff}
L	m	reactor length
M	$kg\,mol^{-1}$	molar mass
Nu	1	Nusselt number $Nu = \frac{h d_s}{\lambda_g}$
p	bar	pressure
Pe	1	Peclet number
Pr	1	Prandtl number $Pr = \frac{c_{p,g}\mu}{\lambda_g}$
R		pellet discretization domain
r	$mol\,kg^{-1}\,s^{-1}$	reaction rate
R_g	$J\,K^{-1}\,mol^{-1}$	ideal gas constant (8.314)
Re	1	Reynolds number $Re = \frac{u \rho_g d_s}{\varepsilon \mu}$
S	K	Sutherland parameter
Sc	1	Schmidt number $Sc = \frac{\mu}{\lambda_g D_{bed}}$
Sh	1	Sherwood number $Sh = \frac{\beta d_s}{D_{bed}}$
t	s	time
T	K	temperature
u	$m\,s^{-1}$	velocity
x		axial discretization domain
X_{CO_2}	1	conversion
$\overline{X}_{CO_2}$	1	time-averaged conversion
y	1	mole fraction
$\bar{y}_{CH_4}^{dry}$	1	time-averaged dry methane mole fraction at the reactor exit
Greek symbols		
β	$m\,s^{-1}$	mass transport coefficient
ε	1	porosity
Δp	$bar\,m^{-1}$	pressure drop
ΔT	K	maximum gas phase temperature difference at the hot spot during oscillation
Δy	1	variation of the mole fraction
$\Delta_R H$	$kJ\,mol^{-1}$	standard reaction enthalpy
η	1	catalyst effectiveness factor
λ	$W\,m^{-1}\,K$	thermal conductivity
λ_{ax}	$W\,m^{-1}$	axial dispersion coefficient for energy
μ	Pa s	kinematic viscosity
ν	1	stoichiometric coefficient
ν_{Diff}	$cm^3\,mol^{-1}$	diffusion volume
$\Phi_{i,j}$	1	parameter for the calculation of the viscosity
ρ	$kg\,m^{-3}$	density
τ	1	tortuosity
ϑ	°C	temperature

Subscripts

bed	bed
g	gas phase
GS	gas-solid
h	hydraulic
i, j	component
Kn	Knudsen
lam	laminar
M	mixture
oil	oil phase
ov	overall
pore	pore
r	radial
s	solid phase
turb	turbulent
wall	wall

Superscripts

s	catalyst surface
ss	steady state
0	inlet
eff	effective
c	catalyst center

References

[1] T. J. Schildhauer, S. M. Biollaz, eds. Hoboken, New Jersey: Wiley, **2016**. DOI: 10.1002/9781119191339.

[2] M. Götz, J. Lefebvre, F. Mörs, A. McDaniel Koch, F. Graf, S. Bajohr, R. Reimert, T. Kolb. *Renewable Energy* **2016**, 85, 1371–1390. DOI: 10.1016/j.renene.2015.07.066.

[3] A. Ursúa, I. San Martín, E. L. Barrios, P. Sanchis. *Int. J. Hydrogen Energy* **2013**, 38 (35), 14952–14967. DOI: 10.1016/j.ijhydene.2013.09.085.

[4] S. Rönsch, J. Schneider, S. Matthischke, M. Schlüter, M. Götz, J. Lefebvre, P. Prabhakaran, S. Bajohr. *Fuel* **2016**, 166, 276–296. DOI: 10.1016/j.fuel.2015.10.111.

[5] S. Matthischke, R. Krüger, S. Rönsch, R. Güttel. *Fuel Process. Technol.* **2016**, 153, 87–93. DOI: 10.1016/j.fuproc.2016.07.021.

[6] H. van Doesburg, W. A. de Jong. *Chem. Eng. Sci.* **1976**, 31 (1), 45–51. DOI: 10.1016/0009-2509(76)85007-5.

[7] H. van Doesburg, W. A. de Jong. *Chem. Eng. Sci.* **1976**, 31 (1), 53–58. DOI: 10.1016/0009-2509(76)85008-7.

[8] R. Yadav, R. G. Rinker. *Ind. Eng. Chem. Res.* **1992**, 31 (2), 502–508. DOI: 10.1021/ie00002a009.

[9] R. Underwood, C. Bennett. *J. Catal.* **1984**, 86 (2), 245–253. DOI: 10.1016/0021-9517(84)90370-1.

[10] M. Marwood, R. Doepper, A. Renken. *Appl. Catal., A* **1997**, 151 (1), 223–246. DOI: 10.1016/S0926-860X(96)00267-0.

[11] E. Vesselli, J. Schweicher, A. Bundhoo, A. Frennet, N. Kruse. *J. Phys. Chem. C* **2011**, 115 (4), 1255–1260. DOI: 10.1021/jp106551r.

[12] R. Yadav, R. G. Rinker. *Chem. Eng. Sci.* **1990**, 45 (11), 3221–3226. DOI: 10.1016/0009-2509(90)80214-Y.

[13] K. Klusáček, V. Stuchlý. *Catal. Today* **1995**, 25 (2), 169–174. DOI: 10.1016/0920-5861(95)00106-P.

[14] V. Stuchly, K. Klusacek. *J. Catal.* **1993**, 139 (1), 62–71. DOI: 10.1006/jcat.1993.1007.

[15] M. Marwood, F. van Vyve, R. Doepper, A. Renken. *Catal. Today* **1994**, 20 (3), 437–448. DOI: 10.1016/0920-5861(94)80137-1.

[16] M. Marwood, R. Doepper, A. Renken. *Can. J. Chem. Eng.* **1996**, 74 (5), 660–663. DOI: 10.1002/cjce.5450740516.

[17] R. Güttel. *Chem. Eng. Technol.* **2013**, 36 (10), 1675–1682. DOI: 10.1002/ceat.201300223.

[18] S. Rönsch, J. Köchermann, J. Schneider, S. Matthischke. *Chem. Eng. Technol.* **2016**, 39 (2), 208–218. DOI: 10.1002/ceat.201500327.

[19] A. El Sibai, L. Rihko-Struckmann, K. Sundmacher. *12th International Symposium on Process Systems Engineering and 25th European Symposium on Computer Aided Process Engineering*. Ed. by J. K. Huusom, K. V. Gernaey, R. Gani. Vol. 37. Computer Aided Chemical Engineering. Amsterdam: Elsevier, **2015**, 1157–1162. DOI: 10.1016/B978-0-444-63577-8.50038-3.

[20] X. Li, B. Yang, Y. Zhang. *J. Process Control* **2013**, 23 (10), 1360–1370. DOI: 10.1016/j.jprocont.2013.09.003.

[21] X. Li, J. Li, B. Yang, Y. Zhang. *Chin. J. Chem. Eng.* **2015**, 23 (2), 389–397. DOI: 10.1016/j.cjche.2014.11.007.

[22] R. Currie, D. Nikolic, M. Petkovska, D. S. Simakov. *Isr. J. Chem.* **2018**, 40, 3703. DOI: 10.1002/ijch.201700134.

[23] J. Bremer, K. H. G. Rätze, K. Sundmacher. *AIChE J.* **2017**, 63 (1), 23–31. DOI: 10.1002/aic.15496.

[24] S. Rönsch, A. Ortwein, S. Dietrich. *Chem. Eng. Technol.* **2017**, 40 (12), 2314–2321. DOI: 10.1002/ceat.201700229.

[25] M. Sudiro, A. Bertucco, G. Groppi, E. Tronconi. *20th European Symposium on Computer Aided Process Engineering*. Vol. 28. Computer Aided Chemical Engineering. Elsevier, **2010**, 691–696. DOI: 10.1016/S1570-7946(10)28116-6.

[26] P. J. Lunde. *Ind. Eng. Chem. Process Des. Dev.* **1974**, 13 (3), 226–233. DOI: 10.1021/i260051a007.

[27] S. Rönsch, S. Matthischke, M. Müller, P. Eichler. *Chem. Ing. Tech.* **2014**, 86 (8), 1198–1204. DOI: 10.1002/cite.201300046.

[28] D. Schlereth, O. Hinrichsen. *Chem. Eng. Res. Des.* **2014**, 92 (4), 702–712. DOI: 10.1016/j.cherd.2013.11.014.

[29] J. Ducamp, A. Bengaouer, P. Baurens. *Can. J. Chem. Eng.* **2017**, 95 (2), 241–252. DOI: 10.1002/cjce.22706.

[30] M. Belimov, D. Metzger, P. Pfeifer. *AIChE J.* **2017**, 63 (1), 120–129. DOI: 10.1002/aic.15461.

[31] M. Gruber, C. Wieland, P. Habisreuther, D. Trimis, D. Schollenberger, S. Bajohr, O. vonMorstein, S. Schirrmeister. *Chem. Ing. Tech.* **2018**, 90 (5), 615–624. DOI: 10.1002/cite.201700160.

[32] G. F. Froment. *Chemical Reaction Engineering*. Vol. 109. American Chemical Society, **1972**. Chap. 1, 1–55. DOI: 10.1021/ba-1972-0109.ch001.

[33] B. Eisfeld, K. Schnitzlein. *Chem. Eng. Sci.* **2001**, 56 (14), 4321–4329. DOI: 10.1016/S0009-2509(00)00533-9.

[34] J. Kopyscinski, T. J. Schildhauer, F. Vogel, S. M. Biollaz, A. Wokaun. *J. Catal.* **2010**, 271 (2), 262–279. DOI: 10.1016/j.jcat.2010.02.008.

[35] J. Xu, G. F. Froment. *AIChE J.* **1989**, 35 (1), 88–96. DOI: 10.1002/aic.690350109.

[36] J. Witte, J. Settino, S. M. Biollaz, T. J. Schildhauer. *Energy Convers. Manage.* **2018**, 171, 750–768. DOI: 10.1016/j.enconman.2018.05.056.

[37] F. Koschany, D. Schlereth, O. Hinrichsen. *Appl. Catal., B* **2016**, 181, 504–516. DOI: 10.1016/j.apcatb.2015.07.026.

[38] W. R. Kang, K. B. Lee. *Korean J. Chem. Eng.* **2013**, 30 (7), 1386–1394. DOI: 10.1007/s11814-013-0047-2.

[39] M. Defalco, L. Dipaola, L. Marrelli. *Int. J. Hydrogen Energy* **2007**, 32 (14), 2902–2913. DOI: 10.1016/j.ijhydene.2007.04.014.

[40] B. E. Poling, J. M. Prausnitz, J. O'Connell. 5. ed. New York NY u.a.: McGraw-Hill, **2001**.

[41] S. Elnashaie, S. S. Elshishini. Vol. 7. Topics in chemical engineering. Philadelphia, Pa.: Gordon and Breach, **1993**.

[42] P.J. Linstrom, W.G. Mallard. Gaithersburg MD, 20899: National Institute of Standards and Technology.

[43] Sasol Germany GmbH. Ed. by Sasol Germany GmbH. [accessed 14.05.2018]. URL: https://bit.ly/2LKdjlo.

[44] E. Tsotsas. *VDI-Wärmeatlas*. Berlin, Heidelberg: Springer Berlin Heidelberg, **2013**, 1517–1534. DOI: 10.1007/978-3-642-19981-3_102.

[45] E. N. Fuller, P. D. Schettler, J. C. Giddings. *Ind. Eng. Chem.* **1966**, 58 (5), 18–27. DOI: 10.1021/ie50677a007.

[46] R. H. Perry, D. W. Green. 8. ed. New York, NY: McGraw-Hill, **2008**.

[47] J. Solsvik, H. A. Jakobsen. *Chem. Eng. Sci.* **2011**, 66 (9), 1986–2000. DOI: 10.1016/j.ces.2011.01.060.

[48] K. R. Rout, H. A. Jakobsen. *Can. J. Chem. Eng.* **2015**, 93 (7), 1222–1238. DOI: 10.1002/cjce.22202.

[49] K. Ghaib. *Chem. Ing. Tech.* **2016**, 88 (8), 1102–1108. DOI: 10.1002/cite.201500180.

[50] S. Z. Abbas, V. Dupont, T. Mahmud. *Int. J. Hydrogen Energy* **2017**, 42 (5), 2889–2903. DOI: 10.1016/j.ijhydene.2016.11.093.

[51] R.-Y. Chein, C.-T. Yu, C.-C. Wang. *Fuel* **2016**, 185, 394–409. DOI: 10.1016/j.fuel.2016.07.123.

[52] N. R. Parlikkad, S. Chambrey, P. Fongarland, N. Fatah, A. Khodakov, S. Capela, O. Guerrini. *Fuel* **2013**, 107, 254–260. DOI: 10.1016/j.fuel.2013.01.024.

[53] M. Soomro, R. Hughes. *Can. J. Chem. Eng.* **1979**, 57 (1), 24–28. DOI: 10.1002/cjce.5450570104.

[54] C. S. Sharma, P. Harriot, R. Hughes. *Chem. Eng. J.* **1975**, 10 (1), 73–80. DOI: 10.1016/0300-9467(75)88019-1.

[55] P. Harriot. *Chem. Eng. J.* **1975**, 10 (1), 65–71. DOI: 10.1016/0300-9467(75)88018-X.

[56] C. Ullrich, T. Bodmer, C. Hübner, P. B. Kempa, E. Tsotsas, A. Eschner, G. Kasparek, F. Ochs, M. H. Spitzner. *VDI-Wärmeatlas*. Berlin, Heidelberg: Springer Berlin Heidelberg, **2013**, 629–708. DOI: 10.1007/978-3-642-19981-3_28.

[57] V. Gnielinski. *VDI-Wärmeatlas*. Berlin, Heidelberg: Springer Berlin Heidelberg, **2013**, 839–840. DOI: 10.1007/978-3-642-19981-3_50.

[58] V. Gnielinski. *VDI-Wärmeatlas*. Berlin, Heidelberg: Springer Berlin Heidelberg, **2013**, 785–792. DOI: 10.1007/978-3-642-19981-3_42.

[59] L. Kiewidt, J. Thöming. *Chem. Eng. Sci.* **2015**, 132, 59–71. DOI: 10.1016/j.ces.2015.03.068.

[60] Process Systems Enterprise. **2018**. URL: www.psenterprise.com/gproms.

[61] R. Güttel, T. Turek. *Chem. Eng. Sci.* **2009**, 64 (5), 955–964. DOI: 10.1016/j.ces.2008.10.059.

CHAPTER 4

"Science, my lad, is made up of mistakes, but they are mistakes which it is useful to make, because they lead little by little to the truth."

(Jules Verne, A Journey to the Center of the Earth)

Spray-Dried Ni Catalysts with Tailored Properties for CO_2 Methanation

B. Kreitz, A. Martínez Arias, J. Martin, A. P. Weber, T. Turek.
Catalysts **2020**, 10(12), 1410
https://doi.org/10.3390/catal10121410

Abstract

A catalyst production method that enables the independent tailoring of the structural properties of the catalyst, such as pore size, metal particle size, metal loading or surface area, allows to increase the efficiency of a catalytic process. Such tailoring can help to make the valorization of CO_2 into synthetic fuels on Ni catalysts competitive to conventional fossil fuel production. In this work, a new spray-drying method was used to produce Ni catalysts supported on SiO_2 and Al_2O_3 nanoparticles with tunable properties. The influence of the primary particle size of the support, different metal loadings, and heat treatments were applied to investigate the potential to tailor the properties of catalysts. The catalysts were examined with physical and chemical characterization methods, including X-ray diffraction, temperature-programmed reduction, and chemisorption. A temperature-scanning technique was applied to screen the catalysts for CO_2 methanation. With the spray-drying method presented here, well-organized porous spherical nanoparticles of highly dispersed NiO nanoparticles supported on silica with tunable properties were produced and characterized. Moreover, the pore size, metal particle size, and metal loading can be controlled independently, which allows to produce catalyst particles with the desired properties. Ni/SiO_2 catalysts with surface areas of up to $40\,m^2\,g^{-1}$ with Ni crystals in the range of 4 nm were produced, which exhibited a high activity for the CO_2 methanation.

Keywords: spray-drying, Ni catalysts, CO_2 methanation, temperature-scanning reactor, aerosol synthesis

Supporting information for this publication is reprinted in Appendix B.

4.1. Introduction

Highly dispersed Ni nanoparticles supported on well-organized porous structures are promising catalysts for several applications such as steam and dry reforming of methane [1, 2] and ethane [3, 4], and methanation of CO [5, 6] and CO_2 [7, 8]. Especially the CO_2 methanation, which is part of the power-to-gas process, is becoming more important to tackle the needs for a sustainable natural gas economy. The dynamic operation of the CO_2 methanation in flexible load scenarios imposes challenges on the catalyst to perform well, even under drastic concentration and temperature variations [9–11]. For the improvement of the CO_2 methanation process and the other mentioned processes, it is, therefore, necessary to produce catalysts with long-term stability, sintering- and coking resistance as well as high activity and selectivity towards desired products. These properties are influenced on the microscale by the size of the metal crystals, the pore size, and the metal/support interaction. Hence, in the production of the catalysts, it is of great interest to tailor the catalyst and the support to meet the specifications of the task at hand. Various ceramic carriers are investigated for CO_2 methanation, such as γ-Al_2O_3, SiO_2, TiO_2, CeO_2, and ZrO_2 [8, 12–14]. Carriers with basic surface properties like Al_2O_3 and CeO_2 show a high CO_2 methanation activity due to the interaction of CO_2 with basic adsorption sites [15]. Ni supported on structured mesoporous SiO_2 nanoparticles also has a high activity and SiO_2 supports have the potential to be tailored [16].

In recent literature, several production methods for Ni/SiO_2 catalysts have been tested, aiming to influence the pore system and Ni crystal size. Aziz et al. [16] prepared mesostructured silica nanoparticles using a sol-gel method. These showed approximately 50 % higher activity compared to classical impregnated Ni/SiO_2 catalysts. A mesoporous silica molecular sieve with a highly accessible pore system was prepared by Chen et al. [17], which proved to be a more active support than amorphous SiO_2. By using the ammonia evaporation method and colloidal silica as starting material, Ye et al. [18] were able to increase the surface area of the SiO_2 support by $140\,m^2\,g^{-1}$ compared to commercial carriers and to decrease the Ni crystal size. Furthermore, Zhu et al. [19] prepared a bimodal pore structure with pores in the range of 5 to 50 nm by impregnation of SiO_2 nanoparticles.

Most of the catalysts are produced by impregnation methods of the different support materials [19–22], co-precipitation [23], so-gel [16], and flame synthesis [24, 25]. The first three of these methods are usually batch processes and require various time-consuming steps. Moreover, there is a loading limitation for impregnation methods, which is in the range of 30 % depending on the pore volume, as well as a direct correlation between the pore size and the metal particle size [26–28]. In addition, the metal particle size is dependent on the metal loading. Usually, metal dispersion decreases with increasing metal loading. Flame synthesis is a fast and single-step process that does not require a post-heat treatment of the particles as the thermal decomposition occurs directly in the flame due to the high temperatures. However, the high cost of the precursor and the difficulties of producing porous materials are the drawbacks of this method, which still needs to be improved [29]. Another possible way of producing catalysts is the spray-drying method. It is a simple, efficient, continuous, fast, and easily scaleable process to synthesize nanoparticles in a few preparation steps [30]. In previous work, Martínez and Weber [31] presented a method for synthesizing highly dispersed Co_3O_4 nanoparticles supported on silica with tunable properties such as pore size, surface area, metal particle size, and metal loading by spray-drying a colloidal silica suspension with dissolved metal nitrate. Furthermore, they show how to

control the pore size and the metal particle size independently, as well as a design guide to determine the metal particle size for a certain metal concentration per surface area.

Ni/SiO_2 and Ni/γ-Al_2O_3 catalysts are produced in this study with the spray-drying process presented by Martínez and Weber [31]. Variation in the primary particle size of the silica, Ni loading, and thermal treatment are studied to provide a design guide for the catalytic materials. Catalysts are examined with physical and chemical characterization techniques such as X-ray diffraction, temperature-programmed reduction, and chemisorption. The CO_2 methanation is used as a test reaction to investigate the activity of the produced catalysts. To enable a quick screening of the materials, a temperature-scanning technique, developed by Wojciechowski and Asprey [32, 33] is applied, which was successfully used to investigate the kinetics of CO oxidation [34] and ammonia synthesis [35]. The results from this work will provide a guideline to vary catalysts properties such as pore size, metal particle size, and the metal/support interaction. This tailoring of the catalysts enables us to investigate the structure-activity relation for the CO_2 methanation on Ni/SiO_2 catalysts.

4.2. Results and Discussion

4.2.1. Morphological Examination

The particles synthesized in this work, referred to as building blocks (BB), were produced from a suspension of water, nickel nitrate, and colloidal nanoparticle suspension (SiO_2 or Al_2O_3). The prepared suspension was atomized and sprayed into a tube furnace operated at 673 K to evaporate the solvent and to decompose most of the $Ni(NO_3)_2$ to NiO, leading to the formation of a NiO/SiO_2 nanoparticle. A detailed scheme of the setup can be found in previous work [31]. During the drying in the tube furnace, the evaporation of the solvent in the droplets initiated a self-assembly process leading to spherical dry particles formed by several small single nanoparticles. In this study, BB formed by two different supports, SiO_2 with two different primary particle sizes (8 and 20 nm), here named as BB(8) and BB(20) and Al_2O_3 with a primary particle size of 50 nm ($BB(Al_2O_3)$), using two different nickel loadings of 10 and 20 wt% were produced. The nickel loading in the BB can easily be adjusted by adding different nickel nitrate amounts to the prepared suspension before the spray-drying process. Continuously synthesized nanoparticles were collected on a filter and heat-treated in a muffle oven at two different temperatures of 673 K and 973 K to adjust the NiO nanoparticle size. Temperatures higher than 973 K were not used in this work to avoid sintering of SiO_2 nanoparticles, which is discussed in more detail in the supporting information (SI) (see Figures S1 and S2). A tree summarizing the produced samples is provided in Figure 4.1.

Figure 4.2 shows the SEM and TEM micrographs of BB(20) and $BB(Al_2O_3)$ with 20 wt% of Ni after production (c and d), and after the heat treatment in a muffle oven for 4 h at 973 K(a, b, e, and f). The SEM images reveal that the spray-drying method produces a broad particle size distribution of spherical nanoparticles with diameters up to 300 nm. Each of these agglomerates consists of many tightly packed single SiO_2 nanoparticles with a size of 20 nm (for BB(20)) and well-distributed NiO nanoparticles (darker dots), which can be seen in Figure 4.2c,e. TEM images with BB(8) and BB(45) show the same behavior (see Figure S3). Furthermore, it can be observed that the size of the NiO nanoparticles grew during the heat treatment due to the sintering effect. $BB(Al_2O_3)$ are also compact

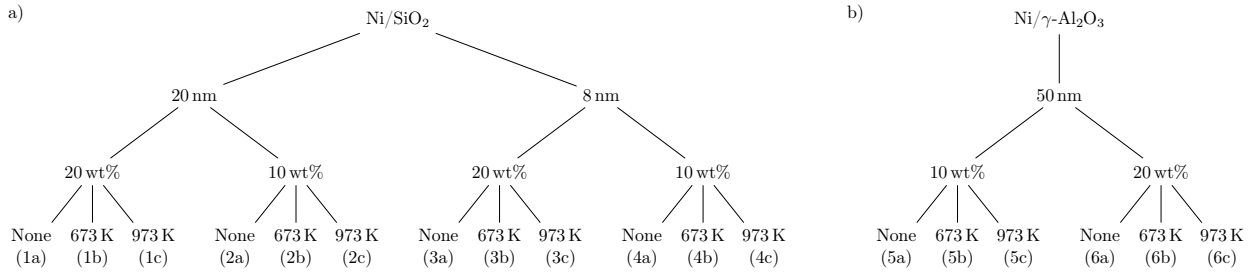

Figure 4.1.: Tree for the production of the (a) Ni/SiO_2 and (b) $Ni/\gamma\text{-}Al_2O_3$ catalysts. The first node is the size of the primary particles (SiO_2 or Al_2O_3) of the support in the colloidal suspension, the second node is the Ni loading, and the third child node is the temperature of the thermal treatment after the synthesis. The names of the samples are placed in parentheses.

spheres formed by single Al_2O_3 nanoparticles. However, for BB(Al_2O_3), it is not possible to observe clusters of NiO crystals (see Figure 4.2d,f).

4.2.2. Elemental Analysis

The catalysts were produced in a single batch and a part of this batch was calcined at 673 K and 973 K. That is why the samples with one BB and nominal loading, e.g., BB(20) with 10 wt%, have the same Ni content (13 wt%) and traces of Na (0.003 wt%) and K (0.019 wt%) for the three different calcination temperatures. K and Na can affect the activity of the silica and alumina catalysts [36, 37]. Traces of Na and K can originate from the Ni nitrate or the silica suspension and the presence of Na can create basic sites on the support. Studies show that Na enhances the CO_2 methanation activity of Ni/SiO_2 catalysts [37], whereas it increases the CO selectivity in Ni/Al_2O_3 catalysts [38].

The measured Ni content in the silica catalysts is always higher than the value, which was initially provided in the atomizer (see Table 4.1). For the alumina catalysts, the amount of Ni is lower (see Table 4.2). The amount of potassium in all catalyst samples is in the range of 0.02 wt% and thus negligible. The concentration of Na varies in the different samples. A negligible amount of Na is obtained for the BB(20), but for the catalysts with BB(8) and BB(Al_2O_3), the amount of Na is in the range of 0.1 wt%. Catalysts produced with BB(20) show a lower Na concentration compared to the ones produced from BB(8). The influence of basic sites will be further investigated with CO_2 temperature-programmed desorption (TPD) experiments.

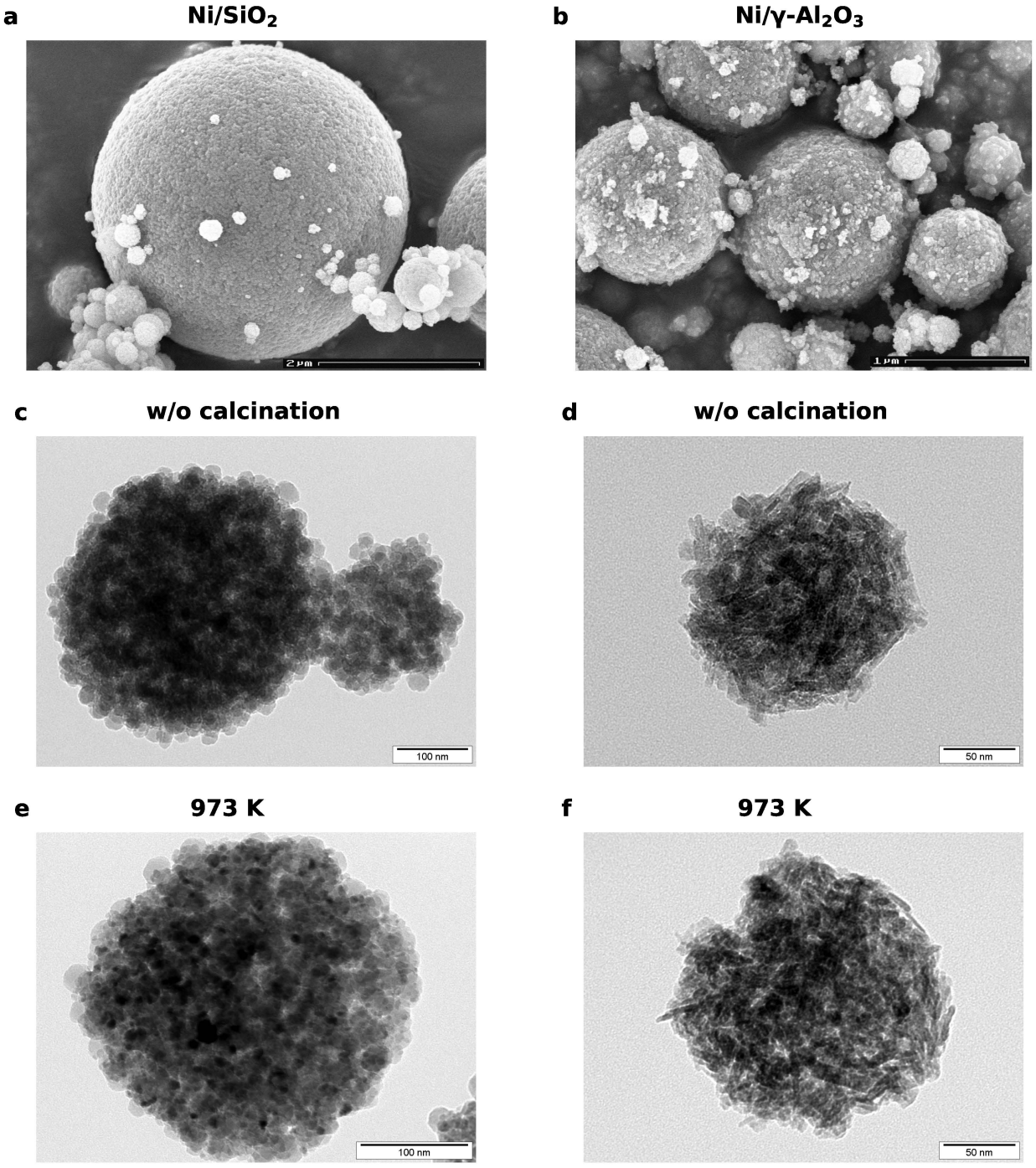

Figure 4.2.: SEM images of the (a) BB(20) and (b) BB(Al_2O_3) with a Ni loading of 20 wt%. TEM micrographs of (c) BB(20) and BB(Al_2O_3) (d) after production (without (w/o) calcination). (**e**) BB(20) and (**f**) BB(Al_2O_3) after calcination at 973 K for 4 h.

Table 4.1.: Summary of the characterization results for all Ni/SiO_2 catalysts. The naming convention applied in this work is provided in Figure 4.1. The samples that were not calcined (1a, 2a, 3a, 4a) loose mass during the reduction because of the decomposition of remaining nitrates. This mass loss was measured with a thermogravimetric analysis (see Table S1) and accounted for in the evaluation.

Property	Unit	1a	1b	1c	2a	2b	2c	3a	3b	3c	4a	4b	4c	Method
Surface area	$m^2\,g^{-1}$	-	110	96	-	111	103	-	184	153	-	199	181	BET
Pore volume	$mm^3\,g^{-1}$	-	281	269	-	290	272	-	357	334	-	398	375	BJH
Average pore size	nm	-	9.0	9.3	-	9.1	8.6	-	6.4	6.6	-	6.7	6.6	BJH
Ni loading	wt%	20.9	20.9	20.9	13.0	13.0	13.0	23.1	23.1	23.1	12.2	12.2	12.2	ICP-OES
Na content	wt%	0.01	0.01	0.01	<0.003	<0.003	<0.003	0.12	0.12	0.12	0.15	0.15	0.15	ICP-OES
K content	wt%	0.018	0.018	0.018	0.019	0.019	0.019	0.014	0.014	0.014	0.011	0.011	0.011	ICP-OES
H_2 uptake	$\mu mol\,g^{-1}$	402	181	93	254	171	58	460	271	110	324	205	95	H_2 chemisorption
Metal surface area	$m^2\,g^{-1}$	34.3	16.3	8.9	28.1	17.6	8.4	40.5	23.8	12.0	34.6	21.1	11.3	H_2 chemisorption
Average Ni crystal size	nm	4.1 (4.5)	8.6 (6.8)	15.9 (8.3)	3.1 (3.2)	5.0 (4.7)	10.4 (5.4)	3.9 (4.3)	6.5 (5.1)	12.9 (5.9)	2.4 (2.0)	3.9 (2.5)	7.3 (2.8)	H_2 chemisorption (XRD)
Ni dispersion	%	24.6	11.7	6.3	32.4	20.2	9.7	26.2	15.4	7.8	42.4	25.9	13.9	H_2 chemisorption
Degree of reduction	%	91.9	87.0	82.7	70.8	76.6	53.9	89.2	89.2	71.4	73.5	76.3	66.2	O_2 chemisorption
CO_2 uptake	$\mu mol\,g^{-1}$	78.5	26.6	-	-	-	-	126.3	53.5	16.9	-	-	-	CO_2 chemisorption

Table 4.2.: Summary of the characterization results for the $Ni/\gamma\text{-}Al_2O_3$ catalysts. It was not possible to determine the NiO size for the alumina catalysts with XRD because only $NiAl_2O_4$ was formed.

Property	Unit	5a	5b †	5c †	6a	6b	6c †	Method
Surface area	$m^2\,g^{-1}$	-	178	123	-	155	99	BET
Pore volume	$mm^3\,g^{-1}$	-	337	331	-	311	293	BJH
Average pore size	nm	-	5.9	8.0	-	6.4	8.7	BJH
Ni loading	wt%	9.0	9.0	9.0	15.1	15.1	15.1	ICP-OES
Na content	wt%	0.16	0.16	0.16	0.17	0.17	0.17	ICP-OES
K content	wt%	0.0055	0.0055	0.0055	0.0046	0.0046	0.0046	ICP-OES
H_2 uptake	$\mu mol\,g^{-1}$	7	-	-	143	69	-	H_2 chemisorption
Metal surface area	$m^2\,g^{-1}$	5.8	-	-	28.3	18.1	-	H_2 chemisorption
Average Ni crystal size	nm	14.5	-	-	2.9	4.5	-	H_2 chemisorption
Ni dispersion	%	7.1	-	-	34.7	22.3	-	H_2 chemisorption
Degree of reduction	%	9.6	-	-	39.6	29.8	-	O_2 chemisorption
CO_2 uptake	$\mu mol\,g^{-1}$	140.9	-	-	125.6	-	-	CO_2 chemisorption

† With the applied reduction method, it was not possible to reduce $NiAl_2O_4$, which did not allow for a proper determination of the H_2 adsorption capacity, because the detected amounts are too small.

4.2.3. Physisorption

The pore size distributions of BB(8), BB(20), BB(45), and BB(Al_2O_3) with 20 wt% Ni calcined at 673 K, are illustrated in Figure 4.3a. It can be observed that the average pore size increases with an increasing primary particle size of the silica. Smaller pores with a narrow size distribution are formed for smaller SiO_2 nanoparticles. On the other hand, the total pore volume increases as the size of the SiO_2 nanoparticles is decreased (see Table 4.1), which indicates that the porosity of the BB decreases with increasing the SiO_2 primary particle size. These results agree with the observations that the arrangement, or ordering ability of larger nanoparticles, is easier than the arrangement of smaller nanoparticles [31, 39–41]. The pore size of BB(8), as well as the surface area and the total pore volume, is very similar to the pore size distribution of BB(Al_2O_3).

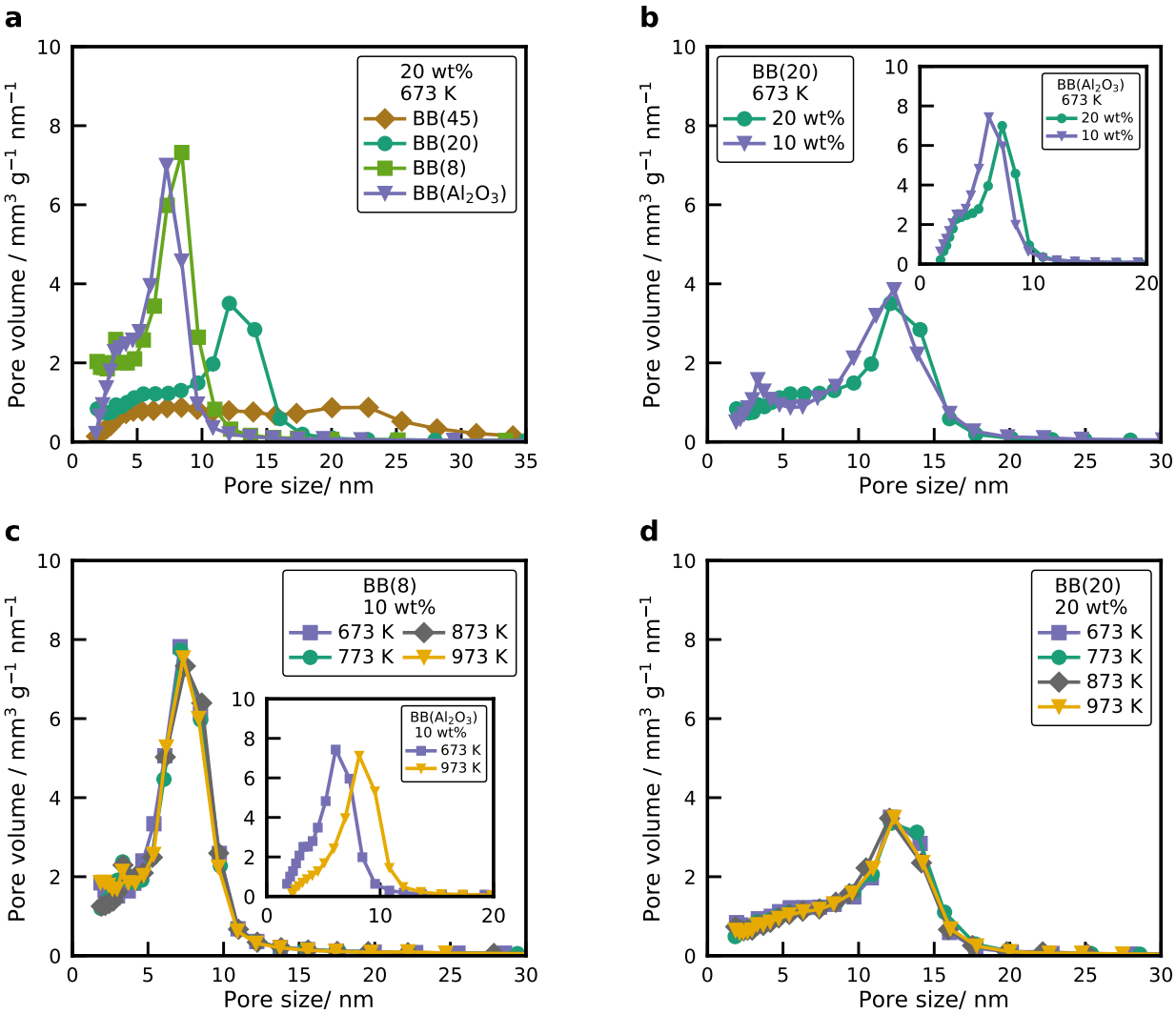

Figure 4.3.: (a) Pore size distribution of BB(8), BB(20), BB(45), and BB(Al_2O_3) with 20 wt% of Ni, calcined at 673 K. (b) Pore size distribution of BB(20) and BB(Al_2O_3) (inset) with two different nickel loadings (10 and 20 wt%), calcined at 673 K. (c) Pore size distribution of BB(8) and BB(Al_2O_3) (inset) with 10 wt% of Ni calcined at different temperatures. (d) Pore size distribution of BB(20) with 20 wt% of Ni calcined at different temperatures.

Figure 4.3b shows the pore size distribution of BB(20) with two different nickel loadings. The pore size distribution of the BB is not affected by the different nickel loadings, whereas the total pore volume

of the BB decreases with increasing Ni loading because the NiO nanoparticles occupy the free space. The same behavior was observed for a primary particle size of 8 nm with two different Ni loadings. This confirms that the final structure of the NiO/SiO_2 nanoparticles mainly depends on the primary particle size of the silica. This is contrary to catalysts produced via incipient wetness impregnation, where the pore size decreases with increasing Ni loading [26–28, 42]. However, an increase in the nickel loading for BB(Al_2O_3) results in a small shift towards larger pores with lower total pore volume (see inset Figure 4.3b and Table 4.2). For BB(Al_2O_3) the nickel reacts with the support and creates a new crystalline structure, consisting of crystalline $NiAl_2O_4$ as well as γ-Al_2O_3. The new crystalline structure induces morphological changes on the particle, which results in a different pore structure. With higher Ni loading the share of $NiAl_2O_4$ increases, which slightly changes the pore size distribution.

The pore size distribution of BB(8) with 10 wt% Ni calcined at different temperatures is displayed in Figure 4.3c. It can be observed that the pore size distribution of the NiO/SiO_2 system does not change with increasing calcination temperature, while the size of the NiO nanoparticle increases. The same behavior is obtained for BB(20) with 20 wt% of Ni (see Figure 4.3d). However, for the BB(Al_2O_3), the pore size increases with higher calcination temperatures (see Figure 4.3c inset), which is due to the changes in the structure of the Al_2O_3 nanoparticles because of sintering (see Figure S2). The experimental results show that pore size distribution, total pore volume, and specific surface area of the BB can be easily adjusted by varying the SiO_2 primary particle size. For NiO nanoparticles supported on silica, there is no correlation between the pore size, the NiO nanoparticle size, and the nickel loading. These experiments agree with previous work from our group [31, 41] for cobalt oxide nanoparticles supported on silica. However, further experiments have to be performed for BB(Al_2O_3) with different primary particle sizes. So far, it can observed that the pore size of BB(Al_2O_3) is influenced by the nickel loading and the different calcination temperatures.

4.2.4. XRD

The XRD patterns of BB(20) and BB(Al_2O_3) with 20 wt% Ni after production and after the heat treatment at different temperatures are illustrated in Figure 4.4. Higher calcination temperatures resulted in diffractograms with more pronounced reflections for the SiO_2 catalysts (see Figure 4.4a), which indicates that the NiO nanoparticle size increased due to sintering effects. The average size of the NiO nanoparticles was calculated from the Scherrer Equation (4.1) using the full-width at the half-maximum value of the peak with maximum intensity, which is the NiO(200) facet. The average NiO nanoparticle size of the different samples are plotted in Figure 4.5.

The XRD profiles of BB(Al_2O_3) with 20 wt% of Ni directly after production and heat treatment at two different temperatures are plotted in Figure 4.4b, as well as the XRD profile of BB(Al_2O_3) without Ni. Only Ni aluminate spinel structures were formed and no reflections corresponding to NiO nanoparticles were found, even for the low calcination temperature. Furthermore, it can be seen that there is a phase transition in the crystalline structure before and after calcination. A boehmite structure is formed for temperatures below 673 K, whereas for temperatures higher than 673 K, a phase transition to γ-Al_2O_3 and $NiAl_2O_4$ is observed (see Figure S4a). Increasing the nickel loading in BB(Al_2O_3) shifts the reflections towards smaller angles (see Figure S4b), which indicates a volume increase in the unit cell due to the incorporation of the bigger Ni atoms in the alumina spinel structure. With a Rietveld analysis, it was possible to simulate the XRD pattern assuming only γ-Al_2O_3 and $NiAl_2O_4$ and to derive the lattice

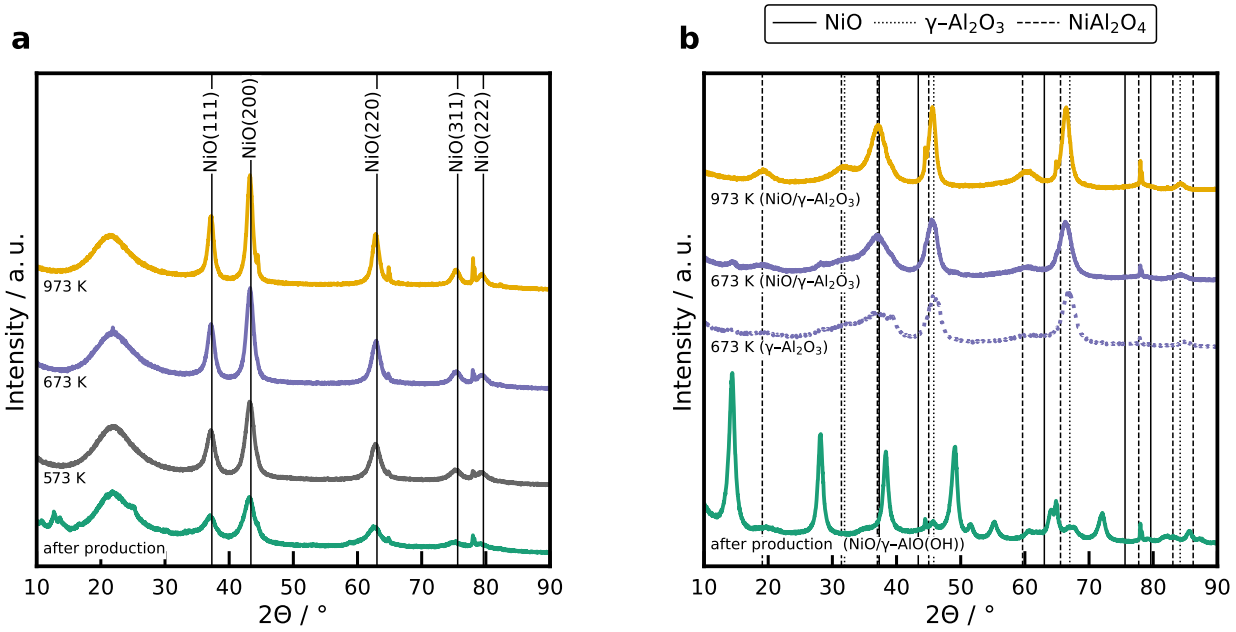

Figure 4.4.: (a) XRD patterns of the 20 wt% Ni/SiO_2 catalyst with BB(20) after production, and after calcination at different temperatures. The broad reflection at $2\Theta = 22°$ is assigned to amorphous silica and the reflections at 38.2, 44.6, 65.0, 78.0, and 78.1° are caused by the Al sample holder. (b) XRD patterns of the 10 wt% Ni/Al_2O_3 catalyst after production, and after calcination at 673 K and 973 K for 4 h. Reflections for the boehmite structure obtained after production is provided in Figure S4a.

constant of γ-Al_2O_3. The lattice constant as a function of the Ni loading is presented in Figure S4c. A higher nickel loading increases the lattice constant of the γ-Al_2O_3, which is reasonable as the ionic radius of Ni is higher than the ionic radius of Al [43]. Results from the Rietvield analysis agree well with reported literature values [44, 45].

The sintering of metal oxide nanoparticles is known to be temperature- and size-dependent [46, 47]. However, the sintering of metals can be affected by other factors such as melting point [48], the shape and composition of the nanoparticle [49], the interaction between the support and the metal [50], or the metal loading [50, 51]. Especially the metal loading will have a large impact on the nanoparticle growth. For instance, for higher metal loadings, the ratio between the total mass of metal per surface area of the support (m_{Ni}/a_{SiO_2} ratio) increases, and thus, the metal particle size increases, e.g., BB(20) and 20 wt% Ni has a ratio of 2.0 mg m^{-2}, whereas for BB(20) and 10 wt% of Ni the ratio is 1.13 mg m^{-2}. Herein, the growth of the NiO nanoparticle as a function of the nickel loading inside the BB was investigated. Figure 4.5a shows the NiO nanoparticle size of BB(20) for the different nickel loadings, calcined at different temperatures. Increasing the nickel loading increases the size of the NiO nanoparticles for the same calcination temperature. For instance, for higher nickel loadings (e.g., 20 wt% of Ni in BB), the size of the NiO nanoparticles presents a stronger increase with the temperature, whereas for low nickel loadings (e.g., 5 wt% of Ni in BB), the growth of the NiO nanoparticles is very small. In any case, the size of the NiO nanoparticles increases linearly with increasing calcination temperature, which is in agreement with the experimental results of other groups [50, 52].

As mentioned before, the m_{Ni}/a_{SiO_2} ratio also plays an important role in the final size of the NiO nanoparticle. Thus, the BB formed with two different SiO_2 primary particle sizes (BB(8) and BB(20)) for two different nickel loadings (10 and 20 wt%) were compared to investigate the influence of the size of the NiO nanoparticle as a function of the metal mass and absolute surface area of the support. Figure 4.5b shows the average NiO nanoparticle sizes of the different BB calcined at different temperatures. For BB formed with smaller SiO_2 primary particle size, smaller NiO nanoparticles result, compared to the BB formed with bigger SiO_2 nanoparticles at the same loading. Moreover, the size of the NiO nanoparticles was very similar for BB(20) with 10 wt% of Ni, compared to the NiO nanoparticle size of BB(8) and 20 wt%. Notice that for these two catalyst, the m_{Ni}/a_{SiO_2} ratio is very similar. BB(20) and 10 wt% Ni has a ratio of 1.13 mg m^{-2}, whereas for BB(8) and 20 wt% of Ni, the ratio is 1.23 mg m^{-2}, which explains the similar size of the NiO nanoparticles. The dependence of the m_{Ni}/a_{SiO_2} ratio on the NiO crystal size is clearly illustrated in Figure 4.5c. Notice that the NiO size for three different SiO_2 primary particle sizes and Ni loadings shows a linear increase in the NiO crystal size with increasing m_{Ni}/a_{SiO_2} ratio. As shown before, the NiO crystal size depends on the temperature, but the correlation between m_{Ni}/a_{SiO_2} ratio and average NiO crystal size stands to reason for all of the investigated temperatures. These results are in agreement with the work of Martínez and Weber [31] for Co_3O_4 nanoparticles supported on silica. However, the assumption that the same m_{Ni}/a_{SiO_2} ratio results in the same NiO nanoparticle size is only valid when the same materials are used (e.g different nickel loadings, silica nanoparticles with different sizes). Loosdrecht et al. [50] compared the results of the NiO nanoparticle size when the same nickel loading was distributed over two different supports (SiO_2 and TiO_2), while the specific surface area for both supports was kept constant. They observed that the size of the nickel oxide nanoparticles was different for the two supports due to the different behavior of nucleation and growth on the support. The linear regression in Figure 4.5c can be used as a design guide to tailor the NiO crystal size to a specific value by choosing the size of the primary particle and the temperature of the post-heat treatment.

All of the XRD patterns were reported for the calcined samples. Therefore, the determined crystal size refers to the NiO crystal. In order to determine the crystal size of Ni, the catalyst samples were reduced and passivated with synthetic air at room temperature using a pulse method [53]. Figure S5a shows the diffractogram of the Ni/SiO_2 catalyst formed using BB(20) with 20 wt%, calcined at 673 K) after calcination, while Figure S5b shows a diffractogram after reduction and passivation. It can be seen that large Ni reflections with broad low-intensity NiO reflections were obtained for the passivated sample. This allows to determine the Ni crystal size. The NiO crystal size determined from the NiO(111) reflection for the non-reduced catalyst with BB(20), 20 wt% calcined at 673 K is 6.8 nm. For the reduced and passivated catalyst, the Ni crystal size was calculated from the Ni(111) reflection and amounts to 6.9 nm. No change in the crystal size is determined upon reduction. Therefore, the values determined for NiO can be used as the size of the Ni crystals. Small-angle X-ray scattering (SAXS) measurements of this catalyst (see Figure S6) show a monomodal Ni particle size with a most frequent Ni crystal size of 7 nm, which fits the XRD results.

According to the experimental results presented above, it can be concluded that the size of the NiO nanoparticles can be controlled by varying the calcination temperature in a post-heat treatment after the synthesis of the BB. Furthermore, it can be seen that there is a dependence on the amount of nickel per surface area of the support (mass of nickel per surface of silica), which agrees well with the experimental results of Martínez and Weber [31]. This observation can be used as a design guide to synthesize metal

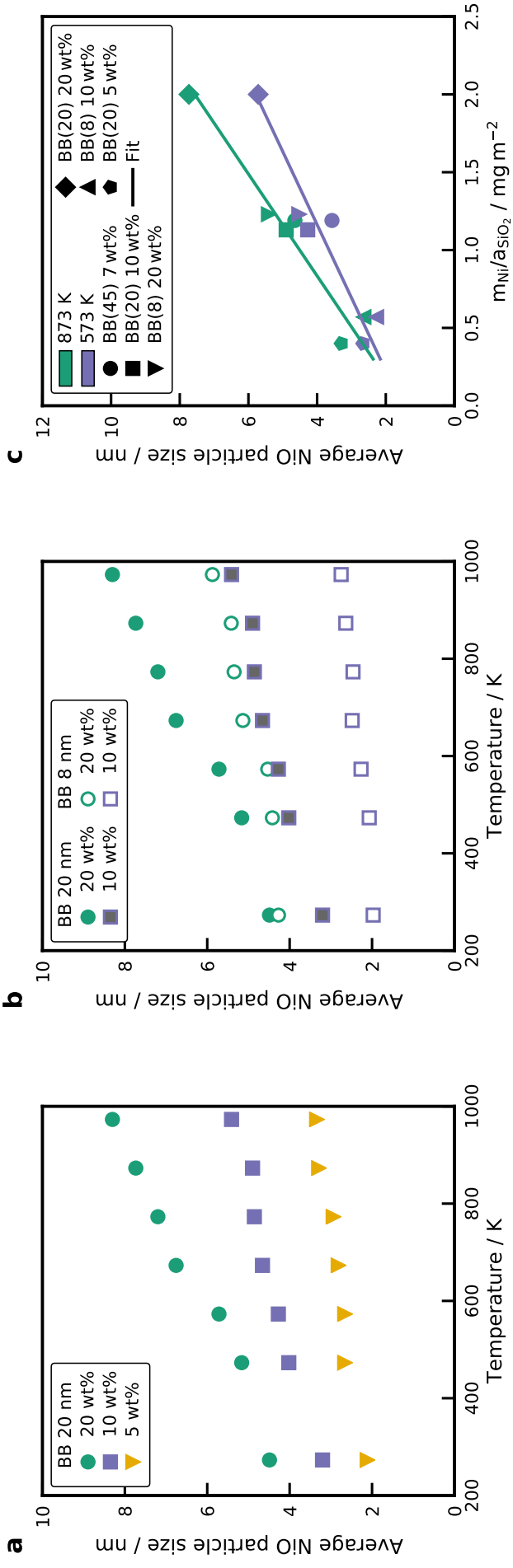

Figure 4.5.: Average NiO nanoparticle size of the different samples calculated using the Scherrer equation Equation (4.1) for (a) BB(20) with different Ni loading, calcined at different temperatures and (**b**) comparison of BB(8) and BB(20) with two different Ni loadings at different calcination temperatures. (c) Average NiO crystal size in dependence of the m_{Ni}/a_{SiO_2} ratio for various catalysts with different SiO_2 primary particle sizes (8, 20 and 45 nm) and Ni loadings (5, 10 and 20 wt%) at two temperatures (see Table S2). A linear regression is displayed to illustrate the observed trend.

oxide nanoparticles supported on spherical silica nanoparticles with defined metal nanoparticle size for a specific metal concentration per surface area of the support for a chosen calcination temperature. On the other hand, this design guide can not be applied for BB(Al_2O_3) with Ni as it was not possible to produce dispersed NiO nanoparticles on the Al_2O_3 surface due to the formation of $NiAl_2O_4$.

4.2.5. Adsorption and Degree of Reduction

H_2 adsorption was performed to determine the amount of active Ni sites. Active metal surface area, Ni crystal diameter and the dispersion were calculated using Equations (4.3) to (4.5). The adsorption capacity was determined from a volumetric isotherm with the back-extrapolation of the linear part (see Figure S7). Results are summarized in Table 4.1 for SiO_2 and Table 4.2 for Al_2O_3. It is evident that the H_2 adsorption capacity is a strong function of the calcination temperature because of the XRD results. The highest H_2 uptake is always determined for the uncalcined samples. An increase in the calcination temperature increases the size of the Ni particles, as shown by the diffractograms, and reduces the active metal surface area. The catalyst with BB(8) and 20 wt% has a monolayer coverage of 460 µmol g^{-1}, which corresponds to a Ni surface area of 40 $m^2 g^{-1}$ and a Ni crystal size of 3.9 nm. After calcination at 673 K this value decreases to 271 µmol g^{-1}, 23.8 $m^2 g^{-1}$, and the crystal size increases to 6.5 nm. The catalyst produced using BB(20) with 10 wt% has the smallest Ni crystal size of 2.4 nm and the highest dispersion of 42.4%. Particle sizes determined via H2 adsorption and XRD are in reasonable agreement for the uncalcined samples and those after calcination at 673 K. However, the crystal size calculated from H_2 adsorption for the samples with a calcination temperature of 973 K deviates significantly.

After calcination at high temperatures, the samples become harder to reduce, seen by the degree of reduction (*DOR*). The *DOR* for BB(20) with 20 wt% of Ni was 91.9% when reduced in pure H_2 at 723 K (10 K min^{-1}) for 1 h, whereas after calcination at 673 K this value drops to 87% and to 82.7% after calcination at 973 K. Ni particle sizes measured with XRD indicate smaller Ni crystals, which interact strongly with the support and cannot be entirely reduced. Catalysts with a loading of 10 wt% are even more difficult to reduce after calcination at 973 K compared to those with a higher loading and show a *DOR* of only 54% (BB(20)) and 66% (BB(8)). A higher Ni loading leads to bigger NiO crystals, which are easier to reduce [54, 55].

4.2.6. Temperature-Programmed Reduction

Temperature-programmed reduction (TPR) profiles of all catalysts are displayed in Figure 4.6a. The NiO reference has a single reduction peak with a maximum at 650 K and a long tailing to higher temperatures. When comparing TPR profiles of Ni/SiO_2 catalysts with the literature, it has to be kept in mind that water in the gas phase can significantly alter the reduction profiles of silica catalysts [56]. High water concentrations in the gas phase retard the reduction due to the formation of surface nickel silicates, which cover the NiO crystals and are more challenging to reduce [56]. The reduction profile of the silica catalysts show the same behavior for different calcination temperatures. Therefore, the catalyst with BB(20) and 20 wt% (Figure 4.6a top) is explained in greater detail. TPR profiles of the catalysts can be deconvoluted by fitting Gaussian profiles to the recorded spectra, which is illustrated for this catalyst after calcination at 673 K in Figure 4.6b (top) and 973 K in Figure 4.6b (bottom). Silica catalysts

with a metal loading of 20 wt% show four discernible overlapping peaks, whereas the 10 wt% catalysts have five.

A sharp peak with a maximum at 520 K is observed for the uncalcined sample, which corresponds to the decomposition of remaining nitrates. This is also evidenced by the recorded mass spectrometer (MS) signal and displayed in the SI (see Figure S8). The short residence time of the catalyst (1.6 s) in the tubular furnace at 673 K is not sufficient to decompose all the nitrates. After thermal pretreatment at 673 K or 973 K, the first peak diminishes, and three overlapping peaks remain visible. The decomposition peak for the catalyst with BB(20), 10 wt%, and without calcination is shifted to a higher temperature of 540 K. For the 10 wt% samples, a second low-temperature peak is observed at a temperature of 538 K. This reduction peak can be attributed to Ni_2O_3, which is formed by the decomposition of $Ni(NO_3)_2$ in H_2 atmosphere [57]. Mile et al. [54] reported that Ni_2O_3 is reduced at temperatures of 523 K. The main reduction peak for the 20 wt% catalysts occurs at a temperature of 600 K for BB(20) with 20 wt% and at 630 K for the BB(8) with the same loading. For the lower loadings, this is shifted to higher temperatures of 700 K. Smaller NiO nanoparticles are formed with a lower Ni loading, and these small NiO particles were harder to reduce than big NiO crystals [54, 58]. A high-temperature shoulder is observed with a maximum temperature of 730 K, which can be associated either with particles, in which SiO_4 is incorporated into the NiO lattice [59], or with 1:1 Ni phyllosilicates [55, 58, 60]. SiO_4 retards the reduction of the bulk NiO and causes a higher temperature peak at 730 K. The Ni phyllosilicates form a layered structure, where the Ni^{2+} ions were in an octahedral configuration [55, 58, 60]. Louis et al. [58] reported a formula of $Ni_3Si_2O_5(OH)_4$ for a 1:1 phyllosilicate, which is also known as antigorite according to Coenen [61]. The reduction peak of these 1:1 phyllosilicates is in the range of 773 K to 973 K. With the characterization methods used in this work, it was not possible to precisely identify the formed silicate, and the comparison with literature was not definite because of the retarding effect of gaseous water, which can induce the formation of surface silicates during the reduction [56].

After calcination at 673 K for 4 h the decomposition of the precursor is complete, and three peaks remain visible at 580 K, 650 K, and 800 K. The low-temperature shoulder is in the same temperature range as the reduction of Ni_2O_3 [54, 58]. The reduction peak at 630 K is in line with the NiO reference (650 K) and thus indicating the reduction of NiO, which interacts only to a small extent with the silica surface, also referred to as bulk NiO. Literature values for the reduction of bulk NiO on silica are in the range of 673 K [54, 58]. The high-temperature peak is extended to higher temperatures and is a result of the silicate formation.

An increase in the calcination temperature to 973 K shifts the reduction profiles to higher temperatures. A small reduction peak is observed at 650 K, which is bulk NiO, but the main reduction occurs at 730 K. The main reduction peak is again caused by either 1:1 phyllosilicates or the migration of SiO_4. The peak with a temperature of 900 K at the maximum can be a result of 2:1 phyllosilicates ($Ni_3Si_4O_{10}(OH)_2$), which are even more stable than the 1:1 silicates and have a reduction peak ranging from 873 to 1,028 K [55]. When comparing the TPR profiles of the uncalcined samples with the ones calcined at 673 K, it can be seen that the main reduction peak increases slightly to higher temperatures for a loading of 20 wt%. At the same time, it decreases to lower temperatures for a metal loading of 10 wt%. In the one-step calcination and reduction process, it is possible to create even smaller and more dispersed Ni crystals compared to the classical calcination before reduction [62]. The shift to high temperatures can result from smaller NiO crystals, which are harder to reduce [54]. Since the smaller crystals provide a higher contact area to the silica surface, it is also possible that silicates are more easily formed,

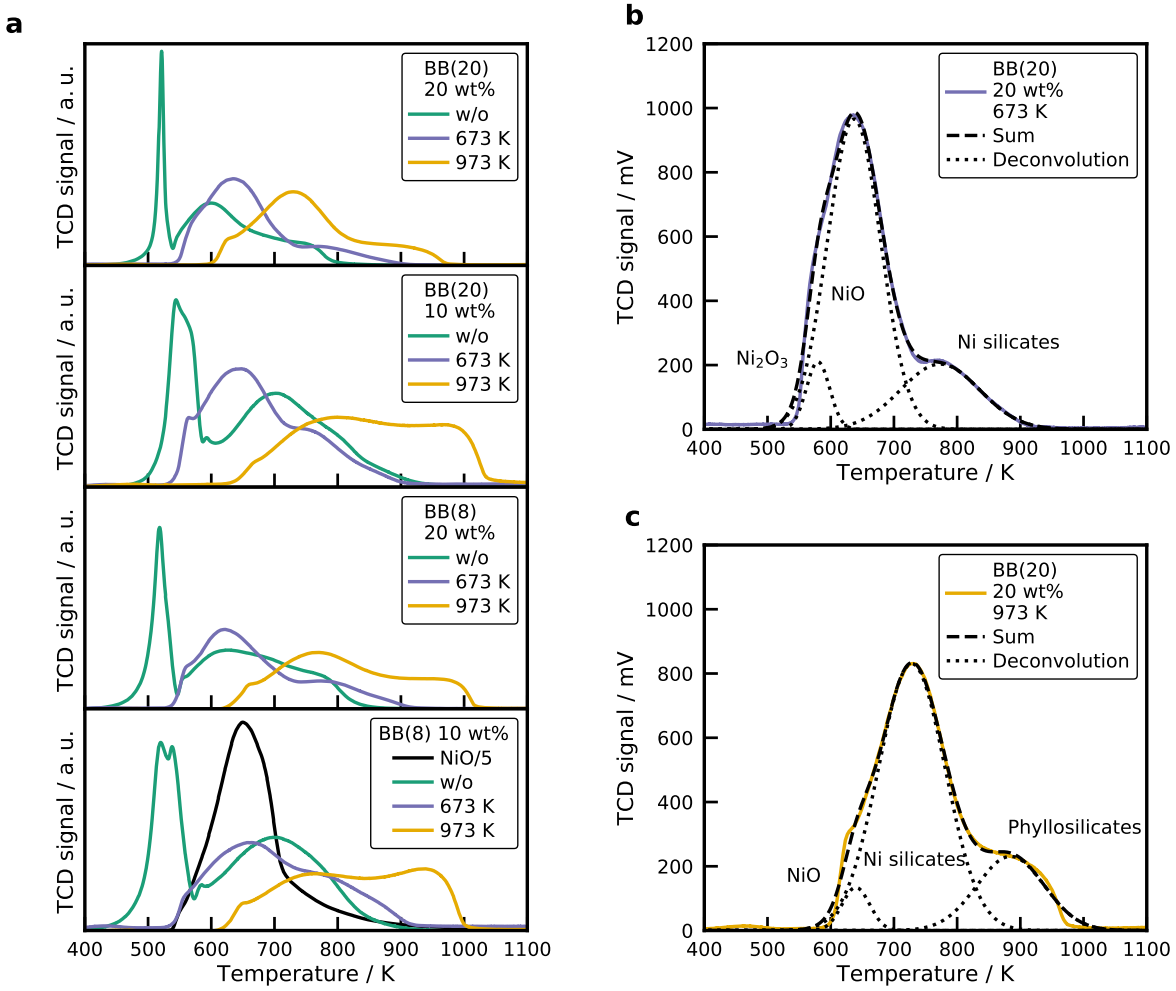

Figure 4.6.: (a) Temperature-programmed reduction profiles (TPR) for all Ni/SiO_2 catalysts. TPR profiles of the BB(20) with 20 wt% Ni catalyst calcined at (b) 673 K and (c) 973 K with a Gaussian deconvolution of the signal. *Conditions:* $m_{cat} = 20\,mg$, $\beta = 10\,K\,min^{-1}$, $\dot{V}_{H_2/Ar} = 30\,mL_N\,min^{-1}$.

which increases the reduction temperature as well. The second explanation is more likely since the Ni particle size of the catalyst with BB(8), 10 wt% without calcination (2.0 nm) and with calcination (2.5 nm), does not differ significantly, whereas the peak temperature changes by 50 K. It seems that the presence of H_2 amplifies the formation of Ni silicates.

The particle size of the primary SiO_2 particles has only a small influence on the reduction profiles for the calcined samples. The TPR profiles reveal a higher share of hard to reduce species, e.g., the height of the main reduction peak is decreased compared to the BB(20) profile, and the height of the high-temperature peak is increased. The small particles provide a higher surface area and, therefore, facilitate the formation of Ni silicates, which form especially at the metal/support interface [55, 60]. For the uncalcined catalysts, the difference is more pronounced and the main reduction peak is shifted to higher temperatures of 700 K.

Interesting TPR results are obtained for the alumina catalyst, which are displayed in Figure 4.7. The uncalcined samples also shows a nitrate decomposition peak. A broad low-intensity second peak is observed, starting at 700 K with the maximum at 1,050 K. The peak is clearly the reduction of $NiAl_2O_4$, also evidenced by the XRD patterns and the shift of the γ-Al_2O_3 reflection (see Figure S4). Contributions

at lower temperatures arise from Ni^{2+} ions incorporated into octahedral and tetrahedral voids in the alumina lattice [38, 59]. After calcination at 673 K for 3 h, the first peak is removed and a broad low-temperature reduction peak is observed. The reduction sets in at 800 K and reaches the maximum at 1,050 K again for the samples with 10 wt%. Calcination at 973 K shifts the starting point and the peak to even higher temperatures. Higher calcination temperatures favor the formation of the crystalline $NiAl_2O_4$, which is also observed by XRD (see Figure S4).

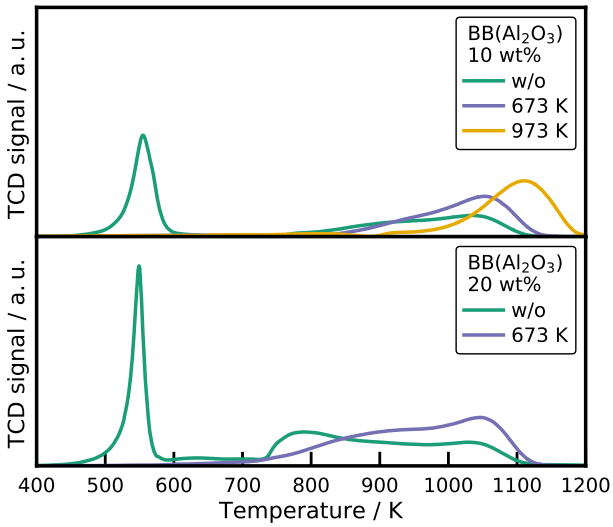

Figure 4.7.: The TPR profiles of the spray-dried Ni/Al_2O_3 catalysts. *Conditions:* $m_{cat} = 20\,mg$, $\beta = 10\,K\,min^{-1}$, $\dot{V}_{H_2/Ar} = 30\,mL_N\,min^{-1}$.

For the sample with a higher loading of 20 wt%, an additional peak at 800 K is observed corresponding to Ni^{2+} incorporated into octahedral voids in the alumina lattice [38]. The calcined samples show the same behavior as for the lower Ni loading. Surprising is that even for the uncalcined catalyst, the main reduction peak is in a temperature range for small NiO crystals and $NiAl_2O_4$. The XRD pattern shows only reflections for crystalline $NiAl_2O_4$ and no NiO reflections at all.

4.2.7. Temperature-Programmed Desorption

Figure 4.8a displays the recorded desorption profiles after CO_2 adsorption at flow conditions for the catalysts with BB(8), 10 wt% and BB(20), 20 wt%. The CO_2 desorption from the $Ni/\gamma\text{-}Al_2O_3$ catalyst (20 wt% without calcination) is shown in Figure 4.8b. Nearly identical profiles were observed for all catalysts. CO_2 starts to desorb at a temperature of 380 K, reaches the maximum desorption rate around 450 K and shows a long tailing up to 800 K. At high temperatures, it is possible to observe the desorption of CO with a maximum at 700 K. The height of the desorption profiles decreases for the catalysts, which were calcined at higher temperatures and consequently have a smaller Ni surface area. No significant differences are observed between the CO_2 desorption from the Ni/SiO_2 catalysts and the $Ni/\gamma\text{-}Al_2O_3$ catalyst (see Figure 4.8b). In addition, no clear effect of the Na concentration on the CO_2 desorption profiles from the catalysts with 20 wt% calcined at 673 K with BB(20) and BB(8) is obtained.

CO_2 uptakes for the Ni/SiO_2 catalysts, measured with volumetric adsorption and listed in Table 4.1 show a similar trend as the desorption profiles. Catalysts with a high Ni surface area adsorb more CO_2. It is also

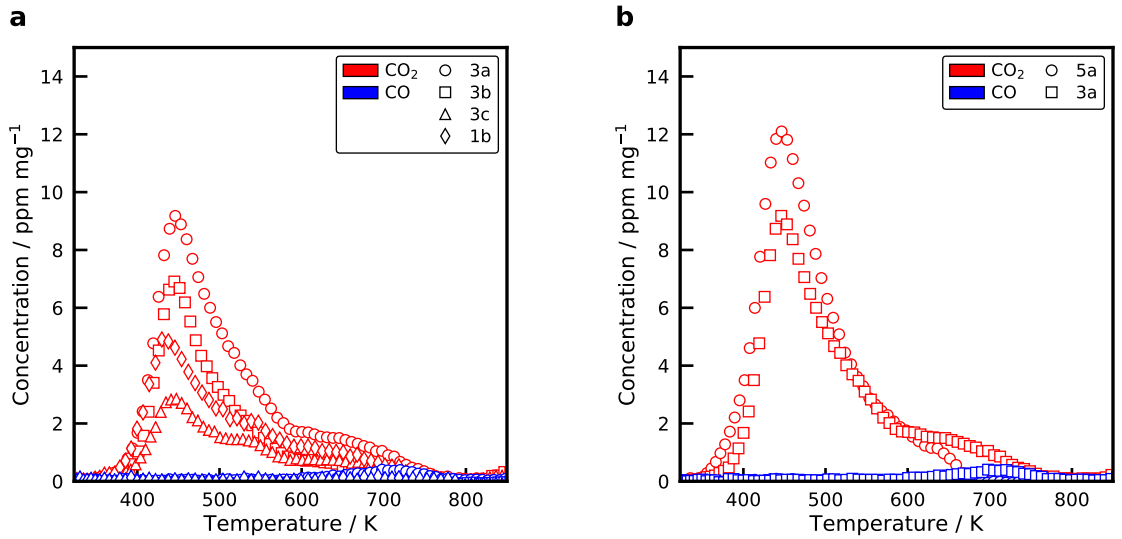

Figure 4.8.: Temperature-programmed desorption of selected (a) Ni/SiO_2 catalysts and (b) $Ni/\gamma\text{-}Al_2O_3$ catalysts after CO_2 adsorption at flow conditions at 383 K for 1 h. *Conditions:* $m_{cat} = 30\,mg$, $\beta = 20\,K\,min^{-1}$, $\dot{V}_{Ar} = 30\,mL_N\,min^{-1}$.

demonstrated that the formation of phyllosilicates, which are created at high calcination temperatures, does not form additional basic adsorption sites for CO_2. However, the Ni/Al_2O_3 catalyst adsorbs more CO_2 compared to the Ni/SiO_2 catalyst with the highest metal surface area. The $Ni/\gamma\text{-}Al_2O_3$ has a smaller metal surface area, but a high amount of basic adsorption sites on the $\gamma\text{-}Al_2O_3$ surface. CO_2 can form weak, medium or strong bonds with the basic adsorption sites [63]. Usually, it is assumed that CO_2 adsorbs only at basic sites on the support. However, Ewald and Hinrichsen [63] showed that CO_2 dissociates under flow conditions at an elevated temperature and adsorbs onto the Ni surface. It is, therefore, of great interest to deconvolve the desorption profiles in the desorption from basic sites and from the Ni surface. Due to the close resemblance of the desorption profiles from the silica and alumina catalysts, it indicates that the binding strength on the Ni surface and on basic sites is similar.

4.2.8. Activity of the Catalysts

Classical isothermal kinetic measurements are the most often used tool to screen the activity of catalytic materials. The drawback of this method is the time consumption to attain new steady-states. That is why only a few points in the conversion-temperature diagrams are typically mapped. The temperature-scanning technique developed by Wojciechowski and Asprey [32, 33] amplifies this process by applying a temperature ramp as during the temperature-programmed reduction. The concentration profile obtained with the temperature-scanning technique is displayed in Figure 4.9a for the catalyst 1b (BB(8), 10 wt%, calcined at 673 K) with a temperature ramp of $20\,K\,min^{-1}$. Concentration profiles are reported on a dry basis because of an inaccurate measurement of the H_2O concentration due to condensation in piping. The solid lines in Figure 4.9 are the equilibrium composition, which is calculated via the minimization of the free Gibbs energy using Cantera [64]. Thermodynamic properties of the gas-phase species were taken from the Active Thermochemical Tables (ATcT) [65, 66]. Methane formation sets in at a temperature of approximately 500 K. It goes through a maximum at 650 K before it reaches the equilibrium concentration. CO forms directly at the beginning, together with CH_4, and goes through a local maximum at 580 K, which is illustrated in more detail in Figure 4.9b.

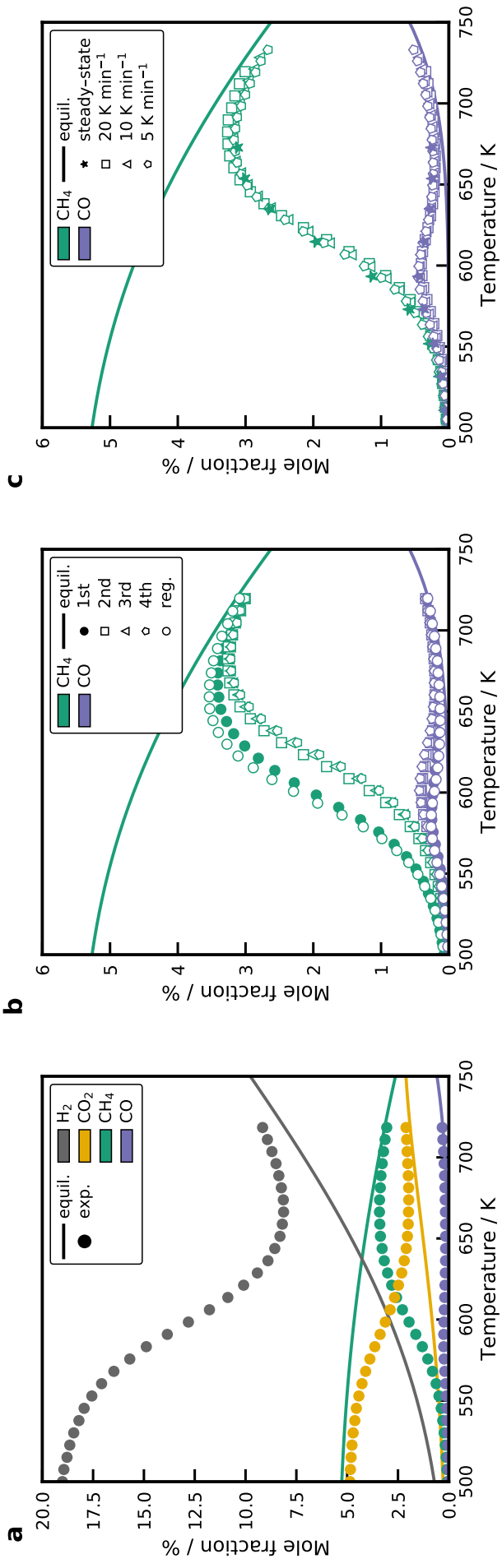

Figure 4.9.: (a) Concentration profile (on a dry basis) of the temperature-scanning experiment for the catalyst formed using BB(8), 10 wt%, and calcined at 673 K (1b) compared to the equilibrium composition. (b) Repeated temperature-scanning results for the 1b catalyst with a temperature ramp of 20 K min^{-1}. After the fourth run, the sample was regenerated by oxidation in synthetic air at 773 K and reduced again. (c) Comparison of temperature-scanning profiles for different scanning rates, as well as steady-state results for the 1b sample. Experimental data is reduced for presentation. *Conditions:* $m_{cat} = 30\,mg$, $WHSV = 100\,L_N\,h^{-1}\,g^{-1}$.

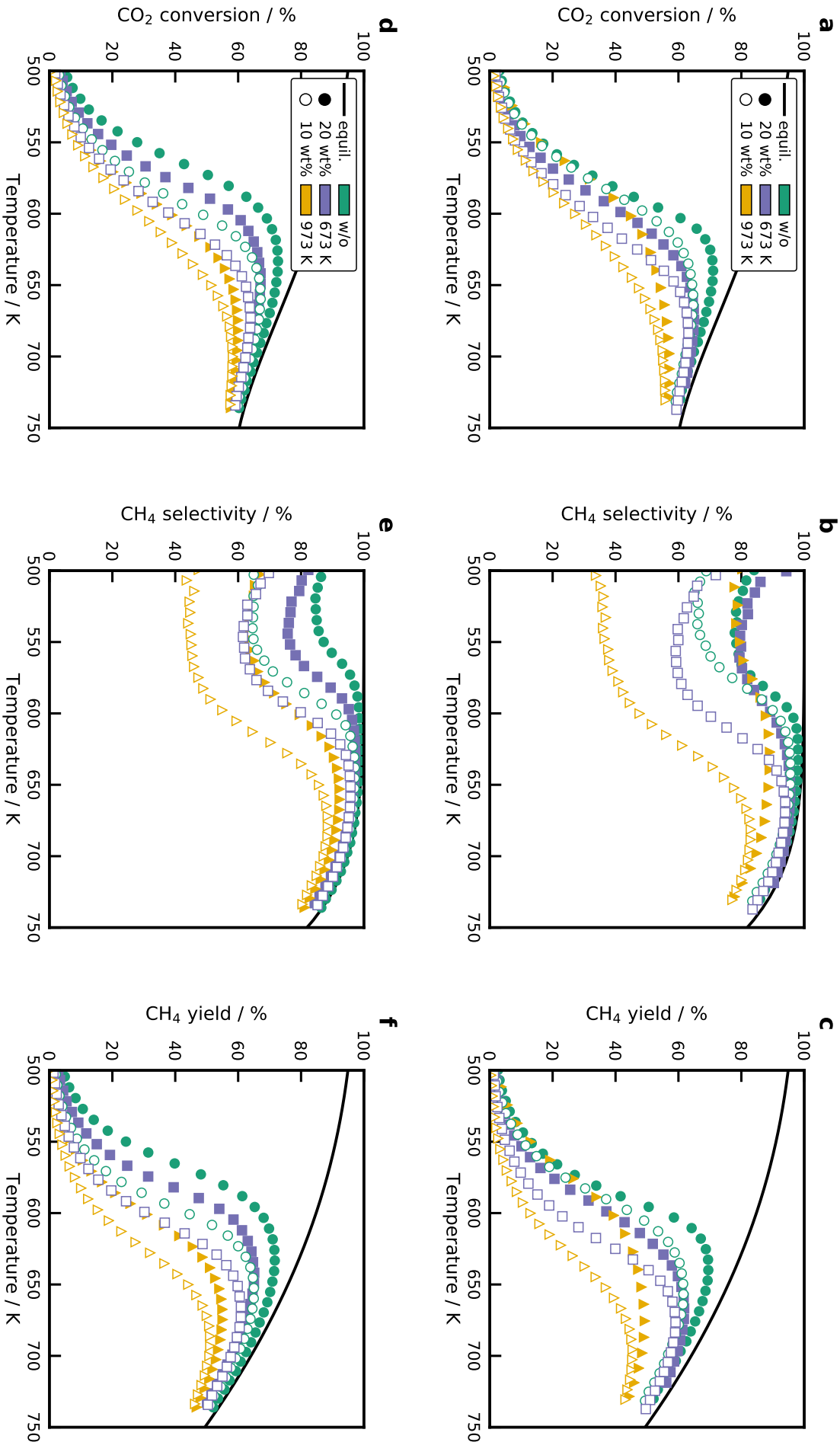

Figure 4.10.: CO_2 conversion, CH_4 selectivity, and CH_4 yield for BB(20) (a–c) and BB(8) (d–f). Solid lines represent the equilibrium. All figures share the same legend. *Conditions:* $m_{cat} = 30\,mg$, $\beta = 20\,K\,min^{-1}$, $WHSV = 100\,L_N\,h^{-1}\,g^{-1}$.

Figure 4.10a displays the measured CO_2 conversion for the Ni/SiO_2 catalysts. The carbon mass balance is always closed within $\pm 2\%$. Selectivity profiles show a low CH_4 selectivity at low temperatures. At the beginning of the methane formation at around 500 K, a more or less distinct formation of CO is observed. The CO concentration surpasses a maximum and declines with increasing temperature. Since this peak is also observed in the steady-state experiments, it can be ruled out as desorption from adsorbed CO, which could have been created during the dissociative adsorption of CO_2 at low temperatures. Weatherbee and Bartholomew [67] observed a CO formation on Ni/SiO_2 catalysts at low temperatures as well. It has to be kept in mind that the overall conversion is low, so it does not significantly affect the CH_4 yield. CO_2 dissociates on the Ni surface to form adsorbed CO^*. Due to the high binding energy of CO^*, the Ni surface is nearly entirely covered with CO^* at low temperatures, which blocks the adsorption of H_2. When the temperature is increased, CO^*will start to desorb, enabling the adsorption of H^* and the methane formation sets in. This can explain the local maximum of CO at the beginning of the methane formation. The influence of calcination temperature on the performance of the catalysts is similar for all BB and Ni loadings. An increase in the calcination temperature leads to a decrease in the activity of the catalyst. Conversion profiles are shifted to higher temperatures and the highest possible conversion is obtained for the samples without further thermal pretreatment. Next to the decrease in the CO_2 conversion, the selectivity to methane decreases as well. This includes the selectivity at low temperatures, as well as at the conversion maximum. On the one hand, the higher calcination temperatures produce larger Ni nanoparticles, which will have a lower Ni surface area and a higher share of Ni terrace sites. On the other hand, the particles have a stronger metal/support interaction.

The usage of different sizes of the SiO_2 primary particles affects the size of the Ni crystals, as shown in the characterization section. Comparing the conversion profiles at loadings of 10 wt% and 20 wt% shows that the smaller primary particle size is also beneficial in terms of activity and CH_4 selectivity. Obviously, an increase in metal loading leads to a higher CO_2 conversion. However, the true activity changes cannot be determined by comparing the conversion. Instead, the turnover frequency needs to be compared. Interesting results are obtained for the selectivity profiles. A higher selectivity towards methane is obtained for the catalysts with a higher metal loading. The highest methanation activity is obtained for the catalysts with BB(8), 20 wt% Ni, and without thermal treatment, which has the highest metal surface area. Those samples with a small Ni loading of 10 % and high calcination temperature of 973 K have the lowest methane yield. The proposed spray-drying method shows a high potential for producing optimized Ni/SiO_2 catalysts with higher metal surface areas by increasing the Ni loading further without adjusting the physical properties, such as the pore size.

Figure 4.11 shows the results for the temperature-scanning of the $Ni/\gamma\text{-}Al_2O_3$ catalysts. Only two catalysts were tested, which have a Ni loading of 20 wt%. These catalyst exhibit a reasonable H_2 uptake despite the low *DOR*, indicating finely dispersed NiO particles. Surprisingly, the $Ni/\gamma\text{-}Al_2O_3$ catalyst without calcination reaches a maximum CO_2 conversion of 71 %, which is close to the performance of the best Ni/SiO_2 catalyst (BB(8), 20 wt%, without calcination) with 73 %. In addition, the CH_4 selectivity is superior to the Ni/SiO_2 catalyst. For the catalyst that was calcined at 673 K it can be observed that the activity drops, which is expected due to the lower *DOR*. The decrease in activity is accompanied by a lower CH_4 selectivity. As shown in by the TPD results and the CO_2 chemisorption, the $\gamma\text{-}Al_2O_3$ support provides a high share of basic adsorption sites that interact strongly with CO_2. Moreover, basic sites play an important role in the CO_2 methanation mechanism, and can improve the activity by altering the mechanism [15].

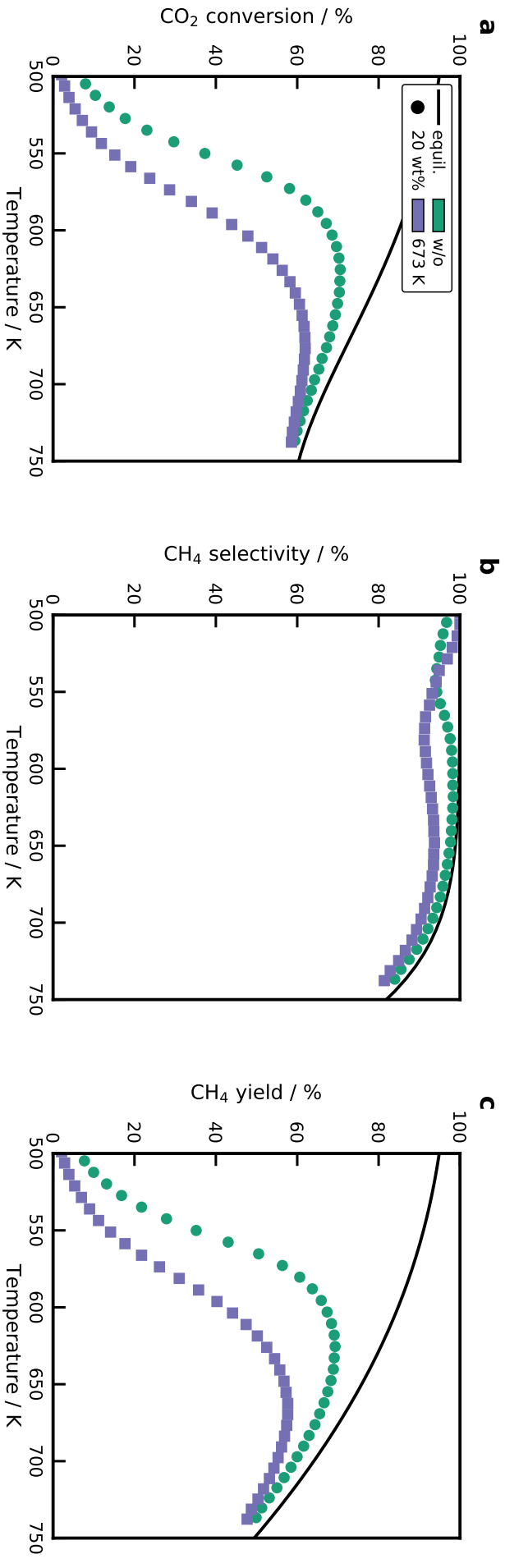

Figure 4.11.: (a) CO_2 conversion, (b) CH_4 selectivity, and (c) CH_4 yield for the Ni/γ-Al_2O_3 catalysts. Only the two catalysts were tested, which have a sufficient *DOR*. *Conditions:* $m_{cat} = 30\,mg$, $\beta = 20\,K\,min^{-1}$, $WHSV = 100\,L_N\,h^{-1}\,g^{-1}$.

Ni aluminates can also be used industrially for high-temperature processes, where the required high reduction temperatures can be attained such as the dry reforming of CH_4 [68]. The strong interaction of Ni aluminates or Ni silicates serves as anchoring site for the Ni crystals once they are reduced. These anchoring sites can prevent sintering of the Ni and provide small Ni crystals at high temperatures and, consequently, a high active surface area [68].

4.2.9. Activation Energies and Turnover Frequencies

Reaction rates for the CH_4 formation were calculated based on the differential fixed-bed assumption, which allows an evaluation up to a conversion of 10 %. Figure S9 shows the Arrhenius dependence of the methane formation rates for selected catalysts. The slope does not change much between the different catalysts and an average activation energy of $84 \pm 4\,\mathrm{kJ\,mol^{-1}}$ is obtained for all Ni/SiO_2 catalysts. The values agree well with the literature data, which is in the range of 75 to $88\,\mathrm{kJ\,mol^{-1}}$ [16, 67, 69–71]. The Ni/Al_2O_3 catalyst has an activation energy of $76\,\mathrm{kJ\,mol^{-1}}$, which reasonable compares to literature data [23, 38]. Figure 4.12a shows the turnover frequencies, calculated for the Ni/SiO_2 catalysts at a constant temperature of 530 K.

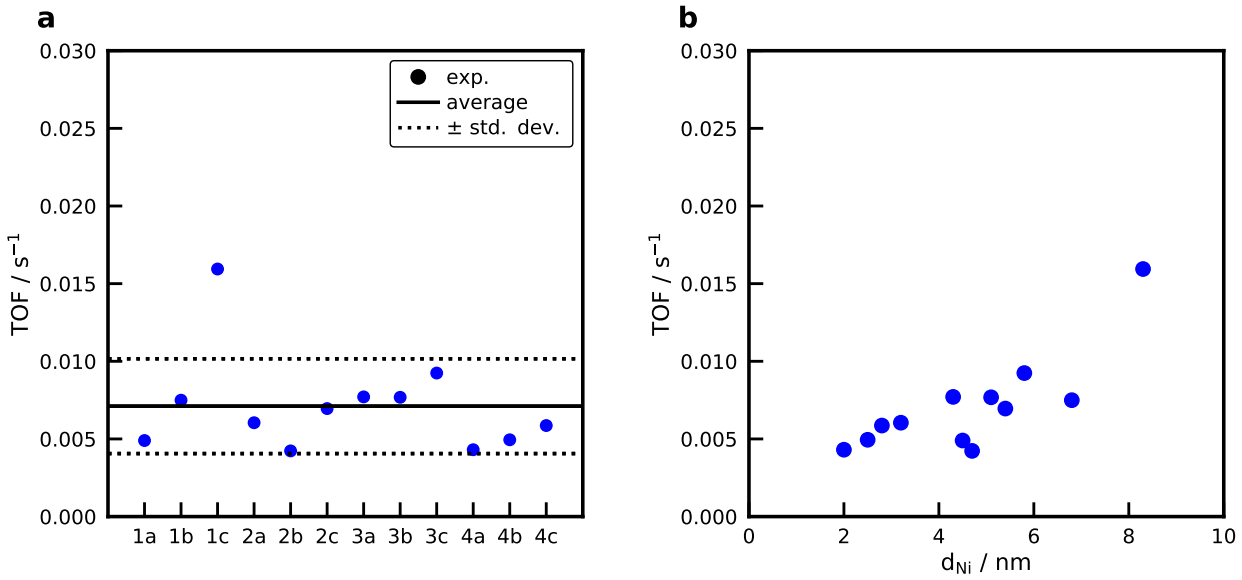

Figure 4.12.: (a) Turnover frequencies (CO_2 to CH_4) of the Ni/SiO_2 catalysts at a temperature of 530 K. For the naming convention of the samples refer to the production tree Figure 4.1. (b) Turnover frequency in dependence of the Ni particle size. *Conditions:* $m_{cat} = 30\,\mathrm{mg}$, $\beta = 20\,\mathrm{K\,min^{-1}}$, $WHSV = 100\,\mathrm{L_N\,h^{-1}\,g^{-1}}$, $X_{CO_2} < 10\,\%$.

At this temperature, the CO_2 conversion for all catalysts is below 10 %. This means that the concentration in the gas phase varies, but the difference is small that is why it can be neglected. An average TOF of $7.1 \times 10^{-3}\,\mathrm{s^{-1}}$ is obtained for all samples. The $Ni/\gamma\text{-}Al_2O_3$ show a significantly higher TOF of $37.1 \times 10^{-3}\,\mathrm{s^{-1}}$. Figure 4.12b shows the TOF as a function of the Ni crystal size determined with XRD, revealing no correlation between the Ni crystal size and the TOF. The catalyst 1c (BB(20), 20 wt%, calcined at 973 K) with a Ni crystal size of 8.3 nm shows a significantly higher activity compared to the rest of the catalysts. This is in contrast to results from Vogt et al. [72] who report a clear structure-sensitivity for the CO_2 methanation below 6 nm with a maximum TOF at approximately 2 nm, at a temperature of 673 K for Ni/SiO_2 catalysts. On the other hand, no structure sensitivity is observed

by Beierlein et al. [38] for the CO_2 methanation on Ni/Al_2O_3 catalysts. Usually, the equilibrium shape of the Ni crystal changes significantly below 7 nm and reaches a nearly constant facet distribution for bigger crystals [73], which explains why a structure-sensitivity should be observed in small Ni crystals. However, Weber et al. [74] observed a maximum TOF for the CO methanation at 15 nm on gasborne Ni nanoparticles. Due to the fast evaporation of the water in the droplets in the spray-drying procedure and the high cooling rates, it is questionable whether the equilibrium shape of the Ni crystal is obtained. As a conclusion, we can say that for the studied operation point at 530 K and conversion below 10 % no clear structure-activity relation can be derived for the spray-dried Ni/SiO_2 catalysts. More catalysts with larger Ni crystal sizes need to be produced to provide a clearer trend that can now be easily done by applying the tailoring guide in Figure 4.5c.

4.3. Materials and Methods

4.3.1. Materials

Ammonium stabilized aqueous colloidal silica suspensions with an average particle diameter of 8 nm (Köstrosol 0830AS, 30 wt%, pH 9.6), 20 nm (Köstrosol 2040AS, 40 wt%, pH 9.3), and 45 nm (Köstrosol 0830AS, 30 wt%, pH 9.6) were obtained from CWK Chemiewerk Bad Köstritz GmbH (Bad Köstritz, Germany). The silica nanoparticles were used as support for the NiO nanoparticles. Colloidal Al_2O_3 nanoparticle suspension (pseudo-Boehmite, (AlO(OH)) 50 nm, 20 wt%, pH 4, Alfa Aesar, Ward Hill, MA, USA) was also used as a support for the NiO nanoparticles. Nickel nitrate, $Ni(NO_3)_2 \cdot 6\,H_2O$ (99 %, Sigma-Aldrich, St. Louis, MO, USA), was added to the suspension as the precursor for the production of nickel oxide nanoparticles. Deionized water was utilized in all synthesis suspensions. All of the materials in this work were used without further purification.

4.3.2. Experimental Setup and Synthesis of the NiO/SiO_2 Nanoparticles

The particles synthesized in this study were produced by spray-drying a colloidal silica suspension containing dissolved $Ni(NO_3)_2$ and deionized water. Prepared suspensions (pH of approximately 6.7) were atomized using an aerosol nebulizer (AGK 2000, Palas GmbH, Karlsruhe, Germany), with pressurized air as carrier gas at a flow rate of 7.7 L min^{-1}. The produced droplets were dried in a tube furnace at 673 K with a short residence time of 1.6 s. The dried particles, also named as BB, were collected on a filter and heat-treated in a muffle oven to adjust the NiO nanoparticle size. A schematic drawing of the setup can be found in previous work [31]. In this study, NiO nanoparticles supported on two different supports (SiO_2 and Al_2O_3) with two different Ni loadings (10 and 20 wt%) for two different heat treatment conditions were investigated. For the NiO nanoparticles supported on silica, BB formed with two different SiO_2 primary particle sizes (8 and 20 nm) were produced and characterized. For the NiO nanoparticles supported on alumina, BB created with Al_2O_3 primary particles with a size of 50 nm were synthesized as well. Figure 4.1 summarizes the catalysts produced within this work.

4.3.3. Physical Characterization

The structure and morphology of the catalysts were examined with transmission electron microscopy (TEM) and scanning electron microscopy (SEM). TEM was performed with a JEOL JEM-2100 microscope (JEOL Ltd., Akishima, Tokyo, Japan) operated at 160 kV. For the preparation of the TEM samples, the particles were deposited onto a copper grid coated with a carbon film. SEM was carried out with a Zeiss DSM Gemini 982 (Zeiss, Jena, Germany) operated at 5 kV. X-ray diffraction (XRD) diagrams were recorded in $\omega/2\Theta$-geometry using Cu-Kα radiation (λ =1.5406 Å) operated at 40 kV and 40 mA (Empyrean, PANalytical, Almelo, Netherlands). Angles of 2Θ between 10 and 90° were measured with a step length of 0.026° and a step time of 200 s. The NiO nanoparticle size was determined using the Scherrer equation (4.1) with a shape factor $k = 0.9$ and the line broadening of the NiO(200) line at $2\Theta = 43.3°$. The full width at half-maximum of the reflection was corrected using LaB_6 as a reference.

$$d = \frac{K_f \lambda}{\beta cos(\Theta)} \tag{4.1}$$

Small-angle X-ray scattering (SAXS) was used to measure the size of the single primary particles that form the BB. These experiments took place on the above-described diffractometer equipped with a SAXS stage operated at 45 kV and 40 mA. The produced particles were placed in a sample holder between two mylar foils and were measured in a range from −0.115 to 5° 2Θ, with a step size of 0.01° 2Θ for 2.2 s per step. Nitrogen adsorption–desorption isotherms were recorded at 77 K (ASAP 2020, Micromeritics Instrument Corporation, Norcross, GA, USA). The Brunauer-Emmett-Teller (BET) method was used to calculate the specific surface area of the BB. The pore size distributions and total pore volume of the BB were calculated according to the Barrett-Joyner-Halenda (BJH) model, using the results from the desorption. Typically, a sample mass of 100 to 150 mg was degassed at a temperature of 250 °C for 2 h before analysis.

4.3.4. Chemical Characterization

Temperature-programmed reduction (TPR) experiments were conducted in the BelCat-M device (MicrotracBEL Corp., Osaka, Japan). 20 mg of the catalyst were degassed at 393 K for 60 min in Ar atmosphere to remove adsorbed species. The TPR was conducted with a 10 % H_2/Ar mixture at a volumetric flow rate of 30 $mL_N\,min^{-1}$ and the temperature was linearly raised with a temperature ramp of 10 $K\,min^{-1}$ from 323 to 1,223 K. A thermal conductivity detector (TCD) was used to analyze the hydrogen consumption after the effluent gas was passed over a molecular sieve with a pore size of 3 Å. The amount of Ni in the sample was determined by assuming that only NiO was reduced and the TCD was calibrated for a NiO reference (99.998 %, AlfaAesar, Ward Hill, MA, USA).

The nickel dispersion and crystallite size were measured by H_2 adsorption and subsequent O_2 titration in a volumetric adsorption apparatus (3Flex, Micromeritics Instrument Corporation, Norcross, GA, USA). A sample of 80 mg was reduced at 723 K for 1 h in pure H_2 with a volumetric flow rate of 50 $mL_N\,min^{-1}$. All gases used in this study were of quality 5.0 and passed over O_2 and H_2O traps to remove contaminants. After reduction, the catalyst was evacuated for 1 h before the sample was cooled to the adsorption temperature of 323 K. An adsorption isotherm was recorded from 3 to 550 mbar with an equilibration interval of 1 min. Following the H_2 adsorption, the sample was heated in vacuum to 673 K (10 $K\,min^{-1}$) and evacuated for 1 h before the O_2 adsorption was carried out at this temperature. Back-extrapolation

of the linear part of the isotherm to zero pressure was used to calculate the uptake of either H_2 or O_2. From the adsorption experiments, the degree of reduction (DOR) (Equation (4.2)), the corrected dispersion D (Equation (4.5)), the specific metal surface area a_{Ni} (Equation (4.3)), and the Ni crystallite size d_{Ni} (Equation (4.4)) were calculated. CO_2 adsorption isotherms are also recorded for selected samples. Due to a strong adsorption of CO_2 on possible basic surface sites, a double isotherm was performed.

$$DOR = \frac{a_{cat} f_{calibration}}{2 m_{cat} Q_{O_2}} \tag{4.2}$$

$$a_{Ni} = Q_{H_2} z N_A \sigma_{Ni} \frac{1}{DOR} \tag{4.3}$$

$$d_{Ni} = \frac{6000 \omega_{Ni}}{\rho_{Ni} a_{Ni}} \tag{4.4}$$

$$D = 2 a_{Ni} W_{Ni} \frac{100}{\omega_{Ni}} \tag{4.5}$$

A spherical shape of the Ni crystals was assumed [75] and the following parameters were used: M_{NiO} is the molar mass (58.69 g mol^{-1}), N_A is the Avogadro constant, ω_{Ni} the Ni loading, σ_{Ni} is the surface area of a Ni atom (6.51 Å^2), and ρ_{Ni} is the Ni density (8.9 g cm^{-3}).

CO_2 temperature-programmed desorption was applied to investigate the interaction of CO_2 with basic sites on the support and the Ni crystals. A mixture of 9.87% CO_2 in He is passed over the catalyst in a flow experiment at 383 K for 60 min. Then the catalyst is purged with Ar for 15 min and cooled to 323 K to start the TPD with a temperature ramp of 20 K min^{-1} to 1,073 K.

4.3.5. Methanation Experiments

CO_2 methanation experiments were conducted in the BelCat-M connected to a mass spectrometer (MS) (GAM200, InProcessInstruments, Bremen, Germany). 30 mg of the sample was placed in a modified sample holder [53] and fixed with quartz wool plugs. A temperature-scanning experiment was performed to investigate the activity of the catalysts. In these experiments, a stoichiometric mixture of H_2/CO_2 with Ar as internal standard (20/5/75 %) flowed through the catalyst bed with a volumetric flow rate of 50 mL$_N$ min^{-1}, and the temperature was raised with a constant heating rate of 20 K min^{-1} from 323 K to 723 K. A thermocouple was placed directly above the catalyst bed. The exit gas concentration was measured with the MS, which was calibrated with certified gas mixtures for H_2, CO_2, CO, CH_4 and Ar. A measurement time of 0.4 s per cycle was achieved. The CO_2 conversion (X_{CO_2}), CH_4 selectivity (S_{CH_4}), and CH_4 yield (Y_{CH_4}) were determined from the measured exit gas composition with Equations (4.6) to (4.8) using Ar as an internal standard.

$$X_{CO_2} = 1 - \frac{x_{Ar}^{in} x_{CO_2}^{out}}{x_{Ar}^{out} x_{CO_2}^{in}} \tag{4.6}$$

$$S_{CH_4} = \frac{x_{CH_4}^{out}}{x_{CH_4}^{out} + x_{CO}^{out}} \tag{4.7}$$

$$Y_{CH_4} = S_{CH_4} X_{CO_2} \tag{4.8}$$

Reaction rates were calculated at temperatures where the conversion was below 10 %, so that differential fixed-bed conditions could be assumed. The methane formation rate r_{CH_4} was calculated with

$$r_{CH_4} = \frac{\dot{V}_N^{in} \alpha x_{CH_4}^{out} p_N}{m_{cat} R T_N} \tag{4.9}$$

where α accounts for the volume contraction with the change in the concentration of the internal standard Ar. The activation energy was determined from the calculated rates and temperatures. In combination with the amount of exposed Ni atoms measured with H_2 adsorption, it was possible to determine the turnover frequency TOF:

$$TOF = \frac{r_{CH_4}}{2Q_{H_2}} \tag{4.10}$$

4.4. Conclusions

Highly dispersed NiO nanoparticles supported on silica with a well organized porous structure and tunable properties were produced by spray-drying. According to our experimental results, we proved that the presented method is a flexible process that can be extended for the preparation of the catalyst particles containing different metals, which was done in previous work for Co_3O_4/SiO_2 catalysts. With this method, the pore size, the total pore volume, and the specific surface area of the catalyst can be easily adjusted by varying the primary particle size of the SiO_2 support. One of the biggest advantages of the method presented here for the NiO/SiO_2 system is the independent control of the NiO nanoparticle size and the pore size. The size of the NiO nanoparticles can be tailored with the ratio of the mass of Ni to the surface area of the support and calcination temperature, whereas the pore size depends only on the size of the primary SiO_2 particle.

Ni/SiO_2 catalysts with metal surface areas of up to $40\,m^2\,g^{-1}$ and 42 % dispersion were synthesized. These catalysts were produced without further thermal treatment and the decomposition of remaining nitrates occurred during the reduction. In order to increase the metal surface area, it is, therefore, of interest to produce the particles in H_2 atmosphere. $Ni/\gamma\text{-}Al_2O_3$ catalysts were produced with the same method, but it is not possible to tailor the catalyst properties as good as for the Ni/SiO_2 catalysts. The finely dispersed NiO in close contact with a high surface area alumina leads to the formation of crystalline $NiAl_2O_4$, which is challenging to reduce but can provide a well-dispersed catalyst for high-temperature processes. The spray-drying procedure is a universal method that can be extended to various catalytic systems and even used to produce bimetallic catalysts.

The temperature-scanning methanation experiment allowed for a fast and efficient screening of the catalysts. The catalyst with the highest metal surface area showed the highest methane yield. Selectivity toward CO depends on the metal/support interaction. High calcination temperatures lead to the formation of Ni phyllosilicates, which are difficult to reduce. The highest activity and Ni surface area were observed for those samples without further thermal treatment. Since the crystal size was varied for the catalysts, it was possible to investigate the structure-activity relations for the CO_2 methanation for the Ni/SiO_2 and $Ni/\gamma\text{-}Al_2O_3$ catalysts. The $Ni/\gamma\text{-}Al_2O_3$ catalyst showed a high methanation activity due to the presence of basic sites on the support. No conclusive dependence of the TOF on the Ni crystal size was observed for the Ni/SiO_2 catalysts. The tailoring guide proposed in this work will now

allow to design Ni/SiO_2 catalysts with defined Ni crystal sizes that will be investigated with the temperature scanning technique in a Berty reactor setup to unravel structure-activity relations for higher temperatures and conversions.

Funding

The authors gratefully acknowledge financial support from the Deutsche Forschungsgemeinschaft (DFG, German Research Foundation) within the SPP 1570 with the project number WE 2331/13-3 and TU 89/9-3 and the DFG project 290019031. Part of this work is supported and financed by Clausthal University of Technology, project Catalytic and Microbial Methanation as Basis for Sustainable Energy Storage (CliMb).

Acknowledgements

The authors thank the Institute of Mineral and Waste Processing, Waste Disposal and Geomechanics of Clausthal University of Technology (ICP-OES) and CWK Chemiewerk Bad Köstritz GmbH for providing colloidal silica nanoparticles. A.M. and B.K. gratefully acknowledge the fruitful discussions on the XRD with Alessio Zandona. We acknowledge financial support by the Open Access Publishing Fund of Clausthal University of Technology.

Abbreviations

The following abbreviations are used in this manuscript:

TPR	Temperature-programmed reduction	TPD	Temperature-programmed desorption
XRD	X-ray diffraction	TEM	Transmission Electron Microscopy
SEM	Scanning Electron Microscopy	TCD	Thermal conductivity detector
MS	Mass spectrometer	BB	Building-Blocks
SAXS	Small-angle X-ray scattering	BET	Brunauer-Emmett-Teller method
BJH	Barrett-Joyner-Halenda model		

List of Symbols

Latin symbols

a	area	m^2
D	dispersion	-
DOR	degree of reduction	%
d	diameter	m
f	calibration factor	$mol\,m^{-2}$
K	Scherrer form factor	-
m	mass	g
p	pressure	bar
Q	adsorbed amount	$mol\,g^{-1}$
R	ideal gas constant	$J\,mol^{-1}\,K^{-1}$
r	reaction rate	$mol\,s^{-1}\,g^{-1}$
S	selectivity	-
T	temperature	K
$\dot{V}$	volume flow	$mL\,min^{-1}$
W	molar mass	$g\,mol^{-1}$
w	metal loading	-
$WHSV$	weight hourly space velocity	$L_N\,h^{-1}\,g^{-1}$
X	conversion	-
x	molar fraction	-
Y	yield	-
z	adsorption stoichiometry	-

Greek symbols

α	volume reduction (x_{Ar}^{in}/x_{Ar}^{out})	-
β	temperature ramp	$K\,min^{-1}$
Θ	Bragg angle	°
λ	wavelength	m
ρ	density	$kg\,m^{-3}$
σ	surface area	m^2

Subscripts		Superscripts	
calibration	calibration	in	inlet
cat	catalyst	out	outlet
f	form factor		
N	normal conditions		

References

[1] S. Tomiyama, R. Takahashi, S. Sato, S. Toshiaki, Y. Satoshi. *Appl. Catal., A* **2003**, 241 (1), 349–361. DOI: 10.1016/S0926-860X(02)00493-3.

[2] Y. Zhang, W. Wang, Z. Wang, X. Zhou, Z. Wang, C.-j. Liu. *Catal. Today* **2015**, 256, 130–136. DOI: 10.1016/j.cattod.2015.01.016.

[3] X. Huang, R. Reimert. *Fuel* **2013**, 106, 380–387. DOI: 10.1016/j.fuel.2012.09.081.
[4] Z. Xie, B. Yan, J. H. Lee, Q. Wu, X. Li, B. Zhao, D. Su, L. Zhang, J. G. Chen. *Appl. Catal., B* **2019**, 245, 376–388. DOI: 10.1016/j.apcatb.2018.12.070.
[5] J. Sehested, S. Dahl, J. Jacobsen, J. R. Rostrup-Nielsen. *J. Phys. Chem.. B* **2005**, 109 (6), 2432–2438. DOI: 10.1021/jp040239s.
[6] B. Nematollahi, M. Rezaei, E. N. Lay. *Int. J. Hydrogen Energy* **2015**, 40 (27), 8539–8547. DOI: 10.1016/j.ijhydene.2015.04.127.
[7] S. Rönsch, J. Köchermann, J. Schneider, S. Matthischke. *Chem. Eng. Technol.* **2016**, 39 (2), 208–218. DOI: 10.1002/ceat.201500327.
[8] J. Gao, Q. Liu, F. Gu, B. Liu, Z. Zhong, F. Su. *RSC Adv.* **2015**, 5 (29), 22759–22776. DOI: 10.1039/C4RA16114A.
[9] B. Kreitz, J. Friedland, R. Güttel, G. D. Wehinger, T. Turek. *Chem. Ing. Tech.* **2019**, 91 (5), 576–582. DOI: 10.1002/cite.201800191.
[10] B. Kreitz, G. D. Wehinger, T. Turek. *Chemical Engineering Science* **2019**, 195, 541–552. DOI: 10.1016/j.ces.2018.09.053.
[11] B. Kreitz, J. Brauns, G. D. Wehinger, T. Turek. *Chem. Ing. Tech.* **2020**, 43 (45), 20332. DOI: 10.1002/cite.202000019.
[12] P. Frontera, A. Macario, M. Ferraro, P. Antonucci. *Catalysts* **2017**, 7 (12), 59. DOI: 10.3390/catal7020059.
[13] J. Ashok, S. Pati, P. Hongmanorom, Z. Tianxi, C. Junmei, S. Kawi. *Catal. Today* **2020**. DOI: 10.1016/j.cattod.2020.07.023.
[14] W. Wei, G. Jinlong. *Front. Chem. Sci. Eng.* **2011**, 5 (1), 2–10. DOI: 10.1007/s11705-010-0528-3.
[15] Q. Pan, J. Peng, T. Sun, S. Wang, S. Wang. *Catal. Commun.* **2014**, 45, 74–78. DOI: 10.1016/j.catcom.2013.10.034.
[16] M. Aziz, A. A. Jalil, S. Triwahyono, R. R. Mukti, Y. H. Taufiq-Yap, M. R. Sazegar. *Appl. Catal., B* **2014**, 147, 359–368. DOI: 10.1016/j.apcatb.2013.09.015.
[17] C.-S. Chen, C. S. Budi, H.-C. Wu, D. Saikia, H.-M. Kao. *ACS Catal.* **2017**, 7 (12), 8367–8381. DOI: 10.1021/acscatal.7b02310.
[18] R.-P. Ye et al. *Energy* **2019**, 188, 116059. DOI: 10.1016/j.energy.2019.116059.
[19] P. Zhu, Q. Chen, Y. Yoneyama, N. Tsubaki. *RSC Adv.* **2014**, 4 (110), 64617–64624. DOI: 10.1039/C4RA12861C.
[20] Y. J. Huang, J. A. Schwarz. *Appl. Catal.* **1987**, 30 (2), 239–253. DOI: 10.1016/S0166-9834(00)84116-0.
[21] G. Li, L. Hu, J. M. Hill. *Appl. Catal., A* **2006**, 301 (1), 16–24. DOI: 10.1016/j.apcata.2005.11.013.
[22] J. Ashok, M. L. Ang, S. Kawi. *Catal. Today* **2017**, 281, 304–311. DOI: 10.1016/j.cattod.2016.07.020.
[23] F. Koschany, D. Schlereth, O. Hinrichsen. *Appl. Catal., B* **2016**, 181, 504–516. DOI: 10.1016/j.apcatb.2015.07.026.
[24] G. Chiarello, I. Rossetti, L. Forni. *J. Catal.* **2005**, 236 (2), 251–261. DOI: 10.1016/j.jcat.2005.10.003.
[25] M. Compagnoni, A. Tripodi, A. Di Michele, P. Sassi, M. Signoretto, I. Rossetti. *Int. J. Hydrogen Energy* **2017**, 42 (47), 28193–28213. DOI: 10.1016/j.ijhydene.2017.09.123.
[26] A. M. Saib, M. Claeys, E. van Steen. *Catal. Today* **2002**, 71 (3), 395–402. DOI: 10.1016/S0920-5861(01)00466-7.
[27] Ø. Borg, S. Eri, E. A. Blekkan, S. Storsæter, H. Wigum, E. Rytter, A. Holmen. *J. Catal.* **2007**, 248 (1), 89–100. DOI: 10.1016/j.jcat.2007.03.008.
[28] D. Song, J. Li. *J. Mol. Catal. A: Chem.* **2006**, 247 (1-2), 206–212. DOI: 10.1016/j.molcata.2005.11.021.

[29] R. Koirala, S. E. Pratsinis, A. Baiker. *Chem. Soc. Rev.* **2016**, 45 (11), 3053–3068. DOI: 10.1039/c5cs00011d.

[30] L. Gradon, R. Balgis, T. Hirano, A. M. Rahmatika, T. Ogi, K. Okuyama. *J. Aerosol Sci.* **2020**, 149, 105608. DOI: 10.1016/j.jaerosci.2020.105608.

[31] A. Martínez Arias, A. P. Weber. *J. Aerosol Sci.* **2019**, 131, 1–12. DOI: 10.1016/j.jaerosci.2019.02.003.

[32] B. Wojciechowski. *Catal. Today* **1997**, 36 (2), 167–190. DOI: 10.1016/S0920-5861(96)00219-2.

[33] S. Asprey. *Catal. Today* **1997**, 36 (2), 209–226. DOI: 10.1016/S0920-5861(96)00221-0.

[34] B. Wojciechowski, S. P. Asprey. *Appl. Catal., A* **2000**, 190 (1-2), 1–24. DOI: 10.1016/S0926-860X(99)00271-9.

[35] C. Liebner, D. Wolf, M. Baerns, M. Kolkowski, F. J. Keil. *Appl. Catal., A* **2003**, 240 (1-2), 95–110. DOI: 10.1016/S0926-860X(02)00415-5.

[36] C. Vogt, J. Wijten, C. L. Madeira, O. Kerkenaar, K. Xu, R. Holzinger, M. Monai, B. M. Weckhuysen. *ChemCatChem* **2020**, 12 (10), 2792–2800. DOI: 10.1002/cctc.202000327.

[37] T. A. Le, T. W. Kim, S. H. Lee, E. D. Park. *Catal. Today* **2018**, 303, 159–167. DOI: 10.1016/j.cattod.2017.09.031.

[38] D. Beierlein, D. Häussermann, M. Pfeifer, T. Schwarz, K. Stöwe, Y. Traa, E. Klemm. *Appl. Catal., B* **2019**, 247, 200–219. DOI: 10.1016/j.apcatb.2018.12.064.

[39] L. Zeng, A. P. Weber. *J. Aerosol Sci.* **2014**, 76, 1–12. DOI: 10.1016/j.jaerosci.2014.05.003.

[40] K. Okuyama, I. Wuled Lenggoro. *Chem. Eng. Sci.* **2003**, 58 (3-6), 537–547. DOI: 10.1016/S0009-2509(02)00578-X.

[41] J. Röhrbein, A. M. Arias, A. P. Weber. *Chem. Ing. Tech.* **2017**, 89 (12), 1739–1751. DOI: 10.1002/cite.201600184.

[42] A. Y. Khodakov, A. Griboval-Constant, R. Bechara, V. L. Zholobenko. *J. Catal.* **2002**, 206 (2), 230–241. DOI: 10.1006/jcat.2001.3496.

[43] R. D. Shannon. *Acta Crystallogr., Sect. A: Found. Adv.* **1976**, 32 (5), 751–767. DOI: 10.1107/S0567739476001551.

[44] H. C. St. O'Neill, W. A. Dollase, C. R. Ross. *Phys. Chem. Miner.* **1991**, 18 (5), 302–319. DOI: 10.1007/BF00200188.

[45] R.-S. Zhou, R. L. Snyder. *Acta Crystallogr., Sect. B: Struct. Sci.* **1991**, 47 (5), 617–630. DOI: 10.1107/S0108768191002719.

[46] A. Cao, R. Lu, G. Veser. *Phys. Chem. Chem. Phys.* **2010**, 12 (41), 13499–13510. DOI: 10.1039/c0cp00729c.

[47] T. W. Hansen, A. T. Delariva, S. R. Challa, A. K. Datye. *Acc. Chem. Res.* **2013**, 46 (8), 1720–1730. DOI: 10.1021/ar3002427.

[48] A. Cao, G. Veser. *Nat. Mater.* **2010**, 9 (1), 75–81. DOI: 10.1038/nmat2584.

[49] J. M. Petroski, Z. L. Wang, T. C. Green, M. A. El-Sayed. *J. Phys. Chem. B* **1998**, 102 (18), 3316–3320. DOI: 10.1021/jp981030f.

[50] J. van de Loosdrecht, A. M. van der Kraan, A. J. van Dillen, J. W. Geus. *J. Catal.* **1997**, 170 (2), 217–226. DOI: 10.1006/jcat.1997.1741.

[51] W. Zoz, R. Gonzalez. *Appl. Catal., A* **1993**, 102 (2), 181–200. DOI: 10.1016/0926-860X(93)80228-I.

[52] A. Y. Khodakov. *Braz. J. Phys.* **2009**, 39 (1a), 171–175. DOI: 10.1590/S0103-97332009000200008.

[53] J. Friedland, B. Kreitz, H. Grimm, T. Turek, R. Güttel. *ChemCatChem* **2020**, 12 (17), 4373–4386. DOI: 10.1002/cctc.202000278.

[54] Brynmor Mile, Diane Stirling, Michael A. Zammitt, Antony Lovell, Maurice Webb. *J. Catal.* **1988**, 114 (2), 217–229. DOI: 10.1016/0021-9517(88)90026-7.

[55] P. Burattin, M. Che, C. Louis. *J. Phys. Chem. B* **1999**, 103 (30), 6171–6178. DOI: 10.1021/jp990115t.

[56] J. Zieliński. *Catal. Lett.* **1995**, 31 (1), 47–56. DOI: 10.1007/BF00817032.
[57] S.-C. Ho, T.-C. Chou. *Ind. Eng. Chem. Res.* **1995**, 34 (7), 2279–2284. DOI: 10.1021/ie00046a009.
[58] C. Louis, Z. X. Cheng, M. Che. *J. Phys. Chem.* **1993**, 97 (21), 5703–5712. DOI: 10.1021/j100123a040.
[59] L. Zhang, J. Lin, Y.-W. Chen. *J. Chem. Soc., Faraday Trans. 1* **1992**, 88 (14), 2075–2078. DOI: 10.1039/FT9928802075.
[60] P. Burattin, M. Che, C. Louis. *J. Phys. Chem. B* **2000**, 104 (45), 10482–10489. DOI: 10.1021/jp0003151.
[61] J. W. Coenen. *Appl. Catal.* **1989**, 54 (1), 65–78. DOI: 10.1016/S0166-9834(00)82355-6.
[62] C. H. Bartholomew. *J. Catal.* **1976**, 45 (1), 41–53. DOI: 10.1016/0021-9517(76)90054-3.
[63] S. Ewald, O. Hinrichsen. *Appl. Catal., A* **2019**, 580, 71–80. DOI: 10.1016/j.apcata.2019.04.005.
[64] D. G. Goodwin, R. L. Speth, H. K. Moffat, B. W. Weber. https://www.cantera.org. Version 2.4.0. **2018**. DOI: 10.5281/zenodo.1174508.
[65] B. Ruscic, D. H. Bross. Active Thermochemical Tables (ATcT) Values Based on ver. 1.122g of the Thermochemical Network. **2019**.
[66] A. Burcat, B. Ruscic, et al. Tech. rep. Argonne National Lab.(ANL), Argonne, IL (United States), **2005**.
[67] G. D. Weatherbee, C. H. Bartholomew. *J. Catal.* **1981**, 68 (1), 67–76. DOI: 10.1016/0021-9517(81)90040-3.
[68] L. Karam, J. Reboul, N. El Hassan, J. Nelayah, P. Massiani. *Molecules* **2019**, 24 (22), DOI: 10.3390/molecules24224107.
[69] M. Aziz, A. A. Jalil, S. Triwahyono, M. Saad. *Chem. Eng. J.* **2015**, 260, 757–764. DOI: 10.1016/j.cej.2014.09.031.
[70] W. L. Vrijburg, J. W. A. van Helden, A. J. F. van Hoof, H. Friedrich, E. Groeneveld, E. A. Pidko, E. J. M. Hensen. *Catal. Sci. Technol.* **2019**, 9 (10), 2578–2591. DOI: 10.1039/C9CY00532C.
[71] J. Ren, H. Guo, J. Yang, Z. Qin, J. Lin, Z. Li. *Appl. Surf. Sci.* **2015**, 351, 504–516. DOI: 10.1016/j.apsusc.2015.05.173.
[72] C. Vogt, E. Groeneveld, G. Kamsma, M. Nachtegaal, L. Lu, C. J. Kiely, P. H. Berben, F. Meirer, B. M. Weckhuysen. *Nat. Catal.* **2018**, 1 (2), 127–134. DOI: 10.1038/s41929-017-0016-y.
[73] D. W. Blaylock, Y.-A. Zhu, W. H. Green. *Top. Catal.* **2011**, 54 (13-15), 828–844. DOI: 10.1007/s11244-011-9704-z.
[74] A. P. Weber, M. Seipenbusch, G. Kasper. *J. Nanopart. Res.* **2003**, 5 (3), 293–298. DOI: 10.1023/A:1025507600570.
[75] G. Ertl, H. Knözinger, F. Schüth, J. Weitkamp. Weinheim, Germany: Wiley-VCH Verlag GmbH & Co. KGaA, **2008**. DOI: 10.1002/9783527610044.

"Science, my friend, science. Supposed to make life easier, I thought."

(Nicomo Cosca, Best served cold, Joe Abercrombie)

CHAPTER 5

Microkinetic Modeling of the CO_2 Desorption from Supported Multifaceted Ni Catalysts

B. Kreitz, G.D. Wehinger, C. F. Goldsmith, T. Turek.
J. Phys. Chem. C **2021**, 125(5), 2984-3000
https://doi.org/10.1021/acs.jpcc.0c09985

Abstract

The conversion of CO_2 into valuable products with hydrogenation reactions on Ni catalysts requires a fundamental understanding of the interaction of CO_2 with the Ni surface. Microkinetic modeling is used to investigate the interaction of CO_2 with a multifaceted Ni crystal and compared to temperature-programmed desorption (TPD) experiments from supported Ni catalysts. TPD experiments were performed for a Ni/γ-Al_2O_3 and Ni/SiO_2 catalyst. Uncertainties in the DFT-derived model parameters were accounted for by a global uncertainty analysis (GUA). Based on the model, the adsorption and desorption of CO_2 exhibits a structure-sensitivity for the investigated Ni facets. Whereas the initial multifaceted TPD model is not in quantitative agreement with the experimentally recorded desorption profile, the GUA reveals a feasible set of model parameters that are in close agreement with the data. The comparison of the desorption profiles of the different catalysts and the multifacet simulation shows that desorption of CO_2 from basic sites and from the Ni facets overlap and thus have similar desorption kinetics.

Keywords: Temperature-programmed desorption, Nickel catalyst, Microkinetic modeling, Basic sites, Carbon dioxide

Supporting information for this publication is reprinted in Appendix C.

5.1. Introduction

The catalytic activation of the CO_2 molecule for the production of valuable chemicals is one of the crucial tasks for this century. In particular, hydrogenation reactions are extensively investigated to produce a variety of synthetic fuels, such as the production of methane in the power-to-gas process [1, 2]. Besides methanation, the interaction of CO_2 with Ni catalysts is also important for other reactions such as water-gas-shift [3–6], dry reforming [6], and steam reforming of methane [3, 7, 8]. The interaction is often studied by temperature-programmed desorption, which is applied to the supported Ni catalyst as well as to the Ni crystal facets. Ni nanoparticles consist to a large extent of the flat (111), (100), the open (110) as well as the stepped (211) surface [9, 10].

TPD studies of single crystals at UHV conditions show a structure-sensitivity of the CO_2 adsorption. Desorption from the Ni(100) facet shows CO as well as CO_2 peaks [11, 12]. On the Ni(110) surface, CO_2 is chemisorbed at low temperatures, but at high temperatures, only CO is observed to desorb with O^* remaining on the surface [13, 14]. XPS studies show that the surface coverage changes for the different Ni facets [15, 16]. A structure-sensitivity in the CO_2 adsorption and activation was also observed for these Ni facets in a recent DFT study from Vogt et al. [9].

The interaction of CO_2 with these single facets is of interest, but even more, the interaction with real supported Ni catalysts, where the Ni nanoparticles consist of a distribution of these facets [10, 17]. Ni is usually dispersed on ceramic supports such as γ-Al_2O_3 or CeO_2 because of beneficial properties due to basic sites [18–21]. CO_2 adsorbs in various configurations on these sites, with binding energies ranging from pure physisorption to strongly bound species [22–25]. The investigation of the interaction of CO_2 with supported Ni catalysts in the presence of basic sites on the support is, therefore, a complicated procedure and depends significantly on the conditions [24]. All TPD studies on CO_2 adsorption on Ni/γ-Al_2O_3 catalysts focus only on the differentiation between adsorption on Ni and basic sites with different binding strength on the support. Multiple CO_2 and CO desorption peaks are usually detected during the TPD [24, 26]. The different CO_2 peaks are explained by desorption from basic sites from the support with different binding strengths. It is possible to use supports with an acidic surface like SiO_2, which interacts with CO_2 to a minor extent and reduce the complexity [27]. Until now, the discussion of the CO_2 desorption profiles from supported catalysts does not consider desorption from different Ni facets, which are present in a supported Ni catalyst and, as shown above, is structure-sensitive.

Microkinetic modeling can be used to connect the first principle results with experimental observations and applied to model desorption profiles from the single facet and multifaceted catalysts. Next to the elementary reactions itself, a complete parametrization with activation energies and thermodynamic parameters is required. These parameters can be derived from DFT calculations, but they are affected by uncertainties because of the approximations made in the exchange-correlation functional [28, 29]. The uncertainty in the model parameters can significantly affect the outcome of the model [28]. The literature survey reveals a significant gap between the interaction of CO_2 with multifaceted supported catalysts and the observed structure-sensitivity on ideal crystal facets.

The objective of this work is to bridge this gap by combining microkinetic modeling with an experimental investigation of the CO_2 desorption from supported Ni catalysts to unravel the interaction of CO_2 with the different Ni facets. Therefore, we derive a thermodynamically consistent microkinetic model of a multifaceted Ni nanoparticle to simulate the adsorption and desorption of CO_2. DFT calculations are

performed to determine the thermodynamic parameters of the adsorbates on Ni(111), Ni(100), Ni(110), and Ni(211). The equilibrium shape of a Ni nanoparticle consisting of these four facets is calculated with a Wulff construction. CO_2 desorption is experimentally investigated from a Ni/γ-Al_2O_3 and a Ni/SiO_2 catalysts, to study the desorption from the support with its basic sites and the Ni crystals. The intensively-studied H_2 desorption is used as a test case to validate the model of the TPD setup. Global uncertainty analysis is applied to the microkinetic model to investigate the effects of uncertainties in the first-principle parameters on the simulated desorption profiles and to determine which parameters are relevant. The multifaceted microkinetic model with the uncertainty analysis is a tool to compare results from ab-initio calculations with experiments on technical supported catalysts at ambient pressure to provide new insights into the CO_2 desorption and consequently its activation on different Ni facets.

5.2. Materials and Methods

5.2.1. Experimental Methods

Catalyst Preparation and Characterization

For the experiments, an 11 wt% Ni catalyst was prepared via incipient wetness impregnation of a γ-Al_2O_3 support, as described in Friedland et al. [30]. The Ni/γ-Al_2O_3 catalyst was reduced in H_2 at 723 K for 12 h approached with a temperature ramp of 3 K min^{-1}. A 20 wt% Ni/SiO_2 catalyst was prepared with a spray-drying method described in the work of Martínez and Weber [31]. Briefly, an aqueous solution of colloidal silica and $Ni(NO_3)_2$ was atomized and sprayed into a tubular furnace operated at 673 K to dry and calcine the particles. The obtained particles were treated in a muffle furnace at 673 K for 3 h. This catalyst was activated in pure H_2 at 723 K (10 K min^{-1}) for 1 h. Information on the chemicals used within this study can be found in the Supporting Information (SI).

Characterization of the catalyst was done for the calcined samples and after reduction and passivation. After reduction, the catalyst was oxidized with synthetic air at room temperature using a pulse method [30] to inject 30 consecutive pulses of synthetic air into an Ar carrier gas to ensure a low O_2 concentration. The catalyst surface area was measured with N_2 physisorption (3Star, Micromeritics Instrument Corp) at 77 K and evaluated with the Brunauer-Emmett-Teller (BET) method. The Barrett-Joyner-Halenda (BJH) method was used to determine the pore size distribution and the pore volume using the desorption branch. Skeleton density was measured with a He pycnometer (Pycnomatic ATC, Quantachrome). The nickel loading, as well as the concentration of Na and K of the catalyst, were measured with optical emission spectroscopy using inductively coupled plasma (ICP-OES 5100, Agilent) after dissolution in an acid mixture. Transmission electron microscopy (TEM) was used to examine the catalysts (JEOL JEM-2100, 160 kV).

X-ray diffraction (XRD) measurements (Empyrean, PANalytical) were performed with $\omega/2\Theta$ scan using Cu-Kα radiation (40 kV, 40 mA). The Ni crystal size was determined from a Rietveld fit (Highscore plus software, PANalytical). A Rietveld analysis was used to fit the whole XRD profile, including Ni and NiO phases for the silica catalyst and additionally considering γ-Al_2O_3 and crystalline $NiAl_2O_4$ for the alumina catalyst. LaB_6 was used as a reference for the peak broadening of the setup. The same device was used for small-angle X-ray scattering (SAXS) to determine the particle size distribution of the Ni crystals.

Static Adsorption

The adsorption of H_2 and CO_2 was studied with volumetric adsorption measurements (3Flex, Micromeritics Instrument Corp). A sample with a mass of 80 mg was placed in a flow-through chemisorption tube and fixed with quartz wool and filter disks. After reduction, the sample was evacuated at 10 K above the reduction temperature for 60 min and then cooled to the adsorption temperature of 323 K. An adsorption isotherm from 1 mbar to 900 mbar was recorded with an equilibration time of 1 min. The CO_2 adsorption was investigated employing a double isotherm with an evacuation of 60 min after the first run at the adsorption temperature. After the static adsorption experiment, the catalyst was evacuated for 60 min, and the free space was measured with He. The degree of reduction (DOR) was determined by performing an O_2 adsorption at 773 K and measuring the O_2 uptake. The uptake was determined with the back-extrapolation of the linear part of the adsorption isotherm to zero pressure [32]. H_2 uptake and DOR were used to determine the Ni surface area, crystal size, and dispersion. The equations are provided in the SI.

Temperature-Programmed Desorption

A catalyst testing unit (BelCat-M2, BelJapan Inc.) connected to a mass spectrometer (MS) (GAM200, InProcessInstruments) was used to perform flow adsorption experiments and to record desorption profiles. The experimental setup is described in detail in previous work [30] and only briefly explained here. The MS was calibrated with certified calibration gas mixtures using Ar as an internal standard. A catalyst sample of 40 mg was used and placed in a sample tube with an inner diameter of 5 mm and fixed with quartz wool plugs, which resulted in a catalyst bed length of 4 mm. The temperature was measured directly above the catalyst bed with a shielded thermocouple. CO_2 adsorption was performed in a flow adsorption experiment with a 9.87 % CO_2/He (50 $mL_N\,min^{-1}$) mixture for 1 h at an elevated temperature of 383 K. After adsorption, the catalyst was flushed with Ar (30 $mL_N\,min^{-1}$) for 15 min and cooled to 323 K. A temperature ramp of 20 $K\,min^{-1}$ was used for the TPD.

Temperature-Programmed Reduction

Temperature-programmed reduction (TPR) experiments were performed in the pulse adsorption setup with a 10.1 % H_2/Ar mixture using a temperature ramp of 10 $K\,min^{-1}$ from 323 K to 1,223 K. H_2O and CO_2 were removed from the catalyst before the TPR by degassing the sample of 20 mg at 473 K approached with 10 $K\,min^{-1}$ for 1 h while flushing with He. The exhaust gas was passed over a molecular sieve (3 Å) to remove H_2O and analyzed with a thermal conductivity detector. A volumetric flow rate of 30 $mL_N\,min^{-1}$ was used for the TPR.

5.2.2. Theoretical methods

DFT calculations

Spin-polarized electronic structure calculations were performed within the Atomic Simulation Environment (ASE) [33] using the Vienna ab-initio Simulation Package (VASP) [34, 35] with plane-wave

pseudopotentials. The RPBE [36] exchange-correlation functional with a generalized gradient approximation was applied to calculate the valence electrons with a cutoff energy of 400 eV. Van-der-Waals interactions are accounted for by the semi-empirical DFT-D3 method [37]. Methfessel-Paxton first-order spreading with a smearing of 0.2 eV was used. Ni (111), (100), and (110) facets were modeled by a (3×3) and (211) by a (1×3) supercell, with periodic boundary conditions and a vacuum of 10 Å above the slab. The Ni lattice constant was optimized for the RPBE functional, and a value of 3.48 Å was obtained, which is close to the experimental value of 3.52 Å [38]. The two top layers were fully relaxed with the adsorbate, while the two bottom layers were fixed for the Ni(111), Ni(100), and Ni(110). Six layers were relaxed for Ni(211). The Ni slabs were sampled with a Monkhorst-Pack grid of (3×3×1) for Ni(111), Ni(100), and Ni(110) and (4×3×1) for Ni(211). For the computation of the gas-phase species, a grid of (2×2×2) was applied. Structures were relaxed until all forces were below 0.02 eV Å^{-1}. For the vibration analysis, the entire slab was fixed, and the vibration frequencies were calculated with ASE. The zero-point corrected binding energies of the adsorbates, $\Delta E_{\mathrm{b}}^{\mathrm{A}^*}$, were referenced to the computed energy of the gas-phase precursor $E^{\mathrm{A}_{(\mathrm{g})}}$

$$\Delta E_{\mathrm{b}}^{\mathrm{A}^*} = E^{\mathrm{A}^*} - E^{\mathrm{A}_{(\mathrm{g})}} - E^{\mathrm{Ni}} \tag{5.1}$$

Statistical thermodynamic methods were applied to derive thermodynamic properties from the binding energies and the partition functions of the adsorbates with the approach outlined by Blondal et al. [39]. A Wulff construction was performed with Pymatgen [40] to determine the equilibrium shape of a Ni nanoparticle consisting of the four investigated facets and assuming a truncated octahedron shape. Surface energies for the four Ni facets were taken from Tran et al. [40].

Microkinetic modeling

In this work, the mean-field approximation [41] was used, and it was assumed that there is only one adsorption site on the Ni surface, which is the site with the highest binding energy. The Cantera [42] simulation framework was used in Python to model the TPD setup with the multifaceted Ni nanoparticle. It was assumed that the thin catalyst bed of approx. 4 mm has a uniform concentration and temperature, meaning that it can be described by the governing equations of an isothermal continuously stirred tank reactor (CSTR). During the TPD experiment, the temperature of the reactor was raised with a linear temperature ramp. The model assumes that the catalyst and gas maintain thermal equilibrium, which implies that the heat transfer between both phases is faster than the temperature ramp. The mass balance for each gas-phase species in an isothermal CSTR is formulated in Equation (5.2) and the mass balance for the adsorbed species in the form of a coverage Θ_{i} is Equation (5.3) [43]

$$\frac{d\left(mY_{\mathrm{i}}\right)}{dt} = \dot{m}_{\mathrm{in}} Y_{\mathrm{i,in}} - \dot{m}_{\mathrm{out}} Y_{\mathrm{i,out}} + \sum_{f=1}^{N_{\mathrm{F}}} a_{\mathrm{cat}} X_{\mathrm{f}} \dot{s}_{\mathrm{i,f}} W_{\mathrm{i}} \tag{5.2}$$

$$\frac{d\Theta_{\mathrm{i}}}{dt} = \frac{\dot{s}_{\mathrm{i}} \sigma_{\mathrm{i}}}{\Gamma} \tag{5.3}$$

where W_{i} is the molar mass, Y_{i} is the mass fraction, $\dot{m}$ the mass flow rates for inlet and outlet, $\dot{s}_{\mathrm{i}}$ is the net production rate, Γ is the surface site density, a_{cat} is the specific catalyst surface area, and σ_{i} is the number of surface sites covered by an adsorbate, which is always one within this study. A linear combination was assumed for the contribution from each facet $f \in N_{\mathrm{F}}$ to the total production rate, which

was weighted by the fraction of the facet X_f. Weatherbee and Bartholomew [44] also demonstrated that a CSTR model could fairly well describe the TPD experiment obtained with a differential fixed-bed. The catalyst was modeled as a reactive surface, which was coupled to the gas phase by the production rate $\dot{s}_i$. The production rate of each species was calculated by Equation (5.4) accounting for all reactions $j \in M$ with the corresponding net stoichiometric coefficient $\nu_{i,j}$

$$\dot{s}_i = \sum_{j=1}^{M} \nu_{i,j} r_j \tag{5.4}$$

where r_j is the net rate of the reaction, calculated from the difference between the forward and reverse rates. The rate constants for the adsorption k_f were parameterized via sticking coefficients s_j [43]

$$k_{f,j} = \frac{s_j}{\Gamma^n} \sqrt{\frac{RT}{2\pi W_i}} \tag{5.5}$$

where s_j is the dimensionless sticking coefficient and n accounts for the adsorption stoichiometry. The surface reactions were described by the Arrhenius approach in Equation (5.6) with the pre-exponential factor A and an activation energy $E_{a,j}$

$$k_{f,j} = A_j \exp\left(\frac{-E_{a,j}}{RT}\right) \tag{5.6}$$

A consistent set of activation energies for the Ni facets were taken from Vogt et al. [9], but the pre-exponential coefficients were not reported. Therefore, the pre-exponential factor was estimated with the method proposed by Carvalho et al. [5]:

$$A_j = \frac{k_b T}{h} \exp\left(\omega_j \left(\frac{\Delta S_j}{R} - \frac{\Delta S_{j,TST}}{R}\right)\right) \tag{5.7}$$

The entropy change of the reaction ΔS_j was calculated from the entropy of the adsorbates and the entropy change of the transition state $\Delta S_{j,TST}$, which was assumed to be zero as an order of magnitude estimate of the pre-exponential coefficient and ω was assumed to be 0.5 [5]. Rate constants of the reverse reaction k_r were computed from the equilibrium constant K_c to ensure thermodynamic consistency

$$k_{r,j} = \frac{k_{f,j}}{K_c} \tag{5.8}$$

The concentration equilibrium constant K_c for each reaction was connected to the general equilibrium constant K_p through [5, 43]

$$K_c = K_p \left(\frac{p}{RT}\right)^{\sum_{i=1}^{N_g} \nu_i} \Gamma^{\sum_{i=1}^{N_s} \nu_i} \tag{5.9}$$

The general equilibrium constant can be calculated from the free enthalpy change of the reaction $\Delta_R G$ [43]

$$K_p = \exp\left(\frac{-\Delta_R G}{RT}\right) \tag{5.10}$$

The well-studied desorption of H_2 (Equation (5.11)) was used to validate the microkinetic model. In this study, we assumed that CO_2 adsorbs non-dissociatively (Equation (5.12)) and it can undergo subsequent dissociation reactions. The adsorbed CO_2^* can decompose on the surface to CO^* and O^*

(Equation (5.14)), where the CO^* can desorb (Equation (5.13)). Adsorbed CO^* can further dissociate and form surface C^* and O^* (Equation (5.15)).

$$H_2 + 2\,^* \rightleftharpoons 2\,H^* \tag{5.11}$$

$$CO_2 + \,^* \rightleftharpoons CO_2^* \tag{5.12}$$

$$CO + \,^* \rightleftharpoons CO^* \tag{5.13}$$

$$CO_2^* + \,^* \rightleftharpoons CO^* + O^* \tag{5.14}$$

$$CO^* + \,^* \rightleftharpoons O^* + C^* \tag{5.15}$$

For the simulation of the H_2 desorption profiles, it was possible to specify the initial coverage on the different Ni facets since it is always dissociated. This was not possible for the CO_2 adsorption since we did not want to make any assumptions on the nature of the adsorbed CO_2, e.g. whether it is dissociated or not. Therefore, we chose to simulate the flow adsorption experiment, with the subsequent cooling, before the TPD was started. This ensures a coverage only predicted by the model. As a simplification, surface diffusion from one facet to another was not considered, and therefore the only exchange between the facet occurs through the gas phase via desorption and readsorption.

Analysis of the microkinetic model

Sensitivity analysis

Local sensitivity analysis was applied to the model, where the heat of formation of the adsorbates and the activation energies were perturbed by $\pm$ 1 kJ mol^{-1}. Instead of normalizing the sensitivity response, the effect of the variation was analyzed by the shift in the peak height and the location of the peak of the simulated TPD profile.

Global uncertainty analysis

We investigated the effect of uncertainties in the DFT derived parameters by means of a global uncertainty analysis (GUA). In the GUA, all microkinetic model parameters were varied randomly and uncorrelated in the uncertainty range, which was assumed for the parameters. Reaction barriers predicted by DFT are assumed to be within $\pm$20 kJ mol^{-1} [29, 41], while the accuracy of the heat of formation of the adsorbates is assumed to be $\pm$15 kJ mol^{-1} [29]. The pre-exponential factors of the surface reactions were kept constant since the variation of the activation energy causes a larger effect on the reaction rate due to the exponential dependence. Sticking coefficients were varied for the adsorption reactions instead of activation energies by an order of magnitude up and down, but the highest possible sticking probability was unity. In this work, the method discussed by Blaylock et al. [45] was used to adjust the heat of formation of adsorbates to experimental values (see DFT calculations below), which shifts the error of the thermodynamic parameter from DFT accuracy to the experimental accuracy. Therefore, we assumed that the heat of formation of all adsorbates was subjected to an uncorrelated variation of $\pm$10 kJ mol^{-1}. For each facet, this amounts to two sticking coefficients, two activation energies, and four heats of formation. Perturbation parameters for this multidimensional problem were generated with Sobol sequences. The Sobol sequence generates low-discrepancy quasi-random numbers

in the high-dimensional space [46]. For the uncertainty analysis, the activation energy, sticking coefficient, and the heat of formation of the adsorbates were varied in the uncertainty range, which is defined by Equations (5.16) to (5.18)

$$E_{a,j,m} = E_{a,j} + 20\,\mathrm{kJ\,mol^{-1}} \cdot (1 - 2x_{j,m}^{sobol}) \tag{5.16}$$

$$\Delta_f H_{j,m} = \Delta_f H_j + 10\,\mathrm{kJ\,mol^{-1}} \cdot (1 - 2x_{j,m}^{sobol}) \tag{5.17}$$

$$s_j = s_j \cdot 10^{(1-2x_{j,m}^{sobol})} \tag{5.18}$$

where $x_{j,m}^{sobol} \in [0, 1]$ is unique for each perturbed parameter and m is the number of simulation runs. Additionally, the Wulff construction assumed an equilibrium nanoparticle shape, but this distribution of facets may not be an accurate representation of the active system. We, therefore, included a variation of the facet distribution, but we constrained it to the four investigated facets. Three additional dimensions were required to vary the distribution in reasonable ranges. The concentration of step sites (Ni(211) and Ni(110)) was varied between 0 to 20 %, whereas the share of terrace sites (Ni(100) and Ni(111), $X_{Terrace}$) was varied accordingly between 80 to 100 %. The share of the Ni(111) facet in the terrace site contribution was allowed to vary between 0 to 100 %. The rest is always the Ni(100) facet. This was similarly assumed for the stepped sites and is expressed in Equations (5.19) to (5.23)

$$X_{Terrace,m} = 1 - 0.2x_m^{sobol} \tag{5.19}$$

$$X_{Ni(111),m} = X_{Terrace,m}x_m^{sobol} \tag{5.20}$$

$$X_{Ni(100),m} = 1 - X_{Ni(111),m} \tag{5.21}$$

$$X_{Ni(211),m} = (1 - X_{Terrace,m})x_m^{sobol} \tag{5.22}$$

$$X_{Ni(110),m} = 1 - X_{Ni(211),m} \tag{5.23}$$

The number of parameters independently and simultaneously varied in the GUA for the multifaceted model amounts to 35. Throughout this study, it was assumed that the uncertainties are uncorrelated. On a single facet, likely true that the binding energies of O^* and C^* are largely uncorrelated, but the binding energies of C^*, CO^*, and CO_2^* are correlated [41, 47]. Correlation between the parameters can affect the range of the GUA [28]. Uncorrelated variations can be considered as a worst-case scenario and will, therefore, span a broad range of possible results.

5.3. Results and Discussion

5.3.1. Characterization of the Catalyst

The results from the catalyst characterization are summarized in Table 5.1. A more detailed discussion of the XRD, BET, and TPR measurements is provided in the SI. The Ni/γ-Al_2O_3 catalyst exhibits a small reduction peak from 473 to 573 K and one broad reduction peak ranging from 623 to 1,098 K (see Figure S1). Next to a reduction peak, which agrees with the NiO reference, the Ni/SiO_2 catalyst shows an additional overlapping peak at high temperatures. The reduction peak at high temperatures indicates strong metal/support interactions, such as the formation of nickel silicates [48]. TEM images of the passivated catalysts are shown as an inset in Figure 5.1 and in large resolution in the SI (see Figure S2). The TEM images of both catalysts show an even distribution of the Ni on the support and no irregularities regarding the crystal size. The presence of alkali metals in the catalyst can significantly

influence the CO_2 methanation activity and selectivity [49–51]. Na can also create basic adsorption sites on the silica and, therefore, influence the activation of the CO_2 molecule [51]. Elemental analysis of the catalysts shows that the prepared alumina catalyst does not contain any Na or K traces. The silica catalyst contains 0.11 wt% of Na and 0.015 wt% of K.

Table 5.1.: Characterization of the Ni/γ-Al_2O_3 catalyst, the γ-Al_2O_3 support and Ni/SiO_2 catalyst with the SiO_2 support used in this study.

Property	Unit	Ni/γ-Al_2O_3	γ-Al_2O_3	Ni/SiO_2	SiO_2	Method
Particle size	µm	160-250	160-250	-	-	Sieve
Skeleton density	$kg\,m^{-3}$	3501	3233	1986	-	He pycnometry
Surface area	$m^2\,g^{-1}$	169	193	109	140	BET
Pore volume	$mm^3\,g^{-1}$	394	476	281	229	BJH
Average pore size	nm	7.2	8.9	9.0	5.2	BJH
Ni loading	wt%	11.1	-	18.0	-	ICP-OES
Na content	wt%	0	-	0.11	-	ICP-OES
K content	wt%	0	-	0.015	-	ICP-OES
Metal surface area	$m^2\,g^{-1}$	12.6	-	11.9	-	H_2 chemisorption
Average Ni crystal size	nm	6.0 (4.4)	-	10.1 (6.7)	-	H_2 chemisorption (XRD)
Ni dispersion	%	16.9	-	9.9	-	H_2 chemisorption
Degree of reduction	%	75.4	-	87.0	-	O_2 chemisorption
CO_2 uptake (total)	$\mu mol\,g^{-1}$	212.7	189.4	26.6	-†	CO_2 chemisorption
CO_2 uptake (irrev.)	$\mu mol\,g^{-1}$	123.3	103.6	24.4	-†	CO_2 chemisorption

† The adsorption isotherms of the silica support produced with the spray-drying did not show CO_2 adsorption at low partial pressures.

Evaluating the XRD patterns for the Ni/γ-Al_2O_3 is a complicated procedure due to the overlapping of Ni, NiO, and γ-Al_2O_3 (see Figure S3). A distinct NiO(111) reflection is observed at an angle of 37° along with the typical reflections of NiO, γ-Al_2O_3 and $NiAl_2O_4$ (see Figure S3). The shifted reflection for γ-Al_2O_3 indicates the formation of crystalline $NiAl_2O_4$ [49]. The calcined silica catalyst shows reflections in the same positions as the NiO reference, whereas the passivated catalyst shows high-intensity Ni and broad low-intensity NiO reflections. Due to the complicated XRD pattern of the alumina catalyst, a Rietveld fit was applied, which was used to fit the full profile (see Figure S4). While the Rietveld fit matches perfectly to the measured pattern of the silica catalyst, it shows some deviations for the Ni/γ-Al_2O_3. The deviations are caused by the complexity of the signal due to the overlapping of reflections from different phases. Main uncertainties in the fitting procedure are the small γ-Al_2O_3 crystals and the correct determination of the background. An average Ni crystal size for the alumina catalyst of 4.4 nm and 6.7 nm for the Ni/SiO_2 catalyst were obtained, which are always smaller compared to the value determined by H_2 chemisorption.

The particle size distribution measured with SAXS is displayed in Figure 5.1a for the Ni/γ-Al_2O_3 catalyst, which shows a bimodal Ni crystal size distribution with an average value of 8.0 nm and a most frequent value of 7.0 nm. This value is higher than the value determined from the H_2 chemisorption of 6 nm. There is a second peak observed with SAXS in the range of 90 to 100 nm, which is not in accordance with the TEM results. Since only a few TEM images were evaluated, it is not clear whether this large Ni size is indeed present or rather a mistake of the SAXS fitting procedure. Figure 5.1b is the distribution for the Ni/SiO_2 catalyst, which has two distinct peaks with a maximum of 7 nm and 27 nm. The first peak can be attributed to the NiO crystals and the second to the SiO_2 primary particles used for the

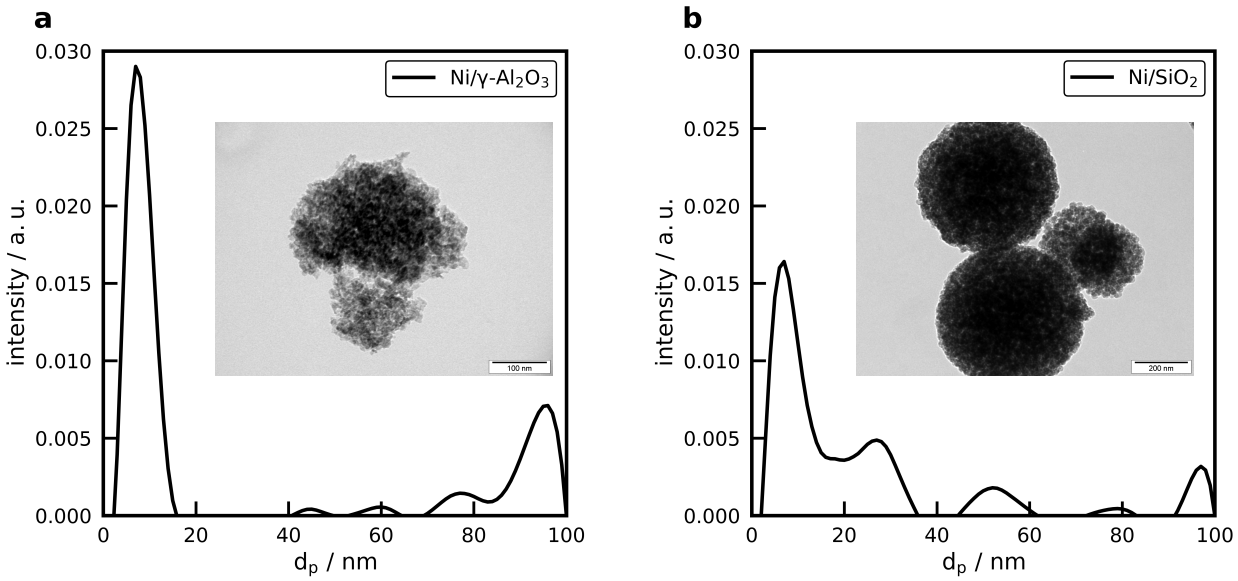

Figure 5.1.: Ni crystal size distribution obtained from the SAXS measurement of (a) Ni/γ-Al_2O_3 and (b) Ni/SiO_2. High resolution TEM pictures are provided in Figure S2.

spray-drying. It is not possible to explain the peaks at higher diameters, but due to the low intensity, it might be a result of the SAXS fit.

5.3.2. Static Adsorption

The Ni/γ-Al_2O_3 catalyst adsorbs a total CO_2 amount of 212.7 µmol g^{-1} with an irreversible uptake of 123.3 µmol g^{-1}. From this measurement, it cannot be deduced whether CO_2 adsorbs on the Ni surface or on basic sites on the support. There are strong binding sites on both phases and with the method of the double isotherm, both are detected. This can be seen by the high irreversible uptake of CO_2 on the support. Upon impregnation, Ni will also cover some of the strong binding sites while possibly creating new binding sites on Ni and on the metal/support interface. CO_2 adsorbs on basic sites on the support in various configurations with different binding strengths, which are classified as weak, medium, and strong basic sites. A weak interaction with the support is in the form of bicarbonates formed on hydroxylated Al_2O_3 [22]. CO_2 binds to the oxygen atom of the lattice and forms a carbonate, which either binds in the form of a monodentate or bends over and creates a bidentate carbonate [22, 24, 25, 52]. Monodentate carbonate has a higher binding energy compared to bidentate carbonate [24]. A strong chemisorption bond is formed when the carbonate binds in a bridge mode on an Al-O and Al site [24].

The adsorption isotherm for the support (see Figure 5.2a) also shows a steep increase in the uptake at low CO_2 partial pressures. This is attributed to strong basic sites on the alumina. CO_2 is mostly adsorbed on the strong basic sites in the form of bridged carbonate and monodentate carbonate [22, 24]. The steep increase is followed by a linear increase with increasing partial pressure caused by adsorption on medium and weak basic sites in the form of bidentate carbonate and bicarbonate. Figure 5.2a shows that the slopes of the linear trajectory for the support and the catalyst are nearly identical. This means that at higher partial pressures, all the adsorption sites on the Ni crystals are occupied, and weak adsorption on the support occurs. The alumina adsorbs irreversibly 103.6 µmol g^{-1}, which corresponds

to 0.32 sites nm^{-2} (based on the BET surface area). This value is higher than a reported literature value of 0.14 sites nm^{-2} for dehydrated Al_2O_3 [53]. It has to be kept in mind that the Al_2O_3 was not dehydrated in this study. Thus, the higher adsorption capacity of the support is reasonable.

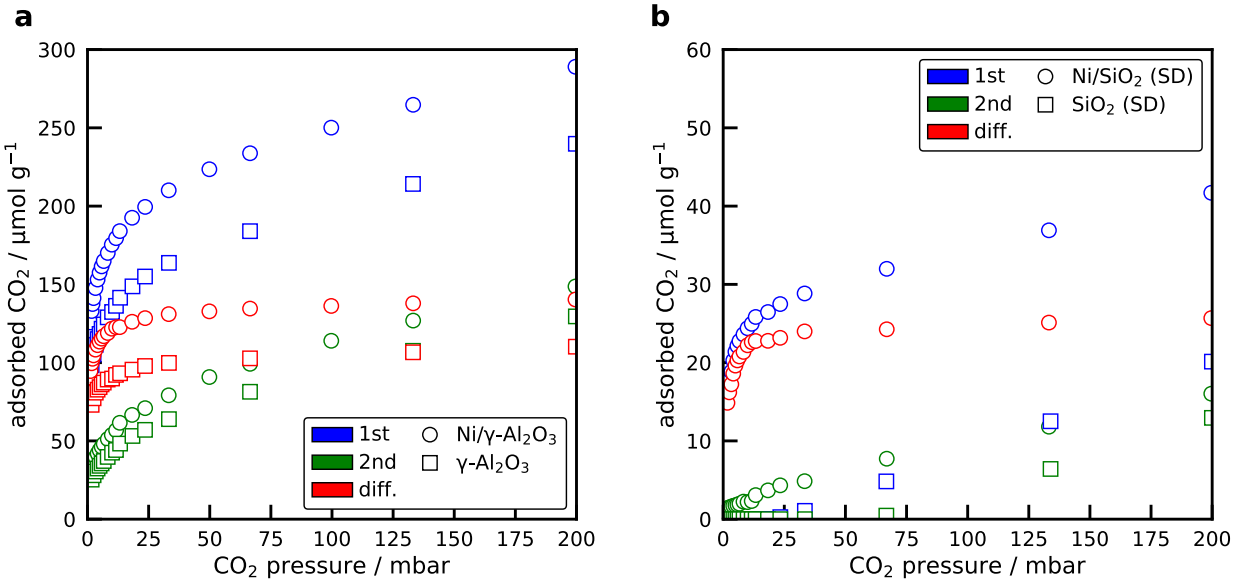

Figure 5.2.: Volumetric CO_2 adsorption isotherms for (a) the Ni/γ-Al_2O_3 catalyst (circle) and (b) the Ni/SiO_2 catalyst with their corresponding supports (squares). All isotherms are recorded at a temperature of 323 K.

The Ni/SiO_2 catalyst shows high uptake at low partial pressures in the first run (see Figure 5.2b). In the second adsorption isotherm, a linear increase of uptake with pressure is obtained, starting at nearly zero. It means that for this catalyst, CO_2 is only adsorbing irreversibly on the Ni facets and physisorption occurs on the support. This is supported by the adsorption isotherms recorded for the support, which does not show irreversible adsorption at low partial pressures. CO_2 can weakly adsorb in the form of bicarbonate to hydroxyl groups on the silica surface. An amount of 24.4 µmol g^{-1} adsorbs irreversibly on the Ni crystals.

The deposition of Ni atoms on the alumina creates a Ni/Al interface. Due to the created interface, CO_2 can adsorb on three different sites: the Ni crystal, the metal/support interface and the support. Therefore, it is not possible to elucidate from the irreversible uptake of the adsorption isotherm, where CO_2 adsorbs since catalyst and support show a high share of strong adsorption sites. In order to access the role of the adsorption capacity of the Ni/Al interface, the relationship between the Ni nanoparticle size and the fraction of interface atoms is used. Shekhar et al. [54] and Cargnello et al. [55] have shown that with increasing particle size, the amount of the surface, interface, and corner atoms change with a characteristic slope. This approach was used to determine where a reaction proceeds on the catalyst [6]. In a double logarithmic plot of the reaction rate over the particle size, this can be concluded based on the slope. If the reaction proceeds on the surface the rate depends on $d^{-0.9\pm0.1}$, on the interface $d^{-1.9\pm0.2}$, or the corner atoms $d^{-2.6\pm0.2}$ [55]. Instead of the reaction rate, we plotted the logarithm of the adsorbed amount over the logarithmic particle size. Figure 5.3 shows the obtained data points and the linear regression.

The particle size was adjusted by sintering the catalyst in H_2 atmosphere at elevated temperatures and the experimental procedure is described in the SI. After each sinter phase, a H_2 chemisorption is

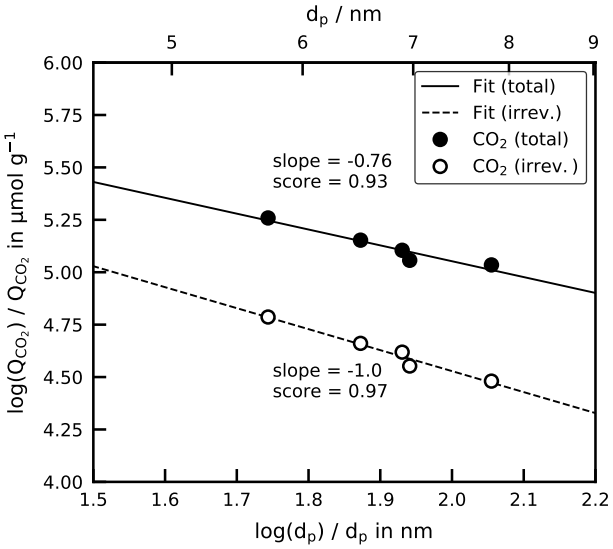

Figure 5.3.: Total and irreversible CO_2 adsorption capacity in dependence of the Ni particle size for the Ni/γ-Al_2O_3 catalyst. The Ni particle size is varied by sintering in H_2 atmosphere.

conducted to determine the Ni particle size. Afterward, the catalyst is evacuated at a high temperature to remove adsorbed H_2 and a CO_2 chemisorption is performed. This experiment shows that the slope of this fit for the total ($d^{-0.76}$), as well as the irreversible adsorption ($d^{-1.0}$), is close to the theoretical value for the surface atoms. As a result, it can be assumed that the created interface between the Ni nanoparticles and the γ-Al_2O_3 does not adsorb CO_2 in significant amounts. Whether the interface plays a role in the methanation mechanism cannot be discussed only based on the adsorbed amount of CO_2 and is subject to further studies. However, Beierlein et al. [49] reported that the metal/support interface does not affect the CO_2 methanation rate. This simplifies the discussion of the TPD profiles from the alumina catalyst because it can be differentiated between the support and the Ni crystals.

With the determined Ni surface area of the Ni/SiO_2 catalyst, it is possible to determine the site concentration of CO_2, which amounts to $2.0\times10^{-10}\,\mathrm{mol\,cm^{-2}}$. Suppose for the Ni/$\gamma$-$Al_2O_3$ that the impregnation does not occupy the strong binding sites (irreversible uptake) on the support and the metal/support interface does not contribute to the adsorption capacity. In that case, it is possible to subtract the irreversible adsorption capacity of the support from the catalyst. This results in an amount of $19.7\,\mu\mathrm{mol\,g^{-1}}$. With the Ni surface area of this catalyst, the site concentration is calculated to be $1.6\times10^{-10}\,\mathrm{mol\,cm^{-2}}$, which is close to the value of the silica catalyst. This demonstrates that it is possible to determine the CO_2 uptake on the Ni crystals for a Ni/γ-Al_2O_3 by applying the method of double isotherms for the support and the catalyst. If it is assumed that the CO_2 is entirely dissociated and that O^* covers one adsorption site and CO^* two sites [32], this results in a coverage of 49 % of the alumina and 55 % of the silica catalyst at the temperature of 323 K. Both adsorbates show high repulsive interaction, which can explain the lower than monolayer coverage [56].

5.3.3. Temperature-Programmed Desorption

The desorption of H_2 from the Ni/γ-Al_2O_3 catalyst, a well-studied system, was studied as a test case for the applied methods and to validate the microkinetic model of the multifaceted Ni catalyst. Experimental desorption spectra for various initial coverages and the detailed discussion can be found in the SI (see

Figure S6). Briefly, the desorption profiles agree with several literature results [44, 57–59]. Figure 5.4 shows the recorded CO_2 desorption profiles following the adsorption at flow conditions at 383 K. The noisy experimental data is smoothed for presentation and the error bar is the amplitude of the variation. Figure 5.4a displays the desorption from Ni/γ-Al_2O_3 and the γ-Al_2O_3 support. Desorption from the support shows a single broad peak with a maximum at 448 K and a long tailing at higher temperatures. The maximum desorption rate fits to the desorption from basic sites with medium strength, which bind CO_2 in the form of bidentate carbonate [23–25]. Desorption at higher temperatures can be attributed to monodentate carbonate and bridged carbonate [23, 24]. The desorption profile of the alumina support compares well to the profile reported by Dewaele and Froment [53] after adsorption at 373 K. Since no multiple desorption peaks are observed, it can be concluded that the heat of adsorption of CO_2 on the γ-Al_2O_3 has a broad distribution [53], which is in agreement with the results from Manchado et al. [22]. The alumina catalyst reveals two CO_2 peaks and an additional CO peak. The position of the first peak is identical to the support at 451 K, but the height is increased. CO desorption starts at 600 K and reaches the maximum rate at 689 K, which is also the position of the second CO_2 peak. 128.8 µmol g^{-1} CO_2 desorb from the catalyst, whereas only 80.6 µmol g^{-1} of CO_2 desorb from the support. The amount of CO desorbed is 1.5 µmol g^{-1}. Results from the TPD experiments are summarized in Table 5.2.

Figure 5.4b shows the calculated desorption profile from the Ni/γ-Al_2O_3 catalyst when the profile of γ-Al_2O_3 is subtracted. The resulting difference is an oversimplification since it implicitly assumes that upon impregnation, Ni crystals do not block any adsorption sites on the support and the metal/support interface does not contribute significantly to the uptake. While the latter assumption is proven (see Static Adsorption), the first one is certainly not a good approximation, and, therefore, the calculated CO_2 concentration has only limited meaning. Still, this profile shows the qualitative desorption from the Ni crystals. The desorption profile is deconvoluted by fitting Gaussian peaks to the experimental data. The primary purpose behind these deconvolution curves is to illustrate that the desorption profiles can be described by three overlapping peaks; no attempt is made to provide a physical interpretation to the shape of the peaks.

A close resemblance is observed for the silica and the alumina catalyst (see Figure 5.4c). In this case, it is also possible to identify three overlapping peaks, and the last one at the highest temperatures is accompanied by CO. The maximum of the first peak is at 437 K and the maximum CO desorption rate occurs around 709 K with a rather flat profile, which is close to the peak from the CO desorbing from the Ni/γ-Al_2O_3. The silica support shows only a small desorption peak of CO_2 with a maximum at 441 K and an amount of 0.5 µmol g^{-1}.

Table 5.2.: Peak temperatures (T_{peak}) and amounts of CO_2 (Q_{CO_2}) and CO (Q_{CO}) desorbed during the CO_2-TPD after adsorption at flow conditions at 383 K for 60 min. *Conditions:* m_{cat} = 40 mg, $\beta = 20\,K\,min^{-1}$, $\dot{V}_{Ar} = 30\,mL_N\,min^{-1}$.

	CO_2		CO	
Catalyst	Q_{CO_2} / µmol g^{-1}	T_{peak} / K	Q_{CO} / µmol g^{-1}	T_{peak} / K
Ni/γ-Al_2O_3	128.8	451	1.5	689
γ-Al_2O_3	80.6	448	0	-
Ni/SiO_2	39.3	437	1.1	709
SiO_2	0.5	441	0	-

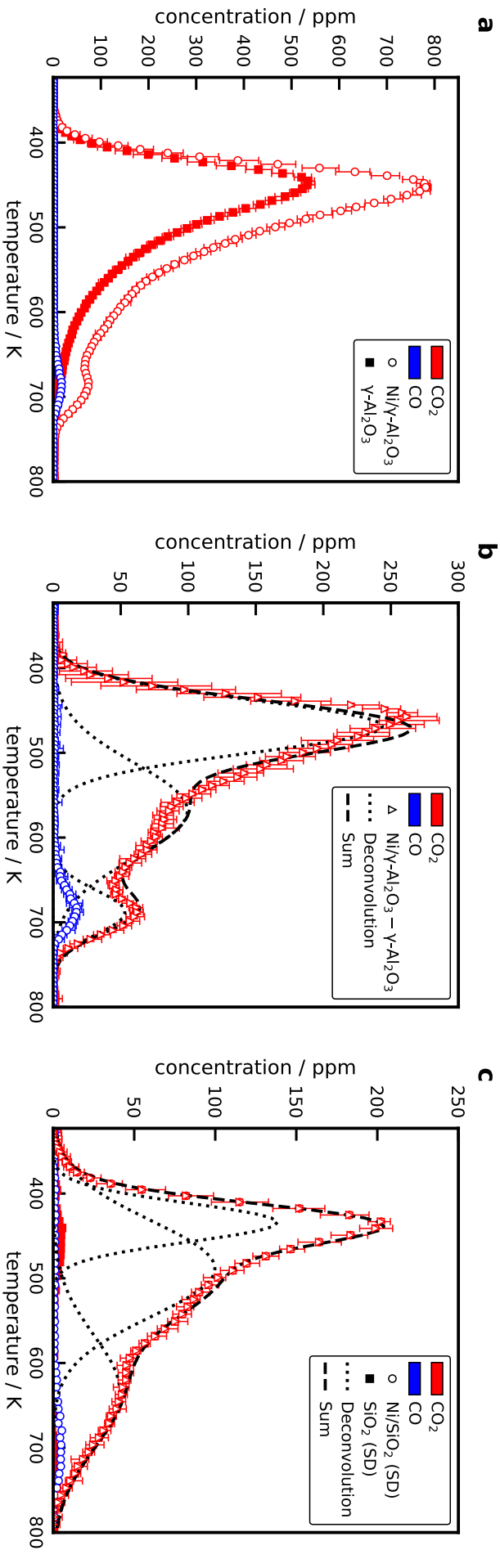

Figure 5.4.: Desorption profiles of (a) Ni/γ-Al_2O_3 and (c) Ni/SiO_2 after CO_2 adsorption at 383 K for 60 min. Results of the desorption from the support are also displayed. (b) Desorption from the Ni/γ-Al_2O_3 catalyst with subtracted desorption from the support. The deconvolution of the desorption curve with Gaussian peaks is only intended to guide the eye and highlight overlapping peaks. *Conditions:* $m_{cat} = 40\,mg$, $\beta = 20\,K\,min^{-1}$, $\dot{V}_{Ar} = 30\,mL_N\,min^{-1}$.

Both catalysts show a peak with a maximum of around 450 K. Comparing the alumina catalyst and support shows that the peak height of the first CO_2 peak is increased for the catalyst. Moreover, the alumina catalyst shows a higher desorption rate at all temperatures, but the profile compared to the support remains unchanged. This allows speculations about the nature of the adsorbed CO_2 on the $Ni/\gamma\text{-}Al_2O_3$. Usually, the increase of the first peak is attributed solely to an increase of basic sites on the support or due to the metal/support interface [26]. However, as shown by the measured CO_2 uptake for different Ni crystal sizes (see Figure 5.3), it can be concluded that the metal/support interface does not play a significant role for the CO_2 adsorption capacity. The Ni/SiO_2 catalyst provides new insights since the support showed nearly no CO_2 uptake. It means that we can assume that the desorption is occurring from adsorption sites on the Ni crystals. The close resemblance to the alumina sample regarding the shape and width of the profile shows that desorption from basic sites and desorption from sites on the Ni catalyst exhibit similar desorption kinetics. The discernible peaks from the silica catalyst could be a result of the desorption from different Ni facets, which will be explored with the microkinetic model. Falconer and Zağli [60] performed the CO_2 adsorption at a temperature of 383 K and observed in the TPD a single CO_2 peak with a maximum at 543 K and multiple CO peaks (460 K and 700 K). The position of the main CO_2 peak is higher than in this study, which can be a result of the higher temperature ramp of $90\,\mathrm{K\,min^{-1}}$. But a peak around 500 K is also observed. The second CO peak observed by Falconer and Zağli [60] agrees with the CO peak from both catalyst. However, no CO peak at lower temperatures is detected.

5.3.4. DFT Calculations

The equilibrium shape of the Ni nanoparticle obtained from the Wulff construction with the following Ni surface energies: (111) $1.92\,\mathrm{J\,m^{-2}}$, (100) $2.21\,\mathrm{J\,m^{-2}}$, (211) $2.24\,\mathrm{J\,m^{-2}}$, and (110) $2.29\,\mathrm{J\,m^{-2}}$ [40] is depicted in Figure 5.5. The composition of the nanoparticle is: (111) 69.23 %, (100) 21.10 %, (211) 4.39 %, and (110) 5.28 %. (111) and (100) facets are separated by a (211) step. The (110) surface forms the edges of the octahedral shape and is a boundary between different (111) facets. The equilibrium shape of a metal nanoparticle can depend on surface coverage, adsorbate, and surrounding gas atmosphere [61, 62]. Therefore, it can be possible that the shape of the Ni nanoparticle and with it the facet distribution changes during the TPD, when the surface coverage decreases due to desorption. This could induce changes in the nanoparticle shape and consequently affect the desorption profile. However, considering a dynamic Ni nanoparticle is too complicated and as a simplification, we assumed a constant Ni nanoparticle shape.

The results from the DFT calculations for the four Ni facets are summarized in Table 5.3 and compared to literature values. The total energies, vibrational frequencies, and geometries are reported in Table S1. Different adsorption sites were tested on all facets and the most stable site is reported. The binding energy of H^* is almost constant among the different Ni facets with values of -2.76 eV and only slightly less stable on the Ni(110) surface by 0.16 eV. H^* adsorbs on fcc site on Ni(111), on the hollow site on Ni(100), on the 3-fold hollow site of the step on Ni(211) and on the short-bridge position on Ni(110). Oxygen adsorbs in the same position as H^* on the Ni(111) and Ni(211) facet, with binding energies of -4.7 eV and -4.88 eV, respectively. Compared to the (111) surface, O^* is stabilized on the (100) facet by -0.3 eV and destabilized on the (110) facet by 0.1 eV. On the Ni(111) facet C^* is adsorbed in the hcp position with a binding energy of -6.45 eV, which is in good agreement to literature values [4,

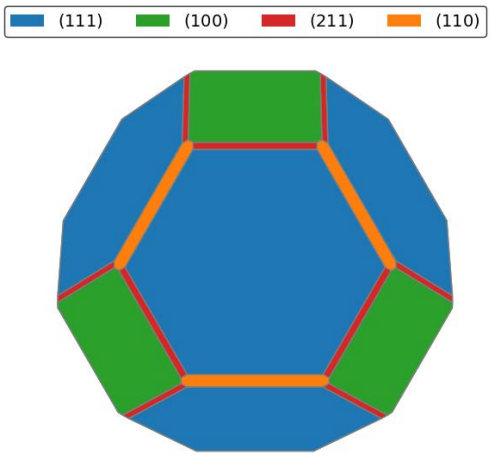

Figure 5.5.: Equilibrium shape of the Ni nanoparticle determined via Wulff construction.

10]. C^* binds stronger to the other facets with the strongest bond to the hollow position on Ni(100) with −7.75 eV, followed by −7.33 eV on the B5 site on Ni(211) and −7.16 eV on the hollow site on the Ni(110) surface. The binding energy of CO^* is constant for the Ni(111), Ni(100), and Ni(211) facet and slightly higher on the Ni(110) with −1.87 eV. This behavior is comparable to experimental results [63]. DFT-D3 [37] has been used in previous studies to describe the van-der-Waals interaction of CO_2^* with Ni surfaces and produced results consistent with TPD experiments [64]. CO_2^* is only loosely bound in a linear configuration on the atop position of the (111) surface with a binding energy of −0.22 eV, which is also the binding energy and configuration on the (100) facet. This shows that CO_2^* is only physisorbed and not stable at higher temperatures [65]. On the (110) facet CO_2 is adsorbed in a bent configuration with the carbon atom on the short-bridge site and both oxygen atoms on atop sites. This configuration forms the strongest bond with −0.4 eV. Other studies report a hollow-up geometry to be the most stable, which was also observed in experiments [64]. But the energy difference between the adsorption sites is small, allowing different adsorption configurations [66, 67].

On the (211) surface CO_2 is also adsorbed in a bent configuration in the bridge position on the step with a lower binding energy of −0.36 eV, which is comparable to the value reported by Catapan et al. [4]. The thermodynamic properties of the adsorbates, such as heat of formation, entropy, and heat capacity, are calculated from the vibration frequencies with the method described by Blondal et al. [39]. An advantage of this method is that the calculated heats of formation of the adsorbates do not depend on the DFT energy of gas-phase precursor, which is not accurately described by the exchange-correlation functional [39]. While DFT performs reasonably well when predicting heats of surface reactions, it is more difficult to predict heats of adsorption that are in agreement with experimental values [45, 68]. Heats of reactions are predicted more accurately because of the cancellation of errors, which is lacking for heats of adsorption. The approach outlined by Blaylock et al. [45] is used to adjust the heat of formation of important intermediates to match an experimentally determined heat of adsorption, while the calculated temperature dependence of enthalpy, entropy and heat capacity is still used from the electronic structure calculation. In this case experimental values for CO^*, O^*, and H^* are used. The remaining adsorbates are adjusted by keeping the heats of reaction constant, based on the reasoning described above [45]. Results of the standard enthalpies of formation on the Ni facets are reported in Table 5.4.

Table 5.3.: Zero-point corrected binding energies (eV) of the different Ni facets at $\Theta = 1/9$ ML compared with literature values. The binding energy is calculated with Equation (D.1).

	Ni(111)		Ni(100)		Ni(110)		Ni(211)	
	This study	Literature	This study	Literature	This study	Literature	This study	Literature
H^*	−2.76	−2.77 [4], −2.8 [45], −2.64 [10]	−2.78	−2.64 [10]	−2.60	−2.68 [69]	−2.76	−2.73 [4], −2.66 [10]
O^*	−4.70	−4.81 [4], −4.5 [45], −5.14 [10]	−5.02	−5.46 [10]	−4.61	−5.38 [70]	−4.88	−4.81 [4], −5.32 [10]
C^*	−6.45	−6.61 [4], −6.0 [45], −6.35 [10]	−7.75	−7.76 [10]	−7.16	−7.09 [70]	−7.33	−7.45 [4], −7.31 [45]
CO^*	−1.82	−2.09 [4], −1.85 [9], −1.5 [45], −1.56 [10]	−1.81	−1.81 [9], −1.53 [10]	−1.87	−1.81 [9]	−1.82	−2.09 [4], −1.93 [9], −1.60 [10]
CO_2^*	−0.22	−0.12 [4], 0.25 [9], 0.03 [45], 0.31 [67]	−0.22	−0.17 [9], −0.14 [67]	−0.40	−0.31 [4], −0.43 [9], −0.42[67]	−0.35	−0.41 [9], −0.36 [4]

Table 5.4.: Standard enthalpies of formation ($kJ\,mol^{-1}$) of the adsorbates on the investigated Ni facets derived by DFT and adjusted to match experimental heats of adsorption of O_2, H_2, and CO on the Ni facets. The adjusted heats of formation are used for the microkinetic model.

species	Ni(111)		Ni(100)		Ni(110)		Ni(211)	
	DFT	Adj.	DFT	Adj.	DFT	Adj.	DFT	Adj.
H^*	−54	−48 [71]	−55	−48 [71]	−38	−45 [71]	−54	−48
O^*	−238	−220 [63]	−266	−275 [63]	−226	−238 [63]	−254	−310 [72]
C^*	155	123	29	28	86	83	69	99
CO^*	−225	−240 [63]	−222	−233 [63]	−228	−243 [63]	−225	−251 [73]
CO_2^*	−388	−385	−384	−403	−403	−429	−402	−483

The DFT calculation overestimates the O^* binding energy on the Ni(111) facet by 35 kJ mol^{-1} compared to 440 kJ mol^{-1} [63], but on the Ni(100) and Ni(110) facet, the DFT derived value is lower by approx. 20 kJ mol^{-1} [63]. An initial heat of adsorption of 620 kJ mol^{-1} is measured by Karmazyn et al. [72] for O^* on the (211) facet, which is 120 kJ mol^{-1} higher than the theoretical value. They report a strong coverage dependence for adsorption on the (211), with a sharp decrease of 160 kJ mol^{-1} if the coverage on the step reaches 0.5 ML. For a consistent application of the adjustment of the heat of adsorption, the heat of formation of O^* on the (211) surface is adjusted to match the low coverage value. The high value of the heat of formation of O^* on the (211) facets leads to an increase in the heat of formation of CO_2^* by 80 kJ mol^{-1}, which is significantly higher than on the other facets. The heat of adsorption of CO is underestimated by 15 kJ mol^{-1}, only for the Ni(211) facet this value is higher with 25 kJ mol^{-1}. By using this method, the heat of formation of CO_2^* needs to be slightly decreased on Ni(111) and increased for Ni(100) and Ni(110).

5.3.5. Microkinetic Modeling

Results from the catalyst characterization are used to investigate whether the TPD experiments are affected by transport limitations. The criteria proposed by Demmin and Gorte [74, 75] were used to evaluate the impact of diffusion, readsorption, and lag time on the TPD profiles (see SI). Based on these criteria, it was necessary to account for the effect of readsorption, which is done in the model, but concentration gradients in the catalyst pellets could be neglected. Table 5.5 summarizes the parameterized microkinetics used in this study. The activation barrier for the H_2 adsorption and the sticking probability was taken from Carvalho et al. [5]. Sticking coefficients for CO_2 were obtained from the literature for Ni(100) [11] and Ni(110) [12, 13]. For the (111) [(211)] surface, it was assumed that CO_2 has the same sticking probability as on the (100) [(110)] surface. The activation barriers for the surface reactions were taken from Vogt et al. [9] and the pre-exponential factors were estimated from the entropy change of the reaction (see Equation (5.7)). Thermodynamic values for the gas-phase species were taken from the Active Thermochemical Tables (ATcT) [76, 77]. The multifaceted TPD model is validated by comparing the simulation results with the experimentally recorded H_2 desorption profiles from the Ni/γ-Al_2O_3 catalyst for various initial coverages. Since the purpose of the H_2-TPD is only the validation of the model, no further H_2 desorption experiments are conducted with the silica catalyst. The TPD is simulated with the microkinetic model by specifying the initial surface coverage of H^* as the value, which desorbs during the TPD. All facets have the same initial coverage.

With the microkinetic model, the peak temperature is underestimated (see Figure S11), which is typical since the heats of adsorption for H_2 on Ni/γ-Al_2O_3 are higher than the values from the single crystal [44]. The H_2-TPD experiments were used to optimize the theoretically determined heat of formation of H^* on all facets. We kept the difference between the facets and added a constant value to the heat of formation. The position of the peak, as well as the relative differences between the profiles, can be predicted when the heat of formation of H^* is increased by 7.5 kJ mol^{-1}. An area averaged heat of adsorption of 110 kJ mol^{-1} is obtained for the theoretically constructed nanoparticle. However, the peak is too narrow and the height of the peak does not fit. This is clearly a result of the neglect of coverage effects. A high coverage will lead to a decrease in the heat of formation, which reduces the activation barrier of the desorption reaction. This simply means that more desorbs at low temperatures when the coverage is high.

Table 5.5.: Multifaceted microkinetic model for the simulation of the H_2-TPD and CO_2-TPD.

	No.	reaction	A / $cm^2\,mol^{-1}\,s^{-1}$ or s / 1	E_a / $kJ\,mol^{-1}$	$\Delta_R H$ / $kJ\,mol^{-1}$	$\Delta_R S$ / $J\,mol^{-1}\,K^{-1}$
Ni(111)[a]	1	$H_2 + 2\,{}^*_{(111)} \rightleftharpoons H^*_{(111)} + H^*_{(111)}$	0.1	3.8	-96.2 (-119.6)[b]	-126.9
	2	$CO_2 + {}^*_{(111)} \rightleftharpoons CO^*_{2(111)}$	7×10^{-3}	0	7.7	-96.5
	3	$CO + {}^*_{(111)} \rightleftharpoons CO^*_{(111)}$	0.8	0	-130.0	-156.4
	4	$CO^*_{2(111)} + {}^*_{(111)} \rightleftharpoons CO^*_{(111)} + O^*_{(111)}$	4.2×10^{19}	50	-74.7	-64.1
	5	$C^*_{(111)} + O^*_{(111)} \rightleftharpoons CO^*_{(111)} + {}^*_{(111)}$	7.3×10^{21}	153	-142.7	21.8
Ni(100)	6	$H_2 + 2\,{}^*_{(100)} \rightleftharpoons H^*_{(100)} + H^*_{(100)}$	0.1	3.8	-96.2 (-119.6)	-115.9
	7	$CO_2 + {}^*_{(100)} \rightleftharpoons CO^*_{2(100)}$	7×10^{-3}	0	-9.8	-89.8
	8	$CO + {}^*_{(100)} \rightleftharpoons CO^*_{(100)}$	0.8	0	-122.0	-152.2
	9	$CO^*_{2(100)} + {}^*_{(100)} \rightleftharpoons CO^*_{(100)} + O^*_{(100)}$	5.4×10^{19}	15	-104.2	-62.1
	10	$C^*_{(100)} + O^*_{(100)} \rightleftharpoons CO^*_{(100)} + {}^*_{(100)}$	7.6×10^{21}	209	14.9[c]	20.0
Ni(110)	11	$H_2 + 2\,{}^*_{(110)} \rightleftharpoons H^*_{(110)} + H^*_{(110)}$	0.1	3.8	-89.9 (-113.4)	-113.6
	12	$CO_2 + {}^*_{(110)} \rightleftharpoons CO^*_{2(110)}$	0.14	0	-35.7	-106.1
	13	$CO + {}^*_{(110)} \rightleftharpoons CO^*_{(110)}$	0.8	0	-132.0	-137.8
	14	$CO^*_{2(110)} + {}^*_{(110)} \rightleftharpoons CO^*_{(110)} + O^*_{(110)}$	5.5×10^{20}	39	-50.8	-29.3
	15	$C^*_{(110)} + O^*_{(110)} \rightleftharpoons CO^*_{(110)} + {}^*_{(110)}$	2.1×10^{22}	161	-88.1	31.2
Ni(211)	16	$H_2 + 2\,{}^*_{(211)} \rightleftharpoons H^*_{(211)} + H^*_{(211)}$	0.1	3.8	-96.2 (-119.6)	-126.1
	17	$CO_2 + {}^*_{(211)} \rightleftharpoons CO^*_{2(211)}$	0.14	0	-89.8	-113.0
	18	$CO + {}^*_{(211)} \rightleftharpoons CO^*_{(211)}$	0.8	0	-140.0	-150.6
	19	$CO^*_{2(211)} + {}^*_{(211)} \rightleftharpoons CO^*_{(211)} + O^*_{(211)}$	1.8×10^{20}	90	-77.3	-38.9
	20	$C^*_{(211)} + O^*_{(211)} \rightleftharpoons CO^*_{(211)} + {}^*_{(211)}$	7.5×10^{21}	168	-39.6	23.4

[a]Surface site density calculated from the unit cells are: $3.16\times10^{-9}\,mol\,cm^{-2}$ Ni(111), $2.74\times10^{-9}\,mol\,cm^{-2}$ Ni(100), $1.94\times10^{-9}\,mol\,cm^{-2}$ Ni(110), $3.36\times10^{-9}\,mol\,cm^{-2}$ Ni(211)

[b]Optimized values for the heat of reaction of H^* to match the experimental H_2 desorption profiles are in parentheses. The optimized heats of formation for H^* on the Ni facets with the coverage dependence for the Ni(111), Ni(100), and Ni(211) facet are $-60\,kJ\,mol^{-1} + 8.7\,kJ\,mol^{-1}\,\Theta_{H^*}$ and $-57\,kJ\,mol^{-1} + 8.7\,kJ\,mol^{-1}\,\Theta_{H^*}$ for Ni(110).

[c]All reactions are specified in the exothermic direction, except for the CO^* dissociation on Ni(100), which is slightly endothermic but kept in this direction to make it consistent with the other facets.

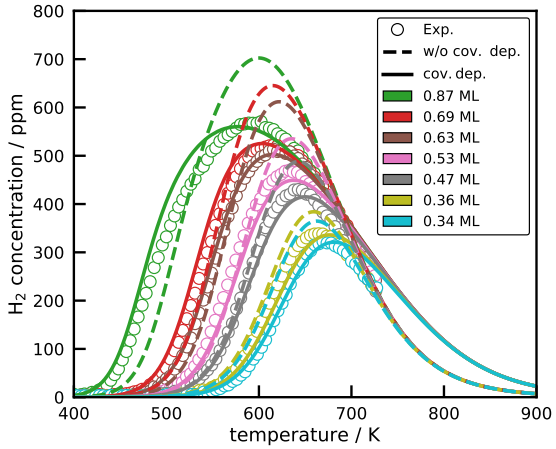

Figure 5.6.: H_2 desorption profiles with varying initial coverage expressed in terms of mono-layers from the $Ni/\gamma\text{-}Al_2O_3$ catalyst compared to the microkinetic simulation of the multifaceted Ni catalyst with optimized heats of formation of H^*. The mono-layer coverage is defined by the uptake of H_2 from the static adsorption at 323 K with 121 µmol g^{-1}. Microkinetic simulations are performed without coverage effects (dashed line) and with a linear coverage dependence of 8.7 kJ mol^{-1} (solid line). *Conditions:* $m_{cat} = 80$ mg, $\dot{V}_{He} = 30\,mL_N\,min^{-1}$, $\beta = 20\,K\,min^{-1}$

In order to show the effect of coverage, a linear dependence of the H^* coverage on the heat of formation of H^* was assumed, similar to the work of Carvalho et al. [5]. Furthermore, it is assumed that the dependence is the same on all facets. Optimization of the heat of formation and the coverage dependence leads to the profiles shown in Figure 5.6. With the coverage dependence, it is now possible to accurately predict the height as well as the peak position. The optimized heat of adsorption is 118 kJ mol^{-1} and the coverage dependence is 8.7 kJ mol^{-1}. This is in good agreement to a heat of adsorption determined by Weatherbee and Bartholomew [44] of 125 kJ mol^{-1} for a similar Ni/Al_2O_3 catalyst. Based on this comparison, the proposed model of the TPD setup can describe the desorption profiles over a wide range of coverages and, therefore, be considered as validated and used to investigate the more complex desorption of CO_2. However, the model is not able to describe the multiple peaks observed for adsorption temperatures of 323 K and 373 K (see Figure S6), which is a consequence of the simplifications made in the coverage dependence, e.g. linear and similar on all facets. Due to the strong adsorption of CO_2 on basic sites of the alumina support, this catalyst is not further used in the microkinetic simulation and only the Ni/SiO_2 catalyst is discussed.

Figure 5.7 shows the CO_2 desorption profiles from the microkinetic simulation of the single facets. A single CO_2 peak is observed during the TPD from Ni(111) with a maximum at 431 K. Heine et al. [15] and Cai et al. [65] observed CO_2 dissociation on the Ni(111) facet with XPS at ambient pressure, supporting the simulation results. CO_2 is entirely dissociated and the initial coverage on the (111) facet is 12.2 % for O^* and CO^*. Chemisorbed CO_2^* is not stable on this facet [15, 65]. CO_2 desorbs from the (111) facet since the activation barrier for the recombination of O^* and CO^* is lower than the direct desorption of CO^* and the desorption of CO_2^* is exothermic. Experimental studies of the CO_2 adsorption on Ni(111) single crystals at ambient pressure show that the Ni surface is oxidized to some extent by surface O^*, formed by CO_2^* dissociation [15, 78]. The oxidized Ni surface can then adsorb CO_2 in the form of carbonates [15] that will also contribute to the desorption profile. The degree of oxidation depends on the adsorption temperature [15]. However, the oxidation of the surface is not complete

and metallic Ni will remain present [15]. Although important to some extent, including morphological changes such as bulk oxidation into a multifaceted microkinetic model is well beyond the state-of-the-art and the scope of the present paper. The colored area in Figure 5.7 shows the possible range of the TPD curves obtained from the GUA when the parameters of the microkinetic model are varied in their assigned uncertainty range. The range between the highest and lowest possible CO and CO_2 concentration at each temperature is filled. It is interesting to see that variations within the uncertainty of the DFT based parameters show drastic effects on the TPD profiles. The GUA analysis for the Ni(111) facet reveals that within the varied parameter range, no significant amounts of CO desorb from the catalyst. Additionally, the peak temperature varies in a rather narrow range. However, the height of the peak reaches values up to 2,000 ppm because the initial surface coverage is increased.

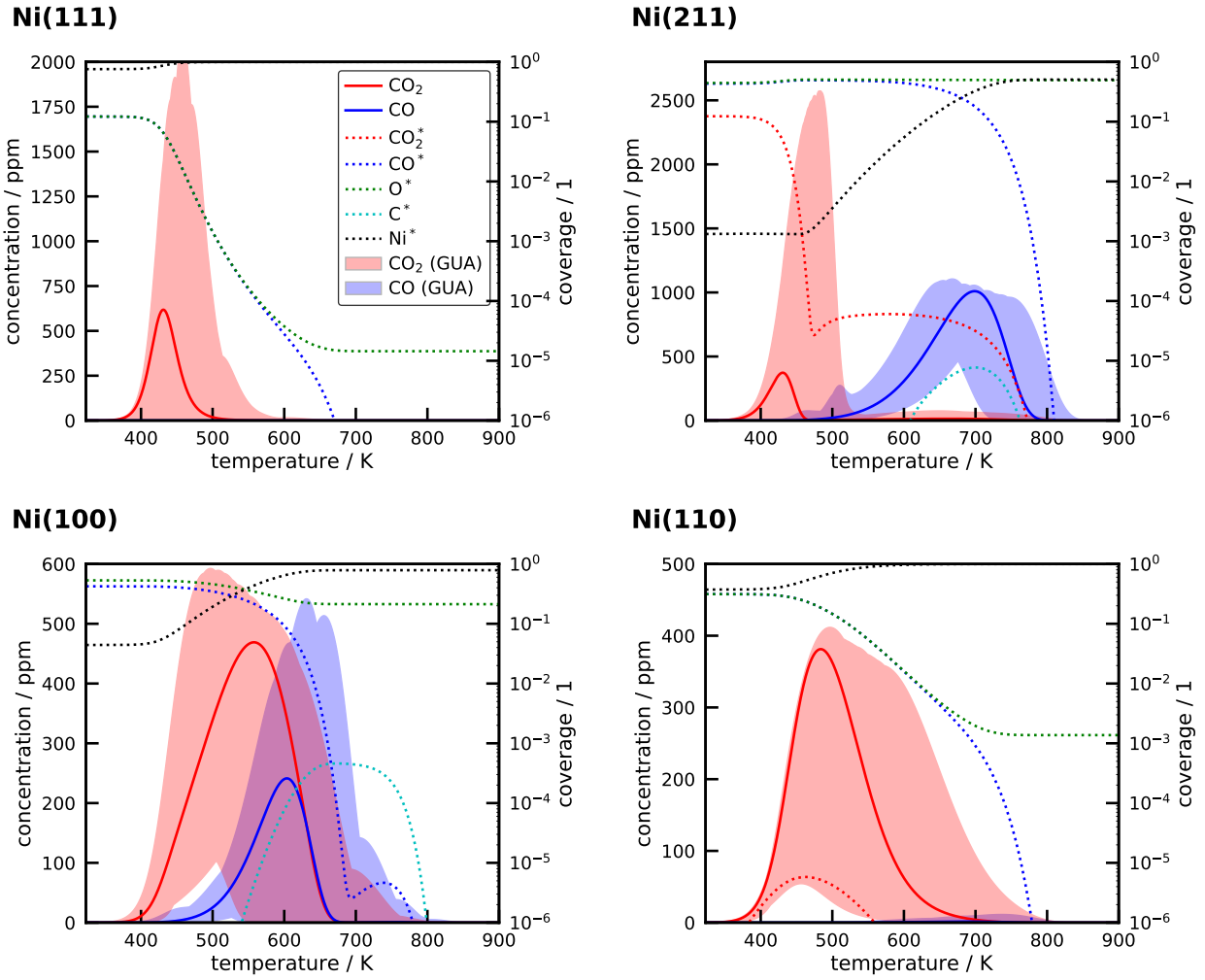

Figure 5.7.: Simulated desorption and coverage profiles of Ni(111), Ni(211), Ni(100), and Ni(110). The parameters for the Ni/SiO_2 catalyst were used in the simulation and it was assumed that the whole metal surface area consists of the simulated facet. The shaded area shows the range of possible solutions from the GUA. 100 simulations are conducted for the GUA of the single-facets.

The Ni(211) facet shows a low-temperature CO_2 peak, which originates from the desorption of chemisorbed CO_2 at temperatures of 431 K. Adjusting the heat of formation of the species, according to Blaylock et al. [45] to match the experimental values for Ni(211) results in a strong chemisorption of CO_2. The activation barrier for the desorption of CO_2 is extremely high and has a value of 86 kJ mol^{-1},

which also explains the high CO_2^* coverage of 12.3 %. The rest of the Ni(211) surface is completely covered with CO^* (43.2 %) and O^* (44.3 %). On the (211) facet, CO^* desorbs because it has a lower activation barrier than the recombination of CO^* and O^*. CO^* is strongly bound to the surface with a value of 134 kJ mol^{-1}, which causes a high-temperature desorption peak at 700 K. It is interesting to note that the (211) facet remains covered by approx. 0.5 ML of O^*. This has been observed experimentally for Ni(110) [14]. At high temperatures, the surface oxygen can induce bulk oxidation of the Ni [15, 16]. The GUA shows that the CO_2 desorption peak increases to similar high values as for Ni(111), while the height of the CO peak varies in a more narrow range. In contrast to Ni(111), the increase is a result of the desorption of chemisorbed CO_2^* instead of the recombination of CO^* and O^*. Some combinations of parameters lead to a second CO_2 peak at high temperatures, which is caused by the recombination.

On the Ni(100) facet, the surface is also entirely covered by CO^* and O^* because it has the lowest activation barrier for the CO_2^* dissociation [9]. Experimental results reveal that CO_2^* is entirely dissociated beyond 200 K [65]. Ni(100), similar to Ni(211) also shows a CO and CO_2 desorption peak. The CO_2 desorption rate reaches its maximum at 558 K, whereas the maximum CO desorption rate is slightly shifted to a higher value of 604 K. Rates for the recombination are higher than the desorption rates in the beginning, but with increasing temperature, CO^* starts to desorb directly. The difference between the activation energy of the recombination and the CO desorption is below 5 kJ mol^{-1}. This is the only facet on which C^* is observed in significant quantities, but it is removed by reaction with O^* at higher temperatures. Cai et al. [65] observed C^* already at room temperature on this facet with XPS. The (100) facet remains covered by 21 % in O^*. In the GUA, the Ni(100) facet shows in all simulations a CO_2 and CO desorption peak.

On the open Ni(110) facet, CO_2 is also dissociated and an initial coverage of 31.4 % of O^* and CO^* is a result. The dissociation of CO_2^* on Ni(110) is also observed experimentally at UHV [64] and higher pressures of 1×10^{-1} mbar [16]. CO_2 desorbs in a single broad peak from the (110) facet, starting at 350 K with a maximum at 484 K. The recombination has a significantly lower activation barrier by 42 kJ mol^{-1} than the desorption of CO^*. Due to the high barrier, a little CO desorbs at high temperatures, leaving some O^* on the surface, which was also observed in TPD experiments [14]. However, no recombination and CO_2 desorption was measured by Ding et al. [14], after CO_2 adsorption at UHV conditions and 90 K. This can be a result of the lower surface coverages typically present at UHV conditions. In addition, readsorption is more pronounced at ambient pressure, which can affect the desorption profile. No surface C^* is observed due to the high reaction barrier of the CO^* dissociation, which is opposed to XPS studies by Roiaz et al. [16]. The desorption profiles obtained in the GUA do not significantly change. The height and position of the CO_2 desorption peak are shifted, but the amount of CO formed is always small.

Local sensitivity analysis is applied to quantify how small perturbations in the heat of formation (see Figure 5.8a) or activation energy (see Figure 5.8b) alter the peak height and position of the maximum of the simulated CO_2 and CO desorption peak. The Ni(111) facet shows the highest sensitivity when the heat of formation is modified. A higher heat of formation of CO^* and O^* increases the peak height by 125 ppm, whereas an increase in CO_2^* decreases the peak by the same value. Increasing the activation energy of the CO_2 dissociation reaction by 1 kJ mol^{-1} decreases the peak height by 120 ppm. This shows that on the (111) facet, everything is determined by the CO_2^* dissociation reaction and the barrier heights of the forward and reverse reaction. The (211) facet shows only a high sensitivity towards

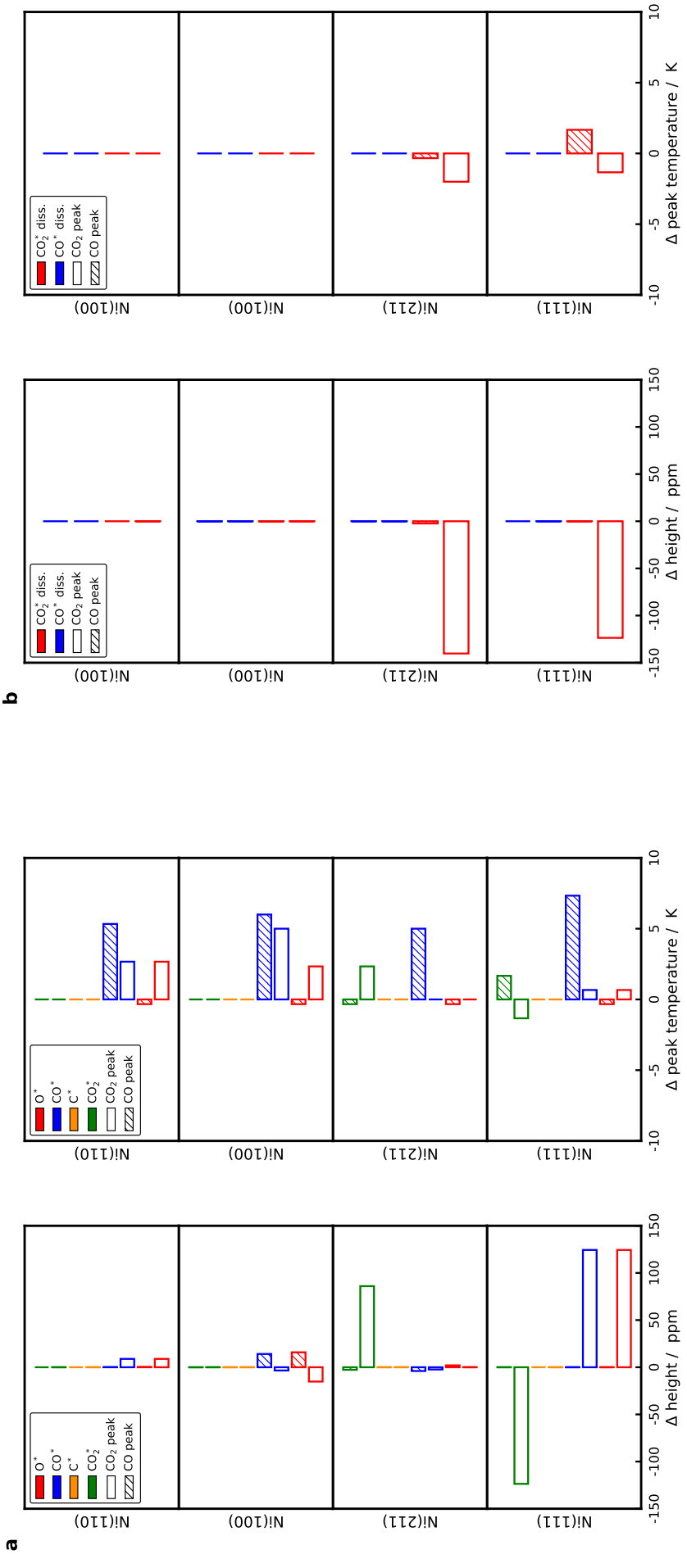

Figure 5.8.: (a) Thermochemistry sensitivity analysis on the peak height (left) and the position of the peak maximum (right) of the CO and CO_2 peak. (b) Sensitivity analysis of the activation energy on the height and position of the desorption peak. The heat of formation of the adsorbates and the activation energy is adjusted by 1 kJ mol^{-1} for the local sensitivity analysis.

the CO_2^* heat of formation, with an increase leading to an increased CO_2 peak, which is caused by a lowering in the CO_2^* desorption barrier. On the (110) and (100) facet, the thermochemistry of CO_2^* is unimportant, whereas small variations in the height are observed for the variation of O^* and CO^*. Varying the sticking coefficient by two orders of magnitude does not influence the desorption profiles. This is also the case for the activation barrier of the CO^* dissociation reaction and the heat of formation of C^*. The four important parameters, which determine the desorption profile, are the heat of formation of CO^*, O^*, CO_2^*, and the activation barrier for the CO_2^* dissociation. Changing the heat of formation of CO^* affects the activation barrier of the CO^* desorption as well as the barrier of the recombination of CO^* and O^*. High CO_2 concentrations are observed for the Ni(111) facet, when the activation barrier of the CO_2 dissociation reaction is raised, either by an increase of E_a or by an increase of the heat of formation of CO^* or O^*. These adjustments increase the initial surface coverage, which causes a higher peak. Local sensitivity analysis for a change of the activation energy or heat of formation by $-1\,\mathrm{kJ\,mol^{-1}}$ is provided in Figure S12 and shows precisely the opposite behavior.

Figure 5.9a compares the experimental desorption profile of the Ni/SiO_2 catalyst with the result from the simulation with the multifaceted microkinetic model. The comparison shows clearly that the simulation cannot accurately predict the recorded profile. Only the beginning of the profile fits, which corresponds to desorption from the (111) facet. A maximum CO_2 desorption rate at 600 K is obtained and a higher CO peak temperature of 650 K. The second peak is mainly caused by the desorption from Ni(100). The shift of the CO peak compared to the single facet is a result of the Ni(211) facet, which binds CO stronger.

The initial coverages for the facets in the multifaceted simulation are not the same as in the single facets run. The gas-phase concentrations are changed, which causes the difference. Based on the coverage profiles (see Figure S13), it is possible to explain the sharp increase in the CO_2 concentration at 460 K. At this temperature, CO_2 desorbs rapidly from the (211) facet and is at the same time produced on the (110) and (100) facet by the recombination of CO^* and O^*. Applying the GUA as before for the single facets, with 35 randomly varied parameters, results in a broad range, which can be expected based on the obtained range from the single facet analysis. GUA of the single facets and the local sensitivity analysis provide an explanation for the variations. Main deviations are caused by variations in the aforementioned four parameters for the Ni(111) and Ni(100). In addition, the variation of the facet distribution has a distinct effect on the desorption profiles.

From the 1000 simulations performed in the GUA, it is now possible to determine the profile with the lowest root-mean-square error (RMSE) (Equation (5.24)) compared to the experimental desorption profile for CO_2 and CO.

$$RMSE = \sqrt{\left(x_{CO_2,exp} - x_{CO_2,sim}\right)^2} + \sqrt{\left(x_{CO,exp} - x_{CO,sim}\right)^2} \tag{5.24}$$

Figure 5.9c shows the results for the facet distribution, which corresponds to the three simulations with the lowest RMSE. With this form of presentation, it is possible to see whether the parameters for the best matches form clusters around a new value, which would indicate the possible range of the parameter. The facet distribution has a slightly higher share of Ni(111) and a lower fraction of Ni(100), whereas the stepped sites remain nearly unchanged compared to the base case. This shows that the Wulff construction provides a reasonable estimate of the facet distribution for small Ni nanoparticles. Due to the large influence of the facet distribution on the desorption profile, a second GUA was performed,

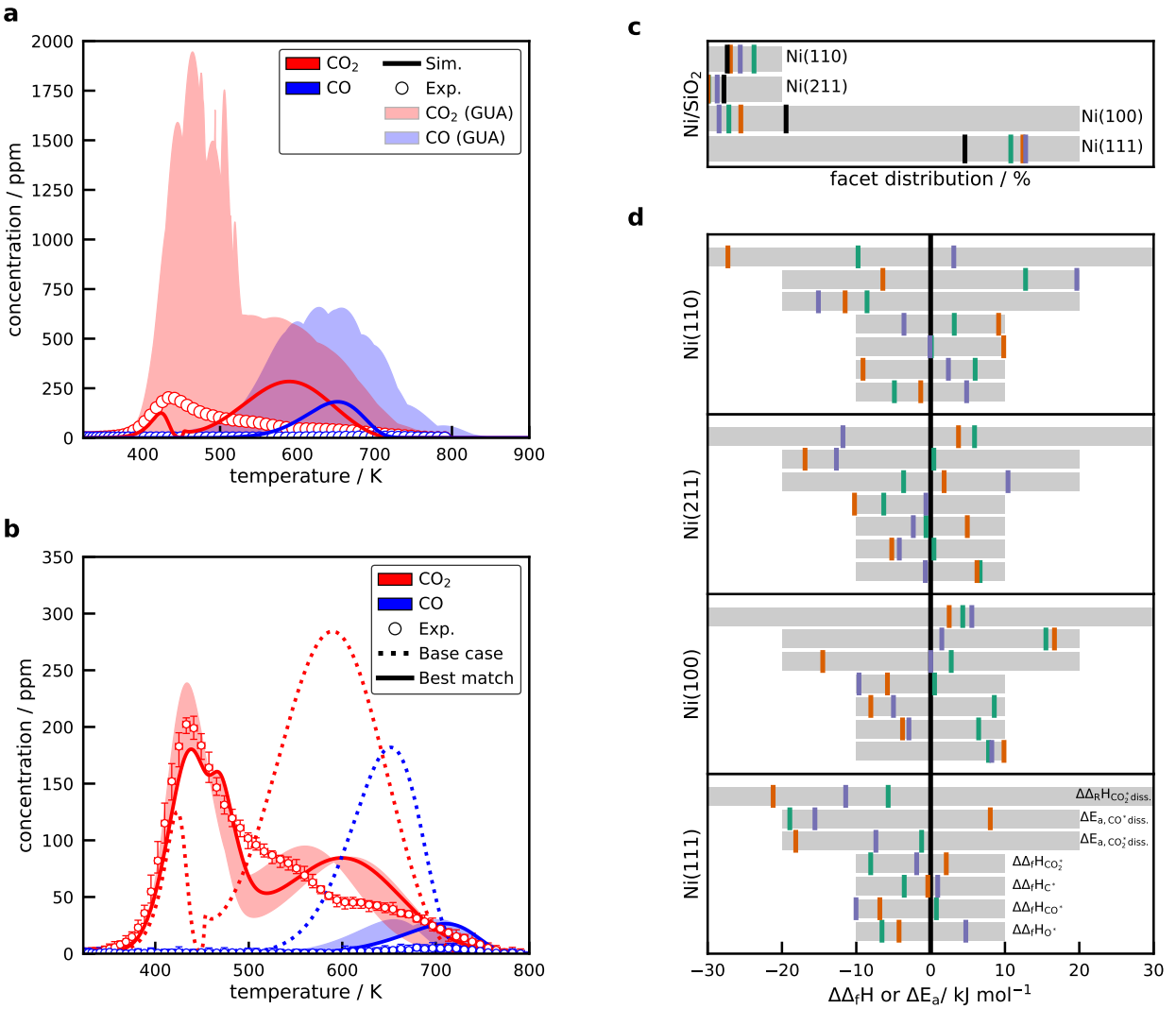

Figure 5.9.: (a) Simulation with the multifaceted microkinetic model compared to the experimental desorption profile of the Ni/SiO_2 catalyst. (b) Comparison of the experimental desorption profile to the base case model and the profile from the GUA with the lowest root-mean-square-error. The shaded area shows the simulation results for the three best fits. 1000 simulations were performed for the multifacet model. (c) Results for the facet distribution from the first GUA. (d) Change in the heats of formation ($\Delta\Delta_f H$) and activation energies (ΔE_a) on the four facets that lead to the simulation results in the shaded area in (b). The black line shows the parameters of the base case and the colored lines show the parameters for the three desorption profiles with the lowest RMSE. Green is the best match. The optimized facet distribution for the Ni/SiO_2 catalyst is: Ni(111)=84.0 %, Ni(100)=5.9 %, Ni(211)=1.0 %, and Ni(110)=9.1 %.

with the averaged facet distribution for the three best fits, and only the parameters of the microkinetic model were varied in the GUA.

A significant difference is observed between the best match and the reference case. The best match shows three CO_2 peaks, with two low-temperature peaks corresponding to desorption from the (111) and (110) facet and a high-temperature peak from the (100) and (211). The shaded region shows the result for the three simulations with the lowest RMSE. The position of the first and second peak from the experiment and the simulation compares well, which is also valid for the height. While the simulated position of

the high-temperature CO peak agrees with the experiments, the height is significantly overestimated. Besides, the range of simulations with a similar RMSE span only a small range for possible solutions.

Figure 5.9d shows the parameters for the heat of formation and activation energy. The result for the best match is displayed in Figure 5.9b. The colored vertical bars indicate the value of the changed parameter referenced to the value of the base case (see Table 5.4 and Table 5.5). For some parameters, it is possible to see a clear grouping of values, while for others, there is no clear dependence. This is the case for the heat of formation of C^* and the barrier of the CO^* dissociation reaction, which agrees with the sensitivity analysis. A grouping is observed for the heat of formation of O^* on the Ni(100) facet. The heat of formation of O^* needs to be decreased, which is reversed for the (110) facet. A lower value for the heat of formation is reasonable since coverage effects, which were neglected in this study, decrease the binding energy due to repulsive interactions. A decrease in the heat of formation by $10\,\mathrm{kJ\,mol^{-1}}$ is necessary for Ni(111). Multiple sets of thermodynamic parameters can be present, which describe the experiments reasonably well since the reverse reaction rates are calculated from the equilibrium constant. The equilibrium constant is calculated from the free enthalpy change of the reaction, which depends on the heat of formation of O^*, CO^*, and CO_2^*. That is why the enthalpy change of the CO_2^* dissociation reactions is included in the diagrams. On the (111) facet, the value needs to be decreased, whereas an increased value is obtained for the (100) facet. The activation barrier for the CO_2^* dissociation needs to be decreased on Ni(111).

The comparison of the simulated desorption profiles and surface coverages of the four Ni facets shows pronounced differences, indicating a structure-sensitivity in the activation of the CO_2 molecule. These results are in good agreement with experimental as well as theoretical studies [9, 78]. With the usage of the multifaceted model, it is possible to reasonably compare recorded desorption profiles from supported Ni catalysts with a microkinetic simulation. Within the given uncertainty of the kinetic and thermodynamic parameters, sets of these exist, which allow for an accurate description of the desorption profile of the Ni/SiO_2 catalyst. The experimentally observed desorption peak at 437 K is a result of the CO_2 desorption from the Ni(111) facet. This also sheds new light on the interpretation of the desorption profile from the $Ni/\gamma\text{-}Al_2O_3$ catalyst, which has the maximum desorption rate at the same temperature. It suggests that the increase of the height is not strictly a result of an increase in the number of basic adsorption sites on the alumina or the metal/support interface but also due to desorption from the Ni(111) facet. The desorption kinetics from basic sites with medium strength and the heat of adsorption have to be similar to the kinetics for Ni(111). This reveals that for the interpretation of desorption profiles in the literature [24, 26], the desorption from different Ni facets must be considered.

For the simulation of the H_2 desorption profiles, it was necessary to include coverage effects in the model to describe the experimental data. O^* and CO^* exhibit strong repulsive interactions [56], which will significantly influence the binding strength. A thermodynamically consistent implementation of coverage effects for this system is, therefore, necessary. The inclusion of thermodynamically consistent coverage effects for the CO_2^* submechanism is beyond the scope of the paper but will be the subject of future studies. The GUA highlights the fact that uncertainties in the DFT derived parameters can result in a broad range of possible desorption profiles. In order to reduce the range of possible solutions, it is necessary to reduce the uncertainty within the DFT methods [68]. Accordingly, more accurate DFT functionals would further constrain the GUA predictions and increase the predictability of the model. For catalyst systems, where CO_2 adsorbs strongly on the support, it is necessary to include basic sites in the model and spillover from the Ni to basic sites on the support and vice versa. Moreover, DFT

calculations with the Ni nanoparticle on the alumina support will be required since the interface can provide different pathways for the activation of the CO_2 molecule [6].

5.4. Conclusion

The interaction of CO_2 with Ni catalysts was investigated with experimental and theoretical methods. A multifaceted microkinetic model of a Ni nanoparticle was proposed and successfully validated for the H_2-TPD. The microkinetic model shows a pronounced structure-sensitivity in the CO_2 activation, which manifests itself in the simulated desorption spectra and surface coverages. Desorption peaks from the Ni(111) and the Ni(211) facet compare well with the experimentally observed peaks. Desorption peaks from all four Ni facets are within the temperature range of the experimental desorption profile.

With the multifaceted model, it was, for the first time, possible to compare the results from ab-initio methods to CO_2-TPD profiles from supported Ni catalysts at ambient pressure. The initial simulated desorption profiles showed significant deviations from the experiments. But the GUA highlights the broad array of possible solutions that can be obtained within the uncertainty that is usually assigned to DFT-derived parameters even for a rather simple system. Within this uncertainty, combination of model parameters exist that provide an accurate description of the experimentally observed profile for the Ni/SiO_2 catalyst. Therefore, the desorption of CO_2 from different Ni facets needs to be taken into consideration when evaluating TPD patterns. This also sheds new light on the desorption from catalysts with basic adsorption sites, as obtained for the Ni/γ-Al_2O_3 catalyst showing that desorption from basic sites and the Ni surface have similar kinetics indeed. The GUA stresses the need for accurate first-principle derived parameters and correct quantification of the uncertainties. Moreover, the method reveals that it is required to account for uncertainties in the model evaluation. This study highlights the increase in complexity when multiple facets are considered in the microkinetic model, but it also demonstrates that it is necessary, when real supported catalysts are to be studied. Therefore, the multifaceted model will be extended and used to investigate the methanation of CO_2 on supported Ni catalysts to elucidate the mechanism and derive a full microkinetic model.

Acknowledgement

Bjarne Kreitz gratefully acknowledges the financial support of the German Academic Exchange Service (DAAD) in the framework of a "DAAD-Doktorandenstipendium" for a research stay at the Brown University in the group of Franklin Goldsmith. The authors thank the Institute of Mineral and Waste Processing, Waste Disposal and Geomechanics of Clausthal University of Technology (ICP-OES), Aurina Martínez from the Institute of Particle Technology of Clausthal University of Technology (XRD, SAXS, Ni/SiO_2 catalyst), and Dr. Alessio Zandona (Rietvield analysis). CFG gratefully acknowledges support from the U.S. Department of Energy, Office of Science, Basic Energy Sciences, under Award #0000232253, as part of the Computational Chemical Sciences Program.

References

[1] M. Götz, J. Lefebvre, F. Mörs, A. McDaniel Koch, F. Graf, S. Bajohr, R. Reimert, T. Kolb. *Renewable Energy* **2016**, 85, 1371–1390. DOI: 10.1016/j.renene.2015.07.066.

[2] S. Rönsch, J. Köchermann, J. Schneider, S. Matthischke. *Chem. Eng. Technol.* **2016**, 39 (2), 208–218. DOI: 10.1002/ceat.201500327.

[3] J. Xu, G. F. Froment. *AIChE J.* **1989**, 35 (1), 88–96. DOI: 10.1002/aic.690350109.

[4] R. C. Catapan, A. A. M. Oliveira, Y. Chen, D. G. Vlachos. *J. Phys. Chem. C.* **2012**, 116 (38), 20281–20291. DOI: 10.1021/jp302488f.

[5] T. P. de Carvalho, R. C. Catapan, A. A. M. Oliveira, D. G. Vlachos. *Ind. Eng. Chem. Res.* **2018**, 57 (31), 10269–10280. DOI: 10.1021/acs.iecr.8b01957.

[6] L. Foppa, T. Margossian, S. M. Kim, C. Müller, C. Copéret, K. Larmier, A. Comas-Vives. *J. Am. Chem. Soc.* **2017**, 139 (47), 17128–17139. DOI: 10.1021/jacs.7b08984.

[7] K. Delgado, L. Maier, S. Tischer, A. Zellner, H. Stotz, O. Deutschmann. *Catalysts* **2015**, 5 (2), 871–904. DOI: 10.3390/catal5020871.

[8] L. M. Aparicio. *J. Catal.* **1997**, 165 (2), 262–274. DOI: 10.1006/jcat.1997.1468.

[9] C. Vogt et al. *Nat. Commun.* **2019**, 10 (1), 5330. DOI: 10.1038/s41467-019-12858-3.

[10] D. W. Blaylock, Y.-A. Zhu, W. H. Green. *Top. Catal.* **2011**, 54 (13-15), 828–844. DOI: 10.1007/s11244-011-9704-z.

[11] J. B. Benziger, R. J. Madix. *Surf. Sci.* **1979**, 79 (2), 394–412. DOI: 10.1016/0039-6028(79)90297-8.

[12] M. P. D'Evelyn, A. V. Hamza, G. E. Gdowski, R. J. Madix. *Surf. Sci.* **1986**, 167 (2-3), 451–473. DOI: 10.1016/0039-6028(86)90717-X.

[13] J. McCarty, J. L. Falconer, R. J. Madix. *J. Catal.* **1973**, 30 (2), 235–249. DOI: 10.1016/0021-9517(73)90070-5.

[14] X. Ding et al. *Phys. Rev. B* **2007**, 76 (19), 395. DOI: 10.1103/PhysRevB.76.195425.

[15] C. Heine, B. A. J. Lechner, H. Bluhm, M. Salmeron. *J. Am. Chem. Soc.* **2016**, 138 (40), 13246–13252. DOI: 10.1021/jacs.6b06939.

[16] M. Roiaz, E. Monachino, C. Dri, M. Greiner, A. Knop-Gericke, R. Schlögl, G. Comelli, E. Vesselli. *J. Am. Chem. Soc.* **2016**, 138 (12), 4146–4154. DOI: 10.1021/jacs.5b13366.

[17] W.-B. Zhang, C. Chen, S.-Y. Zhang. *J. Phys. Chem. C* **2013**, 117 (41), 21274–21280. DOI: 10.1021/jp404569m.

[18] J. Gao, Q. Liu, F. Gu, B. Liu, Z. Zhong, F. Su. *RSC Adv.* **2015**, 5 (29), 22759–22776. DOI: 10.1039/C4RA16114A.

[19] Q. Pan, J. Peng, T. Sun, S. Wang, S. Wang. *Catal. Commun.* **2014**, 45, 74–78. DOI: 10.1016/j.catcom.2013.10.034.

[20] T. A. Le, M. S. Kim, S. H. Lee, T. W. Kim, E. D. Park. *Catal. Today* **2017**, 293-294, 89–96. DOI: 10.1016/j.cattod.2016.12.036.

[21] H. Muroyama, Y. Tsuda, T. Asakoshi, H. Masitah, T. Okanishi, T. Matsui, K. Eguchi. *J. Catal.* **2016**, 343, 178–184. DOI: 10.1016/j.jcat.2016.07.018.

[22] M. Cabrejas Manchado, J. M. Guil, A. Pérez Masiá, A. Ruiz Paniego, J. M. Trejo Menayo. *Langmuir* **1994**, 10 (3), 685–691. DOI: 10.1021/la00015a016.

[23] S. Ewald, M. Kolbeck, T. Kratky, M. Wolf, O. Hinrichsen. *Appl. Catal., A* **2019**, 570, 376–386. DOI: 10.1016/j.apcata.2018.10.033.

[24] S. Ewald, O. Hinrichsen. *Appl. Catal., A* **2019**, 580, 71–80. DOI: 10.1016/j.apcata.2019.04.005.

[25] M. P. Rosynek. *J. Chem. Phys.* **1975**, 79 (13), 1280–1284. DOI: 10.1021/j100580a011.

[26] N. Schreiter, J. Kirchner, S. Kureti. *Catal. Commun.* **2020**, 140, 105988. DOI: 10.1016/j.catcom.2020.105988.

[27] A. Ueno, C. O. Bennett. *J. Catal.* **1978**, 54 (1), 31–41. DOI: 10.1016/0021-9517(78)90024-6.

[28] J. E. Sutton, W. Guo, M. A. Katsoulakis, D. G. Vlachos. *Nat. Chem.* **2016**, 8 (4), 331–337. DOI: 10.1038/nchem.2454.

[29] Z. W. Ulissi, A. J. Medford, T. Bligaard, J. K. Nørskov. *Nat. Commun.* **2017**, 8, 14621. DOI: 10.1038/ncomms14621.

[30] J. Friedland, B. Kreitz, H. Grimm, T. Turek, R. Güttel. *ChemCatChem* **2020**, 12 (17), 4373–4386. DOI: 10.1002/cctc.202000278.

[31] A. Martínez Arias, A. P. Weber. *J. Aerosol Sci.* **2019**, 131, 1–12. DOI: 10.1016/j.jaerosci.2019.02.003.

[32] G. Ertl, H. Knözinger, F. Schüth, J. Weitkamp. Weinheim, Germany: Wiley-VCH Verlag GmbH & Co. KGaA, **2008**. DOI: 10.1002/9783527610044.

[33] A. H. Larsen et al. *J. Phys.: Condens. Matter* **2017**, 29 (27), 273002. DOI: 10.1088/1361-648x/aa680e.

[34] G. Kresse, J. Furthmüller. *Phys. Rev. B* **1996**, 54 (16), 11169–11186. DOI: 10.1103/physrevb.54.11169.

[35] G. Kresse, J. Furthmüller. *Comput. Mater. Sci.* **1996**, 6 (1), 15–50. DOI: 10.1016/0927-0256(96)00008-0.

[36] B. Hammer, L. B. Hansen, J. K. Nørskov. *Phys. Rev. B* **1999**, 59 (11), 7413–7421. DOI: 10.1103/PhysRevB.59.7413.

[37] S. Grimme. *J. Comput. Chem.* **2006**, 27 (15), 1787–1799. DOI: 10.1002/jcc.20495.

[38] C. Kittel. 8th ed. Hoboken, NJ: Wiley, **2005**.

[39] K. Blondal, J. Jelic, E. Mazeau, F. Studt, R. H. West, C. F. Goldsmith. *Ind. Eng. Chem. Res.* **2019**, 58 (38), 17682–17691. DOI: 10.1021/acs.iecr.9b01464.

[40] R. Tran, Z. Xu, B. Radhakrishnan, D. Winston, W. Sun, K. A. Persson, S. P. Ong. *Sci. Dat.* **2016**, 3, 160080. DOI: 10.1038/sdata.2016.80.

[41] M. Salciccioli, M. Stamatakis, S. Caratzoulas, D. G. Vlachos. *Chem. Eng. Sci.* **2011**, 66 (19), 4319–4355. DOI: 10.1016/j.ces.2011.05.050.

[42] D. G. Goodwin, R. L. Speth, H. K. Moffat, B. W. Weber. https://www.cantera.org. Version 2.4.0. **2018**. DOI: 10.5281/zenodo.1174508.

[43] R. J. Kee, M. E. Coltrin, P. Glarborg. Hoboken, NJ: Wiley, **2003**. DOI: 10.1002/0471461296.

[44] G. Weatherbee, C. H. Bartholomew. *J. Catal.* **1984**, 87 (1), 55–65. DOI: 10.1016/0021-9517(84)90167-2.

[45] D. W. Blaylock, T. Ogura, W. H. Green, G. J. O. Beran. *J. Phys. Chem. C.* **2009**, 113 (12), 4898–4908. DOI: 10.1021/jp806527q.

[46] I. Sobol'. *USSR Comp. Math. and Math. Phys.* **1967**, 7 (4), 86–112. DOI: 10.1016/0041-5553(67)90144-9.

[47] F. Abild-Pedersen, J. Greeley, F. Studt, J. Rossmeisl, T. R. Munter, P. G. Moses, E. Skúlason, T. Bligaard, J. K. Nørskov. *Phys. Rev. Lett.* **2007**, 99 (1), 016105. DOI: 10.1103/PhysRevLett.99.016105.

[48] Brynmor Mile, Diane Stirling, Michael A. Zammitt, Antony Lovell, Maurice Webb. *J. Catal.* **1988**, 114 (2), 217–229. DOI: 10.1016/0021-9517(88)90026-7.

[49] D. Beierlein, D. Häussermann, M. Pfeifer, T. Schwarz, K. Stöwe, Y. Traa, E. Klemm. *Appl. Catal., B* **2019**, 247, 200–219. DOI: 10.1016/j.apcatb.2018.12.064.

[50] C. Vogt, J. Wijten, C. L. Madeira, O. Kerkenaar, K. Xu, R. Holzinger, M. Monai, B. M. Weckhuysen. *ChemCatChem* **2020**, 12 (10), 2792–2800. DOI: 10.1002/cctc.202000327.

[51] T. A. Le, T. W. Kim, S. H. Lee, E. D. Park. *Catal. Today* **2018**, 303, 159–167. DOI: 10.1016/j.cattod.2017.09.031.

[52] H.-J. Freund, M. W. Roberts. *Surf. Sci. Rep.* **1996**, 25 (8), 225–273. DOI: 10.1016/S0167-5729(96)00007-6.

[53] O. Dewaele, G. F. Froment. *Appl. Catal., A* **1999**, 185 (2), 203–210. DOI: 10.1016/S0926-860X(99)00105-2.

[54] M. Shekhar, J. Wang, W.-S. Lee, W. D. Williams, S. M. Kim, E. A. Stach, J. T. Miller, W. N. Delgass, F. H. Ribeiro. *J. Am. Chem. Soc.* **2012**, 134 (10), 4700–4708. DOI: 10.1021/ja210083d.

[55] M. Cargnello, V. V. T. Doan-Nguyen, T. R. Gordon, R. E. Diaz, E. A. Stach, R. J. Gorte, P. Fornasiero, C. B. Murray. *Science* **2013**, 341 (6147), 771–773. DOI: 10.1126/science.1240148.

[56] L. C. Grabow, B. Hvolbæk, J. K. Nørskov. *Top. Catal.* **2010**, 53 (5-6), 298–310. DOI: 10.1007/s11244-010-9455-2.

[57] L. Znak, J. Zieliński. *Appl. Catal., A* **2008**, 334 (1-2), 268–276. DOI: 10.1016/j.apcata.2007.10.015.

[58] S. Ewald, S. Standl, O. Hinrichsen. *Appl. Catal., A* **2018**, 549, 93–101. DOI: 10.1016/j.apcata.2017.09.023.

[59] C. H. Bartholomew. *Catal. Lett.* **1990**, 7, 27–51. DOI: 10.1007/BF00764490.

[60] J. L. Falconer, A. E. Zağli. *J. Catal.* **1980**, 62 (2), 280–285. DOI: 10.1016/0021-9517(80)90456-X.

[61] J. E. de Vrieze, G. M. Bremmer, M. Aly, V. Navarro, J. W. Thybaut, P. J. Kooyman, M. Saeys. *ACS Catal.* **2019**, 9 (8), 7449–7456. DOI: 10.1021/acscatal.9b01840.

[62] A. Müller, A. Comas-Vives, C. Copéret. *J. Phys. Chem. C* **2020**. DOI: 10.1021/acs.jpcc.0c08261.

[63] W. A. Brown, R. Kose, D. A. King. *Chem. Rev.* **1998**, 98 (2), 797–832. DOI: 10.1021/cr9700890.

[64] C. Dri, A. Peronio, E. Vesselli, C. Africh, M. Rizzi, A. Baldereschi, M. Peressi, G. Comelli. *Phys. Rev. B* **2010**, 82 (16), DOI: 10.1103/PhysRevB.82.165403.

[65] J. Cai, Y. Han, S. Chen, E. J. Crumlin, B. Yang, Y. Li, Z. Liu. *J. Phys. Chem. C.* **2019**, 123 (19), 12176–12182. DOI: 10.1021/acs.jpcc.8b11698.

[66] X. Ding, V. Pagan, M. Peressi, F. Ancilotto. *Mater. Sci. Eng. C* **2007**, 27 (5-8), 1355–1359. DOI: 10.1016/j.msec.2006.06.024.

[67] S.-G. Wang, D.-B. Cao, Y.-W. Li, J. Wang, H. Jiao. *J. Phys. Chem. B.* **2005**, 109 (40), 18956–18963. DOI: 10.1021/jp052355g.

[68] J. Wellendorff, T. L. Silbaugh, D. Garcia-Pintos, J. K. Nørskov, T. Bligaard, F. Studt, C. T. Campbell. *Surf. Sci.* **2015**, 640, 36–44. DOI: 10.1016/j.susc.2015.03.023.

[69] E. Vesselli et al. *J. Am. Chem. Soc.* **2008**, 130 (34), 11417–11422. DOI: 10.1021/ja802554g.

[70] T. Li, B. Bhatia, D. S. Sholl. *J. Chem. Phys.* **2004**, 121 (20), 10241–10249. DOI: 10.1063/1.1808424.

[71] K. Christmann, O. Schober, G. Ertl, M. Neumann. *J. Chem. Phys.* **1974**, 60 (11), 4528–4540. DOI: 10.1063/1.1680935.

[72] A. D. Karmazyn, V. Fiorin, D. A. King. *J. Am. Chem. Soc.* **2004**, 126 (43), 14273–14277. DOI: 10.1021/ja047165i.

[73] A. D. Karmazyn, V. Fiorin, S. J. Jenkins, D. A. King. *Surf. Sci.* **2003**, 538 (3), 171–183. DOI: 10.1016/S0039-6028(03)00726-X.

[74] R. J. Gorte. *J. Catal.* **1982**, 75 (1), 164–174. DOI: 10.1016/0021-9517(82)90131-2.

[75] R. Demmin, R. J. Gorte. *J. Catal.* **1984**, 90 (1), 32–39. DOI: 10.1016/0021-9517(84)90081-2.

[76] B. Ruscic, D. H. Bross. Active Thermochemical Tables (ATcT) Values Based on ver. 1.122g of the Thermochemical Network. **2019**.

[77] B. Ruscic, R. E. Pinzon, M. L. Morton, G. von Laszevski, S. J. Bittner, S. G. Nijsure, K. A. Amin, M. Minkoff, A. F. Wagner. *J. Phys. Chem. A* **2004**, 108 (45), 9979–9997. DOI: 10.1021/jp047912y.

[78] C. Vogt, E. Groeneveld, G. Kamsma, M. Nachtegaal, L. Lu, C. J. Kiely, P. H. Berben, F. Meirer, B. M. Weckhuysen. *Nat. Catal.* **2018**, 1 (2), 127–134. DOI: 10.1038/s41929-017-0016-y.

"The most exciting phrase to hear in science, the one that heralds new discoveries is not "Eureka" but "that's funny..."

(Isaac Asimov)

CHAPTER 6

Quantifying the Impact of Parametric Uncertainty on Automatic Mechanism Generation for CO_2 Hydrogenation on Ni(111)

B. Kreitz, K. Sargsyan, K. Blöndal, E. J. Mazeau, R. H. West, G.D. Wehinger, T. Turek, C. F. Goldsmith.
J. Am. Chem. Soc. Au **2021**
https://doi.org/10.1021/jacsau.1c00276

Abstract

Automatic mechanism generation is used to determine mechanisms for the CO_2 hydrogenation on Ni(111) in a two-stage process, while considering the correlated uncertainty in DFT-based energetic parameters systematically. In a coarse stage, all the possible chemistry is explored with gas-phase products down to the ppb level, while a refined stage discovers the core methanation submechanism. 5,000 unique mechanisms were generated, which contain minor perturbations in all parameters. Global uncertainty assessment, global sensitivity analysis, and degree of rate control analysis are performed to study the effect of this parametric uncertainty on the microkinetic model predictions. Comparison of the model predictions with experimental data on a Ni/SiO_2 catalyst find a feasible set of microkinetic mechanisms within the correlated uncertainty space that are in quantitative agreement with the measured data, without relying on explicit parameter optimization. Global uncertainty and sensitivity analyses provide tools to determine the pathways and key factors that control the methanation activity within the parameter space. Together, these methods reveal that the degree of rate control approach can be misleading if parametric uncertainty is not considered. The procedure of considering uncertainties in the automated mechanism generation is not unique to CO_2 methanation and can be easily extended to other challenging heterogeneously catalyzed reactions.

Keywords: Rate-based algorithm, RMG, Methanation, Carbon dioxide, Global Uncertainty Analysis

Supporting information for this publication is reprinted in Appendix D.

Methanation is a promising technology for reducing CO_2 emissions while producing sustainable natural gas. From a climate-change perspective, the process is particularly advantageous when excess renewable energy is used to generate the requisite H_2 via water splitting as part of the Power-to-Gas process [1, 2]. However, volatility in renewable energy sources induces challenges on the transient operation of a catalytic reactor [3]. Given that the net reaction, $CO_2 + 4\,H_2 \rightleftharpoons CH_4 + 2\,H_2O$, is exothermic, $\Delta H_{rxn}\,(298\,K) = -164.7\,kJ\,mol^{-1}$, transient operation can lead to undesirable temperature and concentration gradients [4, 5]. Accordingly, an accurate microkinetic mechanism is essential for optimizing reactor performance.

The most commonly used methanation catalyst is Ni, due to its good performance at reasonable costs [2, 7]. Ni(111) has the highest share on a Ni crystal [8], yet its role in CO_2 methanation is unresolved, despite extensive research [9–17]. Experiments with $Ni/\gamma\text{-}Al_2O_3$ catalysts point to the higher activity of Ni(111) terrace sites, whereas experiments on Ni/SiO_2 show a higher activity of Ni(211) steps, which are also considered to be the active site for CO methanation [18]. Lozano-Reis et al. [12] combined density functional theory (DFT) calculations using the BEEF-vdW functional and kinetic Monte Carlo simulations to demonstrate that the Ni(111) surface is inactive for the CO_2 methanation; instead, they argued that the catalyst converts the CO_2 to CO in the reverse water-gas shift (RWGS) reaction, $CO_2 + H_2 \rightleftharpoons CO + H_2O$, with the CO_2^* dissociation being the rate-determining step (RDS). Vogt et al. [10] investigated the four most important Ni facets by DFT with the PBE functional. They showed in a mean-field microkinetic model that although the Ni(111) facet is not as active as the open (110) facet, it still exhibited some methanation activity. These authors identified the dissociation of HCO^* as the RDS, which is supported by Zhou et al. [15] from DFT calculations with the same functional. In addition to these models of CO_2 hydrogenation on Ni(111), other studies focused on the (reverse) water-gas shift reaction [19–21], methanol synthesis [22], and formic acid formation [23]. Apart from the general role/activity of the Ni(111) facet, the dominant reaction network for CO_2 hydrogenation has not been conclusively determined; the aforementioned computational studies disagree about important intermediates, pathways, and the RDS.

The microkinetic mechanism for CO_2 hydrogenation on Ni(111) can be developed based either on surface science experiments assisted by operando methods [9, 10, 13, 24, 25], by computational methods (*e.g.* DFT) [16, 19, 26–29], or better by a combination of both [30–32]. DFT-based microkinetic mechanisms are increasingly common due to the availability of "black-box" electronic structure codes. Although modern DFT functionals are reliable for adsorbate thermochemistry and kinetics, these calculations remain computationally expensive. Accordingly, given a "computational budget", researchers must prioritize which intermediates and transition states to investigate. This process assumes that the researcher knows *a priori* which intermediates and transition states will be important. Consequently, the mechanism generation process can be biased by the developer's expectations [33, 34]. An alternative to DFT-based mechanism development is to use approximate methods that, while less accurate, are orders of magnitude faster. One such method is applying linear scaling (LS) relations, which are based on the d-band model [35]. LS relations can accelerate the procedure [36] and are often used for catalyst screening [28, 29, 37, 38]. Although these approximate methods save computational resources, they still require expertise and intuition to develop the mechanism, and this procedure does not avoid the problem of incompleteness due to bias. An alternative to constructing mechanisms "by hand" is to use computers to propose and evaluate possible elementary reactions [39–46]. One such approach is

the automatic Reaction Mechanism Generator (RMG) of Green and coworkers [43, 47, 48]. Originally developed for gas-phase pyrolysis, RMG has been expanded to include reactions on surfaces [44–47].

The omission (intentional or unintentional) of certain reactions can be characterized as mechanistic or structural uncertainty[49]. In addition to bias, a second problem with microkinetic mechanism generation is parametric uncertainty. All of the DFT-derived parameters carry uncertainties because of the assumptions made in the exchange-correlation functional. Consequently, the DFT-derived binding energies have an uncertainty of $\pm$ 0.3 eV [32, 50–54]. These uncertainties in binding energies for different adsorbates are correlated [34, 51–53] (indeed, some degree of correlation is implicit in LS [35]). The correlation of the uncertainties can be distorted due to systematic uncertainties introduced by the specific DFT functional, *e.g.* overbinding of covalent bonds and inaccurate quantification of dispersion interactions in the PBE functional [55]. In addition to correlation among adsorbate thermochemistry, reaction kinetics are correlated as well, as exemplified by Brønsted-Evans-Polanyi (BEP) relations [56]. The uncertainty in model parameters should be propagated to the outputs of the model, *e.g.* conversion, turnover frequency (TOF) [50–52, 57, 58], and the identification of the most likely product formation pathways within a mechanism [51, 59, 60]. However, given the large uncertainty in model parameters, some pathways or intermediates might have been overlooked when creating the mechanism by hand because of the highly complex landscape of the potential energy surface [34, 53]. Therefore, it is necessary to account for the uncertainty directly in the mechanism generation procedure to provide an exhaustive analysis of all possible reactions and intermediates.

The present work aims to combine experiment, theory, and modeling to develop a microkinetic model for the hydrogenation of CO_2 on Ni(111). Instead of propagating uncertainty from a final microkinetic model to the simulation outputs, we take a novel approach and include the uncertainty directly in the mechanism generation procedure in RMG and propagate the uncertainty to the predicted mechanism. The automatic mechanism generation process is repeated 5,000 times, with each new mechanism including small perturbations in the DFT-derived parameters that can also result in mechanisms with different species and reactions. Therefore, we can discover all possible reactions and intermediates in a vast reaction network. Global sensitivity analysis (GSA) and local sensitivity analysis using the degree of rate control (DRC) [61, 62] are used to identify the most important species and reactions over the whole uncertainty range. The mechanisms are compared against experimental data for a Ni/SiO_2 catalyst in a differential fixed-bed reactor. This comparison determines a feasible set of microkinetic mechanisms in the uncertainty range that quantitatively agree with the experimental data. Combining all of the methods allows us to advance our understanding of the most important pathways for methane formation and the factors that govern the methanation activity on Ni(111). Further, applying the DRC on each unique mechanism shows how versatile the DRC can be in the uncertainty range of current DFT functionals and how much more information on the controlling factors is obtained when global uncertainty is considered. This study provides an example of the benefit of automated mechanism generation and the consideration of uncertainties to discover all the possible chemistry.

6.1. Materials and Methods

Microkinetic Mechanism Generation

Automated mechanism generation was performed with RMG (version 3.0) [47, 48]. A detailed explanation of the RMG software can be found in the work of Gao et al. [43] and the extension to heterogeneously catalyzed reactions in the publication from Goldsmith and West [44]. Only a brief explanation of the key features important for this work is provided. Elementary reactions are grouped according to reaction families, which are templates that convert the chemical graphs of reactants into products. RMG must provide thermodynamic properties and kinetics for each proposed adsorbate and elementary reaction, respectively. RMG combines a database of precompiled values, but it can supplement these databases with rules for predicting the properties of novel species/reactions. The total species population is divided into two groups: core and edge. Core species are essential to the mechanism, and only the reactants are contained in the core at the start of the process. The species in the core are iterated through the reaction families, which potentially will generate new species. RMG uses a rate-based algorithm to expand the mechanism [43, 63]. When RMG proposes a new species, that species starts off in the edge. If the net production rate of that edge species is sufficiently large (based upon user-defined criteria), it is moved from the edge to the core, and the process begins anew. Thus, RMG exhaustively considers all possible reactions that are consistent with the various reaction families for the core species; however, it only retains the species that are kinetically relevant for the conditions of interest.

Thermodynamic properties of the adsorbates on the Ni facet were estimated via LS relations [35] (see Equation (6.1)), which were recently implemented in RMG by Mazeau et al. [45], based on reference values for Pt(111) obtained via BEEF-vdW calculations in Ref. 46. The binding energy of an adsorbate is estimated via:

$$\Delta E_{\mathrm{Ni}}^{\mathrm{AX}} = \Delta E_{\mathrm{Pt}}^{\mathrm{AX}} + \gamma \left(\Delta E_{\mathrm{Ni}}^{\mathrm{A}} - \Delta E_{\mathrm{Pt}}^{\mathrm{A}} \right) \tag{6.1}$$

where $\Delta E_{\mathrm{Pt}}^{\mathrm{AX}}$ is the binding energy of the adsorbate AX^* in the Pt(111) database, where X represents any adsorbate that binds through A^*, $\Delta E_{\mathrm{Ni}}^{\mathrm{A}}$ is the binding energy of the adatom A^*, $\Delta E_{\mathrm{Pt}}^{\mathrm{A}}$ is the analogous property for Pt(111), and the slope γ is related to the degree of saturation for the adsorbate. Accordingly, RMG requires values for $\Delta E_{\mathrm{Ni}}^{\mathrm{H}}$, $\Delta E_{\mathrm{Ni}}^{\mathrm{C}}$, and $\Delta E_{\mathrm{Ni}}^{\mathrm{O}}$ for the Ni(111) facet for use in the LS procedure. These values were obtained from DFT calculations [8]. Additionally, the Pt(111) database in Ref. 46 only considered adsorbates with no more than two heavy atoms (C, N, and O); RMG can use those values to estimate the thermodynamic properties of larger adsorbates [64]. However, we anticipated that three adsorbates – CO_2^*, HCOO^*, and COOH^* – would be essential to the model, and so new DFT values were added to the Pt(111) database. DFT calculations were performed using the RPBE [65] functional in VASP [66, 67] with dispersion correction [68] and converted to thermodynamic properties of the adsorbates, as described in Ref 46. A detailed description of the DFT method is provided in the Supporting Information (SI).

As mentioned above, elementary reactions are provided in the form of templates for a certain reaction family. Kinetic parameters typically are provided as an Arrhenius fit, $k(T) = A \exp(-E_a/RT)$, where A is the pre-exponential factor, E_a is the activation energy, and R is the ideal gas constant. RMG estimates only kinetic parameters in the forward direction; the reverse rate constant is computed from the equilibrium constant, which ensures thermodynamic consistency. In the present study, we assumed

that CO_2 and H_2O adsorb associatively [9, 12, 20]. CH_4, in contrast, has two possible adsorption pathways: association to a physisorbed precursor state CH_4^* (which can then go on to dissociate on the surface) [69, 70], and direct dissociative adsorption to CH_3^* and H^* [9, 12].

RMG includes several libraries of rate constants, which have been taken from values reported in the literature or computed via DFT [47]. However, for the purposes of the present work, all the rate constants were estimated using BEP relations, with one exception, the dissociation of CO_2^*. Due to the comparatively unique structure of CO_2^*, the activation energy for CO_2^* dissociation is not well described by the general BEP relation for cleavage a C=O bond on a surface and was, therefore, included as a specific reaction in a library based on previous work [8]. By eliminating the reaction libraries in favor of the BEP relations, we can systematically quantify the effects of correlated uncertainty in thermodynamic properties (*e.g.* heats of formation) on rate constants and vary all reactions within a given reaction family [56, 71]. Accordingly, the activation energy for surface reactions is estimated using a BEP relation specific for that reaction family:

$$E_a = E_a^0 + \alpha \Delta H_{rxn} \tag{6.2}$$

where the intercept E_a^0 is the characteristic activation energy of a reaction family, and α is the dimensionless slope of the BEP, so that the activation energy scales with the heat of reaction, ΔH_{rxn}. BEP relations are organized in a tree structure with the most general relation at the top (*e.g.* generic bond fission) and more specific child nodes beneath (*e.g.* C-C bond fission). RMG climbs down the tree to the most specific node available to estimate kinetic parameters.

The present work builds upon the pre-existing reaction families for surface kinetics [44, 45], which can be categorized into adsorption/desorption, bond fission, and abstraction. All of the existing BEP values were updated based upon new DFT calculations or literature data. In particular, new values were added for the abstraction families (see SI for details). The overwhelming majority of microkinetic mechanisms consist of only adsorption/desorption and bond fission reactions; the inclusion of bimolecular-to-bimolecular reactions, such as abstraction, have been primarily neglected [33, 34] but can become important, especially at high coverage conditions [72]. As will be demonstrated in the Results section, these abstraction reactions can contribute significantly to the overall reactivity of the system. The rate constants were computing using transition state theory, with the saddle points obtained via the climbing-image nudged elastic band (CINEB) method [73] (see SI for further details). A complete summary of the reaction families, including the BEP relations used for the mechanism generation procedure, is provided in Table S1 and Figures S1 to S10. The initial conditions of the mechanism generation process were set to a stoichiometric H_2/CO_2 mixture, with a vacant Ni(111) surface, at temperatures of 573 K and 673 K, and a pressure of 1 bar. Further parameters and settings used for the generation procedure are summarized in Table S2.

6.1.1. Experiments

CO_2 methanation experiments were conducted with a 20 wt% Ni/SiO_2 catalyst produced with a spray-drying method as described in the work of Kreitz et al. [74]. A solution of colloidal SiO_2 nanoparticles with a primary particle size of 8 nm and $Ni(NO_3)_2$ was sprayed into a tubular furnace operated at 673 K using an atomizer to initiate a one-step calcination and assembly of Ni/SiO_2 nanoparticles. These

nanoparticles were collected on a filter and heat-treated at 673 K for 3 h. The experiments were conducted with a Ni/SiO_2 catalyst because the acidic surface of the silica does not adsorb CO_2 [8] and, therefore, does not participate in the methanation mechanism. Supports with basic surface sites, in contrast, such as γ-Al_2O_3 or CeO_2, can participate in the mechanism and alter pathways [16, 17, 75]. CO_2 methanation experiments were performed in a catalyst testing unit with a differential fixed-bed setup at ambient pressure with a stoichiometric H_2/CO_2 mixture diluted in 75 % Ar at a weight-hourly-space velocity (WHSV) of 100 $L_N\,h^{-1}\,g^{-1}$. A catalyst amount of 30 mg was used, which results in a length of the catalyst bed of 4 mm. The mixture was purified to remove oxygen and water contaminants. Ar was employed as an internal standard and to reduce thermal effects. A temperature-scanning experiment as described in Kreitz et al. [74] was used to investigate the methanation reaction over the entire temperature range up to 773 K. During the temperature scan, the temperature was linearly raised with a rate of 20 $K\,min^{-1}$ (see Table S3 for a summary). The product mole fraction was analyzed with a high temporal resolution using a mass spectrometer. Based on the measured exit gas concentration and using Ar as an internal standard, the CO_2 conversion, CH_4 and CO selectivity, as well as CH_4 yield were calculated. Reaction rates, turnover frequencies, and activation energy were calculated for a conversion below 20 % assuming differential fixed-bed conditions. The catalyst was characterized with transmission electron microscopy, X-ray diffraction, N_2 physisorption, H_2 and CO_2 chemisorption, and temperature-programmed desorption. Further details on the catalyst production, catalyst characterization, the experimental setup, and evaluation can be found in Ref. 8 and 76 and are omitted here for brevity.

6.1.2. Microkinetic modeling

The experimental apparatus was modeled as a plug-flow reactor (PFR) using Cantera [77], which is an open-source suite of tools for problems involving chemical kinetics, thermodynamics, and transport processes. The PFR was modeled as a series of 100 continuously-stirred tank reactors (CSTRs); the number of tanks was tested for convergence. A mean-field microkinetic model was assumed for the Ni(111) facet. All reactions were treated as reversible. Reaction kinetics were implemented in the forward direction, and the reverse rate constant was always calculated from the equilibrium constant, which ensures thermodynamic consistency. The temperature-scanning experiment was modeled by computing steady-state solutions at several temperature increments. This assumption is justified since no deviation between steady-state and transient results was observed in the experiments [74]. The parameters for the simulation are summarized in Table S3. As a simplification, no lateral interactions among the adsorbates were considered in the surface mechanism. The Python source code is available in Ref. 78.

Parametric Uncertainty in Mechanism Generation

Global uncertainty analysis (GUA) was recently added to RMG as a post-processing tool exclusively for gas-phase mechanisms [79]. The effect of parametric uncertainty on the automatic mechanism generation process itself, in contrast, has not been previously investigated. A major component of the current work is to quantify how uncertainties in the model-generation parameters (*e.g.* heats of formation, activation energies) can influence the generated mechanism and the final model predictions. The heats of formation for the gas-phase species were taken from the Active Thermochemical Tables [80, 81] and are known to within ± 0.001 eV; consequently, we assume these values to be "exact" and do not consider the impact of their uncertainty further.

For adsorbates, we assume that the binding energies (and thence heats of formation) are accurate to within $\pm 0.3\,\text{eV}$, in accordance with the DFT uncertainty [50, 51, 82]. As a simplification, we do not consider uncertainty in entropy, which is present as well [32, 54]. Although the uncertainty in the heats of formation is $\pm 0.3\,\text{eV}$, there is also a strong correlation in the uncertainty between the adsorbates [52, 53, 57]. This correlation has led to the development of the LS concept [35] (see Equation (6.1)) and the breakdown of the correlated adsorbate thermochemistry space to the descriptor species C^*, H^*, O^*. Similarly, we can break down the entire uncertainty in the adsorbate thermochemistry to the three LS descriptors as well. The binding energies for C^* and O^* are uncorrelated, as are the binding energies for O^* and H^*. However, a modest correlation exists between C^* and H^* (see Figure S12), which can be exploited to further reduce the thermochemistry space to two descriptors [28, 83, 84]. The probability density function of the binding energy of these three descriptor species can be constructed with the BEEF-vdW functional [52, 57, 85]. As an approximation, we assumed a uniformly distributed uncertainty space and no correlation between the descriptor species in the narrow uncertainty range within this work (see SI for further discussion and demonstration of lack of correlation between $\Delta E_{\text{Ni}}^{\text{H}}$, $\Delta E_{\text{Ni}}^{\text{C}}$, and $\Delta E_{\text{Ni}}^{\text{O}}$). In this work, we exploit the LS concept to propagate the uncertainty in the descriptor species to the uncertainty in the heat of formation of all adsorbates. To ensure the LS concept, we assume that all adsorbates that bind to the surface through the same element (C, H, O) should be perturbed in the same direction. This was achieved by perturbing all adsorbate reference binding energies $\Delta E_{\text{Pt}}^{\text{AX}}$ (and thence heats of formation) in the RMG thermochemistry library by $\delta E_{\text{Pt}}^{\text{AX}}$ for all adsorbates that bind through one of the descriptor species (see SI for explanation). Thus, the perturbed binding energies are given by:

$$\Delta E_{\text{Ni}}^{\text{AX}} = (\Delta E_{\text{Pt}}^{\text{AX}} + \delta E_{\text{Pt}}^{\text{AX}}) + \gamma \left(\Delta E_{\text{Ni}}^{\text{A}} - \Delta E_{\text{Pt}}^{\text{A}} \right) \tag{6.3}$$

Accordingly, we have three perturbation parameters – $\delta E_{\text{Pt}}^{\text{HX}}$, $\delta E_{\text{Pt}}^{\text{CX}}$, and $\delta E_{\text{Pt}}^{\text{OX}}$ – that adjust the heats of formation of the adsorbates in the uncertainty space. Additionally, physisorbed species (such as CH_4^*, CO_2^*, and H_2O^*) are not assumed to bind through a particular element and thus are not subjected to the same LS relations. Rather than treat each physisorbed species individually, we simply assume that the well depths for all physisorbed species are correlated, which depends on the DFT functional and the dispersion correction [55]; this approximation provides the fourth global parameter for adsorbate heats of formation, $\delta E_{\text{Pt}}^{\text{phys}}$. The range of possible values for $\delta E_{\text{Pt}}^{\text{HX}}$, $\delta E_{\text{Pt}}^{\text{CX}}$, and $\delta E_{\text{Pt}}^{\text{OX}}$ is $\pm 0.3\,\text{eV}$; the range for $\delta E_{\text{Pt}}^{\text{phys}}$ is $\pm 0.2\,\text{eV}$. Admittedly, this approach does not completely describe the true uncertainty (correlated and uncorrelated) in the heats of formation for adsorbates; nonetheless, it does capture how systematic errors in DFT-derived energies can be represented in model generation. A more detailed approach could consider a non-uniformly distributed uncertainty space according to the BEEF-vdW functional [52, 57, 85]. This approach is illustrated for CH^*, OH^*, and CO^* in the Supporting Information. As can be seen in Figure S12, our assumption of linear scaling is consistent with the BEEF-vdW ensemble error estimation; moreover, our uncertainty estimates of $\pm 0.3\,\text{eV}$ are in fact quite conservative. Still, as will be demonstrated below, this simplified approach already reveals considerable information about the mechanistic response to correlated parametric uncertainty.

Estimating the correlated uncertainty in the activation energy is an additional challenge. Activation energies within a certain reaction family (*e.g.* breaking of C-H bonds) are correlated via the relation between adsorbate thermochemistry and the activation energy, as is captured by the BEP relation [56, 71]. The uncertainties for activation energies should be larger than for binding energies. The BEP

parameters E_a^0 and α are obtained from linear regression (typically to barrier heights obtained from DFT); accordingly, these parameters should be correlated [86]. However, information on the covariance matrix is seldom available in the literature. Therefore, we did not assume a correlation between α and E_a^0. Instead, we assume that both the intercept and the slope are uncertain, and that the final activation energy is given by

$$E_\mathrm{a} = E_\mathrm{a}^0 + \delta E_\mathrm{a}^0 + (\alpha + \delta\alpha)\Delta H_\mathrm{rxn} \tag{6.4}$$

To be consistent with the uncertainty in DFT-derived binding energies, the characteristic activation energy (intercept) is perturbed by $\delta E_\mathrm{a}^0 = \pm 0.3\,\mathrm{eV}$. The slope is perturbed by $\delta\alpha = \pm 0.15$; this perturbation is conservative compared to uncertainties reported in the literature [72, 87]. Furthermore, the activation energy will be perturbed via changes to the binding energies of the reactants and products via Equation (6.3), which will change ΔH_rxn. Consequently, the total allowable change in the activation energy is larger than that of the binding energy and can vary significantly within a reaction family. As a simplifying assumption, the pre-exponential factor A was not adjusted. This restriction is rather crude, since pre-exponential factors can vary by an order of magnitude [82], but for the temperature range of interest, the uncertainties in the activation energy will have a more significant impact on the overall kinetics. Lastly, we do not assume any correlation among the reaction families. Accordingly, the total number of perturbed parameters is 65: 4 parameters for adsorbate heats of formation, 1 parameter for the activation energy of CO_2^* dissociation, and 30 BEP relations (each with 2 parameters). Overall, the approach outlined in this work for the quantification of the correlated uncertainties can be considered consistent with DFT calculations and catalyst screening studies exploiting the correlation of DFT-derived binding and activation energies.

The next step is to evaluate how perturbations to these 65 parameters within their stated uncertainty bounds affect the size, complexity, and reactivity of the resulting mechanism. This task was accomplished in two stages. In the first stage, RMG was set to build exhaustive mechanisms by using smaller (tighter) convergence criteria (see Table S2). For this stage, a total of 500 distinct mechanisms were generated by employing a quasi-random sampling of the 65 parameters within the uncertainty range. Quasi-random numbers were generated with the low discrepancy Sobol sequence [88] using the SobolEngine from PyTorch [89]. As will be detailed below, these tighter criteria resulted in relatively large mechanisms, including the production of gas-phase products in the ppb range. This set of mechanisms are referred to as "coarse".

In the second stage, the mechanism generation parameters were adjusted to build smaller mechanisms that focused more on the essential methanation kinetics; the convergence criteria were relaxed (loosened), and a maximum number of carbon atoms of 3 was imposed (see Table S2 for complete values). For this stage, a new Sobol matrix of 65×5,000 was generated, which resulted in a total of 5,000 unique mechanisms. This set of mechanisms are referred to as "fine". This dense sampling of the parameter space in the fine set will facilitate a global sensitivity analysis (GSA), described below.

6.1.3. Sensitivity Analysis

Global sensitivity analysis was performed to determine the parameters that contribute the most to the uncertainty of the output while considering the correlation among the input parameters [90]. The GSA was carried out with the UQTk package [91, 92]. Polynomial chaos expansions (PCE) were used to build

a surrogate model based on the 5,000 distinct mechanisms and the corresponding simulation results. PCEs allow analytical extraction of GSA indices via variance decomposition [93]. 4,500 model results were used to build the surrogate model with 3rd order polynomials, and 500 model results were used for the validation of the model. Total and joint sensitivity indices were determined, measuring output variance contributions one or two parameter at a time, respectively.

The sensitivity indices quantify the contribution of the 65 parameters (LS and BEP parameters) to the observable (model) output variance. Therefore, the GSA in our study provides information only on the reaction families and descriptor species but not on on the importance of a single species or single reaction. A local sensitivity analysis was performed to quantify the importance of individual species and reactions [94]. The mechanisms were evaluated with sensitivity analysis in a steady-state CSTR using the degree of rate control (DRC) [61, 62, 95] with respect to the methane formation rate, r_{CH_4}, by

$$X_{RC} = \frac{k_i}{r_{CH_4}} \left(\frac{\partial r_{CH_4}}{\partial k_i} \right) \tag{6.5}$$

where k_i is the forward rate constant of the elementary reaction i. In a brute-force (one-at-a-time) method, both forward and reverse rate constant were perturbed by 1 % for each reaction to maintain thermodynamic consistency. Additional DRC analysis was performed with respect to the stability (thermochemistry) of the adsorbates. The intermediates were stabilized by decreasing the standard state Gibbs free energy of formation $\Delta_f G$ by 0.001 eV. The degree of thermodynamic rate control of the intermediates X_{TRC} [62, 95] is given by

$$X_{TRC} = \frac{1}{r_{CH_4}} \left(\frac{\partial r_{CH_4}}{\partial \left(\frac{-\Delta_f G}{RT} \right)} \right) \tag{6.6}$$

It was ensured that the free energy of all transition states remain unchanged [62, 95]. The perturbations (1 % for rate constants, 0.001 eV for adsorbates) are assumed to be sufficiently small so that the local approximation is valid and that they are not correlated. The DRC for one mechanism has only limited meaning, given the broad range of parametric uncertainty assumed in the mechanism generation process. Accordingly, we performed the DRC analysis in Equation (6.5) and Equation (6.6) for all 5,000 mechanisms in the fine data set. As will be demonstrated below, this comprehensive DRC approach, which covers all possible combinations of parameters, identifies the global uncertainty of the DRC [96].

6.2. Results and Discussion

Mechanism Generation for CO_2 Hydrogenation on Ni(111)

The initial set of 500 generated mechanisms with the coarse settings produced considerably different microkinetic mechanisms, with large variations in overall size, possible gas-phase products and adsorbates (see Figure S15). All generated mechanisms along with the evaluation are made publicly available in Ref. 78. The number of species and reactions in the core ranged from 21 to 64 species and 20 to 450 reactions; the edge contained up to 360 more species and 1,053 different reactions. Mechanisms with many species/reactions were typically unreactive, which seems counter-intuitive at first, but it is a consequence of the flux-based mechanism-expansion procedure. The variability in mechanism size and reactivity is not a flaw of the method, nor is it unique to automated mechanism generation; instead, it is

a natural consequence of the variability in model parameters within their stated uncertainties. Different density functionals that give systematically different (but otherwise correlated) energetics will result in different mechanisms; *e.g.* the microkinetic models proposed by Vogt et al. [10] and Lozano-Reis et al. [12] also show a different number of species and reactions. The fact that most literature mechanisms contain fewer species/reactions has more to do with the computational cost of potential energy surface exploration than the intrinsic complexity of the kinetics. Mechanism developers are forced to make assumptions to reduce complexity that are not based on actual rates but rather experience, which adds bias [33]. If we performed the mechanism generation with only one set of parameters, similar to a single DFT study, we would have missed pathways and intermediates that are possible in the uncertainty range.

Figure 6.1a illustrates the full reaction network discovered from the coarse RMG settings, when all unique species and reactions from all 500 generated mechanism are merged together. RMG discovered 64 unique species and 450 reactions in the core mechanism, with an additional 426 species and 1,205 reactions in the edge. RMG successfully predicted the methanation of CO_2 with various pathways for CH_4 formation. In addition to the expected products of CH_4, CO, and H_2O, RMG predicted numerous other gas-phase species such as ethene, ethane, propane, formaldehyde, methanol, ethanol, formic acid, and acetic acid. Analysis of the edge revealed that RMG considered pathways that lead to larger alkanes, alkenes, alcohols, and acids, with a maximum chain length of C_6. Although RMG successfully found multiple gas-phase products, that does not imply that these species are produced in meaningful quantities. Simulations with all 500 mechanisms demonstrate that only CH_4, CO, and H_2O are the main products for CO_2 hydrogenation on Ni(111) within the uncertainty range (a few percent) (see Figure S16), but the selectivity between CH_4 and CO depends on the combination of parameters. The result is anticipated because Ni is a selective methanation [7, 9] or RWGS catalyst [12, 19, 20] depending on the conditions. The side products with the highest yield is ethane, with concentrations of a few ppm; the other gas-phase species had concentrations of a few ppb. Ethane and propane were also observed experimentally over Ni/Al_2O_3 [97, 98] and Ni/SiO_2 catalysts [10], which suggests that these pathways do indeed exist.

Although it would be feasible to perform sensitivity analyses for these larger mechanisms, it is neither practical nor useful. Additional gas-phase products, and the numerous surface intermediates that are necessary for their production, do not influence the main CH_4 or CO formation pathways. For the fine sampling (5,000 RMG runs), the maximum number of carbon atoms was restricted to 3 and the tolerance parameters were loosened to simplify the more detailed mechanism analysis and to concentrate on the kinetically more significant pathways. The reaction network that results from the fine generation process is illustrated in Figure 6.1b.

The mechanism for CO_2^* methanation is grouped into three main pathways: the formate path (via $HCOO^*$), the carboxyl path (via $COOH^*$), and the redox/carbide pathway with a direct dissociation of CO_2^* to CO^* [10, 12, 70]. In the formate path, CO_2^* is activated by H^* at the carbon atom. $HCOO^*$ then dissociates to formyl (HCO^*), which is further hydrogenated to hydroxymethylene ($HCOH^*$) and hydroxymethyl (H_2COH^*). The C−O bond in hydroxymethyl is then cleaved, forming hydroxyl (OH^*) and methylene (CH_2^*). In the carbonyl pathway, CO_2^* activation occurs at the oxygen atom; the resulting $COOH^*$ can then cleave either the C−O or C=O bond to yield carbon monoxide (CO^*) or hydroxymethylidyne (COH^*), respectively. Direct CO_2^* dissociation occurs in the redox pathway forming CO^*, which can desorb directly or undergo further bond fission to form surface carbon that is subsequently hydrogenated to CH_4. These three pathways are not separate mechanisms; rather, they are coupled

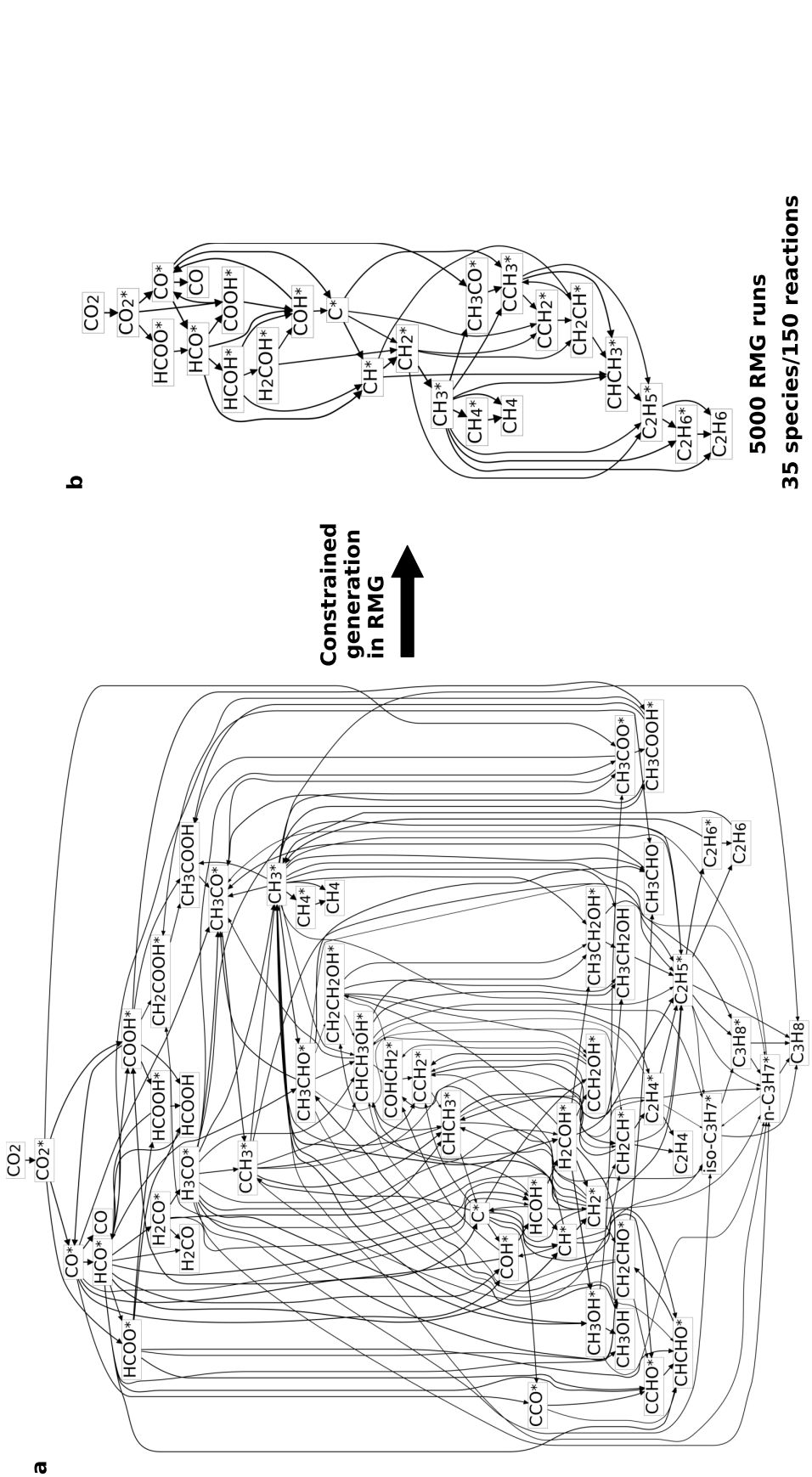

Figure 6.1.: (a) Full reaction network of the core mechanism for the hydrogenation of CO_2 on Ni(111) obtained from coarse generation settings. (b) Constrained reaction network from the fine mechanism generation process.

pathways entangled by various abstraction and dissociation reactions [10, 12]. Importantly, as depicted in Figure 6.1b, RMG found all three major CO_2^* activation routes, as well as the numerous cross-coupling reactions. The constrained mechanisms still contains the production of ethane via various C−C coupling reactions like C−CH_x, CH_x−CH_y, or CH_y−CO.

The combined reaction network discovered by RMG for all 5,000 samples within the correlated uncertainty range shows that only 35 species and a total of 150 reactions are kinetically relevant for the system. Of these reactions, 9 are adsorption/desorption, 36 are dissociation, and 105 are abstraction (see Table S9). The high number of abstraction reactions is in sharp contrast to most of the literature studies, where only dissociation reactions are considered [10, 14, 15]. Some abstraction reactions were considered by Lozano-Reis et al. [12], but usually, these types of reactions are overlooked due to the combinatorial growth of possible reactions to consider [33, 34]. The discovered abstraction reactions are not limited to the oxidative dehydrogenation reactions of R−H by O^* or OH^*, which are the ones that are most often considered in microkinetic models [12, 72]. Larger moieties can be abstracted further down the chain, which creates a whole new set of reactions that are currently not considered in the literature. The presence of these abstraction reactions nicely illustrates the full potential of automated mechanism generation.

The C_1 species discovered are consistent with prior literature mechanisms [10, 12, 14, 15, 70], with the most sophisticated study by Lozano-Reis et al. [12]. It is worth emphasizing that none of these species were included in the input, and thus RMG did not "know" to look for them. Additionally, several new abstraction reactions were predicted by RMG, which have not previously been considered for methanation. Furthermore, none of the other studies includes the formation of C_2 species, even though it is experimentally observed [10, 97, 98]. A predictive microkinetic mechanism should capture all the important pathways that lead to experimentally observable products, even if C−C coupling does not represent a major competing pathway for methanation on Ni(111) under the present conditions.

6.2.1. Microkinetic Modeling

Figure 6.2 shows the experimentally recorded concentration profiles for all species measured during the temperature-scanning experiment on a dry basis (except Ar). The carbon mass balance is always closed within ±2 %. With the current setup, it is not possible to accurately measure the H_2O concentration due to partial condensation in the transfer lines. The experiments show a starting temperature for the CH_4 formation around 500 K, followed by a pronounced CO peak with a maximum at 550 K. A maximum CH_4 formation rate is observed at a temperature of 650 K, with a CH_4 selectivity of 97 %. The CH_4 concentration decreases at higher temperatures, whereas the CO concentration increases according to thermodynamic equilibrium that is reached in the experiment at temperatures beyond 700 K. An activation energy of 84 kJ mol^{-1} was determined, which is comparable to other Ni/SiO_2 catalysts [10, 74, 99, 100]. Results from the microkinetic model generated by RMG with the reference settings show a significantly lower activity at lower temperatures. CH_4 formation starts at 600 K and reaches the maximum rate at 700 K. The production of CO starts at a temperature of 650 K and directly reaches the equilibrium concentration.

Also included in Figure 6.2 are the reactor simulations using the 5,000 different mechanisms. All generated mechanisms adhere to the thermodynamic constraints, which was confirmed according to literature guidelines [101, 102] (see SI). The predicted profiles range from almost no CH_4 formation

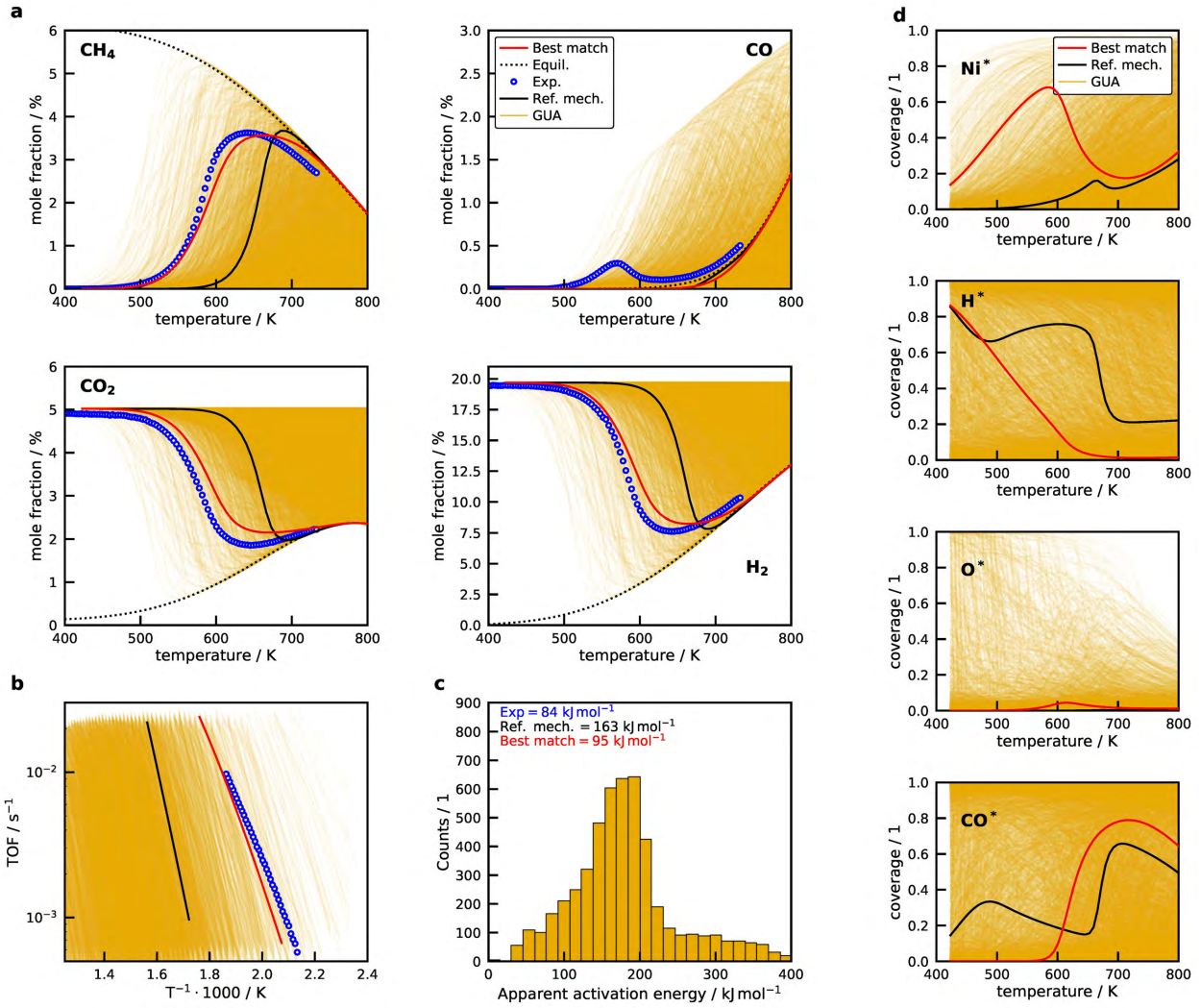

Figure 6.2.: (a) Comparison of measured (open blue circle) and simulated (lines) mole fractions (on dry basis) for the temperature-scanning experiment using the microkinetic models generated by RMG. The dotted black line corresponds to the thermodynamic equilibrium, the solid black line to the generated reference mechanism, and the solid red line to the mechanism with closest agreement to the data. The gold shaded area contains the model solutions of all generated mechanisms, where each mechanism is represented by a solid line. A higher intensity indicates that more simulation results fall into this area. (b) Comparison of the measured and predicted TOFs. (c) Histogram of apparent activation energies calculated from the slope of the TOFs. (d) Simulation results for the four species with highest coverage. The black line is the reference mechanism and the red line is the microkinetic model with closest agreement to the data.

even at high temperatures to an increased activity at low temperatures, with maximums of 5 % at 600 K. Figure 6.2b presents the turnover frequency (TOF) for the system, which was calculated from the average CH_4 formation rate and the amount of exposed Ni surface atoms in the PFR assuming differential conditions. Figure 6.2c presents a histogram of the corresponding apparent activation energy determined from the slope of the TOF. Most of the mechanisms exhibited very low activity, as seen by the dense cluster of lines at higher temperatures in the TOF plot and the broad range of comparatively high activation energies. However, there are also combinations of parameters which result in a very high methanation activity. This distribution in activity is consistent with the Sabatier principle; high activity

is only obtained when key intermediates are bound to the catalyst neither too strongly nor too weakly. The broad range in reactivity is a consequence of the $\pm 0.3\,\mathrm{eV}$ uncertainty in energies (even under consideration of correlation) obtained from electronic structure calculations, which has been pointed out by other studies as well [52, 58]. In other words, for some combination of parameters, the Ni(111) facet is inactive for methanation but only produces CO via the RWGS reaction, and is consequently not the active site for methanation [12]. In contrast, the Ni(111) surface exhibits quite a high methanation activity for other parameter combinations, also in agreement with the literature [10, 15], and could, therefore, be the active site. The correct quantification of correlated uncertainties in the DFT-derived parameters in this study explains the opposite observations and conclusions from Lozano-Reis et al. [12] and Vogt et al. [10] on the activity of Ni(111). Accordingly, it is difficult to establish the importance of the Ni(111) facet for CO_2 methanation with confidence, given the current parametric uncertainty of DFT data, which implies that a DFT study cannot be more conclusive either.

Figure 6.2d summarizes the surface site fractions for the vacant site (Ni^*) and the three adsorbates with the highest coverages (H^*, O^*, CO^*). Profiles for other adsorbates, as well as for CO_2 conversion, CH_4 selectivity, and CH_4 yield are provided in the SI. Depending upon the particular combination of parameters, the surface can be entirely vacant, completely blocked by either H^* or CO^*, or in a few instances, covered by O^*. This range in coverage suggests that it is challenging to make *a priori* assumptions regarding the most-abundant surface intermediates (MASI) with any confidence for this system, given the current accuracy of DFT-derived models, but it can be limited to these three species. The predicted coverages of the reference model are in contrast to the results reported by Vogt et al. [10], who report a Ni(111) surface that was completely saturated with CO^*, but they did not include the possibility of CO^* desorption. In contrast, Lozano-Reis et al. [12] obtained a nearly vacant Ni(111) surface with just around 10 % H^* coverage. Heine et al. [13] observed CO^* on the Ni(111) surface at elevated temperatures during CO_2 methanation, which agrees with the model predictions.

From the computed profiles in Figure 6.2a, it is possible to identify the subset of mechanisms in closest agreement with the experimental data by computing the mean-absolute percentage error (MAPE) for the measured and predicted gas-phase concentrations of CH_4, CO_2, H_2, and CO. The mechanism that had the lowest MAPE for the predictions of all four species against the experimental data is shown as a red line in Figure 6.2. Additionally, there are multiple combinations of parameters that are within 30 % of the lowest MAPE. This ensemble of feasible mechanisms, along with the closest match, is illustrated by the shaded pink region in Figure 6.3a. It should be emphasized that the red line in Figure 6.2 and 6.3, although in quantitative agreement with the measured data, is not the result of an optimization algorithm. All the parameters of the microkinetic model were varied randomly in the global uncertainty assessment within their stated uncertainty ranges consistently with their correlated uncertainties. Admittedly, the approach of drawing a few thousand quasi-random samples from a parameter space and determining the MAPE to the experimental data can be considered as a very crude fitting procedure. The agreement with measured concentrations certainly could be improved by optimizing the pre-exponential factors, optimizing the binding energies and activation energies (within a narrower range), and accounting for coverage dependence [31, 32], but such an attempt at optimization is beyond the scope of the present work. Within the correlated uncertainty space of the microkinetic model parameters for the Ni(111) facet, there are feasible sets that can describe the CO_2 methanation experiments on the Ni/SiO_2 catalyst. Consistent with the guidelines for mechanism analysis outlined by Bhandari et al. [32], with the additional constraints of correlated uncertainties, Ni(111) can be

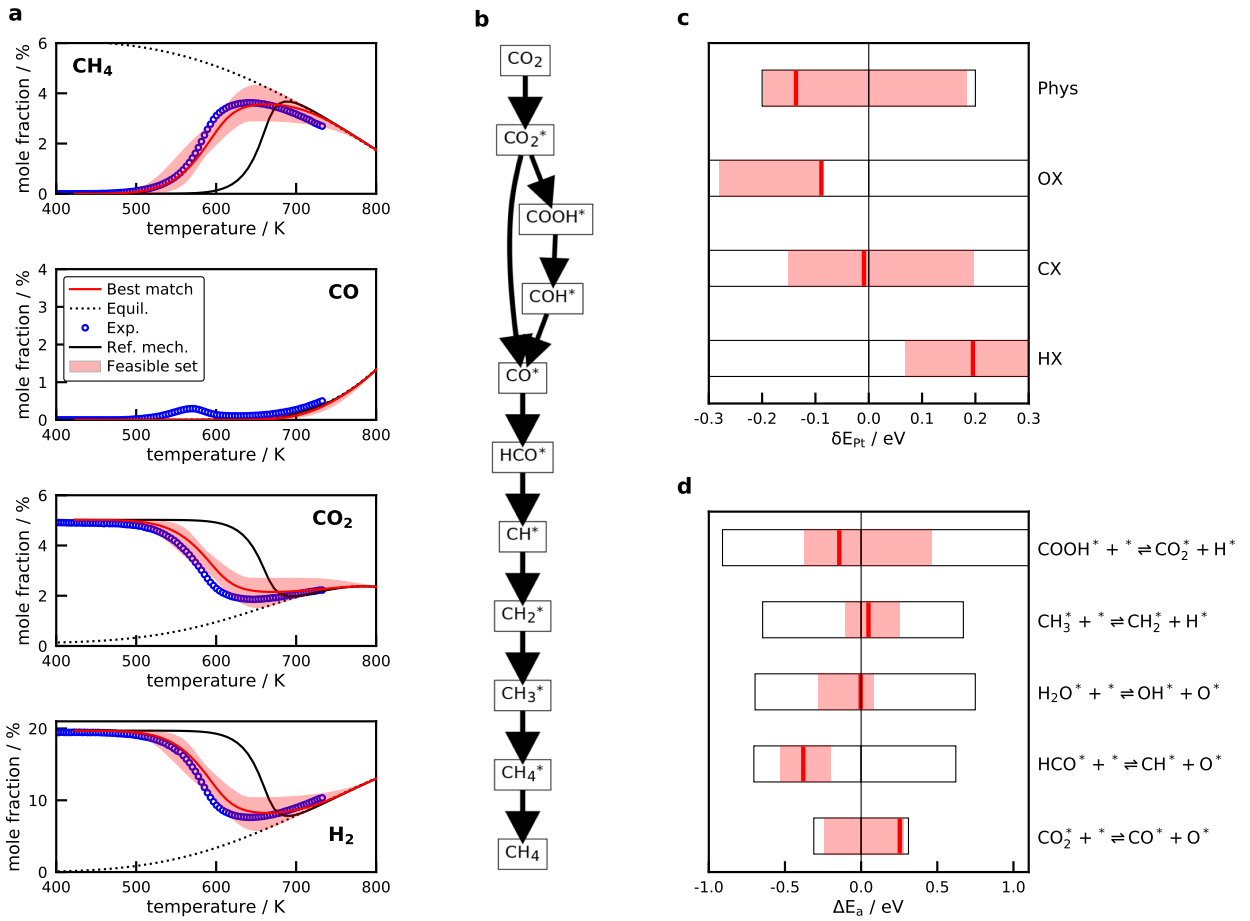

Figure 6.3.: (a) Comparison of the experiments with the mechanisms with the closest agreement to the data from the global uncertainty analysis. The solid black line is the base-case mechanism; the solid red line is the mechanism with the lowest MAPE, and the shaded pink region contains the mechanisms that are within +30 % of the lowest MAPE (the "feasible set"). (b) CH_4 formation pathways of the mechanism with the lowest MAPE compared to the experimental data. Only the intermediates and pathways that contribute significantly to the CH_4 formation rate are displayed. (c) Perturbation parameters δE_{Pt}^{AX} for the LS descriptors that specify the uncertainty in the thermochemistry and (d) the perturbation in the activation energies for the most important reactions based on the sensitivity analysis. The black box shows the possible range of values (uncertainty) and the pink area encloses the values from the feasible sets. The red line reports the parameter of the best match.

considered as an active site for the CO_2 methanation, and we shift our attention to the possible methane formation pathways to gain insights into the methanation mechanism.

The essential pathways for the methanation of CO_2 on Ni(111) for the mechanism in closest agreement to the data are illustrated in Figure 6.3b. At a temperature of 573 K, 75 % of CO^* is produced via the direct dissociation of CO_2^*, and the remaining 25 % comes from various reactions in the carboxyl path, which contradicts conclusion from Vogt et al. [10], who argued that this path does not contribute to CH_4 formation. The only significant source of CH^* (and thus ultimately CH_4^*) is from the dissociation of HCO^*, $HCO^* + CH^* \longrightarrow O^*$. According to the DRC analyses for all 5,000 mechanisms, there is no combination of parameters in which the formate path, $CO_2^* \longrightarrow HCOO^* \longrightarrow HCO^*$, is a significant source of HCO^* (see SI for details). Instead, the overwhelming majority of HCO^* is produced via hydrogenation of CO^*, $CO^* + H^* \longrightarrow HCO^*$, where CO^* is produced via the redox and carboxyl path.

This result is in agreement with Heine et al. [13], who did not observe $HCOO^*$ during CO_2 methanation on Ni(111) in operando XPS studies. Although $HCOO^*$ has been observed in some spectroscopic studies [9, 10, 103, 104] during CO_2 hydrogenation on Ni, our findings support the conclusion that $HCOO^*$ is a spectator species [19, 103, 104].

Figure 6.3c presents the best match and feasible set for the four parameters that govern the uncertainty of the correlated binding energies. The results suggest that all mechanisms in the feasible set require an increase to the heat of formation for H^* (*i.e.* destabilize), and a decrease to the heat of formation of species that bind through oxygen. Variability in the binding energy of adsorbates that bind through carbon, in contrast, is not as important. Figure 6.3d presents similar results for the top five reactions (see Sensitivity Analysis); the most significant deviation from the base case is for HCO^* dissociation, where the feasible set is more tightly clustered around a reduction in the activation energy of 0.4 eV.

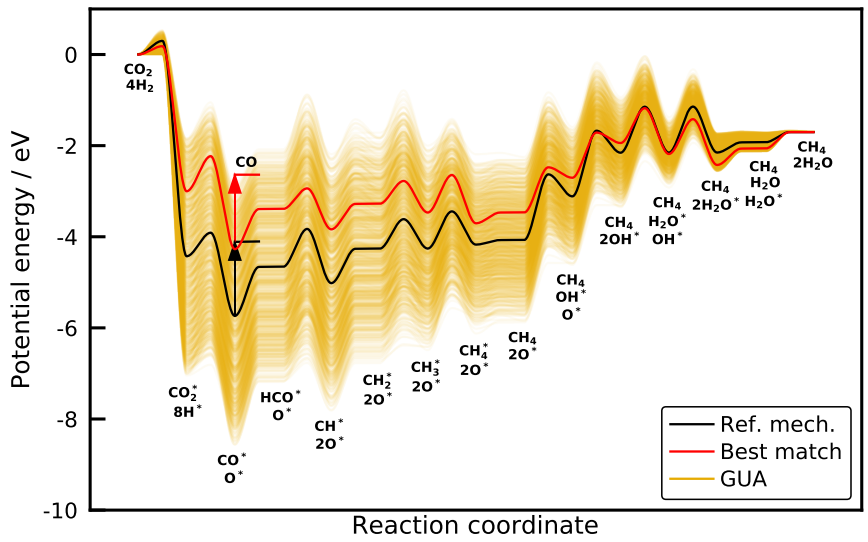

Figure 6.4.: Potential energy diagram for the most dominant CH_4 formation pathway. The balancing H^* atoms are omitted for clarity after the adsorption step. Only a reduced number of 1000 mechanisms is displayed for clarity.

A subset of the potential energy diagram that highlights the main pathway is presented in Figure 6.4. The individual yellow lines represent different possible mechanisms. The large spread in possible values in the initial portion of the potential energy diagram is due primarily to the fact that there are 8 H^*. Adsorbates that bind through carbon (*i.e.* C^*, CO^*, HCO^*) represent the various minima for the first half of the diagram. These minima are all shifted by the same perturbation according to the usage of the LS relation for the propagation of the uncertainty [105]. The difference between the base case (solid black line) and the best match (solid red line), combined with the results from Figure 6.3d, indicates that the majority of the change from the black line to the red line comes from the weakening of the H^* binding energy by 0.2 eV; the binding energies for adsorbates that bind through carbon are not changed significantly. Adsorbates that bind through oxygen (*i.e.* O^*, OH^*) represent the second half of the diagram. Here we see that a decrease in the heats of formation (stabilizing) of 0.1 eV of species that bind through oxygen is needed to improve the agreement. The parameterized mechanism of this reduced network is provided in Table S10 and the complete mechanism in Table S11.

As suggested by Figure 6.4, H^* and CO^* are most likely to be the MASIs on the Ni(111) surface, which also agrees with the simulation results. High activation barriers are obtained for HCO^* formation and

dissociation, as well as the hydrogenation of O^* and OH^*. CO^* does not desorb in the feasible set because the desorption barrier is significantly higher than the hydrogenation to HCO^*. There are several routes for the activation of CO_2^* in the carboxyl pathway that have comparable barriers (see Table S10 and Figure S21 for the free energy surface); either via reaction with H^*, or CO_2^* can abstract a H atom from OH^* or H_2O^*. After the creation of $COOH^*$, there are two possible routes with comparable free energy barriers for its decomposition, with the cleavage of C=O or C−OH. The formation of CO from COH requires an additional step, and the oxidative dehydrogenation of COH^* provides a significantly lower barrier than the direct dissociation, in agreement with results from the activation of CO on Co in the Fischer-Tropsch synthesis [27]. BEP relations providing barriers for bimolecular reactions are coupled to the thermochemistry of multiple species, so the uncertainty range of the barrier can be large. Consequently, the activity of these pathways, which are all relatively close in free energy, can contribute to various extents to the CH_4 formation in the parametric uncertainty range. Figure 6.4 and Figure S21 show that it is currently difficult to predict a certain path within the given accuracy of the present DFT functionals [51, 59, 60].

Although the microkinetic model can accurately predict the measured CO_2 conversion and CH_4 yield, it is currently not able to accurately predict the correct selectivities towards CH_4 and CO at low temperatures (see Figure 6.2a and Figure S18). Some simulations show a CO desorption peak at low temperatures, but this can only occur if the binding energy of CO is lowered, so that CO^* can partially desorb from the catalyst surface before the activation barrier of the step consuming the CO^* is overcome. A likely explanation for the discrepancy in the selectivity is coverage dependence [106]. As mentioned above, no coverage effects were considered in the present study. However, adsorbates like CO^* or O^* show repulsive interactions, which destabilize their binding energies [20, 107]. In general, including coverage effects will affect the binding strength of species and transition states and can significantly alter the potential energy surface [32, 53, 82]. Thus, we suspect that the inability of our model to describe the CO desorption peak is a consequence of neglecting coverage effects, not due to missing kinetic pathways. The inclusion of coverage effects directly in the mechanism generation procedure is the aim of future studies.

6.2.2. Analysis

In a microkinetic model, not all species and reactions are equally important; typically, the variability of the output is determined by just a few species and reactions. The total sensitivity coefficients for the CH_4 concentration, determined from the polynomial chaos expansion, are displayed in Figure 6.5a. Of the 65 parameters that were varied in the global uncertainty analysis, the parameter with the largest sensitivity index is for δE_{Pt}^{HX}, which corresponds to the heat of formation of H^*. This result is unsurprising, given that hydrogenation reactions are critical in methanation and that the heat of formation of H^* affects activation barriers via BEP relation and reverse rates via the equilibrium constant. The next most important parameters are δE_{Pt}^{OX} and δE_{Pt}^{CX} for the heats of formation of adsorbates that bind through oxygen and carbon, respectively. The larger influence of thermochemistry than kinetics was observed in other studies as well [52].

The fourth most important parameter is the reference activation energy for the reaction family for the dissociation of HC=R double bonds. This family provides kinetics for the dissociation of the C=O bond in HCO^*, which many studies consider to be the RDS [10, 15]. Moreover, this reaction is the

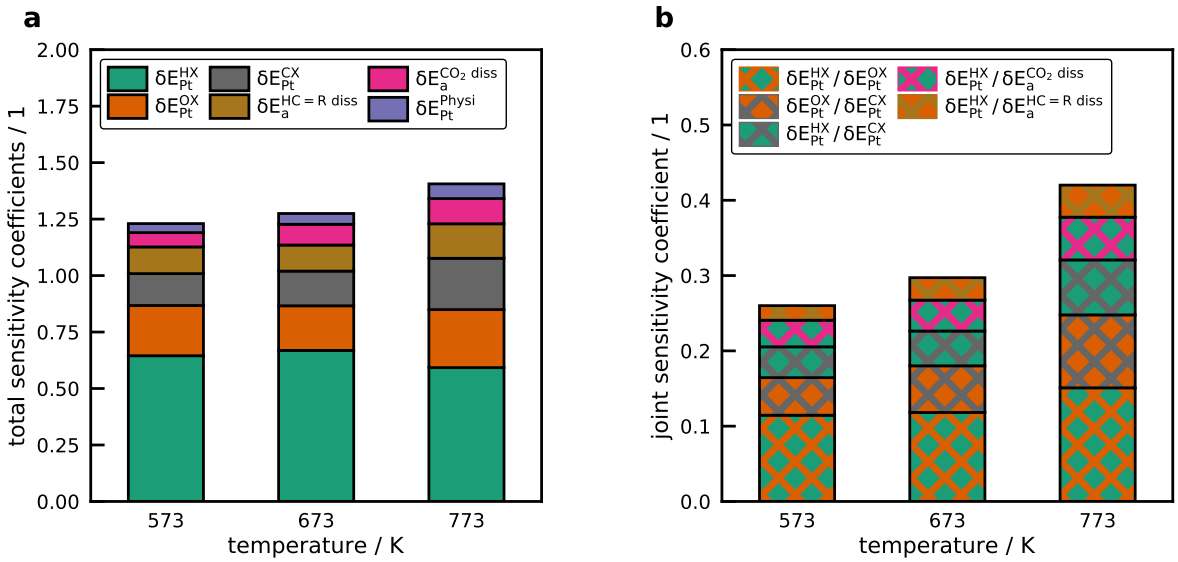

Figure 6.5.: (a) Total sensitivity coefficients for the 6 most influential input parameters on the uncertainty of the CH_4 concentration at different temperatures. (b) The joint sensitivity coefficients with the highest values. The hash combines the pair of colors from the total sensitivity coefficients.

most important pathway for CH^* formation observed in the mechanisms with best agreement to the experiments (see Figure 6.3b and Figure 6.4). The next most sensitive reaction is CO_2^* dissociation, which is also thought to be rate controlling [12].

In a complex microkinetic model, there will be higher-order interactions among the parameters, which are further amplified by the coupling of the thermochemistry with the activation barriers in the BEP relations. These higher-order interactions are captured by the joint sensitivity indices from the PCE method and displayed in Figure 6.5b. The highest joint sensitivities are caused by H^* in combination with O^*, C^*, CO_2^* dissociation, and the HC=R dissociation family.

Figure 6.6 summarizes the results of the degree of rate control analysis. The black boxes in Figure 6.6a-b represent the range of possible DRC values at 573 K for reactions and species, respectively, that were obtained for all 5,000 mechanisms. Also included inside each box is the DRC value for the reference mechanism (vertical black line), the best match (vertical red line) and the ensemble of feasible mechanisms (shaded pink region). According to the DRC analysis, the most important reactions are the dissociation of CO_2^* and the dissociation of the C=O bond in HCO^*, in agreement with the results from the GSA. The results in Figure 6.6a-b nicely highlight the implicit assumptions in the DRC approach and associated challenges that it entails for the current accuracy of DFT-based microkinetic models. For the overwhelming majority of parameter combinations, the dissociation of HCO^* has a positive DRC, implying that increasing the rate constant will increase the rate of CH_4 production. For the feasible set, however, it is zero. The dissociation of CO_2^*, in contrast, has a X_{RC} that ranges from -3 to +1. Additionally, abstraction reactions that convert CO_2^* to $COOH^*$, which are frequently neglected, are rate controlling for some parameter combinations. Equally important, the actual values of X_{RC} for a given reaction can vary considerably. Vogt et al. [10] and Zhou et al. [15] report that the dissociation of HCO^* is the RDS on Ni(111), whereas Lozano-Reis et al. [12] state that the dissociation of CO_2^* is the RDS. The present results suggest that the choice of RDS is, in fact, highly dependent on the microkinetic parameters (and thus the DFT method through which they were obtained). Indeed, both of these

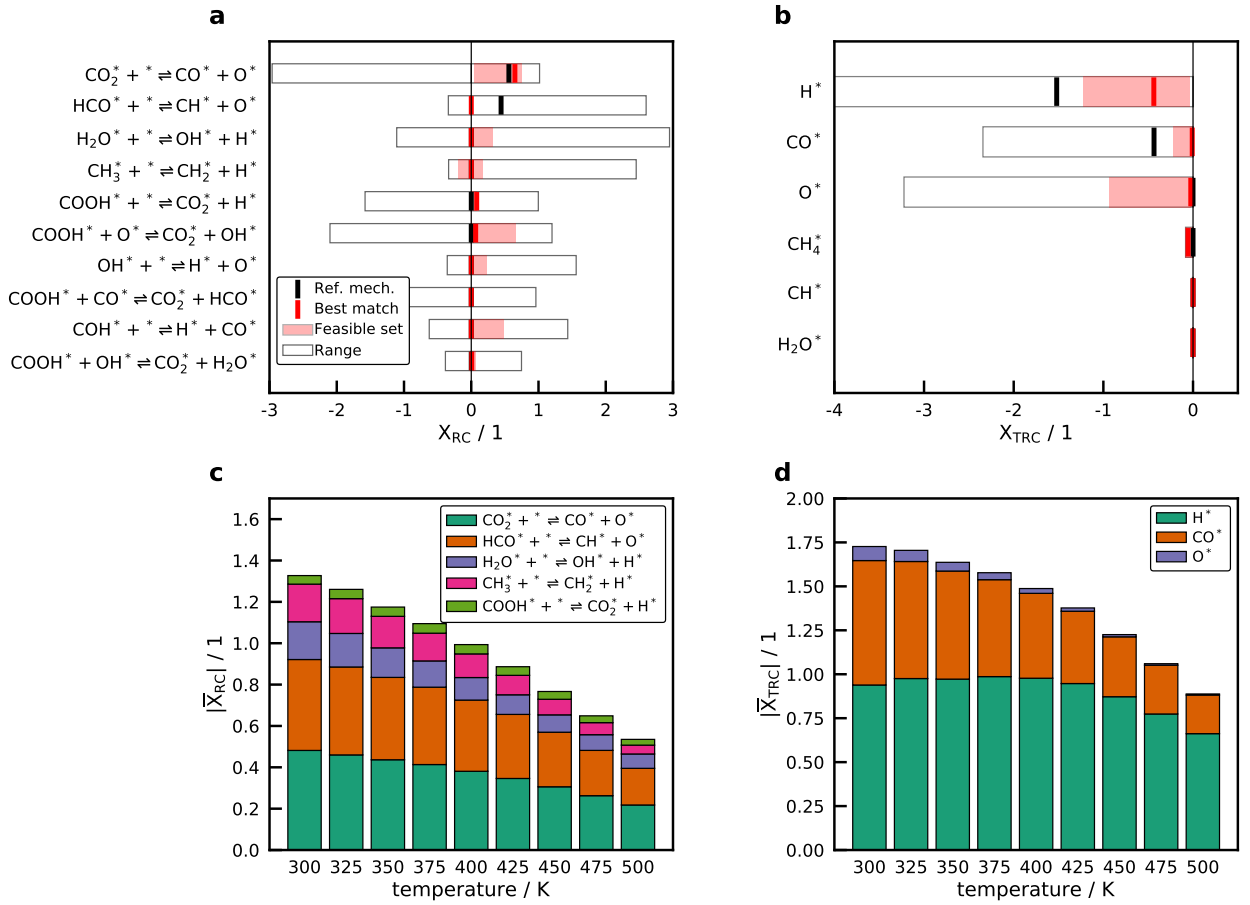

Figure 6.6.: DRC for (a) reactions and (b) adsorbates at 573 K. Only the most important reactions/species are presented, with the reactions/species with the highest absolute average DRC at the top. The black box represents the range of the DRC values for all possible mechanisms; the black line is the reference mechanism; the red line and pink shaded region are the best mechanism and feasible set, respectively. Averaged absolute (c) DRC and (d) thermodynamic DRC at different temperatures.

reactions and many others can be rate-controlling, depending upon small perturbations of parameters within a narrow uncertainty range. For the best match mechanism, CO_2^* dissociation has the largest X_{RC}.

From the thermodynamic DRC, we obtain that the most important species are CO^*, H^*, O^*, while all other adsorbates are never rate controlling over the entire uncertainty range (see Figure S25). This can be explained by the correlation between the thermodynamic DRC and the coverage of the adsorbates [62, 108, 109]. CO^*, H^*, and O^* are the only adsorbates which exhibit a high coverage in the given uncertainty range (see Figure 6.2d). More specific, O^* shows only a high coverage for few combination of parameters and the surface is predominantly covered by either H^*, CO^*, or a combination of both.

In the absence of experimental data, it would not be possible to determine *a priori* which mechanism will provide the closest description of reality – let alone speculate as to the reaction/species with the highest DRC. Accordingly, averaging over the DRC of all mechanisms is a compelling way to predict how the mechanism is likely to respond in the absence of other information. Additionally, it prioritizes which rate constants or thermochemistry should be refined. Figure 6.6c,d plot the average of the absolute value of the DRC at different temperatures for reactions and species, respectively. These figures demonstrate

that 4 reactions and 3 species have a high DRC over the entire temperature range. Of these results, the CO_2^* and HCO^* dissociation, together with heats of formation for H^* and CO^*, are most important, which is consistent with the GSA and the literature [10, 12, 15].

The DRC analysis shows that from the complex reaction network with 150 elementary reactions and 35 species, only a handful have high DRC over the entire uncertainty range and the rest are never rate-controlling (see Figure S24-S25). Thus, every effort should be made to refine the kinetic and thermodynamic parameters for these reactions and species as accurately as possible. Refinement of the parameters can be conducted with more accurate DFT approaches [110] or based on experiments from single crystals [32]. As an example, heats of formation of H^* and CO^* on Ni(111) are available from single crystal studies [111] and can be incorporated in a follow-up study. However, comparing Figure 6.6c,d with Figure 6.6a,b highlights how varied the DRC results can be, depending upon the structure of the underlying mechanism. Our results do not question the DRC concept, because it has a precise meaning for each of the generated mechanism. Rather, these results demonstrate that within the relatively narrow uncertainty range, correlated perturbations significantly alter the potential energy surface, thereby resulting in different rate-controlling reactions or intermediates. Determination of the DRC from a single DFT-derived model is, therefore, not conclusive.

A key finding in Figure 6.6a-b is that critical reactions (CO_2^* and HCO^* dissociation) and species (H^* and CO^*), can exhibit enormous variability in DRC, depending upon the model parameters. Figure 6.7a-c illustrates this variability in X_{TRC} for H^* and X_{RC} for the CO_2^* and HCO^* dissociation over the variation in the uncertainty range. If we focus on the DRC for CO_2^* dissociation (6.7b), we observe two broad clusters. For negative values of ΔE_{a}, the X_{RC} tend to be clustered around 0.0 (because a low barrier leads to a higher rate), and for positive values of ΔE_{a}, the X_{RC} tend to be clustered around 1.0. However, in both cases, there is considerable scatter. Moreover, the feasible set (represented by the red squares) spans the entire horizontal range, with no clearly discernible trend. The results for HCO^* dissociation (6.7c), in contrast, show more structure. The results from the feasible set are all tightly clustered around $-0.6 < \Delta E_{\mathrm{a}} < -0.2$, which result in $X_{\mathrm{RC}} = 0$. When the activation energy for this reaction is increased, the reaction shifts from $X_{\mathrm{RC}} \approx 0$ to $X_{\mathrm{RC}} \approx 1$ and it becomes the RDS. Another clear trend is obtained for the thermodynamic DRC for H^* (Figure 6.7a); as H^* is stabilized on the surface, it has an increasingly inhibiting effect.

By combining these results with the joint sensitivity coefficients from Figure 6.5b, we can begin to see what other parameters contribute the most to the scatter in Figure 6.7a-c. Specifically, for both reactions, the parameter with the highest joint sensitivity coefficient is $\delta E_{\mathrm{Pt}}^{\mathrm{HX}}$ (and therefore the heat of formation for H^*). Variation in X_{TRC} for H^* in Figure 6.7d is mostly vertical; it goes from 0 to -2 as $\delta E_{\mathrm{Pt}}^{\mathrm{HX}}$ is decreased (and thus H^* is made more stable), but $\delta E_{\mathrm{Pt}}^{\mathrm{OX}}$ has very little effect. The surface is covered in H^* under these conditions (see Figure S33), which agrees with observations that X_{TRC} is linked directly to surface coverage [62, 108]. Figure 6.7e,f present heatmaps for X_{RC} of CO_2^* and HCO^* dissociation, respectively. In Figure 6.7e, the values of $X_{\mathrm{RC}} \approx 1$ are generally clustered between $-0.3 < \delta E_{\mathrm{Pt}}^{\mathrm{HX}} < -0.1$, suggesting that CO_2^* dissociation is only rate controlling when H^* is stabilized on the surface. At these conditions the surface is covered in H^* and lacks CO^*, which is why the production of CO^* via CO_2^* dissociation is rate-controlling. However, the HCO^* dissociation is rate controlling over the entire uncertainty range of $\delta E_{\mathrm{Pt}}^{\mathrm{HX}}$ (Figure 6.7f). Figure 6.7d-f clearly indicate that the DRC can change from insensitive to rate controlling within the range of a few meV.

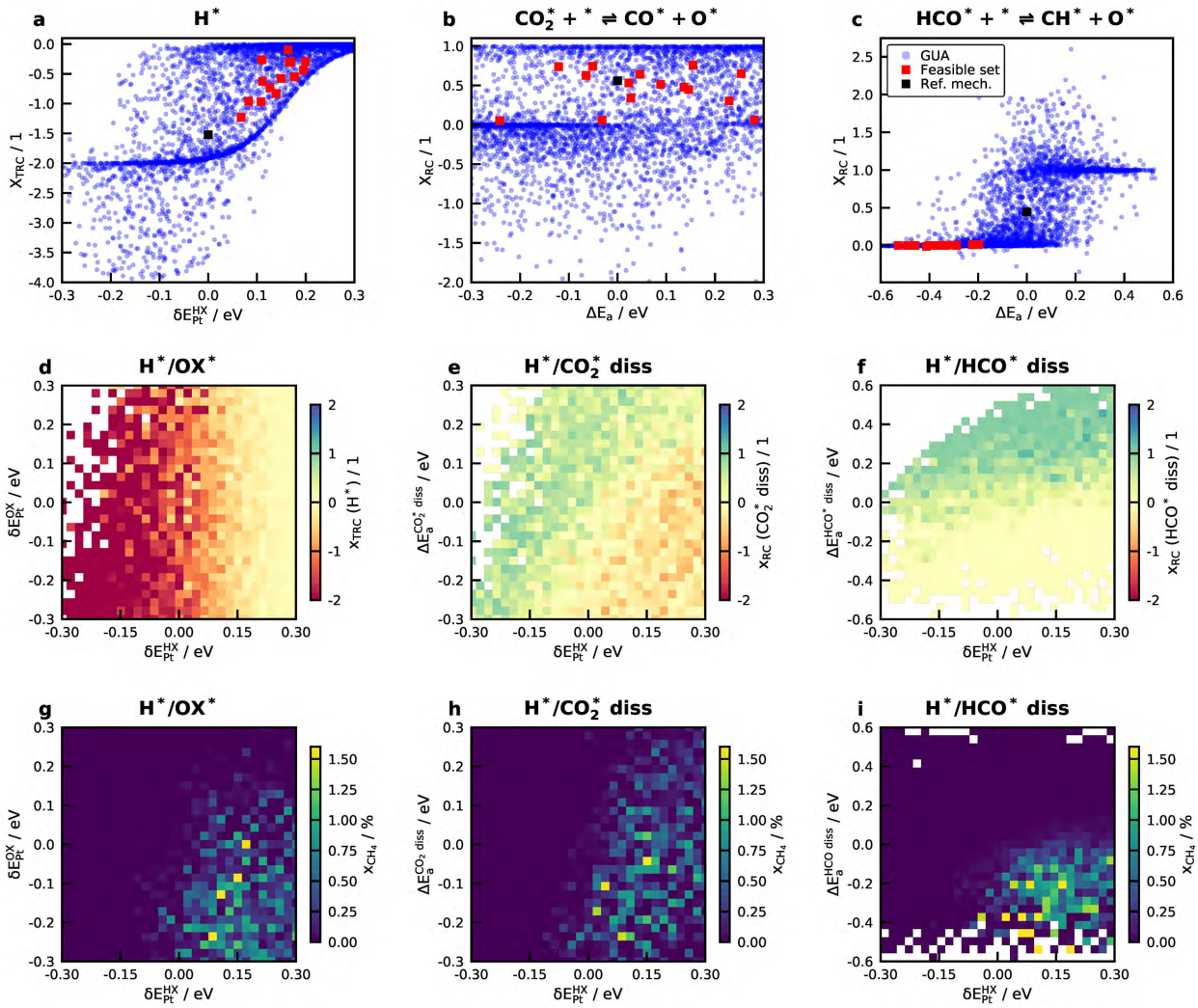

Figure 6.7.: Scatter plots for (a) X_{TRC} of H^* versus change in binding energy, (b) X_{RC} of CO_2^* dissociation, and (c) X_{RC} of HCO^* dissociation versus change in activation energy. Red squares are the values for mechanisms in the feasible set, and the black square is the reference mechanism. (d) Heatmap for X_{TRC} of H^* over δE_{Pt}^{HX} and δE_{Pt}^{OX}. Heatmaps for the DRC for the (e) CO_2^* and (f) HCO^* dissociation as a function of their change in activation energy and δE_{Pt}^{HX}. Heatmaps for CH_4 mole fraction as a function of δE_{Pt}^{HX} and (g) δE_{Pt}^{OX}, h) activation energy of CO_2^* dissociation, (i) activation energy of HCO^* dissociation. The data are sorted into a 30×30 grid and all sensitivity coefficients or CH_4 mole fractions are averaged in these bins. All results are for a temperature of 573 K.

Figure 6.7g-i present heatmaps for CH_4 mole fraction as a function of δE_{Pt}^{OX} as well as the barrier for CO_2^* and HCO^* dissociation in combination with δE_{Pt}^{HX}. Other key parameters are reported in the SI. In Figure 6.7h for CO_2^* dissociation, we can see a vertical area where CH_4 formation is feasible, which is when H^* is destabilized, without a clear dependence on the activation barrier. Figure 6.7i shows that CH_4 is only produced when H^* is destabilized and the barrier for HCO^* dissociation decreased. When the activation barrier for the HCO^* dissociation is increased, no further conversion pathways for CO^* are available, and the surface will be poisoned by CO^*, thereby inhibiting H^* adsorption. Since the activation barrier is determined from the BEP, these points coincide with the pattern for the O^*/H^* dependence (see Figure 6.7g). A decrease in O^* heat of formation lowers the heat of reaction and thus the activation barrier. Looking at the scatter plot (Figure 6.7c), we can now state that HCO^* dissociation is never

rate-controlling when CH_4 is formed, which is why it has also a small DRC for the best cases, and other reactions are rate controlling instead, *e.g.* CO_2^* dissociation for the best match (see Figure 6.6a). These results highlight a severe limitation of the DRC analysis given the large uncertainty of DFT parameters. This does not question the accuracy or meaning of the DRC concept. It simply shows that the factors which control the methanation activity locally (determined with DRC) are not the same as the global properties that truly determine the methanation activity. The global uncertainty assessment indicates that the HCO^* dissociation in combination with H^* and O^* binding energy are the true factors that control the methanation activity of the Ni(111) facet. This can also be seen in Figure 6.3c-d, where these three parameters show a clear grouping of values for the feasible set of parameters that agree well with the experimental data. It indicates that these parameters need to be in a certain range to predict the experiments. The modeling results show that only when H^* is destabilized can other important intermediates (*e.g.* CO^*, O^*) cover the surface and the destabilization decreases several activation barriers. A high CO^* and O^* coverage favor CH_4 production; the H^* surface site fraction for the best cases are actually rather small (see Figure S19). Furthermore, we have seen that all steps with high DRC values are part of the reduced methanation mechanism. Based on our insights gained from the global sensitivity analysis and the global uncertainty of the DRC, we can further hypothesize that the reduced microkinetic model (see Figure 6.3b and Table S10) comprises all the relevant steps and species that determine the methanation activity over the entire uncertainty range, making it the most likely methanation mechanism for the Ni(111) facet.

Finally, we wish to emphasize that the purpose of this analysis is not to provide a definitive mechanism for CO_2 methanation on Ni. In fact, it is difficult to state conclusively whether or not Ni(111) is the active facet. This is neither a flaw in this study, nor the applied methods, nor automated mechanism generation in general. Since all assumptions on the uncertainty in this study represent only the accuracy of present DFT functionals [32, 50–54], it indicates that it is not possible for a pure DFT study to conclusively determine the activity of the Ni(111) facet either. This is evidenced by Lozano-Reis et al. [12] and Vogt et al. [10], who reach completely opposite conclusions while the only difference is the applied DFT functional. Moreover, this result is not unique to methanation; a large variation in activity was also observed by Sutton et al. [52, 58] for ethanol steam reforming or Döpking et al. [50] for the oxygen evolution reaction when uncertainty is considered. However, with the automated mechanism generation, we were able to derive a complete and unbiased mechanism including all the possible chemistry as well as to unravel the reactions and parameters that control the activity over the entire uncertainty range (see Figures 6.3, 6.6 and 6.7), which cannot be done with typical DFT studies.

Feasible sets of microkinetic mechanisms exist within the uncertainty range that agree with the experimental data with remarkable predictive power, but self-consistent sets of parameters can yield virtually every conceivable outcome within this confined uncertainty space of $\pm$ 0.3 eV. Since the experiments can be well described, Ni(111) could be considered as the active site, but we are aware that this comparison is not entirely fair due to the nature of the supported Ni catalyst. The Ni crystals on the supported catalysts are multifaceted, containing the Ni(211), Ni(100), and Ni(110) facet to varying extents [8] and all can contribute to the methanation activity [10]. Ultimately, it will be necessary to repeat the outlined procedure for all four Ni facets independently and combine them in a multifaceted model, as has been done in previous work by some of the authors to describe TPD experiments from a supported Ni catalyst [8]. Such an effort should address both structural and parametric uncertainty [49]. The most obvious structural uncertainty would be coverage effects, and future work should include a systematic

approach to deal with lateral interactions. Parametric uncertainty, in contrast, should be refined with experimental results when applicable [32] or with more advanced electronic structure methods where possible, (*e.g.* hybrid DFT methods [110]). Similarly, the uncertainty correlation in the species energies should be more accurately quantified than the approximate uniform distribution for a more sophisticated error propagation [52, 57], which can be done by using the BEEF-vdW functional [85] (see SI for further discussion). Another challenge for mechanism generation and microkinetic modeling for CO_2 methanation on industrial catalysts is the influence of basic sites on the support for *e.g.* Ni/γ-Al_2O_3 catalysts [8, 75, 112]. Basic supports lead to more active Ni catalysts because the support participates in the activation of CO_2 by providing lower energy pathways at the metal/support interface [16, 17] and should, therefore, be included for these systems.

The combination of linear scaling and BEP relations is commonly used to screen the activity of catalysts over the whole range of transition metals with an assumed microkinetic model, including CO^* methanation [37, 38, 106, 113]. For the screening procedure, the binding energy of the descriptor species is changed by a few eV to move across the various transition metals. Simultaneously, the structure of the underlying microkinetic model is assumed to be static, is often derived from the knowledge for one particular metal/facet, and a single pathway is assumed [28, 29, 37]. Wolcott et al. [108] screened catalysts with the DRC method and observed that the rate-controlling transition state is constant in the range of a few eV. In this study, we showed that within a few meV (i) the mechanism changes significantly, (ii) the activity varies over several orders of magnitude, (iii) the DRC is far from constant, and (iv) global and local rate-controlling parameters are completely different. Consequently, the conclusions drawn from the screening for the most active materials might be incorrect because of the simplified microkinetics. Nonetheless, the usage of these screening techniques has boosted catalyst development and advanced our understanding of several important reactions. Including automated mechanism generation into the catalyst screening procedure with correlated uncertainties is not only beneficial, but rather necessary to discover the whole reaction network for each possible metal or alloy and to truly advance the predictive power of the LS and BEP relations in determining the most active and selective materials [34]. To test our hypothesis we generated an ensemble of 500 distinct mechanism for the Pt(111) surface and all of these simulations show that Pt(111) is inactive for the methanation in agreement with the literature [37, 114] (see Figure S37 for further discussion). Although the purpose of this work is emphatically not catalyst screening, the results suggest that a nickel-like alloy that has a slightly reduced binding energy for H^* and slightly increased binding energy for adsorbates that bind through oxygen, relative to Ni(111), will offer superior production rates for CH_4.

Finally, it is worth emphasizing the computational efficiency of this approach. It took approximately 24 CPU-hours to generate all 5,000 mechanisms. The various sensitivity analyses took an additional $\sim$300 CPU-hours. A single CINEB calculation, in contrast, required approximately 1,300 CPU-hours on the same architecture. In other words, the current approach built and analyzed 5,000 mechanisms in one-fifth of the time required to perform a single transition state calculation.

6.3. Conclusion

The present work presents the first application of automatic mechanism generation for CO_2 hydrogenation to CH_4 on Ni(111) using the open-source automated reaction generation software RMG [43, 44, 47,

48]. Uncertainties in the DFT-based model generating parameters, such as adsorbate binding energies and activation energies, were explored in a systematic manner that is consistent with the underlying correlation using linear scaling and BEP relations. Moreover, this is the first work including correlated parametric uncertainty in a rate-based automated mechanism generation procedure. RMG was capable of discovering a vast reaction network including up to C_6 chemistry, but the main path is the methanation of CO_2 via various routes. The global uncertainty analysis reveals that it is necessary to consider the uncertainties in the model input parameters to discover all possible species and reactions.

CO_2 methanation simulations with all discovered mechanisms in a PFR model show a vast spread of results, allowing various interpretations of the activity of Ni(111) within the uncertainty of DFT functionals. It is even possible to reach opposite conclusions consistent with literature DFT studies. In the correlated uncertainty space, there are also feasible sets of parameters that describe our experimental results from Ni/SiO_2 catalyst with a remarkable accuracy without parameter optimization, further contrasting the role of Ni(111) as the active site. In combination with the global sensitivity analysis, it was possible to determine which factors control the activity of Ni(111) and to derive a most likely methanation mechanism, which is a combination of the redox and carboxyl pathway. The only relevant conversion from CO^* to CH_4 occurs via HCO^* and this reaction together with the thermochemistry of H^* and O^* determines the (in)activity of Ni(111).

The analysis reveals that results from the degree of rate control approach are highly sensitive to the model uncertainty, and that small changes to the parameters can result in completely different RDS or rate-controlling intermediates. A more useful approach is to perform the degree of rate control over the entire uncertainty range, since it quantifies which factors truly control the activity. Therefore, the method provides a hierarchy for parameter refinement with experimental results or more accurate, though likewise more expensive, DFT methods that can ultimately be fed back to RMG and gradually improve the software. Steady-state and transient CO_2 methanation experiments are currently being conducted in a Berty-type reactor to investigate the CO_2 methanation at varying compositions and higher pressures, which will provide a database for the future refinement of the microkinetic model. This new methodology is computationally efficient and can be applied to arbitrary systems in heterogeneous catalysis.

Acknowledgement

BK gratefully acknowledges financial support from the NaWuReT (ProcessNet, DECHEMA) for a virtual research collaboration with CFG in the fall of 2020. BK and TT acknowledge financial support from the Deutsche Forschungsgemeinschaft (DFG, German Research Foundation), project number: 290019031. KS, EM, KB, RHW, and CFG gratefully acknowledge support by the U.S. Department of Energy, Office of Science, Basic Energy Sciences, under Award #0000232253, as part of the Computational Chemical Sciences Program. BK and CFG thank Habib Najm and Judit Zádor for helpful discussions on sensitivity analysis. Sandia National Laboratories is a multimission laboratory managed and operated by National Technology and Engineering Solutions of Sandia, LLC, a wholly owned subsidiary of Honeywell International Inc., for the U.S. Department of Energy's National Nuclear Security Administration under contract DE-NA0003525.

References

[1] M. Götz, J. Lefebvre, F. Mörs, A. McDaniel Koch, F. Graf, S. Bajohr, R. Reimert, T. Kolb. *Renewable Energy* **2016**, 85, 1371–1390. DOI: 10.1016/j.renene.2015.07.066.

[2] C. Vogt, M. Monai, G. J. Kramer, B. M. Weckhuysen. *Nat. Catal.* **2019**, 2 (3), 188–197. DOI: 10.1038/s41929-019-0244-4.

[3] K. F. Kalz, R. Kraehnert, M. Dvoyashkin, R. Dittmeyer, R. Gläser, U. Krewer, K. Reuter, J.-D. Grunwaldt. *ChemCatChem* **2017**, 9 (1), 17–29. DOI: https://doi.org/10.1002/cctc.201600996.

[4] B. Kreitz, G. D. Wehinger, T. Turek. *Chem. Eng. Sci.* **2019**, 195, 541–552. DOI: 10.1016/j.ces.2018.09.053.

[5] K. L. Fischer, M. R. Langer, H. Freund. *Ind. Eng. Chem. Res.* **2019**, 58 (42), 19406–19420. DOI: 10.1021/acs.iecr.9b02863.

[7] J. Gao, Q. Liu, F. Gu, B. Liu, Z. Zhong, F. Su. *RSC Adv.* **2015**, 5 (29), 22759–22776. DOI: 10.1039/C4RA16114A.

[8] B. Kreitz, G. D. Wehinger, C. F. Goldsmith, T. Turek. *J. Phys. Chem. C* **2021**, 125 (5), 2984–3000. DOI: 10.1021/acs.jpcc.0c09985.

[9] C. Vogt, E. Groeneveld, G. Kamsma, M. Nachtegaal, L. Lu, C. J. Kiely, P. H. Berben, F. Meirer, B. M. Weckhuysen. *Nat. Catal.* **2018**, 1 (2), 127–134. DOI: 10.1038/s41929-017-0016-y.

[10] C. Vogt et al. *Nat. Commun.* **2019**, 10 (1), 5330. DOI: 10.1038/s41467-019-12858-3.

[11] D. Beierlein, D. Häussermann, M. Pfeifer, T. Schwarz, K. Stöwe, Y. Traa, E. Klemm. *Appl. Catal., B* **2019**, 247, 200–219. DOI: 10.1016/j.apcatb.2018.12.064.

[12] P. Lozano-Reis, H. Prats, P. Gamallo, F. Illas, R. Sayós. *ACS Catal.* **2020**, 10 (15), 8077–8089. DOI: 10.1021/acscatal.0c01599.

[13] C. Heine, B. A. J. Lechner, H. Bluhm, M. Salmeron. *J. Am. Chem. Soc.* **2016**, 138 (40), 13246–13252. DOI: 10.1021/jacs.6b06939.

[14] J. Ren, H. Guo, J. Yang, Z. Qin, J. Lin, Z. Li. *Appl. Surf. Sci.* **2015**, 351, 504–516. DOI: 10.1016/j.apsusc.2015.05.173.

[15] M. Zhou, B. Liu. *ChemCatChem* **2015**, 7 (23), 3928–3935. DOI: 10.1002/cctc.201500547.

[16] L. Foppa, T. Margossian, S. M. Kim, C. Müller, C. Copéret, K. Larmier, A. Comas-Vives. *J. Am. Chem. Soc.* **2017**, 139 (47), 17128–17139. DOI: 10.1021/jacs.7b08984.

[17] M.-C. Silaghi, A. Comas-Vives, C. Copéret. *ACS Catal.* **2016**, 6 (7), 4501–4505. DOI: 10.1021/acscatal.6b00822.

[18] M. P. Andersson, F. Abild-Pedersen, I. N. Remediakis, T. Bligaard, G. Jones, J. Engbæk, O. Lytken, S. Horch, J. H. Nielsen, J. Sehested. *J. Catal.* **2008**, 255 (1), 6–19. DOI: 10.1016/j.jcat.2007.12.016.

[19] R. C. Catapan, A. A. M. Oliveira, Y. Chen, D. G. Vlachos. *J. Phys. Chem. C.* **2012**, 116 (38), 20281–20291. DOI: 10.1021/jp302488f.

[20] T. P. de Carvalho, R. C. Catapan, A. A. M. Oliveira, D. G. Vlachos. *Ind. Eng. Chem. Res.* **2018**, 57 (31), 10269–10280. DOI: 10.1021/acs.iecr.8b01957.

[21] M. Zhang, B. Zijlstra, I. A. W. Filot, F. Li, H. Wang, J. Li, E. J. M. Hensen. *Can. J. Chem. Eng.* **2020**, 98 (3), 740–748. DOI: 10.1002/cjce.23655.

[22] A. L. Maulana, R. I. D. Putra, A. G. Saputro, M. K. Agusta, Nugraha, H. K. Dipojono. *Phys. Chem. Chem. Phys.* **2019**, 21 (36), 20276–20286. DOI: 10.1039/c9cp02970b.

[23] G. Peng, S. J. Sibener, G. C. Schatz, S. T. Ceyer, M. Mavrikakis. *J. Phys. Chem. C* **2012**, 116 (4), 3001–3006. DOI: 10.1021/jp210408x.

[24] A. Banerjee, V. Navarro, J. W. M. Frenken, A. P. van Bavel, H. P. C. E. Kuipers, M. Saeys. *J. Phys. Chem. Lett.* **2016**, 7 (11), 1996–2001. DOI: 10.1021/acs.jpclett.6b00555.

[25] C. J. K.-J. Weststrate, D. Sharma, D. Garcia Rodriguez, M. A. Gleeson, H. O. A. Fredriksson, J. W. H. Niemantsverdriet. *Nat. Commun.* **2020**, 11 (1), 750. DOI: 10.1038/s41467-020-14613-5.

[26] L. C. Grabow, M. Mavrikakis. *ACS Catal.* **2011**, 1 (4), 365–384. DOI: 10.1021/cs200055d.
[27] G. T. K. K. Gunasooriya, A. P. van Bavel, H. P. C. E. Kuipers, M. Saeys. *ACS Catal.* **2016**, 6 (6), 3660–3664. DOI: 10.1021/acscatal.6b00634.
[28] F. Studt, F. Abild-Pedersen, Q. Wu, A. D. Jensen, B. Temel, J.-D. Grunwaldt, J. K. Nørskov. *J. Catal.* **2012**, 293, 51–60. DOI: 10.1016/j.jcat.2012.06.004.
[29] F. Studt, I. Sharafutdinov, F. Abild-Pedersen, C. F. Elkjær, J. S. Hummelshøj, S. Dahl, I. Chorkendorff, J. K. Nørskov. *Nat. chem.* **2014**, 6 (4), 320–324. DOI: 10.1038/nchem.1873.
[30] B. Demir, T. Kropp, E. B. Gilcher, M. Mavrikakis, J. A. Dumesic. *J. Catal.* **2021**, 279 (6), 337. DOI: 10.1016/j.jcat.2021.03.013.
[31] S. Bhandari, S. Rangarajan, C. T. Maravelias, J. A. Dumesic, M. Mavrikakis. *ACS Catal.* **2020**, 10 (7), 4112–4126. DOI: 10.1021/acscatal.9b05424.
[32] S. Bhandari, S. Rangarajan, M. Mavrikakis. *Acc. Chem. Res.* **2020**, 53 (9), 1893–1904. DOI: 10.1021/acs.accounts.0c00340.
[33] J. T. Margraf, K. Reuter. *ACS Omega* **2019**, 4 (2), 3370–3379. DOI: 10.1021/acsomega.8b03200.
[34] A. Bruix, J. T. Margraf, M. Andersen, K. Reuter. *Nat. Catal.* **2019**, 2 (8), 659–670. DOI: 10.1038/s41929-019-0298-3.
[35] F. Abild-Pedersen, J. Greeley, F. Studt, J. Rossmeisl, T. R. Munter, P. G. Moses, E. Skúlason, T. Bligaard, J. K. Nørskov. *Phys. Rev. Lett.* **2007**, 99 (1), 016105. DOI: 10.1103/PhysRevLett.99.016105.
[36] J. E. Sutton, D. G. Vlachos. *Chem. Eng. Sci.* **2015**, 121, 190–199. DOI: 10.1016/j.ces.2014.09.011.
[37] J. K. Nørskov, T. Bligaard, J. Rossmeisl, C. H. Christensen. *Nat. Chem.* **2009**, 1 (1), 37–46. DOI: 10.1038/nchem.121.
[38] J. K. Nørskov, F. Abild-Pedersen, F. Studt, T. Bligaard. *Proc. Natl. Acad. Sci. U. S. A.* **2011**, 108 (3), 937–943. DOI: 10.1073/pnas.1006652108.
[39] S. Vernuccio, L. J. Broadbelt. *AIChE J.* **2019**, 65 (8), 17. DOI: 10.1002/aic.16663.
[40] S. Rangarajan, A. Bhan, P. Daoutidis. *Appl. Catal.,B* **2014**, 145, 149–160. DOI: 10.1016/j.apcatb.2013.01.030.
[41] S. Rangarajan, R. R. O. Brydon, A. Bhan, P. Daoutidis. *Green Chem.* **2014**, 16 (2), 813–823. DOI: 10.1039/C3GC41386A.
[42] S. Zhang, L. J. Broadbelt, I. P. Androulakis, M. G. Ierapetritou. *Energy Fuels* **2014**, 28 (7), 4801–4811. DOI: 10.1021/ef5010539.
[43] C. W. Gao, J. W. Allen, W. H. Green, R. H. West. *Comput. Phys. Commun.* **2016**, 203, 212–225. DOI: 10.1016/j.cpc.2016.02.013.
[44] C. F. Goldsmith, R. H. West. *J. Phys. Chem. C* **2017**, 121 (18), 9970–9981. DOI: 10.1021/acs.jpcc.7b02133.
[45] E. J. Mazeau, P. Satpute, K. Blöndal, C. F. Goldsmith, R. H. West. *ACS Catal.* **2021**, 73, 7114–7125. DOI: 10.1021/acscatal.0c04100.
[46] K. Blondal, J. Jelic, E. Mazeau, F. Studt, R. H. West, C. F. Goldsmith. *Ind. Eng. Chem. Res.* **2019**, 58 (38), 17682–17691. DOI: 10.1021/acs.iecr.9b01464.
[47] M. Liu et al. *J. Chem. Inf. Model.* **2021**, 61 (6), 2686–2696. DOI: 10.1021/acs.jcim.0c01480.
[48] W. H. Green, R. H. West. https://rmg.mit.edu/. Version 3.0. **2021**.
[49] H. Wang, D. A. Sheen. *Prog. Energy Combust. Sci.* **2015**, 47, 1–31. DOI: 10.1016/j.pecs.2014.10.002.
[50] S. Döpking, C. P. Plaisance, D. Strobusch, K. Reuter, C. Scheurer, S. Matera. *J. Chem. Phys.* **2018**, 148 (3), 034102. DOI: 10.1063/1.5004770.
[51] Z. W. Ulissi, A. J. Medford, T. Bligaard, J. K. Nørskov. *Nat. Commun.* **2017**, 8, 14621. DOI: 10.1038/ncomms14621.
[52] J. E. Sutton, W. Guo, M. A. Katsoulakis, D. G. Vlachos. *Nat. Chem.* **2016**, 8 (4), 331–337. DOI: 10.1038/nchem.2454.

[53] S. Matera, W. F. Schneider, A. Heyden, A. Savara. *ACS Catal.* **2019**, 9 (8), 6624–6647. DOI: 10.1021/acscatal.9b01234.

[54] F. Studt. *Front. Catal.* **2021**, 1, 016105. DOI: 10.3389/fctls.2021.658965.

[55] J. Wellendorff, T. L. Silbaugh, D. Garcia-Pintos, J. K. Nørskov, T. Bligaard, F. Studt, C. T. Campbell. *Surf. Sci.* **2015**, 640, 36–44. DOI: 10.1016/j.susc.2015.03.023.

[56] T. Bligaard, J. K. Nørskov, S. Dahl, J. Matthiesen, C. H. Christensen, J. Sehested. *J. Catal.* **2004**, 224 (1), 206–217. DOI: 10.1016/j.jcat.2004.02.034.

[57] A. J. Medford, J. Wellendorff, A. Vojvodic, F. Studt, F. Abild-Pedersen, K. W. Jacobsen, T. Bligaard, J. K. Nørskov. *Science* **2014**, 345 (6193), 197–200. DOI: 10.1126/science.1253486.

[58] J. E. Sutton, W. Guo, M. A. Katsoulakis, D. G. Vlachos. *Nat. Chem.* **2016**, 8 (4), 331–337. DOI: 10.1038/nchem.2454.

[59] B. Wang, S. Chen, J. Zhang, S. Li, B. Yang. *J. Phys. Chem. C* **2019**, 123 (50), 30389–30397. DOI: 10.1021/acs.jpcc.9b08755.

[60] T. Gu, B. Wang, S. Chen, B. Yang. *ACS Catal.* **2020**, 10 (11), 6346–6355. DOI: 10.1021/acscatal.0c00630.

[61] C. T. Campbell. *J. Catal.* **2001**, 204 (2), 520–524. DOI: 10.1006/jcat.2001.3396.

[62] C. Stegelmann, A. Andreasen, C. T. Campbell. *J. Am. Chem. Soc.* **2009**, 131 (23), 8077–8082. DOI: 10.1021/ja9000097.

[63] R. G. Susnow, A. M. Dean, W. H. Green, P. Peczak, L. J. Broadbelt. *J.Phys. Chem. A* **1997**, 101 (20), 3731–3740. DOI: 10.1021/jp9637690.

[64] C. F. Goldsmith. *Top. Catal.* **2012**, 55 (5-6), 366–375. DOI: 10.1007/s11244-012-9805-3.

[65] B. Hammer, L. B. Hansen, J. K. Nørskov. *Phys. Rev. B* **1999**, 59 (11), 7413–7421. DOI: 10.1103/PhysRevB.59.7413.

[66] G. Kresse, J. Furthmüller. *Phys. Rev. B* **1996**, 54 (16), 11169–11186. DOI: 10.1103/physrevb.54.11169.

[67] G. Kresse, J. Furthmüller. *Comput. Mater. Sci.* **1996**, 6 (1), 15–50. DOI: 10.1016/0927-0256(96)00008-0.

[68] S. Grimme. *J. Comput. Chem.* **2006**, 27 (15), 1787–1799. DOI: 10.1002/jcc.20495.

[69] K. Delgado, L. Maier, S. Tischer, A. Zellner, H. Stotz, O. Deutschmann. *Catalysts* **2015**, 5 (2), 871–904. DOI: 10.3390/catal5020871.

[70] D. Schmider, L. Maier, O. Deutschmann. *Ind. Eng. Chem. Res.* **2021**, 134, 689. DOI: 10.1021/acs.iecr.1c00389.

[71] S. Wang, B. Temel, J. Shen, G. Jones, L. C. Grabow, F. Studt, T. Bligaard, F. Abild-Pedersen, C. H. Christensen, J. K. Nørskov. *Catal. Lett.* **2011**, 141 (3), 370–373. DOI: 10.1007/s10562-010-0477-y.

[72] J. E. Sutton, P. Panagiotopoulou, X. E. Verykios, D. G. Vlachos. *J. Phys. Chem. C* **2013**, 117 (9), 4691–4706. DOI: 10.1021/jp312593u.

[73] G. Henkelman, B. P. Uberuaga, H. Jónsson. *J. Chem. Phys.* **2000**, 113 (22), 9901–9904. DOI: 10.1063/1.1329672.

[74] B. Kreitz, J. Brauns, G. D. Wehinger, T. Turek. *Chem. Ing. Tech.* **2020**, 43 (45), 20332. DOI: 10.1002/cite.202000019.

[75] Q. Pan, J. Peng, T. Sun, S. Wang, S. Wang. *Catal. Commun.* **2014**, 45, 74–78. DOI: 10.1016/j.catcom.2013.10.034.

[76] J. Friedland, B. Kreitz, H. Grimm, T. Turek, R. Güttel. *ChemCatChem* **2020**, 12 (17), 4373–4386. DOI: 10.1002/cctc.202000278.

[77] D. G. Goodwin, R. L. Speth, H. K. Moffat, B. W. Weber. https://www.cantera.org. Version 2.4.0. **2018**. DOI: 10.5281/zenodo.1174508.

[78] B. Kreitz, K. Sargsyan, E. J. Mazeau, K. Blöndal, R. H. West, G. D. Wehinger, T. Turek, C. F. Goldsmith. Version v1.0.2. **2021**. DOI: 10.5281/zenodo.4662852.

[79] C. W. Gao, M. Liu, W. H. Green. *Int. J. Chem. Kinet.* **2020**, 52 (4), 266–282. DOI: 10.1002/kin.21348.

[80] B. Ruscic, R. E. Pinzon, M. L. Morton, G. von Laszevski, S. J. Bittner, S. G. Nijsure, K. A. Amin, M. Minkoff, A. F. Wagner. *J. Phys. Chem. A* **2004**, 108 (45), 9979–9997. DOI: 10.1021/jp047912y.

[81] B. Ruscic, D. H. Bross. Active Thermochemical Tables (ATcT) Values Based on ver. 1.122g of the Thermochemical Network. **2019**.

[82] Z. Ulissi, V. Prasad, D. G. Vlachos. *J. Catal.* **2011**, 281 (2), 339–344. DOI: 10.1016/j.jcat.2011.05.019.

[83] A. J. Medford, A. C. Lausche, F. Abild-Pedersen, B. Temel, N. C. Schjødt, J. K. Nørskov, F. Studt. *Top. Cataly.* **2014**, 57 (1-4), 135–142. DOI: 10.1007/s11244-013-0169-0.

[84] A. J. Medford, A. Vojvodic, J. S. Hummelshøj, J. Voss, F. Abild-Pedersen, F. Studt, T. Bligaard, A. Nilsson, J. K. Nørskov. *J. Catal.* **2015**, 328, 36–42. DOI: 10.1016/j.jcat.2014.12.033.

[85] J. Wellendorff, K. T. Lundgaard, A. Møgelhøj, V. Petzold, D. D. Landis, J. K. Nørskov, T. Bligaard, K. W. Jacobsen. *Phys. Rev. B* **2012**, 85 (23), 316. DOI: 10.1103/PhysRevB.85.235149.

[86] J. Prager, H. N. Najm, K. Sargsyan, C. Safta, W. J. Pitz. *Combust. Flame* **2013**, 160 (9), 1583–1593. DOI: 10.1016/j.combustflame.2013.01.008.

[87] J. E. Sutton, D. G. Vlachos. *Ind. Eng. Chem. Res.* **2015**, 54 (16), 4213–4225. DOI: 10.1021/ie5043374.

[88] I. Sobol'. *USSR Comp. Math. and Math. Phys.* **1967**, 7 (4), 86–112. DOI: 10.1016/0041-5553(67)90144-9.

[89] A. Paszke et al. *Advances in Neural Information Processing Systems 32*. Ed. by H. Wallach, H. Larochelle, A. Beygelzimer, F. d'Alché-Buc, E. Fox, R. Garnett. Curran Associates, Inc., **2019**, 8024–8035.

[90] A. Saltelli, S. Tarantola, F. Campolongo, M. Ratto. Vol. 1. Wiley Online Library, **2004**.

[91] B. Debusschere, H. Najm, P. Pébay, O. Knio, R. Ghanem, O. Le Maître. *SIAM J. Sci. Comput.* **2004**, 26 (2), 698–719. DOI: 10.1137/S1064827503427741.

[92] B. Debusschere, K. Sargsyan, C. Safta, K. Chowdhary. *Handbook of Uncertainty Quantification*. Ed. by R. Ghanem, D. Higdon, H. Owhadi. Springer, **2017**, 1807–1827.

[93] T. Crestaux, O. Le Maître, J. Martinez. *Reliab. Eng. Syst. Safety* **2009**, 94 (7), 1161–1172.

[94] T. Turányi, A. S. Tomlin. Berlin, Heidelberg: Springer Berlin Heidelberg, **2014**. DOI: 10.1007/978-3-662-44562-4.

[95] C. T. Campbell. *ACS Catal.* **2017**, 7 (4), 2770–2779. DOI: 10.1021/acscatal.7b00115.

[96] J. Zádor, I. G. Zsély, T. Turányi, M. Ratto, S. Tarantola, A. Saltelli. *J. Phys. Chem. A* **2005**, 109 (43), 9795–9807. DOI: 10.1021/jp053270i.

[97] S. Abelló, C. Berrueco, D. Montané. *Fuel* **2013**, 113, 598–609. DOI: 10.1016/j.fuel.2013.06.012.

[98] F. Koschany, D. Schlereth, O. Hinrichsen. *Appl. Catal., B* **2016**, 181, 504–516. DOI: 10.1016/j.apcatb.2015.07.026.

[99] M. Aziz, A. A. Jalil, S. Triwahyono, R. R. Mukti, Y. H. Taufiq-Yap, M. R. Sazegar. *Appl. Catal., B* **2014**, 147, 359–368. DOI: 10.1016/j.apcatb.2013.09.015.

[100] W. L. Vrijburg, J. W. A. van Helden, A. J. F. van Hoof, H. Friedrich, E. Groeneveld, E. A. Pidko, E. J. M. Hensen. *Catal. Sci. Technol.* **2019**, 9 (10), 2578–2591. DOI: 10.1039/C9CY00532C.

[101] A. B. Mhadeshwar, H. Wang, D. G. Vlachos. *J. Phys. Chem. B* **2003**, 107 (46), 12721–12733. DOI: 10.1021/jp034954y.

[102] M. Salciccioli, M. Stamatakis, S. Caratzoulas, D. G. Vlachos. *Chem. Eng. Sci.* **2011**, 66 (19), 4319–4355. DOI: 10.1016/j.ces.2011.05.050.

[103] E. Vesselli et al. *J. Phys. Chem. Lett.* **2009**, 1 (1), 402–406. DOI: 10.1021/jz900221c.

[104] T. S. Galhardo, A. H. Braga, B. H. Arpini, J. Szanyi, R. V. Gonçalves, B. F. Zornio, C. R. Miranda, L. M. Rossi. *J. Am. Chem. Soc.* **2021**, 143 (11), 4268–4280. DOI: 10.1021/jacs.0c12689.

[105] P. Ferrin, D. Simonetti, S. Kandoi, E. Kunkes, J. A. Dumesic, J. K. Nørskov, M. Mavrikakis. *J. Am. Chem. Soc.* **2009**, 131 (16), 5809–5815. DOI: 10.1021/ja8099322.

[106] A. C. Lausche, A. J. Medford, T. S. Khan, Y. Xu, T. Bligaard, F. Abild-Pedersen, J. K. Nørskov, F. Studt. *J. Catal.* **2013**, 307, 275–282. DOI: 10.1016/j.jcat.2013.08.002.

[107] L. C. Grabow, B. Hvolbæk, J. K. Nørskov. *Top. Catal.* **2010**, 53 (5-6), 298–310. DOI: 10.1007/s11244-010-9455-2.

[108] C. A. Wolcott, A. J. Medford, F. Studt, C. T. Campbell. *J. Catal.* **2015**, 330, 197–207. DOI: 10.1016/j.jcat.2015.07.015.

[109] Z. Mao, C. T. Campbell. *J. Catal.* **2020**, 381 (4), 53–62. DOI: 10.1016/j.jcat.2019.09.044.

[110] J. Sauer. *Acc. Chem. Res.* **2019**, 52 (12), 3502–3510. DOI: 10.1021/acs.accounts.9b00506.

[111] W. A. Brown, R. Kose, D. A. King. *Chem. Rev.* **1998**, 98 (2), 797–832. DOI: 10.1021/cr9700890.

[112] S. Ewald, O. Hinrichsen. *Appl. Catal., A* **2019**, 580, 71–80. DOI: 10.1016/j.apcata.2019.04.005.

[113] G. Jones, T. Bligaard, F. Abild-Pedersen, J. K. Nørskov. *J. Phys.: Condens. Matter* **2008**, 20 (6), 064239. DOI: 10.1088/0953-8984/20/6/064239.

[114] M. Andersson, T. Bligaard, A. L. Kustov, K. E. Larsen, J. Greeley, T. Johannessen, C. H. Christensen, J. K. Nørskov. *J. Catal.* **2006**, 239 (2), 501–506. DOI: 10.1016/j.jcat.2006.02.016.

"Words in a book are one thing. The true test comes in battle."

(Jon Snow, A Dance with Dragons, George R. R. Martin)

CHAPTER 7

Microkinetic Modeling of the Transient CO_2 Methanation

This thesis aimed to derive microkinetics that can be used to describe the transient methanation of CO_2 on Ni catalysts. With the microkinetics derived in Chapter 6 of the thesis, this task is now possible. Although the temperature-scanning experiment in Chapter 6 involves the usage of a transient method, Chapter 4 revealed that steady-states are attained almost immediately. Moreover, the gas phase composition does not alter considerably. Therefore, additional fully transient CO_2 methanation experiments were conducted by applying periodic concentration forcing to a Ni/SiO_2 catalyst in a Berty reactor setup. The following chapter presents a comparison of the transient CO_2 methanation experiments with simulations using all generated microkinetic models. These results are not published yet. The experimental setup is described first and characterized with residence time measurements. Afterward, the experiments are compared with predictions from the microkinetic model. Parts of the experimental technique for the periodic concentration forcing were published in Ref. 62 and the method for the residence time measurements with the pulse technique in Ref. 126. Supporting information for this chapter is provided in Appendix E.

7.1. Experimental setup

Transient CO_2 methanation experiments are performed in a process unit with a Berty reactor, a continuously stirred tank reactor for heterogeneously catalyzed gas-phase reactions. A P&ID of the experimental setup is provided in Figure 7.1. Gases are supplied from cylinders with a quality of 5.0 except CO_2 (4.5). All gases are further purified with gas traps (VICI AG) to remove traces of O_2, water, CO and S components to below 1 ppb. The gases are dosed with mass flow controllers (EL-Flow Select, Bronkhorst) and mixed in a T-filter. Two redundant gas lines are installed in the unit, which can be supplied with different mixtures of the reactant gases to enable transient experiments (see Figure 7.1a). With the current setup, it is possible to apply step changes or inject pulses via a sample loop (see Figure 7.1b). The gas is preheated in the pipes to the reaction temperature upon entering the Berty reactor and the reactor itself is heated with heating cartridges placed inside the reactor hull. The catalyst is placed in a basket with an inner diameter of 10 mm, above which a turbine sits that rotates with rotation speeds of up to 10,000 min^{-1}. In the basket, the catalyst is fixed using quartz wool and stainless steel meshes with a mesh size of 40 µm. The design of the Berty reactor is described in the work of Haumann et al. [127]. Temperatures are measured inside the reactor at the inlet and above the catalyst bed with Typ K thermocouples. A thermostat cools the rotating shaft of the turbine to prevent overheating of the bearings (see Figure 7.1d). Also, the rotor shaft is constantly flushed with Ar to prevent H_2 from contacting the magnet and water condensation on the cooled shaft. The exhaust gas is kept at 200 °C to prevent the condensation of water. Gas transfer lines are heated with a heating cord wrapped around the pipe. Pressure regulation is achieved with a back pressure regulator (U3L, Equilibar) equipped with a PTFE glass laminate membrane in both gas supply lines.

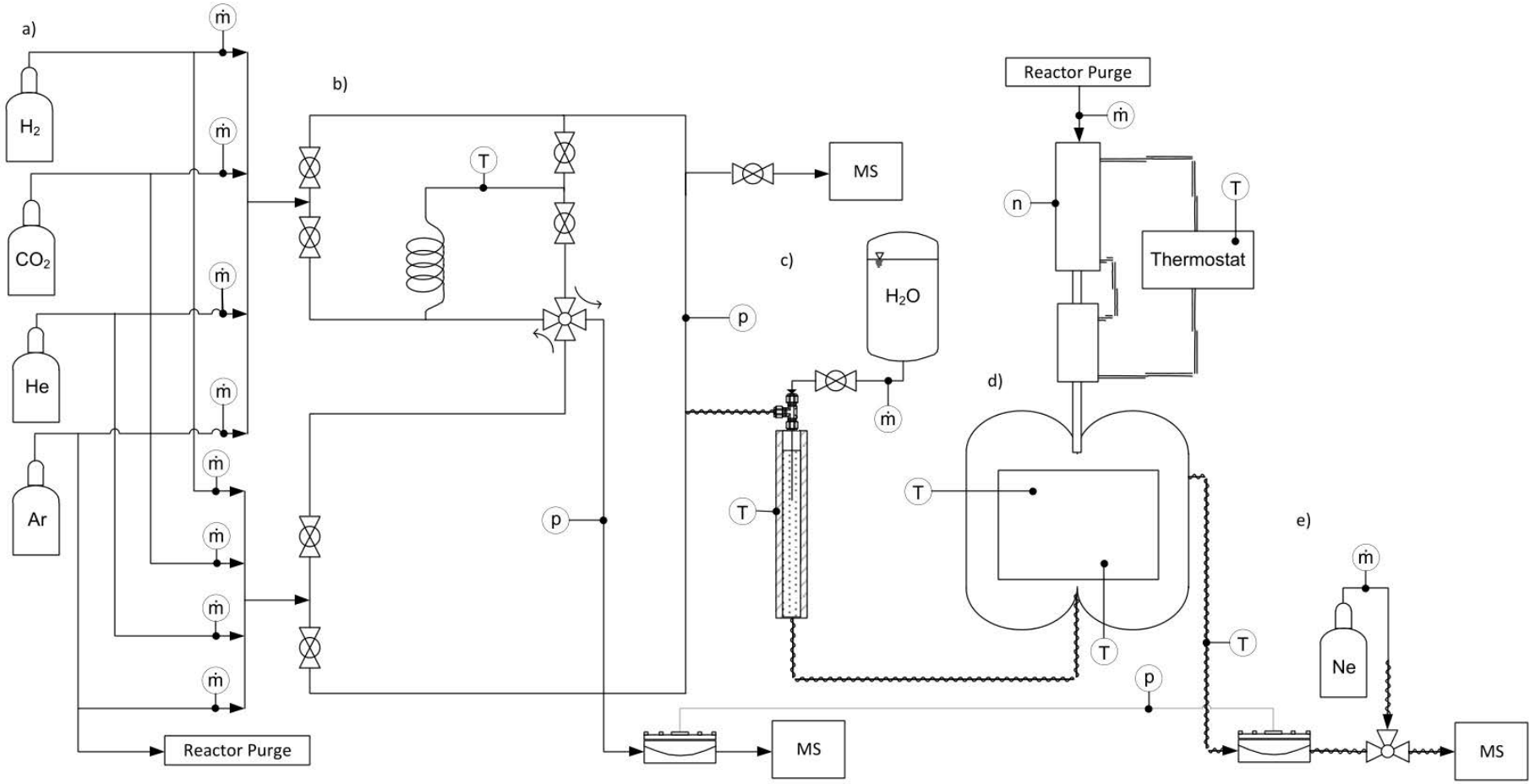

Figure 7.1.: P&ID of the methanation unit. The unit consists of (a) two redundant gas supply lines, (b) various valves to apply step and pulse signals, (c) a water vaporizer, (d) the Berty reactor and (e) the mass spectrometer.

The pressure regulators have the same dome pressure, which results in nearly no pressure difference between both lines upon switching (< 40 mbar) [62]. The exhaust gas is expanded to ambient pressure and then supplied to a mass spectrometer (MS) (GAM 200, InProcessInstruments) (see Figure 7.1e). Directly before the MS, Neon (5.0) is added to the exhaust gas with a mass flow controller (EL-Flow Prestige, Bronkhorst) as an external standard. External standard and the exhaust gas are mixed in a special gas mixing chamber (Bronkhorst) before entering the MS. The external standard provides an excellent method to measure the volumetric flow rate at the exhaust, which changes due to the volume contraction of the methanation reaction and due to pressure differences upon switching of valves, with the temporal resolution of the MS.

A two-staged gas inlet heated to 200 °C is used to establish a proper mass flow to the ionization chamber of the MS. Two capillaries are used with a length of 1.5 m and an inner diameter of 250 µm. The pressure in the ionization chamber is roughly 3×10^{-6} mbar. The mass spectrometer has four inlet ports that measure the reactor exhaust, the bypass gas line, the inlet to the reactor, and a gas line for calibration. Switching between the different inlet ports is achieved with a multi-position valve (VICI AG). The molecules are ionized with an yttrated iridium filament with a low cathode voltage of 40 V, which results in ionization energies on the order of 24.6 to 27.6 eV. This results in nearly no double charging of ^{36}Ar (18 amu) and ^{40}Ar (20 amu) which would cause interference with H_2O (18 amu) and the external standard ^{20}Ne (20 amu) while still allowing to measure a clear ^{4}He signal. The signal is amplified with a secondary electron multiplier (SEM) operated with a voltage of 1,050 V. Calibration of the MS is done with certified gas mixtures (Linde AG) with Ar as an internal standard for the calibration and compared to a reference gas mixture with all components (except Ne). Water is calibrated during a methanation experiment, where the selectivity to methane is almost 100 %. The different mass-to-charge ratios are measured for 0.1 s in upwind direction and the ion currents are converted to concentrations with the calibration matrix using Givens rotation method.

7.2. Transient Methanation Experiments

The reactor is alternately supplied with a H_2/Ar and a CO_2/He mixture for the transient kinetic experiments. Alternation is achieved by switching between the gas lines with the two mixtures, which results in the periodic application of step changes. This operation mode is also denoted as "bang-bang" operation [48]. The bang-bang operation is an easy to apply dynamic operation and provides a periodic perturbation of the system that can be used for kinetic investigation [71]. Periodic switching between two reactant gases can lead to superior productivity compared to the steady-state, which was also seen for the methanation of CO [56, 57]. Although process improvement is not the aim of this study, the periodic operation can be applied and modeled relatively easily. In addition, the periodic experiment can provide valuable insights into the mechanism. The periodic concentration forcing was used to investigate the possible process improvement during CO_2 methanation on a Ni/γ-Al_2O_3 catalyst in a differential fixed-bed reactor with the same unit. Measured reaction rates were inferior to the optimal steady-state reaction rate. Hence, no improvement through transient operation was observed. This study is published in Ref. 62.

The reactants are mixed with an inert tracer for several reasons. First, the dilution reduces the generated reaction heat and enables an isothermal operation. Second, the usage of the internal standard allows to

follow the residence time of the system and to track the start and end of the transients [62, 71]. Third, providing an internal standard simplifies the evaluation of the reaction rates and mass balances of the experiments [62, 128]. The concentration of the internal standards is adjusted to 70 %. Bang-bang operation can be characterized by the cycle split ratio γ [129] (see Equation (7.1)), which characterizes the time during which only CO_2 flows over the system (t_{CO_2}) compared to the total cycle time ($t_{CO_2}+t_{H_2}$).

$$\gamma = \frac{t_{CO_2}}{t_{CO_2} + t_{H_2}} \tag{7.1}$$

The cycle split ratio can have values between 0 (pure H_2) and 1 (pure CO_2). Transient methanation experiments are conducted with the Ni/SiO_2 catalyst, which was used in Chapter 6 for the development of the microkinetic model. However, this catalyst was produced in a new batch and it was necessary to pelletize the nanoparticles. The nanoparticles were pelletized on a pelletizing disc via spraying with an aqueous colloidal SiO_2 solution. The agglomerated particles were calcined at 673 K for 3 h, which resulted in stable particles with a size of a few µm that could safely be handled in the Berty reactor. In the present study, transient experiments were conducted for a cycle time of 120 s, which is $3.4 \times \bar{\tau}$, where $\bar{\tau}$ is the hydrodynamic residence time of the Berty reactor at the reaction conditions and various cycle split ratios. All parameters for the transient methanation experiments are summarized in Table 7.1. The volume of the Berty reactor is determined from the CAD geometry.

Table 7.1.: Conditions for the transient methanation experiments, properties of the catalyst and parameters for the modeling of the Berty reactor.

Properties	Value
Temperature	568 K
Pressure	5 bar
Rotation speed	8,000 min^{-1}
Cycle time	120 s
Catalyst mass	80 mg
Catalyst	20 wt% Ni/SiO_2
H_2 adsorption capacity	222 µmol g^{-1}
Metal surface area	17.4 m^2 g^{-1}
Ni crystal size	7.7 nm
Dispersion	13.0 %
Surface site density Ni(111)	3.16×10^{-9} mol m^{-2}
$A_{Ni(111)}$	1.121 m^2
Reactor volume	98 mL
$\bar{\tau}$	35.46 s
$\dot{V}_{Purge}$(Ar)	95 mL_N min^{-1}
$\dot{V}_{Ne}$	20 mL_N min^{-1}
$\dot{V}_{H_2/Ar}$	300 mL_N min^{-1}
$\dot{V}_{CO_2/He}$	300 mL_N min^{-1}
$x_{H_2} = x_{CO_2}$	30 %
Cycle split ratios γ	0.2, 0.5 and 0.8
Number of periods	10

7.3. Microkinetic Model of the Berty Reactor

The Berty reactor is modeled as a transient CSTR in Cantera [130] with a mean-field microkinetic model. Governing equations for a transient CSTR and the mean-field microkinetics are provided in Chapter 5 and Chapter 6. The setup of the model and the program code is similar to the one used in Chapter 5 and Chapter 6 and is provided in the appendix. When reproducing experimental results with a microkinetic model, a crucial parameter is the metal surface area, which specifies the number of active sites. The metal surface area of the catalyst was determined with H_2 chemisorption according to the method described in Chapter 4 and Chapter 5. In the microkinetic model, only the Ni(111) facet is considered, but when the metal surface area is derived from the H_2 uptake, a distribution of facets is assumed [131]. Consequently, the metal surface area must be calculated under the assumption that the entire catalyst consists of the Ni(111) facet. Only then, a fair comparison can be made because the number of active sites is identical. The active metal surface area of the Ni(111) facet for the model $A_{\mathrm{Ni(111)}}$ is calculated from the determined uptake $Q_{\mathrm{H_2}}$ via

$$A_{\mathrm{Ni(111)}} = \frac{2 Q_{\mathrm{H_2}} m_{\mathrm{cat}}}{\Gamma_{\mathrm{Ni(111)}}} \tag{7.2}$$

where m_{cat} is the catalyst mass and $\Gamma_{\mathrm{Ni(111)}}$ is the surface site density of Ni(111). Properties used for the reactor model are summarized in Table 7.1.

7.4. Comparison of the Microkinetics with Transient Experiments

Before the transient methanation experiments can be conducted, it is necessary to evaluate the residence time behavior of the Berty reactor and to determine whether the reactor can be regarded as an ideal CSTR. Therefore, residence time measurements were performed using the pulse method via injection of a sample loop in a carrier gas stream. A detailed explanation of the residence time measurements using the pulse injection along with the evaluation was published in Ref. 126. Residence time measurements were performed for various rotation speeds of the turbine to see which rotation speed is required for a complete back-mixing. The obtained dimensionless residence time distributions E_Θ and residence time sum F curves are displayed in Figure 7.2a,b.

Even at low rotation speeds of the turbine, a significant amount of back-mixing is achieved, agreeing with the result of Haumann et al. [127]. A direct comparison of the obtained residence time distribution with an ideal CSTR is impossible because of the transfer lines to the Berty reactor and from the reactor to the MS. These transfer lines can be regarded as ideal plug-flow reactors (PFR) and both types can be combined in a compartment model of the setup [132]. The volume of the transfer lines is estimated from the time lag between injection and the first detection of the tracer. A compartment model consisting of an ideal PFR and ideal CSTR in series is included Figure 7.2 according to Equation (7.3) [133].

$$E_\Theta(\Theta) = \begin{cases} 0 & \text{for } \Theta < \Theta_{\mathrm{PFR}} \\ \frac{1}{1-\Theta_{\mathrm{PFR}}} \exp\left(-\frac{1}{1-\Theta_{\mathrm{PFR}}}\Theta + \frac{\Theta_{\mathrm{PFR}}}{1-\Theta_{\mathrm{PFR}}}\right) & \text{for } \Theta \geq \Theta_{\mathrm{PFR}} \end{cases} \tag{7.3}$$

Θ_{PFR} is the dimensionless residence time in the transfer lines. The residence time distribution moves closer to ideal behavior with an increasing rotation speed of the turbine and no differences in the residence time distributions are observed for rotation speeds higher than 5,320 min^{-1}. These experiments

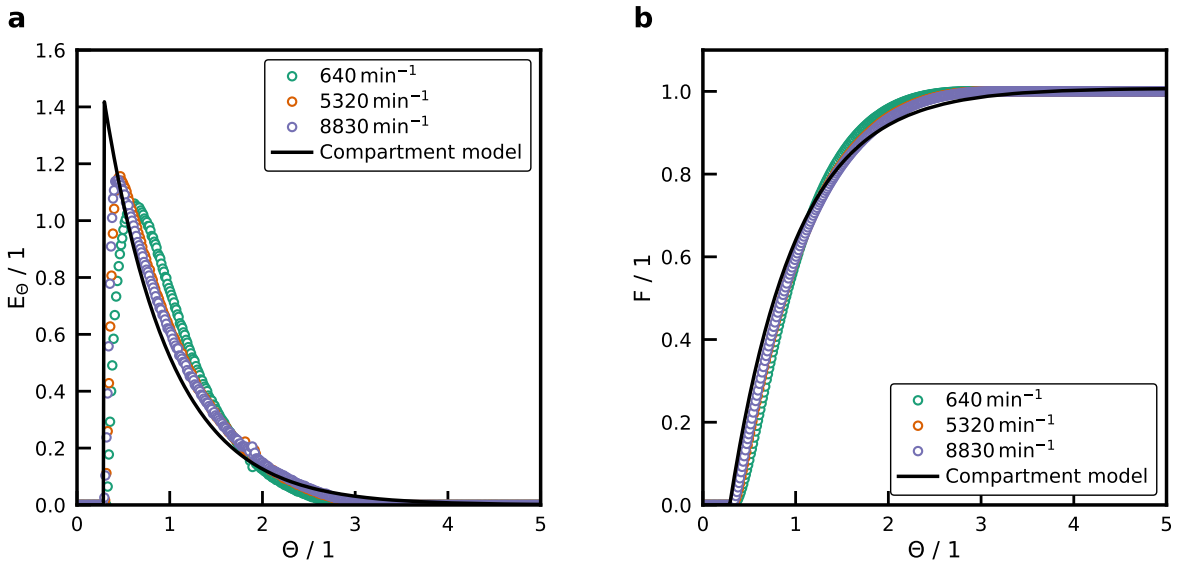

Figure 7.2.: (a) Residence time density distribution and (b) residence time sum curve of the Berty reactor at various turbine rotation speeds compared to the ideal behavior of a compartment model. *Conditions:* $p = 5\,\text{bar}$, $T = 298\,\text{K}$, $\dot{V}_{\text{Ar}} = 299\,\text{mL}_\text{N}\,\text{min}^{-1}$, $m_{\text{cat}} = 300\,\text{mg}$.

demonstrate that the Berty reactor shows almost ideal CSTR behavior at the investigated conditions. The remaining deviations from the ideal behavior are caused by non-ideal plug flow behavior in the pipes and non-ideal injection of a perfect Dirac pulse. CSTR behavior was also confirmed in a CFD simulation of the Berty setup [134]. Only minor variations in the gas-phase concentration were predicted by the CFD simulation. Thus, the setup can be regarded as an ideal CSTR, which simplifies the evaluation procedure and allows the usage of a simple CSTR reactor model to simulate the experiments. Therefore, the gas-phase atmosphere around the catalyst particles is homogeneous and resolved by the MS, which is valuable for kinetic measurements.

Figure 7.3a,c,e show the experimentally recorded concentration profiles for the transient methanation of CO_2 for different cycle split ratios. The catalyst is exposed to the H_2/Ar flow at the beginning of each experiment, which is omitted in Figure 7.3 for clarity. Upon switching from H_2/Ar to CO_2/He flow, a CH_4, H_2O, and CO formation sets in. For the stoichiometric cycle split ($\gamma = 0.2$, see Figure 7.3a), the CH_4 and CO concentrations reach directly a time-invariant pattern, whereas the H_2O concentration shows a smaller signal for the first step change. The evolving concentration profile after the first step change is called the build-up behavior. The CH_4 and H_2O signal have no phase shift in the periodic operation and reach their maximum concentration in the H_2 rich part of the cycle. In contrast, CO production is highest, when the CO_2 concentration reaches its maximum and thus has a phase shift of 180° to the CH_4/H_2O signal. The CO_2 signal and the He signal have no phase shift, indicating only a minor interaction with CO_2 and the catalyst or the support. Similar experiments in a fixed-bed reactor with the same setup and a Ni/γ-Al_2O_3 catalyst showed a significant time lag due to strong reversible adsorption of CO_2 on basic sites of the support [135]. The transient experiment ends with a switch to the H_2/Ar mixture and the concentration profiles for the products and CO_2 decline to zero, which is also denoted as the back-transient. Isothermal operation of the Berty reactor was confirmed in all conducted experiments and temperature variations during the experiments are limited to $\pm 1.5\,\text{K}$. This can also be due to the different thermal conductivity of the gas mixtures in the periodic operation, which is quite different, as shown in Chapter 3.

A more pronounced build-up behavior is obtained for the cycle splits with a higher share of CO_2 in Figure 7.3c, e. Next to the build-up, an overshot in CH_4 and H_2O production is obtained after the last switch from CO_2 to H_2, most pronounced for the cycle split ratio of 0.8. This overshot in the back-transient is a result of a deposit of carbonaceous species on the catalyst surface. A H_2 deficiency is present in the reactor during periodic operation at cycle split ratios higher than the stoichiometric ratio ($\gamma < 0.2$). The H_2 concentration reaches only small values during the H_2 cycle and drops to almost zero in the CO_2 part (see Figure E1, E2). Therefore, the adsorbates cannot be completely hydrogenated to CH_4 and a build-up of carbonaceous deposits occurs on the catalyst surface.

The same information of the temporal profile can far better be explored in the phase space. Since He is injected along with CO_2 as an internal standard, the He concentration tracks the residence time behavior of the system. When relating the measured concentrations to the He concentration, a phase plane diagram can be created (see Figure 7.3b,d,f). From this diagram, it is possible to directly see deviations from the residence time behavior of the system. A detailed explanation is provided for the phase plane diagram for a cycle split ratio of 0.5 in Figure 7.3d. He and CH_4 concentration start at zero and both increase when the switch to CO_2/He is made. For this cycle split, a local maximum is reached at the maximum He concentration. After the switch to H_2/Ar, the He concentration decreases, but the methane concentration increases until the feed is switched to CO_2/He again. This indicates that the methane formation is inhibited in a CO_2 rich atmosphere. For the next cycle, the CH_4 concentration reaches the time-invariant pattern, which is also known as the limit cycle. In this case, the limit cycle rotates clockwise until the end of the experiment, where the back-transient is clearly seen upon switching back to H_2/Ar. Interestingly, the local maximum of the first step corresponds to the various minimums in the CO_2 rich parts of the cycle. The pattern for H_2O is similar to the CH_4 profile, but CO is significantly different. CO formation also starts directly after the switch to CO_2 but reaches the maximum at the maximum He concentration, where CO_2 reaches the maximum concentration in the reactor. This limit cycle rotates counterclockwise. The build-up is only small and no back-transient behavior is obtained for an equal cycle split. The limit cycle for the cycle split ratio of 0.8 shows only small variations because of a smaller amplitude of the H_2 and CO_2 concentration. For the stoichiometric cycle split, low variations in the amplitude are obtained and there is no overshot in the back-transient because of the sufficient H_2 supply.

Transient methanation experiments in the Berty reactor can also provide insights into the mechanism of the CO_2 methanation. Based on the results in Chapter 6, which showed that CO^* is the most stable carbon-containing intermediate on Ni(111), it can be hypothesized that the carbonaceous deposit consists mostly of CO^*. All other carbon-containing intermediates did not exhibit a high coverage on Ni(111) for any combination of the kinetic parameters in the uncertainty range. However, at the higher pressure in these experiments compared to the temperature-scanning experiment and the under-stoichiometric reactant ratio, it is also possible that other adsorbates like surface carbon can be present. A higher gas-phase pressure of the adsorbates shifts the adsorption equilibrium, resulting in a higher coverage. High coverage of adsorbates has a significant effect on the stability of intermediates and pathways [18, 97, 136]. But since the water signal shows an overshot as well, it is more likely that the molecule in the carbonaceous deposit contains oxygen. After the last switch to H_2, this deposit is completely hydrogenated to CH_4 and H_2O. The lack of a phase shift between the CH_4 and H_2O signal could indicate that the rate-determining step is the scission of a C-O bond, which would agree with the result from Chapter 6 that the dissociation of HCO^* is among the most important parameters as

evidenced by the global sensitivity analysis. Hydrogenation of carbonaceous compounds and the surface O^* to OH^* progresses with faster rates. This is just a hypothesis from the observed concentration profiles and a more thorough analysis of the results is required.

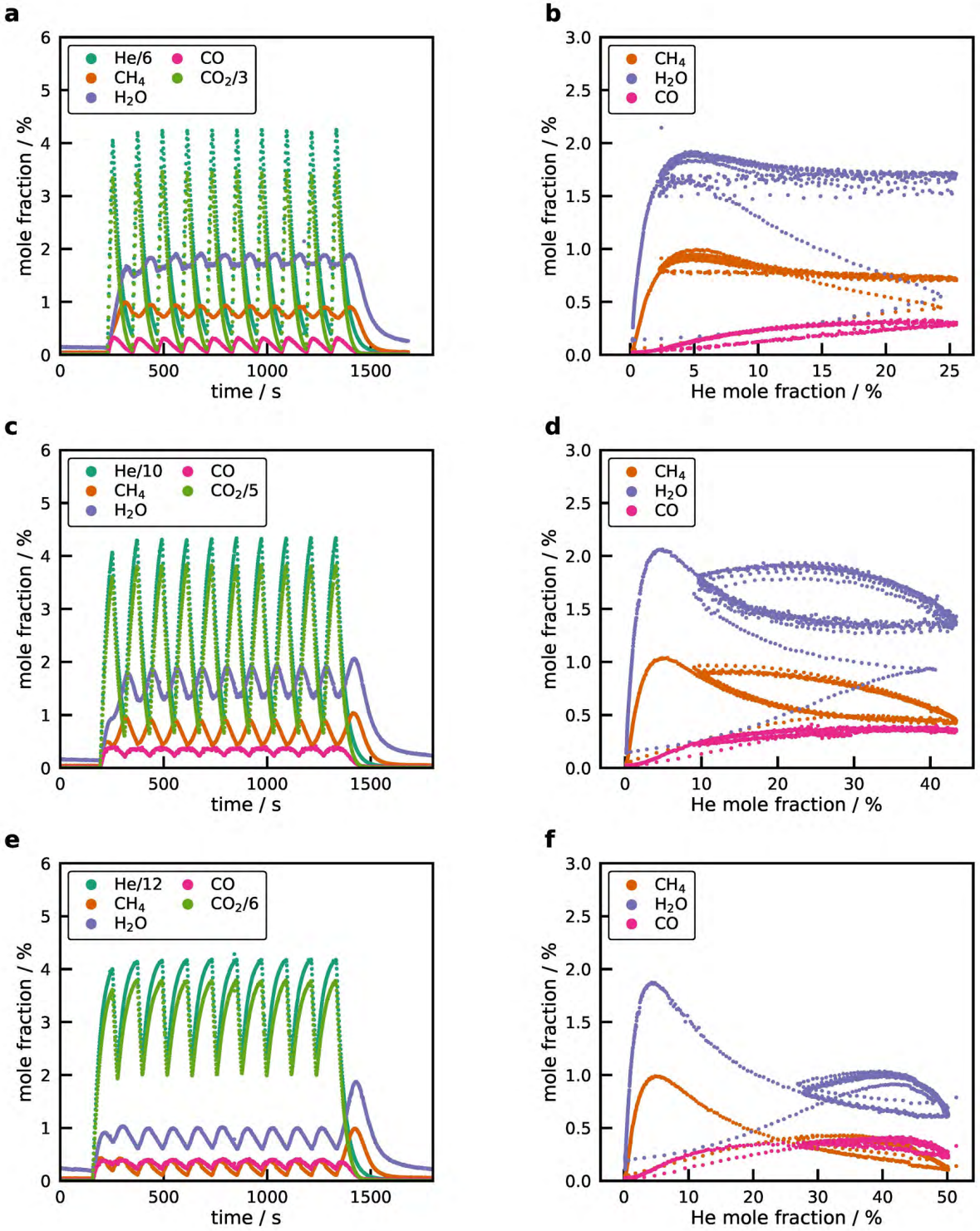

Figure 7.3.: Experimental results for the transient CO_2 methanation in the bang-bang operation with a cycle time of 120 s and cycle split ratios of (a) 0.2, (c) 0.5, and (d) 0.8. (b), (d), and (f) display the phase plane diagram for the products referenced to the internal standard He. Note that the He and CO_2 signal is scaled for illustrative purpose in (a), (c), (e).

In these transient CO_2 methanation experiments, the catalyst is also alternated between a reducing (H_2) and an oxidizing atmosphere (CO_2). Mutz et al. [46, 137] performed similar periodic experiments and observed a constant decline in the methane production of a Ni/Al_2O_3 catalyst. This decline in activity was explained by an oxidation of the Ni catalyst resulting in a loss of active surface area. The phase-plane diagrams in Figure 7.3 show that the limit cycle is time-invariant for all cycle split ratios. Consequently, the Ni catalyst remains metallic in the CO_2 rich atmosphere. Oxygen traces in the CO_2 feed were removed by gas purifiers. In a previous transient methanation study published in Ref. 62 no oxidation of a Ni/γ-Al_2O_3 catalyst was observed as well. Chapter 4 showed that the Ni/SiO_2 catalysts could deactivate in the temperature scanning experiments at high temperatures when CO is formed. It was hypothesized that the deposit is carbon because the activity could only be restored after an oxidation and reduction cycle. Galhardo et al. [36] proved with operando techniques that the deposit is indeed carbon. Although CO is formed in the transient experiments in the Berty reactor, especially for the high cycle split ratio, the catalyst does not deactivate. This suggests that no carbon is formed. Deactivation occurs at temperatures beyond 673 K in the temperature scan, which highlights that the direct dissociation of CO^* to C^* has a substantial barrier (see Chapter 5) [98, 100].

A far more sophisticated and detailed investigation of the mechanism can be conducted with the assistance of the microkinetics generated in Chapter 6 in a multiscale modeling approach. The experiments are reproduced with the microkinetic model taking into account the uncertainty in the model parameters by performing simulations with all 5,000 generated methanation mechanisms. The comparison of the model predictions and the experiments is displayed in Figure 7.4 for a cycle split ratio of 0.5 and further cycle split ratios are provided in the appendix (see Figure E1, E2). Figure 7.4a shows the comparison for the internal standard He to validate the reactor model because He as an inert component is only physically mixed. Thus, it gives information on the residence time behavior. The predictions of the model are in perfect agreement with the recorded concentrations, which highlights that the transient CSTR model with the parameters in Table 7.1 is well suited to describe the transient behavior of the Berty reactor. Figure 7.4a contains all 5,000 simulations but the concentrations of the internal standard remains constant. The volumetric flow rate is not changed significantly due to the low conversion, which explains this result. The microkinetic model can accurately predict the concentration of CO_2 and Ar, but the steady-state H_2 concentration shows a slight deviation, although the transient operation is reasonably described. This might result from the uncertainty of the mass flow controller since it is operated at a low percentage of the full-scale range, which usually means that the value has a higher uncertainty. Predictions of the model for the products show ample variation, which was anticipated due to the strong variation in the simulated concentration profiles in Chapter 6. The measured concentration profiles are well within the uncertainty range of the model predictions. Again, it highlights that the Ni(111) facet can be either active or inactive depending on the set of parameters in a purely DFT-based uncertainty range. A feasible set of parameters was determined in Chapter 6 that described the temperature-scanning experiment with the same catalyst with good accuracy. This mechanism is displayed as a black line in Figure 7.4.

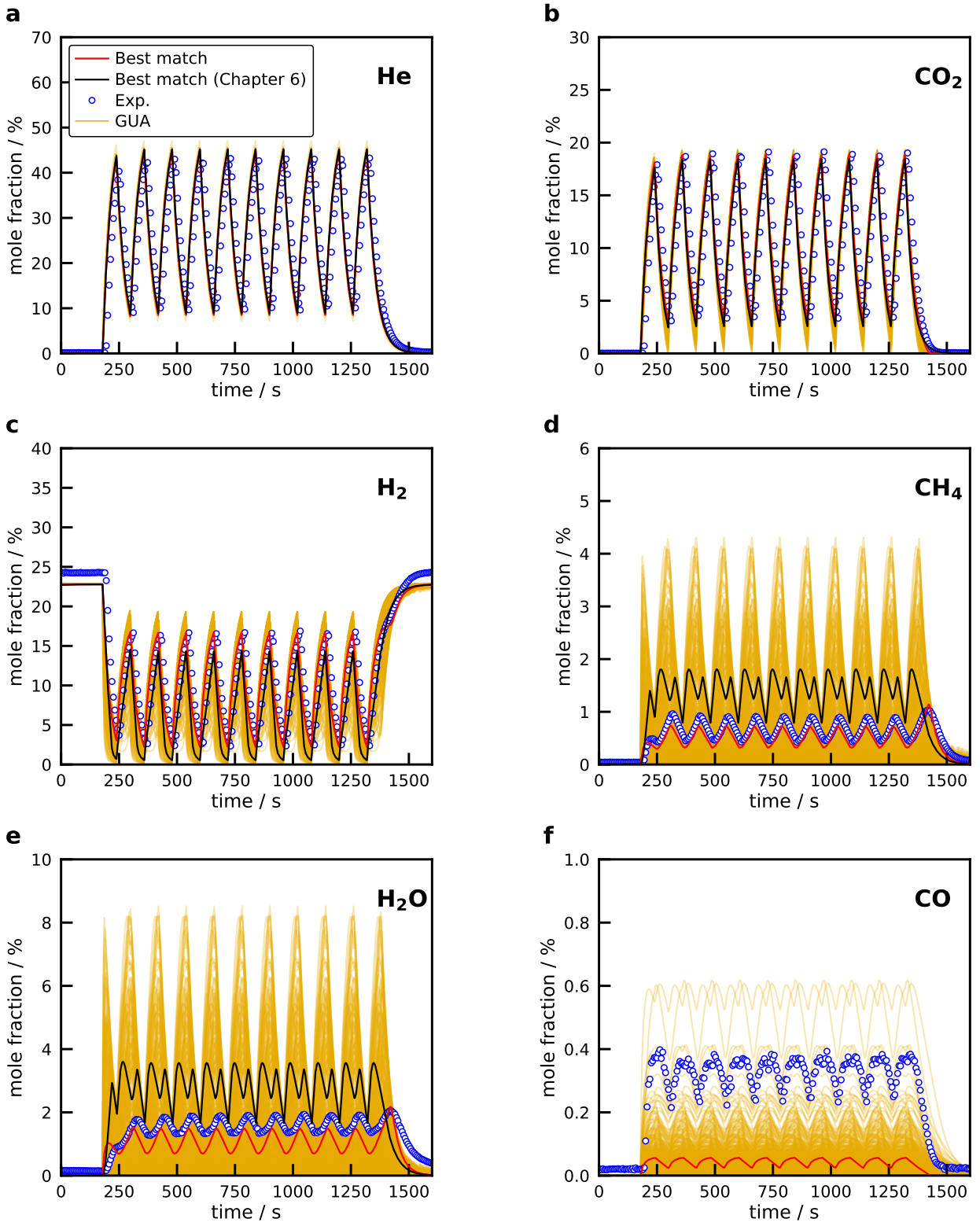

Figure 7.4.: Comparison of transient experiments for (a) He, (b) CO_2, (c) H_2, (d) CH_4, (e) H_2O, and (f) CO with the simulations using all 5,000 generated microkinetic models derived in Chapter 6 for a cycle split ratio of $\gamma = 0.5$. The black line is the feasible set from Chapter 6, and the red line is the feasible set determined for the transient experiments.

It can be clearly seen that this set of parameters cannot describe the experimentally observed concentration profiles for CH_4, H_2O, and CO. Predictions by the model show a bigger variation in the amplitude with high reaction rates in the CO_2 as well as the H_2 rich part of the cycle. In contrast, the experiments show that CH_4 production is highest when H_2 reaches the maximum concentration. Since the reaction rate is high in both cycles, a doubling of the frequency of maximums is observed, which is also obtained for the H_2O profile. Moreover, the model is not able to describe the CO profile at all and predicts that no CO is formed. However, this result is expected since it was not possible to accurately predict the CO concentration in Chapter 6. With the same approach as outlined in Chapter 6, a new feasible set of parameters and the best match is determined, for which the model predictions are in closest agreement to all transient experiments and measured concentrations. The mean absolute percentage error (MAPE) is used as an error measure, which is defined as

$$\mathrm{MAPE} = \frac{1}{N}\sum_{n=1}^{N}\left|\frac{M_\mathrm{n} - P_\mathrm{n}}{M_\mathrm{n}}\right| \tag{7.4}$$

where N is the number of data points, M is the measured concentration, and P is the model prediction. The MAPE was calculated for all measured concentrations (except Ne) and all three cycle split ratios to determine the new feasible set of parameters. The red line in Figure 7.4 shows the mechanism in best agreement with all transient experiments. Predictions for the CH_4 concentration are in remarkable agreement with the experiments (see Figure 7.4d) without any fitting of the data. The microkinetic model can accurately account for the build-up, the overshot of the back-transient and agrees quantitatively with the experiment. Although the best match can predict the CH_4 profile, it is still not possible to accurately describe the CO profile. A small CO formation is obtained and the position of the peaks agrees with the measurement, but the actual value is too low. Thus, the H_2O profile cannot be described as good as the CH_4 profile because the H_2O concentration also depends on the CO concentration due to the reverse water-gas shift reaction.

The best match is compared to the experiments with other cycle split ratios in phase plane diagrams in Figures 7.5 to 7.7. Only the products are illustrated because the reactants are always well described by the model predictions, mainly because of the low conversion. This form of presentation becomes even more advantageous when comparing a model with experiments since deviations like phase shifts can be seen directly due to the internal standard.

These figures show that the microkinetic model can always reasonably describe the CH_4 concentration profile. However, the microkinetic model is quantitatively not able to correctly predict the selectivities. For a cycle split ratio of $\gamma = 0.2$ where the CO concentration is low, the model can also relatively well quantify the produced amount of water (see Figure 7.5). But with increasing selectivity to CO at higher cycle split ratios, the description becomes worse. For some combination of parameters, the microkinetic model can predict a high CO concentration during periodic operation. Still, these models cannot, at the same time, predict the other species, which is a consequence of the correlated uncertainties and probably the neglection of coverage dependence [115], as discussed in Chapter 6.

In this chapter, the question arises why the best match microkinetic model in Chapter 6 fails to describe the transient experiments in the Berty reactor. By definition, microkinetics do not depend on the reactor setup and should be able to predict the kinetics for all operating conditions [17]. It is necessary to recall that the temperature-scanning experiment was conducted with a stoichiometric H_2/CO_2 mixture at atmospheric pressure to explain the difference between the feasible set from Chapter 6 and the transient

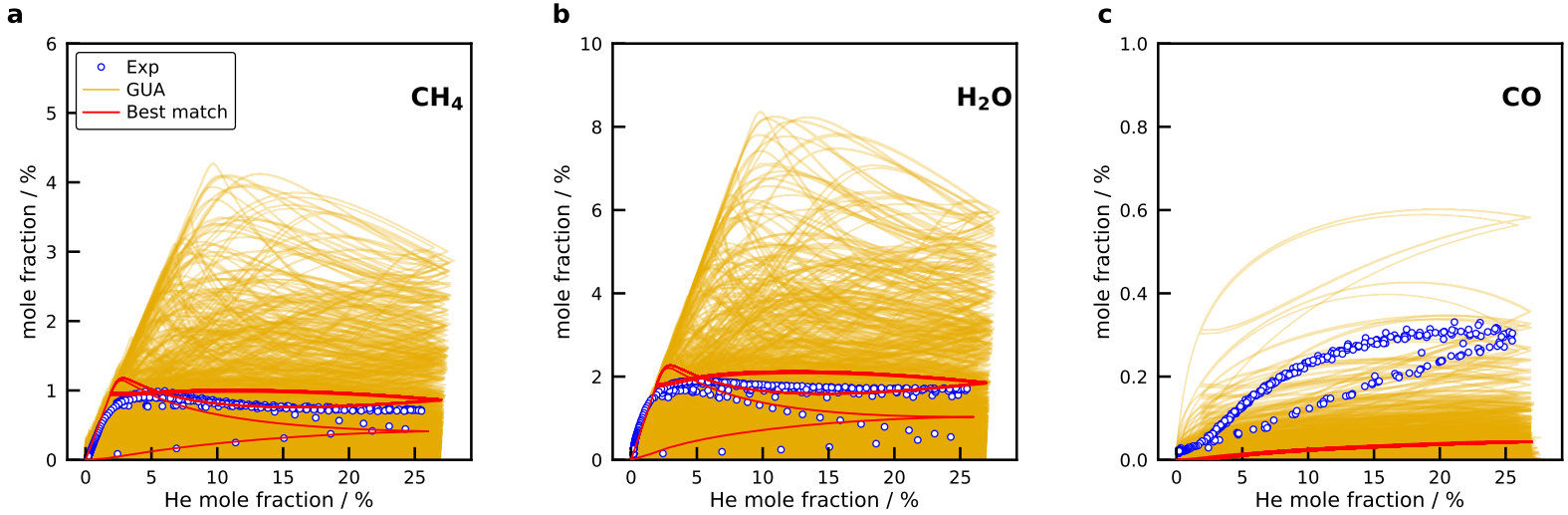

Figure 7.5.: Phase plane diagrams for the comparison of the microkinetic models with the experiments for (a) CH_4, (b) H_2O, and (c) CO at a a cycle split ratio of $\gamma = 0.2$.

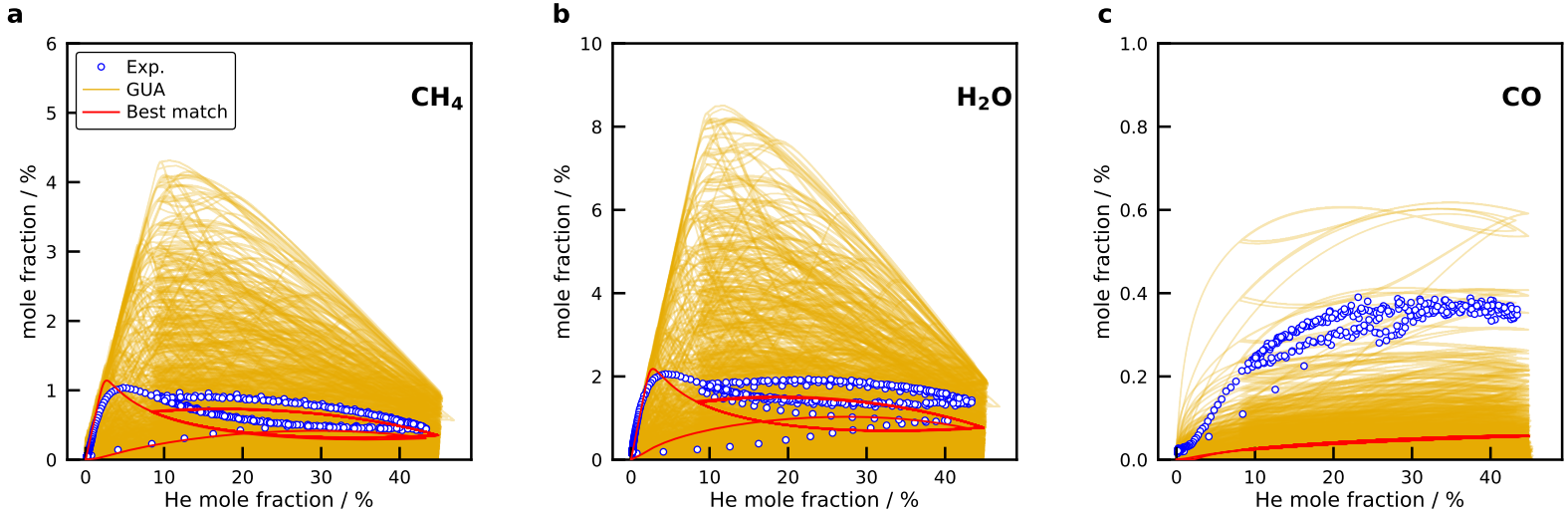

Figure 7.6.: Phase plane diagrams for the comparison of the microkinetic models with the experiments for (a) CH_4, (b) H_2O, and (c) CO at a a cycle split ratio of $\gamma = 0.5$.

experiments. In general, a stoichiometric mixture for the CO_2 methanation always shows the highest reaction rate [84, 85], which was observed in the transient methanation study with the fixed-bed reactor as well [62]. Consequently, the microkinetic model that describes the experimental data in Chapter 6 best represents a set of parameters, which predict a high activity. In the transient methanation experiments, the gas-phase concentration changes and significant deviations from the stoichiometric composition occur. Also, the transient experiments were conducted at a reactor pressure of 5 bar, whereas the temperature-scanning experiment in Chapter 6 was performed at ambient pressure. The higher pressure affects the coverages of the adsorbates, which alters the stability of intermediates and transition states and thus the rates of the surface reactions [17, 97]. The information obtained in the transient experiments with the Berty reactor is more valuable from a kinetic perspective than the data from the temperature-scanning experiment. Due to the intensive back-mixing and the resulting CSTR behavior, the concentration in the gas phase is homogeneous and no axial gradients occur. Therefore, the exact concentration around the catalyst particles is measured, whereas the measured gas-phase concentration in the fixed-bed reactor is only known at the end of the pipe.

Also, the Berty reactor, in combination with the transient CSTR model, is superior compared to the ideal plug-flow reactor model of the temperature-scanning setup in Chapter 6. Deviations from the ideal plug-flow behavior may occur in the temperature-scanning experiment, which is not captured in the simple plug-flow model. In addition, the experiments in the fixed-bed reactor exhibit a considerable concentration gradient across the packed bed. A major benefit of the transient experiments is the drastic variations in the concentration of educts and products. Consequently, the activity of the catalyst and the reaction kinetics are explored for many reaction conditions. Therefore, a microkinetic model that can describe these transient results should provide an even better description of the actual microkinetics of the CO_2 methanation. This does not imply that the results in Chapter 6 are wrong. It rather highlights the challenges in performing and evaluating kinetic experiments to provide the best data for microkinetic investigations.

Next to the model in best agreement with the experiments, several other sets of parameters have an almost equally low MAPE. These results are displayed in Figure 7.8a for a cycle split of $\gamma = 0.5$. The shaded region contains all models that are within $+5\,\%$ of the lowest MAPE. The model predictions are in a narrow compared to all models in Figure 7.4, but still relatively broad compared to the actual experimental data. A remarkable accuracy is obtained for the best match regarding the prediction of the CH_4 concentration, but CO and H_2O are not well predicted. Within the threshold limit of 5 %, there are sets of parameters that can describe the CO profiles, but these decrease the agreement with the CH_4 concentration.

Figure 7.9 displays the coverage profiles during the transient operation for $\gamma = 0.5$. These phase plane diagrams must be interpreted similarly to the phase plane diagrams of the gas-phase concentrations. The He concentration is high in the CO_2 rich part of the cycle. Accordingly, the CO^* coverage is high when CO_2 has a high partial pressure and consequently H^* coverage is low. For the best match, the CO^* coverage is above 0.8, at the maximum He concentration, whereas H^* occupies only 20 % of the Ni(111) surface and the remaining 80 % are vacant sites. This result is surprising because it was anticipated that the surface is either covered in H^* or CO^* at a pressure of 5 bar. However, the binding energy of H^* is significantly decreased for the best case, which is why it is more loosely bound to the Ni surface. In addition, the H^* coverage also decreases with increasing temperature, as was observed during the

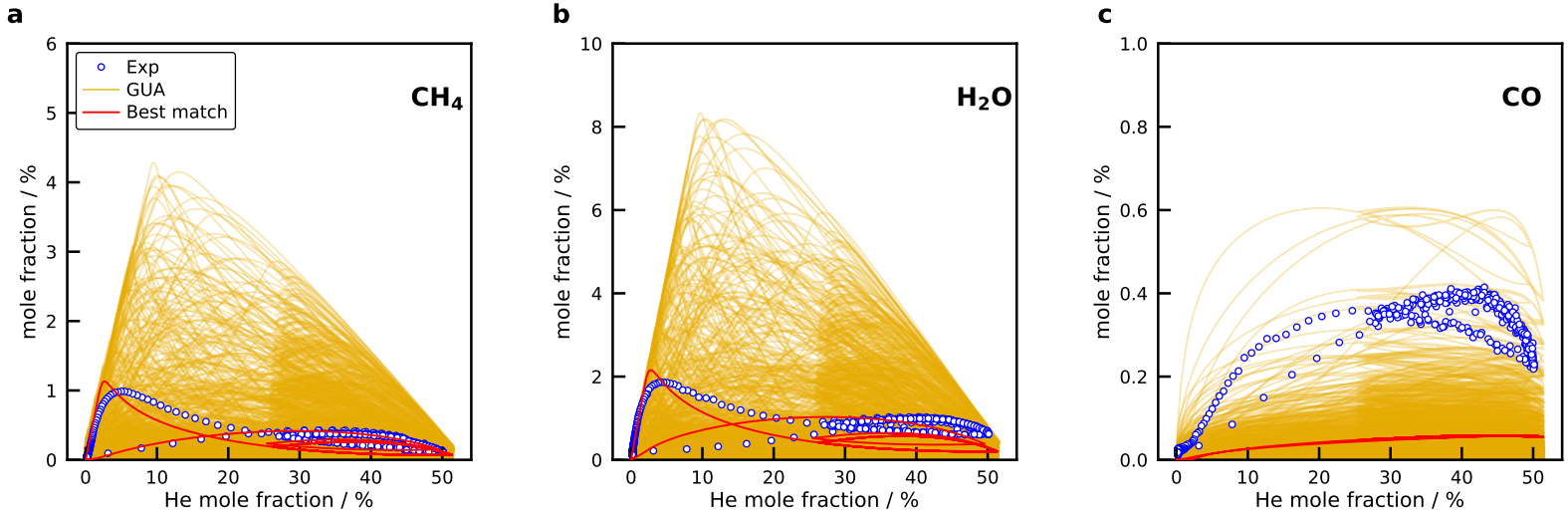

Figure 7.7.: Phase plane diagrams for the comparison of the microkinetic models with the experiments for (a) CH_4, (b) H_2O, and (c) CO at a a cycle split ratio of $\gamma = 0.8$.

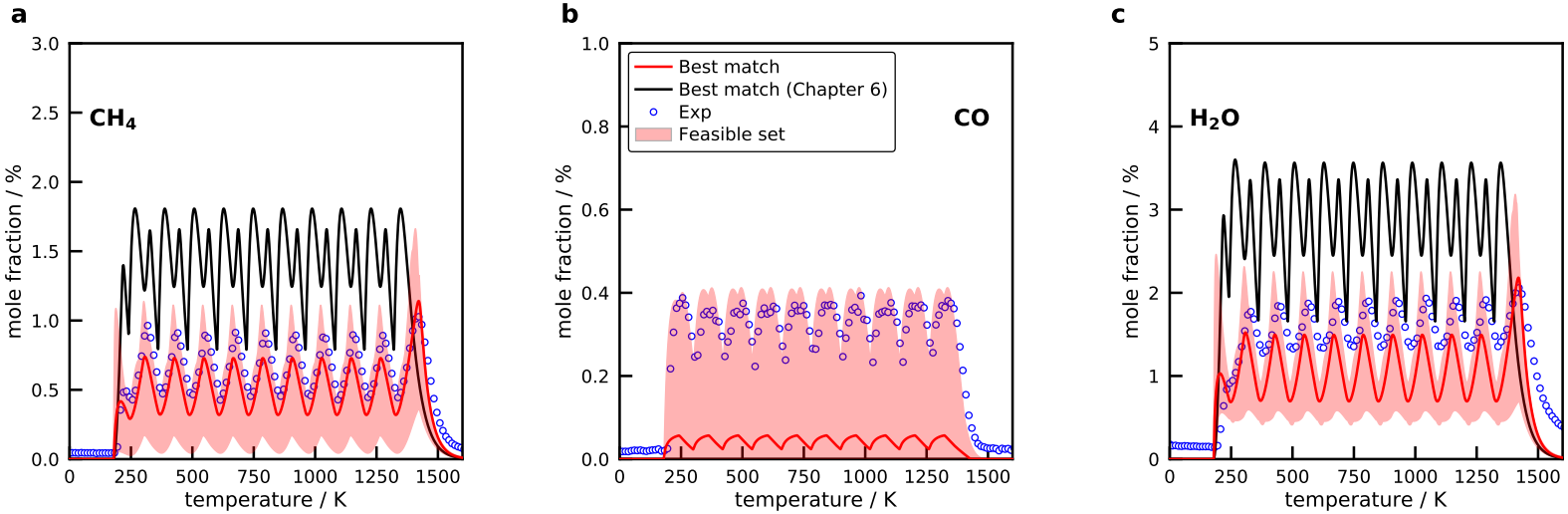

Figure 7.8.: Concentration profiles for the products (a) CH_4, (b) CO, and (c) H_2O compared to the best mechanism (solid red line) and the feasible set of parameters (shaded pink region) which contains the mechanism that are within +5 % of the lowest MAPE for a cycle split of $\gamma = 0.5$.

measurement of H_2 adsorption isotherms on the Ni/SiO_2 catalyst at various temperatures. During the H_2 part of the cycle, the Ni surface is completely cleaned from adsorbed CO^*.

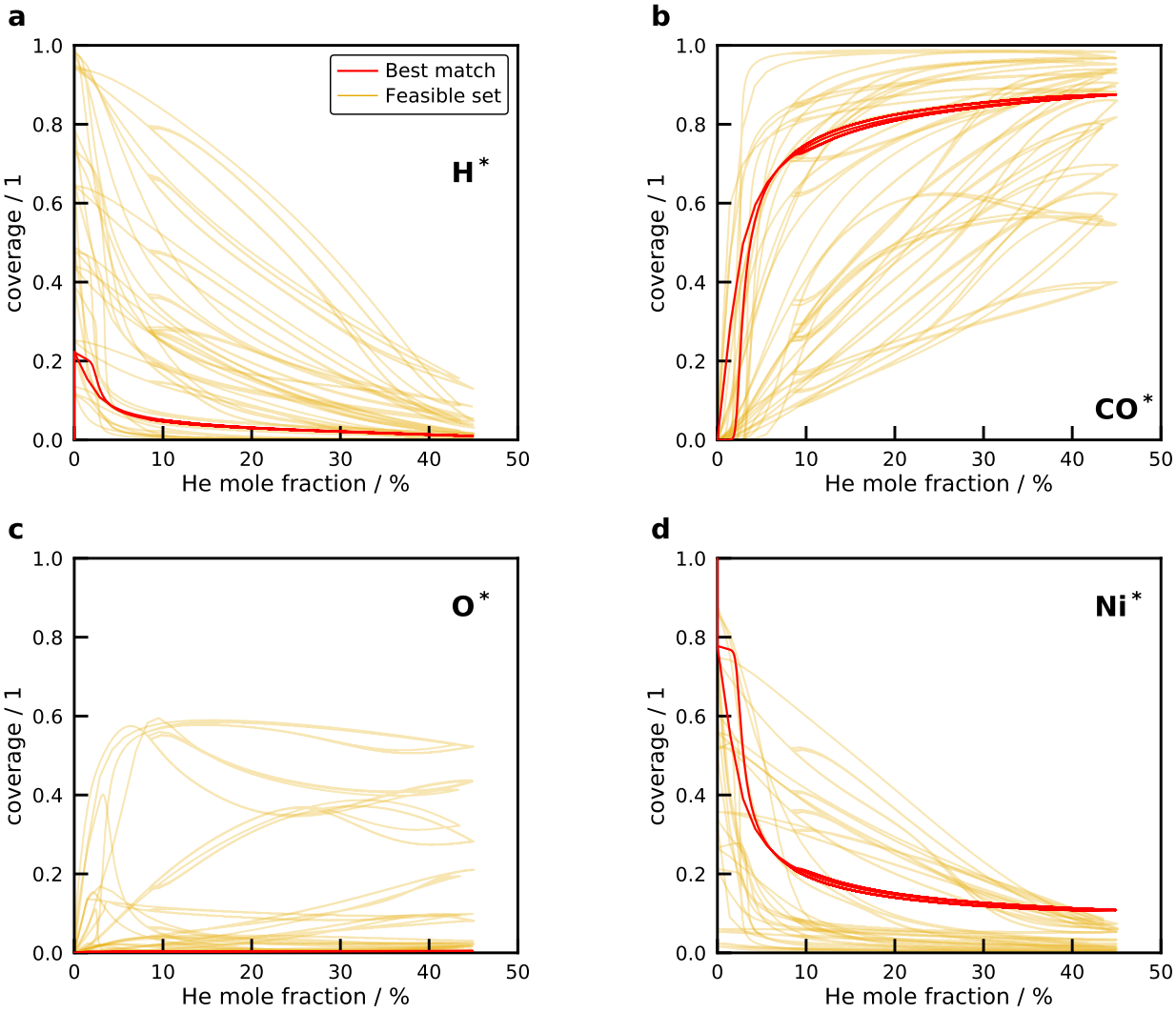

Figure 7.9.: Phase plane diagrams of the surface coverage of (a) H^*, (b) CO^*, (c) O^*, and (d) vacant sites (Ni^*) for a cycle split ratio of $\gamma = 0.5$. The red line shows the best match and the yellow lines illustrate all mechanisms from the feasible set.

Simulations with all mechanisms in the feasible set reveal an extensive spread of solutions, although the gas-phase concentrations do not vary that much. The same behavior was obtained in Chapter 6 of the thesis. A high O^* coverage is observed for some sets of parameters and even complete H^* coverage in the H_2 period. These results, in combination with Chapter 6, indicate that the surface coverage is susceptible to small perturbations within a relatively narrow uncertainty range and an *a priori* prediction of a MASI is not possible. This can also drastically change during the transient operation, which further challenges the assumption of a constant MASI in the steady-state LHHW kinetics.

In analogy with Chapter 6, it is now interesting to see which are the main pathways for CH_4 formation. The important reaction network for the best match to the transient experiments is illustrated in Figure 7.10a. Figure 7.10b displays the reaction path analysis for the mechanism with the best agreement to the temperature-scanning experiments from Chapter 6. The main difference in both mechanisms is the activation of CO_2^*. Activation of CO_2^* occurs only at a significant rate through the direct dissociation

to CO^*, which differs from the result in Chapter 6. The new reaction path analysis shows that CO^* desorption occurs, which is also obtained from the simulation. Similar to the reaction path in Chapter 6, the main path for methane formation is via the formation of formyl (HCO^*) and the HC=O fission to CH^*. In contrast, a small contribution to methylidyne formation comes from the unassisted dissociation of CO^* and the hydrogenation of C^*, which is the carbide pathway. Interestingly, carboxyl is present in the reaction path in Figure 7.10a and it produces CO^* from HCO^*. HCO^* reacts to COH^* via abstraction of H^* in $HCO^* + CO^* \rightleftharpoons COH^* + CO^*$, which is then oxidized to $COOH^*$. Looking at all reaction paths diagrams from the feasible set confirms that the main methane formation pathway is always via the direct dissociation of CO_2^* and the hydrogen-assisted dissociation of CO^*. Some mechanisms exhibit a small contribution from the redox path with a direct dissociation of CO^*. Whether this results from the higher pressure or a consequence of the variety in the gas-phase concentration cannot be elucidated. The reaction path analysis shows that although the simulation results of the new best match and the one from Chapter 6 are different, the main reaction pathway for methane formation is still the same.

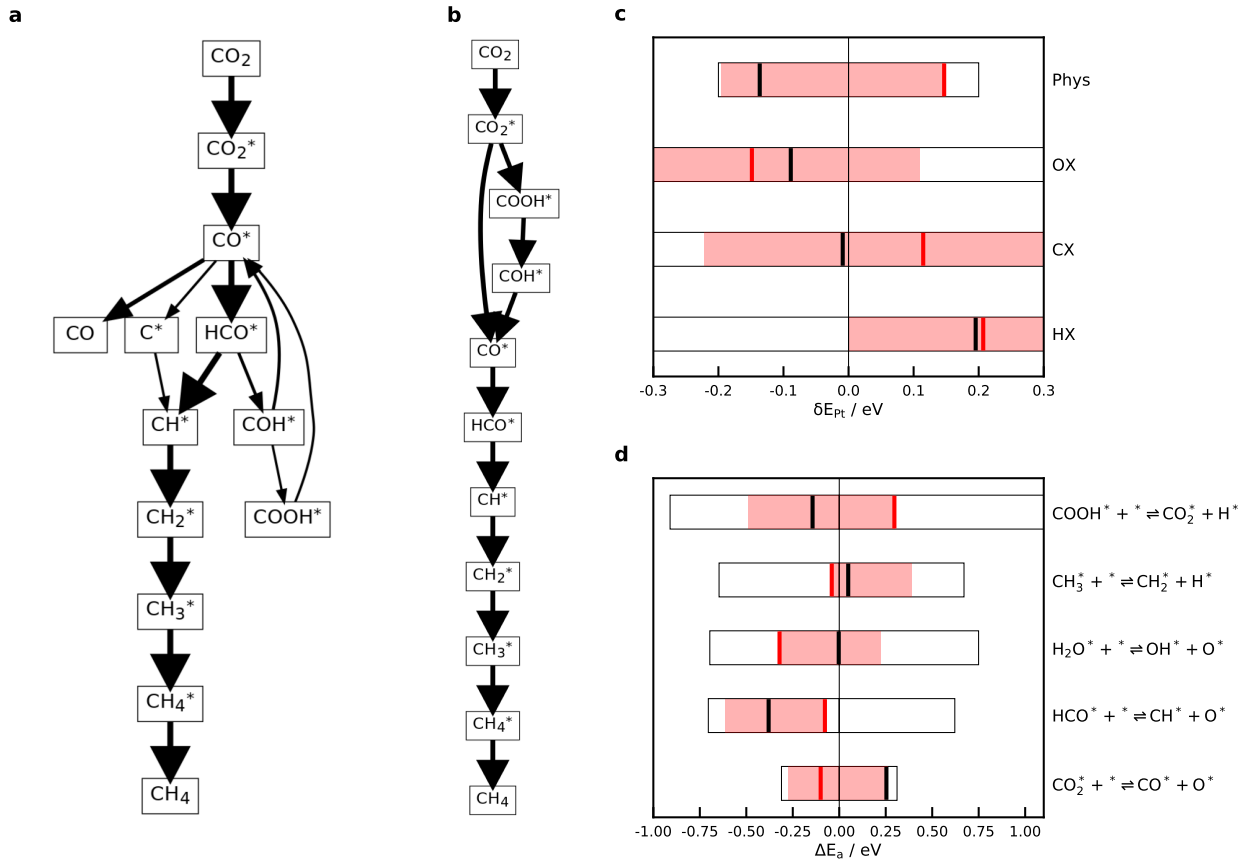

Figure 7.10.: (a) Reaction path of the mechanism in best agreement with the transient experiments including only the kinetically significant pathways. (b) Reaction path of the mechanism in best agreement with the temperature-scanning experiments in Chapter 6. (c) Values for the linear scaling descriptor species and d) the kinetic parameters for the most important reactions. The black box shows the possible range of values and the pink area the values from the feasible sets.

The temperature-scanning experiments in Chapter 4 showed a carbon build-up at high temperatures, which caused the decrease in activity between consecutive runs. Further, Galhardo et al. [36] provide experimental evidence for C^* deposition on Ni/SiO_2 catalysts during CO_2 methanation. However, the simulations in Chapter 6 and also the transient simulations with the model at a temperature of 573 K

show no significant coverage of C^*. This indicates that the direct dissociation of CO^* is too slow to create a carbon pool on the catalyst because of the substantially higher activation barrier compared to the H-assisted dissociation of CO^*. Consequently, it can be hypothesized that the carbon observed in Chapter 4 is formed at the steps and kinks of the Ni crystal in the experiment, which provide lower activation barriers for the C=O scission [100]. Whether the carbon migrates to the terrace site via surface diffusion cannot be elucidated and requires further investigations. For the microkinetic model to capture such effects, it is necessary to include multiple active sites with their own microkinetic model and additional elementary steps for surface diffusion. Overall, the feasible set in Chapter 6 and in this chapter show the identical active pathway for CH_4 formation.

Figure 7.10d,e shows the range of parameters for the feasible set for the four thermochemistry descriptor species and the most important reactions according to the local sensitivity analysis in Chapter 6. Similar to Chapter 6, there is only a grouping of parameters for the binding energy of H^* whereas the other parameters vary almost over the entire uncertainty range. The feasible set shows that it is necessary to decrease the binding energy of H^*. This destabilization allows CO_2^* to adsorb so that a sufficient CO^* coverage can occur. Looking at the parameters for the feasible set in Figure 7.10d,e shows that the activation barrier for HCO^* dissociation and CH_3^* dissociation show a clear grouping. For a good description of the experimental data, it is necessary that the activation barrier for the HCO^* dissociation is decreased, which means that the reaction is made faster. The global sensitivity analysis in Chapter 6 revealed that methane is only formed when the barrier for this reaction is decreased and H^* is destabilized at the same time. Figure 7.10 shows that these two parameters are determining the activity of the Ni(111) facet for the transient simulations as well. Although the set of parameters for the microkinetic model with the best agreement to the transient and temperature-scanning experiments differ, the same two parameters still control the methane formation. Therefore, the aim of future studies should be directed to refine the binding energy and the activation barrier for the HCO^* dissociation with experimental values for Ni(111) [94] or more accurate DFT methods [138, 139]. The results from this chapter further strengthen the hypothesis that the CO_2 methanation on Ni(111) proceeds mostly via unassisted dissociation of CO_2^* and the H-assisted dissociation of CO^*.

"Don't adventures ever have an end?
I suppose not."

(Bilbo Baggins, The Fellowship of the Ring, J.R.R. Tolkien)

CHAPTER 8

Conclusion and Outlook

8.1. Conclusion

The transient operation of CO_2 methanation reactors becomes increasingly important with its usage in the Power-to-Gas process to store large amounts of renewable energy in the form of chemical bonds. This dynamic operation does not only impose various challenges on the reactor operation. It also reveals that the standard methods in reaction engineering to describe the dynamic processes in the reactor and on the catalyst surface need to be revisited. A simulation scenario of a microstructured fixed-bed reactor under dynamic concentration changes was conducted with a detailed heterogeneous model with state-of-the-art Langmuir-Hinshelwood-Hougen-Watson methanation kinetics, which showed large variations in the hot-spot temperature and the produced methane quality. This vast range of variations is caused by the fast reaction kinetics of the CO_2 methanation on Ni catalysts and the high amount of released heat. Although the reaction kinetics are the crucial parameter of the model, the lumped kinetic approaches are only simplified descriptions of the mechanism on the catalyst surface regressed to steady-state experiments. Consequently, they lack predictive power for conditions outside the regressed parameter space and ultimately fail to account for transient effects on the catalyst surface. The dynamic processes on the catalyst and in the reactor can only be quantified with a correct microkinetic model of the CO_2 methanation for the Ni catalyst, where each elementary step of the reaction mechanism is considered. Therefore, a detailed microkinetic analysis of the transient CO_2 methanation on Ni was conducted within this work.

When developing microkinetics for the CO_2 methanation, it is necessary to perform experiments on catalysts where the reactions occur only at the Ni surface. This is a challenge for the CO_2 methanation because CO_2 readily interacts with basic adsorption sites on the support. Ni/SiO_2 and Ni/Al_2O_3 catalysts were produced with a spray-drying method and investigated with temperature-programmed desorption (TPD) and temperature-scanning experiments for the CO_2 methanation. The transient screening experiments allow to explore the activity of the catalyst over the entire temperature range of interest in a significantly shorter time compared to the typical steady-state experiments. The spray-drying methods produced highly active Ni/SiO_2 catalysts with large metal surface areas, whereas the Ni/Al_2O_3 catalysts showed low metal surface areas due to ample Ni aluminate formation. Still, the Ni/Al_2O_3 catalysts exhibited a high activity because of the contribution of the basic sites on the support, which can provide pathways with lower activation barriers at the metal/support interface. Therefore, they are not suited for a microkinetic investigation and the transient kinetic experiments were conducted with a Ni/SiO_2 catalyst instead.

The microkinetic investigation of the methanation with first-principles requires the assumption of a single active Ni facet. As demonstrated in the reviewed literature, the active site for the CO_2 methanation is controversially discussed. However, the Ni crystals on the silica support of the produced catalysts

consist of a contribution of different facets, which determine the shape of the nanometer-sized crystal. This problem is well known as the materials gap in heterogeneous catalysis. It is currently not computationally feasible to perform DFT calculations considering the large nanoparticles on the support. Instead, periodically repeated supercells are used for the electronic structure calculations. For a fair comparison of the first-principles-based microkinetic model with experiments from supported Ni catalysts, it is consequently necessary to include multiple facets into the model. Such a multifaceted and multiscale model was developed within this work, considering the four most important Ni facets. The equilibrium shape of the Ni crystal was theoretically determined using a Wulff construction and used to simulate the TPD experiments. Energetic parameters of the microkinetic model derived from DFT calculations are not exact and possess a relatively large uncertainty. When this uncertainty is propagated to the model predictions, it is possible to identify feasible sets of model parameters that can predict the TPD profiles with reasonable accuracy. Thereby, new insights on the interaction of CO_2 with the different Ni facets can be provided. The multifaceted microkinetic model considering uncertainty revealed that desorption from basic sites and the Ni surface have similar desorption kinetics. Based on the model, it could be concluded that the Ni(111) facet can play an essential role in the adsorption and, thus, the activation of CO_2 on the Ni surface.

That is why the Ni(111) facet was used for the automated generation of methanation mechanisms with the Reaction Mechanism Generator. Based on the model of the TPD experiments and the impact of uncertainty on the model predictions, the uncertainty in the DFT-derived databases was directly included in the generation procedure considering the correlation among the parameters. 5,000 possible methanation mechanisms were generated in a Monte Carlo approach to discover all the possible CO_2 hydrogenation chemistry on Ni(111). From all these mechanisms, feasible sets of parameters exist that can, without any fitting procedure, describe the experimental results on a Ni/SiO_2 catalyst from temperature-scanning experiments in a differential fixed-bed reactor and from transient experiments in a Berty reactor. Merging all discovered mechanisms into a single microkinetic creates the most sophisticated microkinetic model for the CO_2 methanation. The model is thermodynamically consistent at all operating conditions and includes, for the first time, the formation of C_2H_6. Furthermore, this model extends all published microkinetic models and includes new reactions, especially bimolecular-to-bimolecular reactions, which have not been considered so far. The automated mechanism generation procedure conducted in this thesis highlights that the impact of the systematic uncertainty in the DFT methods can significantly affect the mechanistic predictions and simulation results. It reveals that the role of the Ni(111) facet in the methanation mechanism cannot be conclusively determined, but a DFT investigation of the Ni(111) facet cannot be more conclusive either because the assumed uncertainty in this thesis is based on the accuracy of present DFT methods. The study also shows that identifying rate-controlling steps or intermediates with the degree of rate control can be misleading if the uncertainty in the model parameters is not considered. Compared to the DFT-based approach of mechanism generation, this procedure is computationally cheap and unbiased from the researcher's expectations. Although the uncertainty in present-day DFT methods is considerable and leads to a broad spread of results, it is still possible to gain insights into the mechanism. In combination with global and local sensitivity methods, the actual factors that control the methanation activity were derived, which are the HCO^* dissociation barrier and the heat of formation of H^* on Ni(111) that can now be refined with higher-level DFT methods or suitable experiments on Ni(111) crystals.

Feasible sets of microkinetic models exist that can describe the temperature-scanning or transient experiments with remarkable accuracy, but this is not the main product or conclusion of this work, primarily because of open questions and simplifications in the microkinetic model. Instead, the developed methods, especially the automated construction of the reaction networks combined with correlated uncertainty, provide a powerful tool. In principle, the methods can easily be extended to other heterogeneously catalyzed reactions to determine the possible mechanism and identify the crucial parameters that determine the activity of the material. The proposed methodology of mechanism generation is completely honest with the accuracy of first-principles-based methods and demonstrates that results can be easily overinterpreted if uncertainty is neglected. A very promising application is the usage of automated mechanism generation in combination with the typical catalyst screening approach, which is usually based on simplified and incomplete models. For each material in the screening study, it is possible to derive an extensive microkinetic model including all the relevant chemistry at significantly reduced computational costs. This allows to truly advance the predictive power of linear scaling and Brønsted-Evans-Polanyi relations and can help to discover more active or selective materials.

8.2. Outlook

Although a microkinetic model for the CO_2 methanation was successfully developed that can describe transient methanation experiments with reasonable accuracy, there are still open points to address. Currently, the model cannot accurately predict the measured CO concentration profiles either in the temperature-scanning or the transient methanation experiment. It is necessary to include coverage effects in the mechanism to achieve a better description of the selectivity. Coverage effects influence the binding strength and thus the heat of formation of the adsorbates. Usually, coverage effects show repulsive interactions lowering the binding strength, which would lead to a higher rate for CO desorption, especially in H_2 lean conditions, when the coverage is high and high selectivity towards CO is observed. In addition, coverage also has an influence on the transition state, which affects activation barriers (potential energy) and pre-exponential coefficients (vibrational frequencies) of elementary reactions. Therefore, it is necessary to include coverage effects not only for the thermochemistry but also for the reaction kinetics. These points show that coverage effects have a tangible impact on the microkinetics and should also be included in the mechanism generation procedure. Next to coverage dependence, the comparison of the generated models with the experiments reveals further needs for improvement of RMG. In the industrial reactor, the methanation catalyst will most often be Ni/γ-Al_2O_3 due to the superior activity because of the participation of basic sites at the metal/support interface in CO_2 activation. Therefore, it is necessary to include support effects and multiple active sites in the generation procedure. Also, at higher pressures, Eley-Rideal type reactions may become more important, which are currently not considered due to the lack of suitable families and first-principles kinetic parameters.

Another substantial simplification in this work is using a single Ni facet for the simulation of the methanation experiments. For a valid comparison of microkinetic models with experiments on supported catalysts, it is necessary to consider all the relevant facets, as shown by the TPD simulations. The procedure described in this thesis can now be applied for all the remaining facets (Ni(100), Ni(110), and Ni(211)) to generate the possible mechanism under consideration of correlated uncertainties. These mechanisms must then be combined in a multifaceted microkinetic model and compared to transient

CO_2 methanation experiments for validation. Currently, RMG contains only a database for the thermochemistry on the Ni(111) facet. It will be necessary to include new databases for thermochemistry and kinetics on the other facets.

A most likely methanation mechanism for the Ni(111) facet was predicted in this thesis that accounts for most of the CH_4 production at all conditions. The first step to refine this mechanism is to perform DFT calculations or single-crystal experiments to access the thermochemistry of all adsorbates and the activation barriers of the transition states. This will provide more accurate thermochemistry and kinetic parameters. However, even with results from full DFT calculations, a quantification of the uncertainty is still necessary.

The consideration of correlations among the thermodynamic and kinetic parameters is a simplified method of the actual uncertainty correlation. Estimations of the error ensemble with the BEEF-vdW functional for the descriptor species and some adsorbates revealed significantly larger uncertainties. Moreover, the shape of the uncertainty domain deviates considerably from the uniform boundaries. A refinement of the mechanism generation procedure under consideration can be obtained by sampling directly from the DFT-derived uncertainty density distribution.

Ultimately, the goal will be to incorporate the automatically generated microkinetics for all important Ni facets into a multifaceted microkinetic model -including coverage effects-, which is then used in a detailed multiscale model of the reactor setup with a heterogeneous one-dimensional reactor model or computational fluid dynamics simulations. Although very ambitious, this detailed multiscale model can then be used to simulate and design methanation reactors for Power-to-Gas plants with real wind power signals from first-principles.

References

[1] C. McGlade, P. Ekins. *Nature* **2015**, 517 (7533), 187–190. DOI: 10.1038/nature14016.

[2] B. J. van Ruijven, E. de Cian, I. Sue Wing. *Nat. commun.* **2019**, 10 (1), 2762. DOI: 10.1038/s41467-019-10399-3.

[3] Q. Schiermeier, J. Tollefson, T. Scully, A. Witze, O. Morton. *Nature* **2008**, 454 (7206), 816–823. DOI: 10.1038/454816a.

[4] R. Schlögl. *Angew. Chem. Int. Ed.* **2015**, 54 (15), 4436–4439. DOI: 10.1002/anie.201405876.

[5] M. Sterner, I. Stadler. Berlin, Heidelberg: Springer Berlin Heidelberg, **2019**. DOI: 10.1007/978-3-662-55504-0.

[6] G. J. Kramer, M. Haigh. *Nature* **2009**, 462 (7273), 568–569. DOI: 10.1038/462568a.

[7] R. Dittmeyer, M. Klumpp, P. Kant, G. Ozin. *Nat. commun.* **2019**, 10 (1), 1818. DOI: 10.1038/s41467-019-09685-x.

[8] R. Schlögl. *Angew. Chem. Int. Ed.* **2017**, 56 (37), 11019–11022. DOI: 10.1002/anie.201701633.

[9] E. Billig, M. Decker, W. Benzinger, F. Ketelsen, P. Pfeifer, R. Peters, D. Stolten, D. Thrän. *J. CO2 Util.* **2019**, 30 (6331), 130–141. DOI: 10.1016/j.jcou.2019.01.012.

[10] C. Vogt, M. Monai, G. J. Kramer, B. M. Weckhuysen. *Nat. Catal.* **2019**, 2 (3), 188–197. DOI: 10.1038/s41929-019-0244-4.

[11] M. Götz, J. Lefebvre, F. Mörs, A. McDaniel Koch, F. Graf, S. Bajohr, R. Reimert, T. Kolb. *Renewable Energy* **2016**, 85, 1371–1390. DOI: 10.1016/j.renene.2015.07.066.

[12] S. Rönsch, J. Schneider, S. Matthischke, M. Schlüter, M. Götz, J. Lefebvre, P. Prabhakaran, S. Bajohr. *Fuel* **2016**, 166, 276–296. DOI: 10.1016/j.fuel.2015.10.111.

[13] T. J. Schildhauer, S. M. Biollaz, eds. Hoboken, New Jersey: Wiley, **2016**. DOI: 10.1002/9781119191339.

[14] B. Kreitz, J. Brauns, G. D. Wehinger, T. Turek. *Chem. Ing. Tech.* **2020**, 92 (12), 1992–1997. DOI: 10.1002/cite.202000019.

[15] J. Brauns, T. Turek. *Processes* **2020**, 8 (2), 248. DOI: 10.3390/pr8020248.

[16] F. Studt. *Front. Catal.* **2021**, 1, 016105. DOI: 10.3389/fctls.2021.658965.

[17] M. Salciccioli, M. Stamatakis, S. Caratzoulas, D. G. Vlachos. *Chem. Eng. Sci.* **2011**, 66 (19), 4319–4355. DOI: 10.1016/j.ces.2011.05.050.

[18] A. Bruix, J. T. Margraf, M. Andersen, K. Reuter. *Nat. Catal.* **2019**, 2 (8), 659–670. DOI: 10.1038/s41929-019-0298-3.

[19] K. F. Kalz, R. Kraehnert, M. Dvoyashkin, R. Dittmeyer, R. Gläser, U. Krewer, K. Reuter, J.-D. Grunwaldt. *ChemCatChem* **2017**, 9 (1), 17–29. DOI: https://doi.org/10.1002/cctc.201600996.

[20] M. Vannice. *J. Catal.* **1975**, 37 (3), 449–461. DOI: 10.1016/0021-9517(75)90181-5.

[21] J. Gao, Q. Liu, F. Gu, B. Liu, Z. Zhong, F. Su. *RSC Adv.* **2015**, 5 (29), 22759–22776. DOI: 10.1039/C4RA16114A.

[22] C. Vogt, J. Wijten, C. L. Madeira, O. Kerkenaar, K. Xu, R. Holzinger, M. Monai, B. M. Weckhuysen. *ChemCatChem* **2020**, 12 (10), 2792–2800. DOI: 10.1002/cctc.202000327.

[23] M. Andersson, T. Bligaard, A. L. Kustov, K. E. Larsen, J. Greeley, T. Johannessen, C. H. Christensen, J. K. Nørskov. *J. Catal.* **2006**, 239 (2), 501–506. DOI: 10.1016/j.jcat.2006.02.016.

[24] J. Sehested, K. E. Larsen, A. L. Kustov, A. M. Frey, T. Johannessen, T. Bligaard, M. P. Andersson, J. K. Nørskov, C. H. Christensen. *Top. Catal.* **2007**, 45 (1-4), 9–13. DOI: 10.1007/s11244-007-0232-9.

[25] Q. Pan, J. Peng, T. Sun, S. Wang, S. Wang. *Catal. Commun.* **2014**, 45, 74–78. DOI: 10.1016/j.catcom.2013.10.034.

[26] S. Ewald, O. Hinrichsen. *Appl. Catal., A* **2019**, 580, 71–80. DOI: 10.1016/j.apcata.2019.04.005.

[27] S. Ewald, M. Kolbeck, T. Kratky, M. Wolf, O. Hinrichsen. *Appl. Catal., A* **2019**, 570, 376–386. DOI: 10.1016/j.apcata.2018.10.033.

[28] M. Cabrejas Manchado, J. M. Guil, A. Pérez Masiá, A. Ruiz Paniego, J. M. Trejo Menayo. *Langmuir* **1994**, 10 (3), 685–691. DOI: 10.1021/la00015a016.

[29] N. Schreiter, J. Kirchner, S. Kureti. *Catal. Commun.* **2020**, 140, 105988. DOI: 10.1016/j.catcom.2020.105988.

[30] M.-C. Silaghi, A. Comas-Vives, C. Copéret. *ACS Catal.* **2016**, 6 (7), 4501–4505. DOI: 10.1021/acscatal.6b00822.

[31] L. Foppa, T. Margossian, S. M. Kim, C. Müller, C. Copéret, K. Larmier, A. Comas-Vives. *J. Am. Chem. Soc.* **2017**, 139 (47), 17128–17139. DOI: 10.1021/jacs.7b08984.

[32] J. Gao, Y. Wang, Y. Ping, D. Hu, G. Xu, F. Gu, F. Su. *RSC Adv.* **2012**, 2 (6), 2358. DOI: 10.1039/c2ra00632d.

[33] J. Kopyscinski, T. J. Schildhauer, S. M. Biollaz. *Chem. Eng. Sci.* **2011**, 66 (5), 924–934. DOI: 10.1016/j.ces.2010.11.042.

[34] J. Kopyscinski, T. J. Schildhauer, S. M. Biollaz. *Chem. Eng. Sci.* **2011**, 66 (8), 1612–1621. DOI: 10.1016/j.ces.2010.12.029.

[35] J. Lefebvre, S. Bajohr, T. Kolb. *Renewable Energy* **2020**, 151 (1), 118–136. DOI: 10.1016/j.renene.2019.11.008.

[36] T. S. Galhardo, A. H. Braga, B. H. Arpini, J. Szanyi, R. V. Gonçalves, B. F. Zornio, C. R. Miranda, L. M. Rossi. *J. Am. Chem. Soc.* **2021**, 143 (11), 4268–4280. DOI: 10.1021/jacs.0c12689.

[37] L. Kiewidt, J. Thöming. *Chem. Eng. Sci.* **2015**, 132, 59–71. DOI: 10.1016/j.ces.2015.03.068.

[38] D. Schlereth, O. Hinrichsen. *Chem. Eng. Res. Des.* **2014**, 92 (4), 702–712. DOI: 10.1016/j.cherd.2013.11.014.

[39] E. Klemm, H. Döring, A. Geisselmann, S. Schirrmeister. *Chem. Eng. Technol.* **2007**, 30 (12), 1615–1621. DOI: 10.1002/ceat.200700311.

[40] R. Güttel, T. Turek. *Chem. Eng. Sci.* **2010**, 65 (5), 1644–1654. DOI: 10.1016/j.ces.2009.11.002.

[41] R. Güttel, T. Turek. *Chem. Eng. Sci.* **2009**, 64 (5), 955–964. DOI: 10.1016/j.ces.2008.10.059.

[42] M. Loewert, J. Hoffmann, P. Piermartini, M. Selinsek, R. Dittmeyer, P. Pfeifer. *Chem. Eng. Technol.* **2019**, 42 (10), 2202–2214. DOI: 10.1002/ceat.201900136.

[43] R. Schlögl. *ChemCatChem* **2017**, 9 (4), 533–541. DOI: 10.1002/cctc.201700026.

[44] G. Ertl. *Angew. Chem., Int. Ed. Engl.* **2008**, 47 (19), 3524–3535. DOI: 10.1002/anie.200800480.

[45] A. Banerjee, V. Navarro, J. W. M. Frenken, A. P. van Bavel, H. P. C. E. Kuipers, M. Saeys. *J. Phys. Chem. Lett.* **2016**, 7 (11), 1996–2001. DOI: 10.1021/acs.jpclett.6b00555.

[46] B. Mutz, A. Gänzler, M. Nachtegaal, O. Müller, R. Frahm, W. Kleist, J.-D. Grunwaldt. *Catalysts* **2017**, 7 (9), 279. DOI: 10.3390/catal7090279.

[47] K. Robinson, S. Ye, Y. Yap, S. T. Kolaczkowski. *Chem. Eng. Res. Des.* **2013**, 91 (7), 1292–1306. DOI: 10.1016/j.cherd.2013.02.022.

[48] P. L. Silveston, R. R. Hudgins, eds. 1. ed. IChemE Advancing chemical engineering worldwide. Amsterdam and Waltham, Mass.: Elsevier and Butterworth-Heinemann, **2013**.

[49] M. A. Ardagh, O. A. Abdelrahman, P. J. Dauenhauer. *ACS Catal.* **2019**, 9 (8), 6929–6937. DOI: 10.1021/acscatal.9b01606.

[50] M. A. Ardagh, T. Birol, Q. Zhang, O. A. Abdelrahman, P. J. Dauenhauer. *Catal. Sci. Technol.* **2019**, 9 (18), 5058–5076. DOI: 10.1039/C9CY01543D.

[51] M. A. Ardagh, M. Shetty, A. Kuznetsov, Q. Zhang, P. Christopher, D. G. Vlachos, O. A. Abdelrahman, P. J. Dauenhauer. *Chem. Sci.* **2020**, 11 (13), 3501–3510. DOI: 10.1039/C9SC06140A.

[52] C. D. Armstrong, A. R. Teixeira. *React. Chem. Eng.* **2020**, 5 (12), 2185–2203. DOI: 10.1039/D0RE00330A.

[53] A. K. Jain, R. R. Hudgins, P. L. Silveston. *Can. J. Chem. Eng.* **1983**, 61 (6), 824–832. DOI: 10.1002/cjce.5450610609.

[54] K. G. Chanchlani, R. R. Hudgins, P. L. Silveston. *Can. J. Chem. Eng.* **1994**, 72 (4), 657–671. DOI: 10.1002/cjce.5450720416.

[55] R. Underwood, C. Bennett. *J. Catal.* **1984**, 86 (2), 245–253. DOI: 10.1016/0021-9517(84)90370-1.

[56] K. Klusáček, V. Stuchlý. *Catal. Today* **1995**, 25 (2), 169–174. DOI: 10.1016/0920-5861(95)00106-P.

[57] V. Stuchly, K. Klusacek. *J. Catal.* **1993**, 139 (1), 62–71. DOI: 10.1006/jcat.1993.1007.

[58] P. I. Lee, J. A. Schwarz. *Ind. Eng. Chem. Process Des. Dev.* **1986**, 25 (1), 76–83. DOI: 10.1021/i200032a013.

[59] M. Marwood, F. van Vyve, R. Doepper, A. Renken. *Catal. Today* **1994**, 20 (3), 437–448. DOI: 10.1016/0920-5861(94)80137-1.

[60] M. Marwood, R. Doepper, A. Renken. *Can. J. Chem. Eng.* **1996**, 74 (5), 660–663. DOI: 10.1002/cjce.5450740516.

[61] M. Marwood, R. Doepper, A. Renken. *Appl. Catal., A* **1997**, 151 (1), 223–246. DOI: 10.1016/S0926-860X(96)00267-0.

[62] B. Kreitz, J. Friedland, R. Güttel, G. D. Wehinger, T. Turek. *Chem. Ing. Tech.* **2019**, 91 (5), 576–582. DOI: 10.1002/cite.201800191.

[63] B. M. Weckhuysen. *Chem. Comm.* **2002**, (2), 97–110. DOI: 10.1039/b107686h.

[64] M. A. Bañares. *Catal. Today* **2005**, 100 (1-2), 71–77. DOI: 10.1016/j.cattod.2004.12.017.

[65] J. T. Gleaves, G. S. Yablonskii, P. Phanawadee, Y. Schuurman. *Appl. Catal., A* **1997**, 160 (1), 55–88. DOI: 10.1016/S0926-860X(97)00124-5.

[66] J. T. Gleaves, J. R. Ebner, T. C. Kuechler. *Catalysis Reviews* **1988**, 30 (1), 49–116. DOI: 10.1080/01614948808078616.

[67] J. T. Gleaves, G. Yablonsky, X. Zheng, R. Fushimi, P. L. Mills. *J. Mol. Catal. A: Chem.* **2010**, 315 (2), 108–134. DOI: 10.1016/j.molcata.2009.06.017.

[68] A. Raub, H. Karroum, M. Athariboroujeny, N. Kruse. *Catal. Lett.* **2021**, 151 (3), 613–626. DOI: 10.1007/s10562-020-03294-w.

[69] A. Bundhoo, J. Schweicher, A. Frennet, N. Kruse. *J. Phys. Chem. C* **2009**, 113 (24), 10731–10739. DOI: 10.1021/jp902647z.

[70] E. Vesselli, J. Schweicher, A. Bundhoo, A. Frennet, N. Kruse. *J. Phys. Chem. C* **2011**, 115 (4), 1255–1260. DOI: 10.1021/jp106551r.

[71] D. Meyer, J. Friedland, J. Schumacher, R. Güttel. *Chem. Eng. Res. Des.* **2021**, 173, 253–266. DOI: 10.1016/j.cherd.2021.07.011.

[72] C. Ledesma, J. Yang, D. Chen, A. Holmen. *ACS Catal.* **2014**, 4 (12), 4527–4547. DOI: 10.1021/cs501264f.

[73] L. M. Aparicio. *J. Catal.* **1997**, 165 (2), 262–274. DOI: 10.1006/jcat.1997.1468.

[74] J. L. Falconer, J. A. Schwarz. *Catal. Rev.* **2007**, 25 (2), 141–227. DOI: 10.1080/01614948308079666.

[75] S. Matthischke, R. Krüger, S. Rönsch, R. Güttel. *Fuel Process. Technol.* **2016**, 153, 87–93. DOI: 10.1016/j.fuproc.2016.07.021.

[76] S. Matthischke, S. Roensch, R. Güttel. *Ind. Eng. Chem. Res.* **2018**, 57 (18), 6391–6400. DOI: 10.1021/acs.iecr.8b00755.

[77] J. Bremer, K. H. G. Rätze, K. Sundmacher. *AIChE J.* **2017**, 63 (1), 23–31. DOI: 10.1002/aic.15496.

[78] S. Theurich, S. Rönsch, R. Güttel. *Energy Technol* **2020**, 8 (3), 1901116. DOI: 10.1002/ente.201901116.

[79] J. Bremer, K. Sundmacher. *React. Chem. Eng.* **2019**, 4 (6), 1019–1037. DOI: 10.1039/C9RE00147F.

[80] K. L. Fischer, M. R. Langer, H. Freund. *Ind. Eng. Chem. Res.* **2019**, 58 (42), 19406–19420. DOI: 10.1021/acs.iecr.9b02863.

[81] K. L. Fischer, H. Freund. *Chem. Eng. J.* **2020**, 393 (2), 124722. DOI: 10.1016/j.cej.2020.124722.
[82] K. L. Fischer, H. Freund. *Chem. Eng. Process.* **2021**, 159, 108183. DOI: 10.1016/j.cep.2020.108183.
[83] R. T. Zimmermann, J. Bremer, K. Sundmacher. *Chem. Eng. J.* **2021**, 166 (1), 130771. DOI: 10.1016/j.cej.2021.130771.
[84] G. D. Weatherbee, C. H. Bartholomew. *J. Catal.* **1982**, (77), 460–472.
[85] F. Koschany, D. Schlereth, O. Hinrichsen. *Appl. Catal., B* **2016**, 181, 504–516. DOI: 10.1016/j.apcatb.2015.07.026.
[86] J. A. Hernandez Lalinde, P. Roongruangsree, J. Ilsemann, M. Bäumer, J. Kopyscinski. *Chem. Eng. J.* **2020**, 390, 124629. DOI: 10.1016/j.cej.2020.124629.
[87] J. Kopyscinski, T. J. Schildhauer, F. Vogel, S. M. Biollaz, A. Wokaun. *J. Catal.* **2010**, 271 (2), 262–279. DOI: 10.1016/j.jcat.2010.02.008.
[88] J. Xu, G. F. Froment. *AIChE J.* **1989**, 35 (1), 88–96. DOI: 10.1002/aic.690350109.
[89] D. Meyer, J. Schumacher, J. Friedland, R. Güttel. *Ind. Eng. Chem. Res.* **2020**, 59 (33), 14668–14678. DOI: 10.1021/acs.iecr.0c02072.
[90] T. Burger, P. Donaubauer, O. Hinrichsen. *Appl. Catal., B* **2021**, 282 (75), 119408. DOI: 10.1016/j.apcatb.2020.119408.
[91] W. H. Green. *AIChE J.* **2020**, 66 (11), 81. DOI: 10.1002/aic.17059.
[92] R. T. Zimmermann, J. Bremer, K. Sundmacher. *Chem. Eng. J.* **2020**, 387, 123704. DOI: 10.1016/j.cej.2019.123704.
[93] B. Temel, H. Meskine, K. Reuter, M. Scheffler, H. Metiu. *J. Chem. Phys.* **2007**, 126 (20), 204711. DOI: 10.1063/1.2741556.
[94] C. Reece, R. J. Madix. *ACS Catal.* **2021**, 11 (5), 3048–3066. DOI: 10.1021/acscatal.0c05173.
[95] J. Friedland. PhD thesis. TU Clausthal, **2020**.
[96] A. H. Motagamwala, J. A. Dumesic. *Chem. Rev.* **2021**, 121 (2), 1049–1076. DOI: 10.1021/acs.chemrev.0c00394.
[97] S. Matera, W. F. Schneider, A. Heyden, A. Savara. *ACS Catal.* **2019**, 9 (8), 6624–6647. DOI: 10.1021/acscatal.9b01234.
[98] P. Lozano-Reis, H. Prats, P. Gamallo, F. Illas, R. Sayós. *ACS Catal.* **2020**, 10 (15), 8077–8089. DOI: 10.1021/acscatal.0c01599.
[99] M. P. Andersson, F. Abild-Pedersen, I. N. Remediakis, T. Bligaard, G. Jones, J. Engbæk, O. Lytken, S. Horch, J. H. Nielsen, J. Sehested. *J. Catal.* **2008**, 255 (1), 6–19. DOI: 10.1016/j.jcat.2007.12.016.
[100] C. Vogt et al. *Nat. Commun.* **2019**, 10 (1), 5330. DOI: 10.1038/s41467-019-12858-3.
[101] C. Zhi, Q. Wang, B. Wang, D. Li, R. Zhang. *RSC Adv.* **2015**, 5 (82), 66742–66756. DOI: 10.1039/C4RA17096B.
[102] M. Zhou, B. Liu. *ChemCatChem* **2015**, 7 (23), 3928–3935. DOI: 10.1002/cctc.201500547.
[103] J. Ren, H. Guo, J. Yang, Z. Qin, J. Lin, Z. Li. *Appl. Surf. Sci.* **2015**, 351, 504–516. DOI: 10.1016/j.apsusc.2015.05.173.
[104] O. Mohan, S. Shambhawi, R. Xu, A. A. Lapkin, S. H. Mushrif. *ChemCatChem* **2021**, 13 (10), 2420–2433. DOI: 10.1002/cctc.202100073.
[105] W.-B. Zhang, C. Chen, S.-Y. Zhang. *J. Phys. Chem. C* **2013**, 117 (41), 21274–21280. DOI: 10.1021/jp404569m.
[106] D. Beierlein, D. Häussermann, M. Pfeifer, T. Schwarz, K. Stöwe, Y. Traa, E. Klemm. *Appl. Catal., B* **2019**, 247, 200–219. DOI: 10.1016/j.apcatb.2018.12.064.
[107] C. Vogt, E. Groeneveld, G. Kamsma, M. Nachtegaal, L. Lu, C. J. Kiely, P. H. Berben, F. Meirer, B. M. Weckhuysen. *Nat. Catal.* **2018**, 1 (2), 127–134. DOI: 10.1038/s41929-017-0016-y.
[108] K. Delgado, L. Maier, S. Tischer, A. Zellner, H. Stotz, O. Deutschmann. *Catalysts* **2015**, 5 (2), 871–904. DOI: 10.3390/catal5020871.

[109] D. Schmider, L. Maier, O. Deutschmann. *Ind. Eng. Chem. Res.* **2021**, 134, 689. DOI: 10.1021/acs.iecr.1c00389.

[110] D. W. Blaylock, T. Ogura, W. H. Green, G. J. O. Beran. *J. Phys. Chem. C.* **2009**, 113 (12), 4898–4908. DOI: 10.1021/jp806527q.

[111] D. W. Blaylock, Y.-A. Zhu, W. H. Green. *Top. Catal.* **2011**, 54 (13-15), 828–844. DOI: 10.1007/s11244-011-9704-z.

[112] H. Wang, D. A. Sheen. *Prog. Energy Combust. Sci.* **2015**, 47, 1–31. DOI: 10.1016/j.pecs.2014.10.002.

[113] J. Wellendorff, T. L. Silbaugh, D. Garcia-Pintos, J. K. Nørskov, T. Bligaard, F. Studt, C. T. Campbell. *Surf. Sci.* **2015**, 640, 36–44. DOI: 10.1016/j.susc.2015.03.023.

[114] F. Abild-Pedersen, J. Greeley, F. Studt, J. Rossmeisl, T. R. Munter, P. G. Moses, E. Skúlason, T. Bligaard, J. K. Nørskov. *Phys. Rev. Lett.* **2007**, 99 (1), 016105. DOI: 10.1103/PhysRevLett.99.016105.

[115] A. C. Lausche, A. J. Medford, T. S. Khan, Y. Xu, T. Bligaard, F. Abild-Pedersen, J. K. Nørskov, F. Studt. *J. Catal.* **2013**, 307, 275–282. DOI: 10.1016/j.jcat.2013.08.002.

[116] J. Sehested, S. Dahl, J. Jacobsen, J. R. Rostrup-Nielsen. *J. Phys. Chem.. B* **2005**, 109 (6), 2432–2438. DOI: 10.1021/jp040239s.

[117] C. W. Gao, J. W. Allen, W. H. Green, R. H. West. *Comput. Phys. Commun.* **2016**, 203, 212–225. DOI: 10.1016/j.cpc.2016.02.013.

[118] C. F. Goldsmith, R. H. West. *J. Phys. Chem. C* **2017**, 121 (18), 9970–9981. DOI: 10.1021/acs.jpcc.7b02133.

[119] M. Liu et al. *J. Chem. Inf. Model.* **2021**, 61 (6), 2686–2696. DOI: 10.1021/acs.jcim.0c01480.

[120] G. R. Magoon, W. H. Green. *Comput. Chem. Eng.* **2013**, 52, 35–45. DOI: 10.1016/j.compchemeng.2012.11.009.

[121] N. M. Vandewiele, G. R. Magoon, K. M. van Geem, M.-F. Reyniers, W. H. Green, G. B. Marin. *Energy Fuels* **2015**, 29 (1), 413–427. DOI: 10.1021/ef502274r.

[122] F. Seyedzadeh Khanshan, R. H. West. *Fuel* **2016**, 163, 25–33. DOI: 10.1016/j.fuel.2015.09.031.

[123] K. Blondal, J. Jelic, E. Mazeau, F. Studt, R. H. West, C. F. Goldsmith. *Ind. Eng. Chem. Res.* **2019**, 58 (38), 17682–17691. DOI: 10.1021/acs.iecr.9b01464.

[124] E. J. Mazeau, P. Satpute, K. Blöndal, C. F. Goldsmith, R. H. West. *ACS Catal.* **2021**, 73, 7114–7125. DOI: 10.1021/acscatal.0c04100.

[125] S. Kattel, P. Liu, J. G. Chen. *J. Am. Chem. Soc.* **2017**, 139 (29), 9739–9754. DOI: 10.1021/jacs.7b05362.

[126] G. D. Wehinger, B. Kreitz, A. Nagy, T. Turek. *Chem. Eng. J.* **2020**, 389, 124342. DOI: 10.1016/j.cej.2020.124342.

[127] M. Haumann, M. Jakuttis, S. Werner, P. Wasserscheid. *J. Catal.* **2009**, 263 (2), 321–327. DOI: 10.1016/j.jcat.2009.02.024.

[128] J. Friedland, B. Kreitz, H. Grimm, T. Turek, R. Güttel. *ChemCatChem* **2020**, 12 (17), 4373–4386. DOI: 10.1002/cctc.202000278.

[129] R. Yadav, R. G. Rinker. *Chem. Eng. Sci.* **1990**, 45 (11), 3221–3226. DOI: 10.1016/0009-2509(90)80214-Y.

[130] D. G. Goodwin, R. L. Speth, H. K. Moffat, B. W. Weber. https://www.cantera.org. Version 2.4.0. **2018**. DOI: 10.5281/zenodo.1174508.

[131] G. Ertl, H. Knözinger, F. Schüth, J. Weitkamp. Weinheim, Germany: Wiley-VCH Verlag GmbH & Co. KGaA, **2008**. DOI: 10.1002/9783527610044.

[132] M. Löffelholz. Master thesis. TU Clausthal (unpublished). **2019**.

[133] O. Levenspiel. Morrisville, SC: lulu.com, **2013**.

[134] S. Anderson, J. Osiewacz. Group report. TU Clausthal (unpublished). **2020**.

[135] B. Kreitz, G. D. Wehinger, T. Turek. *Chem. Eng. Sci.* **2019**, 195, 541–552. DOI: 10.1016/j.ces.2018.09.053.

[136] L. C. Grabow, B. Hvolbæk, J. K. Nørskov. *Top. Catal.* **2010**, 53 (5-6), 298–310. DOI: 10.1007/s11244-010-9455-2.

[137] B. Mutz, H. W. Carvalho, S. Mangold, W. Kleist, J.-D. Grunwaldt. *J. Catal.* **2015**, 327, 48–53. DOI: 10.1016/j.jcat.2015.04.006.

[138] J. Sauer. *Acc. Chem. Res.* **2019**, 52 (12), 3502–3510. DOI: 10.1021/acs.accounts.9b00506.

[139] S. Bhandari, S. Rangarajan, M. Mavrikakis. *Acc. Chem. Res.* **2020**, 53 (9), 1893–1904. DOI: 10.1021/acs.accounts.0c00340.

APPENDIX A

Supporting Information to Chapter 3

Correlations and Properties

Properties of the cooling medium [1]:

$$c_{p,\mathrm{oil}} = \left(647.94 + 3.325 \cdot \left(\frac{T_{\mathrm{oil}}}{\mathrm{K}}\right)\right) \mathrm{J\,kg^{-1}\,K^{-1}} \tag{A.1}$$

$$\rho_{\mathrm{oil}} = \left(1308.1 - 0.9492 \cdot \left(\frac{T_{\mathrm{oil}}}{\mathrm{K}}\right)\right) \mathrm{kg\,m^{-3}} \tag{A.2}$$

$$\lambda_{\mathrm{oil}} = \left(0.1666 + 0.0001 \cdot \left(\frac{T_{\mathrm{oil}}}{\mathrm{K}}\right)\right) \mathrm{W\,m^{-1}\,K^{-1}} \tag{A.3}$$

$$\mu_{\mathrm{oil}} = \left(6 \cdot 10^{-9} \cdot \left(\frac{T_{\mathrm{oil}}}{\mathrm{K}}\right)^2 - 8 \cdot 10^{-6} \cdot \left(\frac{T_{\mathrm{oil}}}{\mathrm{K}}\right) + 0.0028\right) \mathrm{Pa\,s} \tag{A.4}$$

Viscosity of single components [2]:

$$\mu_{\mathrm{i}} = \left(\sum_{j=0}^{3} \mu_{\mathrm{i,j}} \cdot \left(\frac{\vartheta}{^{\circ}\mathrm{C}}\right)^{j}\right) \mathrm{Pa\,s} \tag{A.5}$$

	$\mu_0 \cdot 1 \times 10^{-5}$	$\mu_1 \cdot 1 \times 10^{-8}$	$\mu_2 \cdot 1 \times 10^{-11}$	$\mu_3 \cdot 1 \times 10^{-15}$
H_2	0.8337	2.202	1.1216	5.1074
CO_2	1.3799	4.8847	1.7863	3.4755
H_2O	0.8115	3.9343	0.71973	7.2056
CH_4	1.0236	3.2886	1.07925	7.0733

The viscosity of the mixture is calculated according to the Wilke approach [3].

$$\mu_{\mathrm{g}} = \sum_{i=1}^{n} \frac{y_{\mathrm{i}} \cdot \mu_{\mathrm{i}}}{\sum_{j=1}^{n} y_{\mathrm{j}} \cdot \Phi_{\mathrm{i,j}}} \tag{A.6}$$

With the parameter $\Phi_{i,j}$:

$$\Phi_{\mathrm{i,j}} = \frac{\left[1 + \left(\frac{\mu_{\mathrm{i}}}{\mu_{\mathrm{j}}}\right)^{\frac{1}{2}} \cdot \left(\frac{M_{\mathrm{j}}}{M_{\mathrm{i}}}\right)^{\frac{1}{4}}\right]^2}{\left[8 \cdot \left(1 + \frac{M_{\mathrm{i}}}{M_{\mathrm{j}}}\right)\right]^{\frac{1}{2}}} \tag{A.7}$$

Strongly coupled with the viscosity is the thermal conductivity of the gas mixture. The correlation for the calculation of the thermal conductivities of the pure components can be found in the work of Elnashaie [4].

$$\lambda_{\mathrm{i}} = 1.163 \cdot \left(\sum_{j=0}^{3} \lambda_{\mathrm{i,j}} \cdot \left(\frac{T_{\mathrm{g}}}{\mathrm{K}}\right)^{j}\right) \mathrm{W\,m^{-1}\,K^{-1}} \tag{A.8}$$

	$\lambda_0 \cdot 1 \times 10^{-2}$	$\lambda_1 \cdot 1 \times 10^{-5}$	$\lambda_2 \cdot 1 \times 10^{-8}$	$\lambda_3 \cdot 1 \times 10^{-12}$
H_2	13.9584	38.5097	−12.5689	47.7818
CO_2	1.38695	6.04059	0.914853	−12.7413
H_2O	0.998229	10.0049	−2.96743	23.0937
CH_4	0.0324699	29.9243	−32.3017	258.011

The thermal conductivity of the gas mixture is calculated via the Wassiljewa approach and the Lindsay-Bromley-Method [4].

$$\lambda_g = \sum_{i=1}^{n} \frac{y_i \cdot \lambda_i}{\sum_{j=1}^{n} y_j \cdot A_{i,j}} \tag{A.9}$$

$$A_{i,j} = 0.25 \cdot \left(1 + \left[\frac{\mu_i}{\mu_j} \cdot \left(\frac{M_j}{M_i}\right)^{\frac{3}{4}} \cdot \frac{T_g + S_i}{T_g + S_j}\right]^{\frac{1}{2}}\right)^2 \cdot \frac{T_g + S_{i,j}}{T_g + S_i} \tag{A.10}$$

With:

$$S_i = 1.5 \cdot T_{b,i} \tag{A.11}$$

$$S_{i,j} = S_{j,i} = F_S \cdot (S_i \cdot S_j)^{\frac{1}{2}} \tag{A.12}$$

In these equations S_i is the Sutherland constant, $T_{b,i}$ is the boiling temperature of the component and F_S is equal to unity for all possible pairs except CO_2/H_2. In this case the parameter has the value 0.735. Values for the boiling temperature of CO_2, H_2O, CH_4 [4] and H_2 [2] are summarized in the following table. Diffusion volumes of CO_2, H_2O, CH_4 are taken from Perry's [5] and the diffusion volume of methane is calculated with atomic diffusion volume increments of C= 16.5 $cm^3\,mol^{-1}$ and H= 1.98 $cm^3\,mol^{-1}$.

	H_2	CO_2	H_2O	CH_4
$T_{b,i}$ / K	79	194.6	373.15	110.70
$\nu_{Diff,i}$ / $cm^3\,mol^{-1}$	7.07	26.9	12.7	24.42

The heat conduction of the packed bed is calculated with the model of Zehner-Bauer-Schlünder [6].

$$B = 1.25 \cdot \left(\frac{1 - \varepsilon_{bed}}{\varepsilon_{bed}}\right)^{\frac{10}{9}} \tag{A.13}$$

$$B_s = \frac{\lambda_s}{\lambda_g} \tag{A.14}$$

$$N = 1 - \frac{B}{B_s} \tag{A.15}$$

$$B_c = \frac{2}{N}\left(\frac{B(B_s - 1)}{N^2 B_s} \ln\left(\frac{B_s}{B}\right) - \frac{B+1}{2} - \frac{B-1}{N}\right) \tag{A.16}$$

$$B_{bed} = \frac{\lambda_{bed}}{\lambda_g} = 1 - \sqrt{1 - \varepsilon_{bed}} + B_c\sqrt{1 - \varepsilon_{bed}} \tag{A.17}$$

For the calculation of the heat and mass transfer from the gas to the catalyst surface the correlation from Gnielinski [7] is used.

$$h_{GS} = \frac{\lambda_g}{d_s} Nu_{GS} \left(1 + 1.5(1 - \varepsilon_{bed})\right) \tag{A.18}$$

$$Nu_{GS} = 2 + \sqrt{Nu^2_{GS,\,lam} + Nu^2_{GS,\,turb}} \tag{A.19}$$

$$Nu_{GS,\,lam} = 0.664 Pr^{0.33} Re^{0.5} \tag{A.20}$$

$$Nu_{GS,\,turb} = \frac{0.037 PrRe^{0.8}}{1 + 2.443 Re^{-0.1}(Pr^{0.67} - 1)} \tag{A.21}$$

$$\beta_{GS} = \frac{D}{d_s} Sh_{GS} \left(1 + 1.5(1 - \varepsilon_{bed})\right) \tag{A.22}$$

$$Sh_{GS} = 2 + \sqrt{Sh^2_{GS,\,lam} + Sh^2_{GS,\,turb}} \tag{A.23}$$

$$Sh_{GS,\,lam} = 0.664 Sc^{0.33} Re^{0.5} \tag{A.24}$$

$$Sh_{GS,\,turb} = \frac{0.037 ScRe^{0.8}}{1 + 2.443 Re^{-0.1}(Sc^{0.67} - 1)} \tag{A.25}$$

The overall heat transfer coefficient is calculated with the α_{wall} model [8].

$$Nu_{wall} = \frac{h_{wall} d_s}{\lambda_g} = \left(1.3 + \frac{5 d_s}{d_h}\right) B_{bed} + 0.19 Re^{0.75} Pr^{0.33} \tag{A.26}$$

$$\lambda_r^{eff} = \lambda_{bed} + \lambda_g \frac{Pe}{K_R} \tag{A.27}$$

$$K_R = 7 \cdot \left(2 - \left(1 - \frac{2 \cdot d_s}{d_h}\right)^2\right) \tag{A.28}$$

$$Pe = \frac{u \cdot d_s \cdot \rho_g \cdot c_{p,g}}{\lambda_g} \tag{A.29}$$

$$\frac{1}{h_{ov}} = \frac{1}{h_{wall}} + \frac{d_h}{8 \lambda_r^{eff}} + \frac{d_{wall}}{\lambda_{wall}} + \frac{1}{h_{oil}} \tag{A.30}$$

The axial dispersion coefficients of heat and mass in a fixed-bed reactor for gas are calculated with the equations below [8].

$$\frac{D_{i,bed}}{D_{i,M}} = 1 - \sqrt{1 - \varepsilon_{bed}} \tag{A.31}$$

$$Pe_0 = \frac{u \cdot d_s}{D_{i,bed}} \tag{A.32}$$

$$\frac{1}{Pe_{mass}} = \frac{1 - \sqrt{1 - \varepsilon_{bed}}}{Pe_0} + 0.5 \tag{A.33}$$

$$Pe_{mass} = \frac{u \cdot d_s}{D_{ax}} \tag{A.34}$$

$$\frac{1}{Pe_{heat}} = \frac{B_{bed}}{Pe} + 0.5 \tag{A.35}$$

$$Pe_{heat} = \frac{u \cdot d_s \cdot c_{p,g} \cdot \rho_g}{\lambda_{ax}} \tag{A.36}$$

The coefficients A and B are required for the pressure drop equation of Eisfeld and Schnitzlein [9].

$$A = 1 + \frac{2}{3 \cdot \left(\frac{d_h}{d_s}\right) \cdot (1 - \varepsilon_{bed})} \tag{A.37}$$

$$B = \left(1.15 \cdot \left(\frac{d_s}{d_h}\right)^2 + 0.87\right)^2 \tag{A.38}$$

The following equations are used for the calculation of the convective heat transfer in the coolant channel in the intermediate flow regime [10]:

$$\gamma = \frac{Re_{oil} - 2300}{10^4 - 2300} \tag{A.39}$$

$$Nu_{L,2300} = \left[49.371 + (Nu_{2,2300} - 0.7)^3 + (Nu_{3,2300})^3\right]^{\frac{1}{3}} \tag{A.40}$$

$$Nu_{2,2300} = 1.615 \left(2300 Pr_{oil} \frac{d}{L}\right)^{\frac{1}{3}} \tag{A.41}$$

$$Nu_{3,2300} = \left(\frac{2}{1 + 22 Pr_{oil}}\right)^{\frac{1}{6}} \left(2300 Pr_{oil} \frac{d}{L}\right)^{\frac{1}{2}} \tag{A.42}$$

$$\xi = \left(1.8 \log 10^4 - 1.5\right)^{-2} \tag{A.43}$$

$$Nu_{T,10^4} = \frac{(\xi/8) 10^4 Pr_{oil}}{1 + 12.7\sqrt{\xi/8}\left(Pr_{oil}^{\frac{2}{3}} - 1\right)} \left[1 + \left(\frac{d}{L}\right)^{\frac{2}{3}}\right] \tag{A.44}$$

$$Nu_{oil} = (1 - \gamma) Nu_{L,2300} + \gamma Nu_{T,10^4} \tag{A.45}$$

Additional Figures

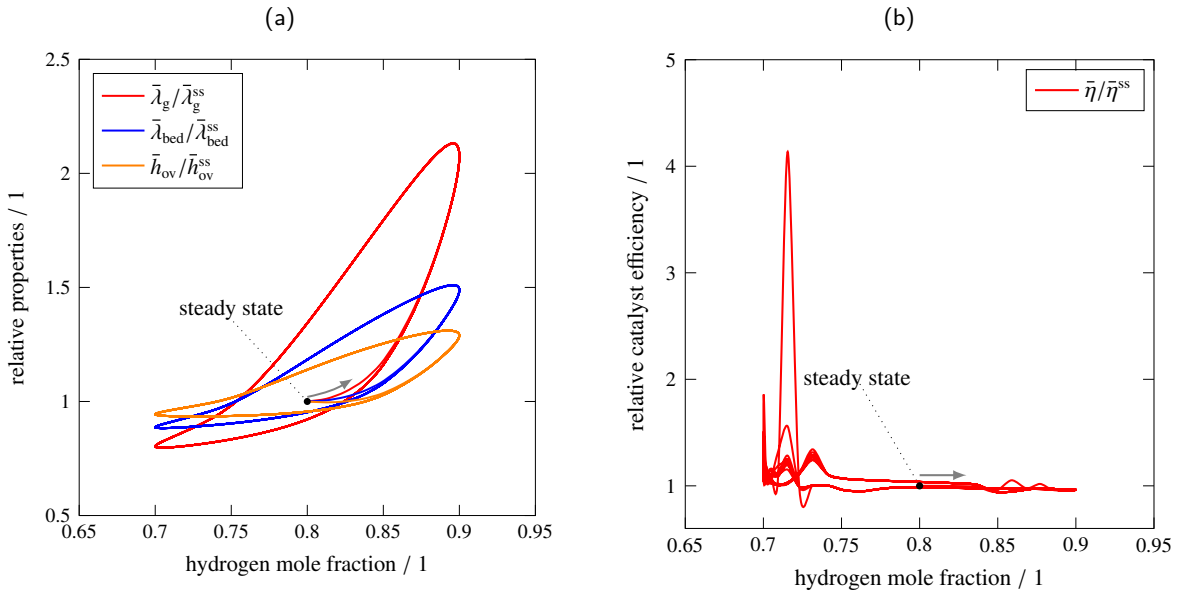

Figure A.1.: (a) Phase plane of the relative heat transfer properties for an amplitude of $\Delta y = 0.1$ and a frequency of $f = 0.1\,s^{-1}$. The black dot in the center represents the mean value of the steady-state profile. (b) Relative variation of the catalyst efficiency. *Conditions:* $T_g^0 = 280\,°C$, $d = 2\,mm$, $d_s = 400\,\mu m$, $p = 8\,bar$, $GHSV = 3{,}143\,h^{-1}$.

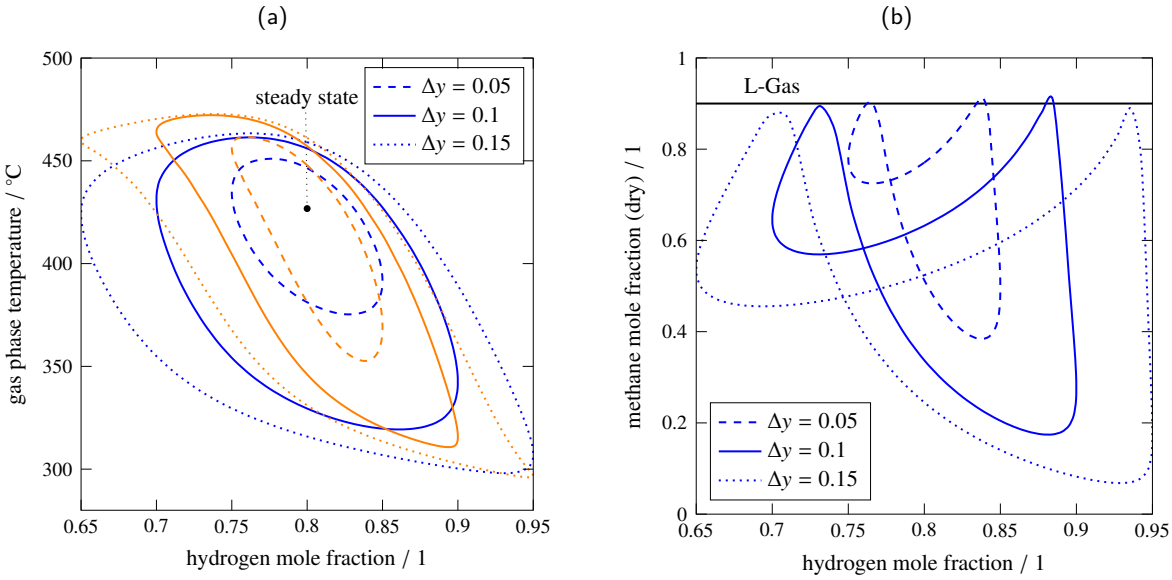

Figure A.2.: Results for the dynamic simulation of the microstructured fixed-bed reactor. (a) Phase plane of the maximum temperatures of the gas phase (T_g) for different amplitudes and a frequency of $f = 0.1\,s^{-1}$ (blue) and $f = 0.05\,s^{-1}$ (orange) . The black dot in the center represents the maximum of the steady-state profile. (b) Variation of the methane outlet concentration for different amplitudes in the phase plane for a frequency of $f = 0.1\,s^{-1}$. *Conditions:* $T_g^0 = 280\,°C$, $d = 2\,mm$, $d_s = 400\,\mu m$, $p = 8\,bar$, $GHSV = 3{,}143\,h^{-1}$.

Comparison between Wilke-Bosanquet and Dusty-Gas model

In this simulation study the Wilke-Bosanquet diffusion model was used, as a compromise between accuracy and complexity. The more accurate Dusty-Gas model adds a higher degree of numerical complexity to the simulation and requires a higher effort to solve the problem. To justify our usage of the simplified diffusion approach, we performed additional calculations to reveal the differences between both models and to verify our assumption. The following figures show the steady state concentration profile of the components in the pellet for a temperature of 350 °C and a pressure of 8 bar.

The properties of the pellet can be found in the manuscript in Table 1. For details on the Dusty-Gas model please refer to the work of Solsvik and Jakobsen [11]. It can be seen that there is only small difference between the Wilke-Bosanquet approach and the Dusty-Gas model. Therefore, the usage of the simplified diffusion model seems reasonable. Additionally, the influence of the convective flow in the dusty-gas model due to the mole change of the reaction has also been investigated, but this turned out to be not significant for the assumed pellet.

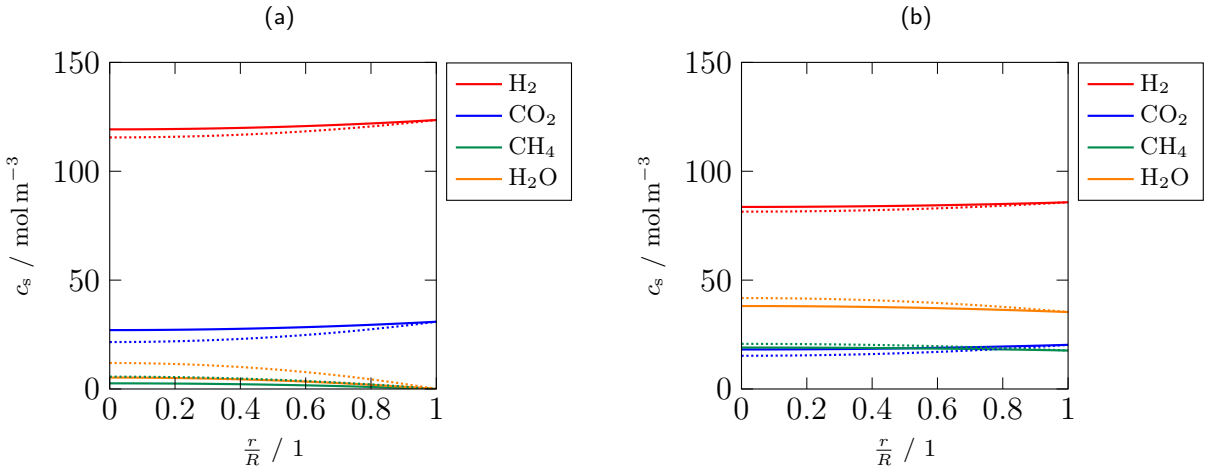

Figure A.3.: Concentration profile in the catalyst pellet calculated with the Wilke-Bosanquet approach (solid) and the Dusty-Gas model (dotted). Figure (a) is calculated for a bulk gas phase composition of $x_{H_2} = 0.8$ and $x_{CO_2} = 0.2$. Figure (b) is the result for the gas phase composition at the hot spot with $x_{H_2} = 0.5553$, $x_{CO_2} = 0.1313$, $x_{CH_4} = 0.1144$ and $x_{H_2O} = 0.2288$. *Conditions:* $T_g = 350\,°C$, $d_s = 400\,\mu m$, $p = 8\,bar$.

References

[1] Sasol Germany GmbH. Ed. by Sasol Germany GmbH. [accessed 14.05.2018]. URL: https://bit.ly/2LKdjlo.

[2] M. Defalco, L. Dipaola, L. Marrelli. *Int. J. Hydrogen Energy* **2007**, 32 (14), 2902–2913. DOI: 10.1016/j.ijhydene.2007.04.014.

[3] B. E. Poling, J. M. Prausnitz, J. O'Connell. 5. ed. New York NY u.a.: McGraw-Hill, **2001**.

[4] S. Elnashaie, S. S. Elshishini. Vol. 7. Topics in chemical engineering. Philadelphia, Pa.: Gordon and Breach, **1993**.

[5] R. H. Perry, D. W. Green. 8. ed. New York, NY: McGraw-Hill, **2008**.

[6] C. Ullrich, T. Bodmer, C. Hübner, P. B. Kempa, E. Tsotsas, A. Eschner, G. Kasparek, F. Ochs, M. H. Spitzner. *VDI-Wärmeatlas*. Berlin, Heidelberg: Springer Berlin Heidelberg, **2013**, 629–708. DOI: 10.1007/978-3-642-19981-3_28.

[7] V. Gnielinski. *VDI-Wärmeatlas*. Berlin, Heidelberg: Springer Berlin Heidelberg, **2013**, 839–840. DOI: 10.1007/978-3-642-19981-3_50.

[8] E. Tsotsas. *VDI-Wärmeatlas*. Berlin, Heidelberg: Springer Berlin Heidelberg, **2013**, 1517–1534. DOI: 10.1007/978-3-642-19981-3_102.

[9] B. Eisfeld, K. Schnitzlein. *Chem. Eng. Sci.* **2001**, 56 (14), 4321–4329. DOI: 10.1016/S0009-2509(00)00533-9.

[10] V. Gnielinski. *VDI-Wärmeatlas*. Berlin, Heidelberg: Springer Berlin Heidelberg, **2013**, 785–792. DOI: 10.1007/978-3-642-19981-3_42.

[11] J. Solsvik, H. A. Jakobsen. *Chem. Eng. Sci.* **2011**, 66 (9), 1986–2000. DOI: 10.1016/j.ces.2011.01.060.

APPENDIX B

Supporting Information to Chapter 4

Sintering of silica particles

High calcination temperatures lead to the sintering of the silica support and the Ni crystals. The effect of sintering for the silica support is illustrated in Figure B.1. Figure B.1a shows the BET surface and total pore volume for the pure SiO_2 support. Pure SiO_2 particles with BB(20) were produced with the same spray-drying procedure only without the Ni nitrate. BET surface area and pore volume remain constant up to a calcination temperature of 800 K, but then a significant sintering sets in. The particles are completely sintered after heat treatment at 1,200 K for 4 h. Figure B.1b shows the SEM micrograph after calcination at 673 K that reveals spherical SiO_2 particles. In contrast, Figure B.1c displays the SiO_2 particles after heat treatment at 1,273 K, which proves the sintering. Within this study, calcination temperatures for the catalysts of 973 K were applied. Adding Ni to the silica hinders the SiO particles from sintering, which is seen by the BET measurements provided in the table in the main manuscript.

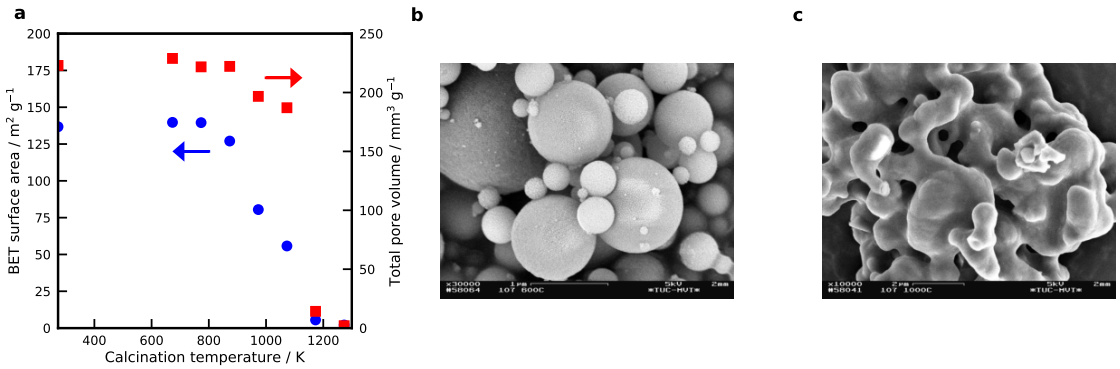

Figure B.1.: (**a**) BET surface area and pore volume of SiO_2 with BB(20) at different calcination temperatures. (**b**) SEM image for the calcination at 673 K. (**c**) SEM image after calcination at 1,273 K.

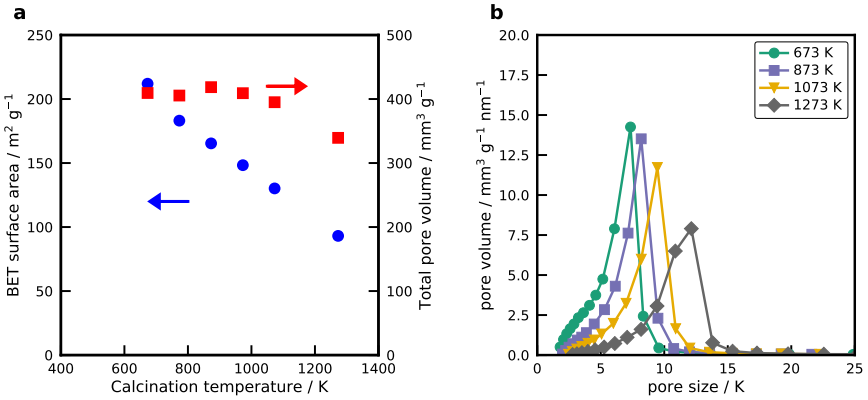

Figure B.2.: (a) BET surface area and pore volume of the Al_2O_3 at different calcination temperatures. (b) Pore size distribution for different calcination temperatures.

TEM images

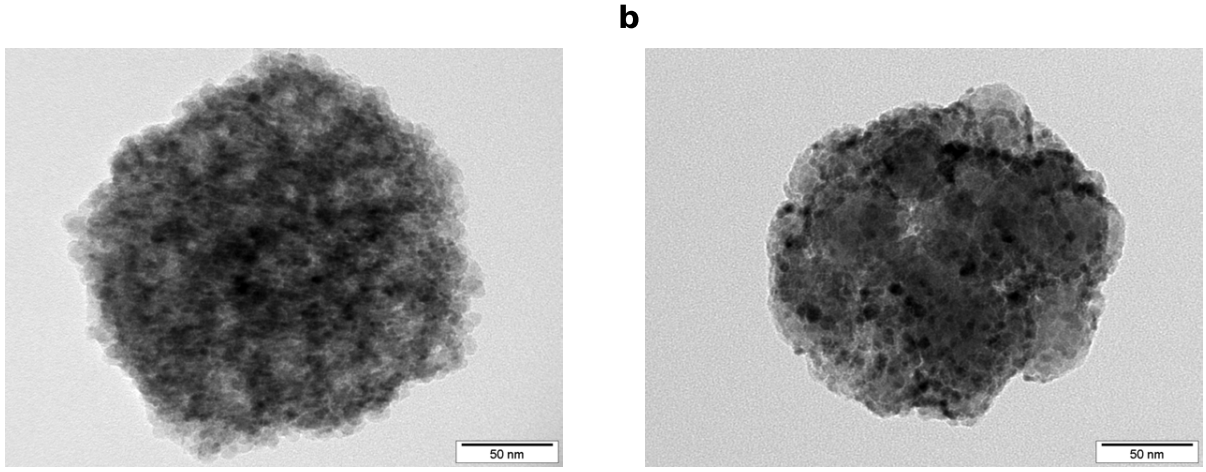

Figure B.3.: TEM micrograph of Ni/SiO_2 catalyst with (a) BB(8) with 20 wt% calcined at 673 K and (b) BB(45) with 5 wt% calcined at 673 K.

TGA

Table B.1 summarizes the thermogravimetric analysis of the catalysts, which were not further heat-treated after the production. These samples show an incomplete decomposition of the nitrates, that is why they loose mass during the reduction. The percentage mass loss at the reduction temperature was required to determine the actual mass of the catalyst sample.

Table B.1.: Table B.1 summarizes the thermogravimetric analysis of the catalysts, which were not further heat-treated after the production. These samples show an incomplete decomposition of the nitrates. That is why they lose mass during the reduction. The percentage mass loss at the reduction temperature was required to determine the actual mass of the catalyst sample.

	unit	1a	2a	3a	4a	5a	6a
mass loss	%	19.3	11.2	14.3	14.4	21.6	21.9

XRD

Figure B.4a shows the recorded XRD patterns for the spray-dried Ni/Al_2O_3 catalyst after production and after calcination at 673 K. Directly after production a boehmite structure is obtained. This transforms after calcination to the γ-Al_2O_3 phase. However, in both cases no crystalline NiO is observed, which indicates that the NiO reacts with the Al_2O_3 and forms crystalline $NiAl_2O_4$. Figure B.4c compares the lattice constant of γ-Al_2O_3 in dependence of the Ni loading with results from Zhou et al. [1] and O'Neil et al. [2].

SAXS

The result from the SAXS measurement is displayed in Figure B.6 for the Ni/SiO_2 catalyst with BB(20) 20 wt% calcined at 673 K. Several peaks are observed for different particle sizes. The first peak at

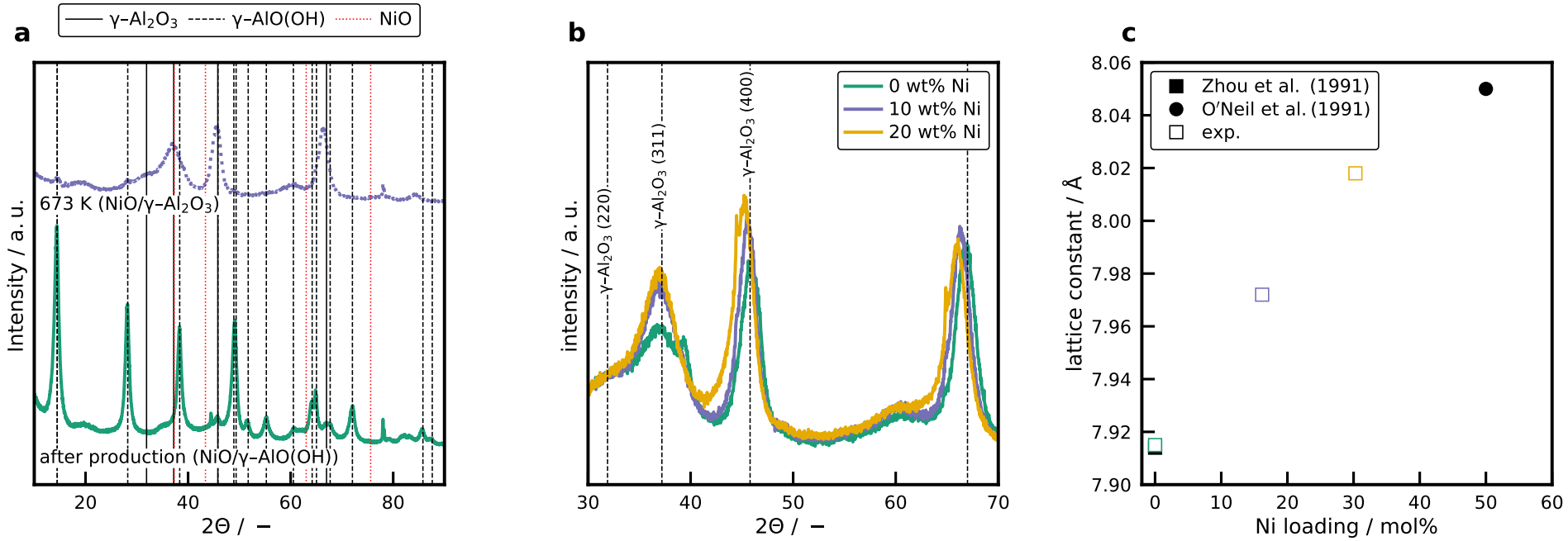

Figure B.4.: (a) XRD patterns of the spray-dried Ni/Al_2O_3 catalyst after production and after calcination at 673 K. Reflections for γ-Al_2O_3, γ-AlO(OH), and NiO are marked. (b) XRD patterns of $BB(Al_2O_3)$ calcined at 673 K with different nickel loadings. (c) Lattice constant of the crystalline structure as a function of the Ni loading in $BB(Al_2O_3)$.

Table B.2.: Average NiO particle sizes (in nm) determined with XRD for the Ni/SiO_2 catalysts with different Ni loadings and SiO primary particle sizes of 8 nm, 20 nm and 45 nm after calcination at different temperatures. The last row is the m_{Ni}/a_{SiO_2} ratio.

	BB(20)			BB(8)		BB(45)
Temperature / K	20 wt%	10 wt%	5 wt%	20 wt%	10 wt%	7 wt%
273	4.5	3.2	2.1	4.3	2.0	-
473	5.2	4.0	2.7	4.4	2.1	3.51
573	5.7	4.3	2.7	4.5	2.3	3.57
673	6.8	4.7	2.8	5.1	2.5	3.97
773	7.2	4.9	2.9	5.3	2.5	4.11
873	7.7	4.9	3.3	5.4	2.6	4.65
973	8.3	5.4	3.3	5.9	2.8	4.59
m_{Ni}/a_{SiO_2} / mg m^{-2}	2.0	1.13	0.40†	1.23	0.56	1.19†

† No measured Ni loadings from ICP are available for these samples and the m_{Ni}/a_{SiO_2} is calculated with the nominal loading. This value is subjected to a higher error.

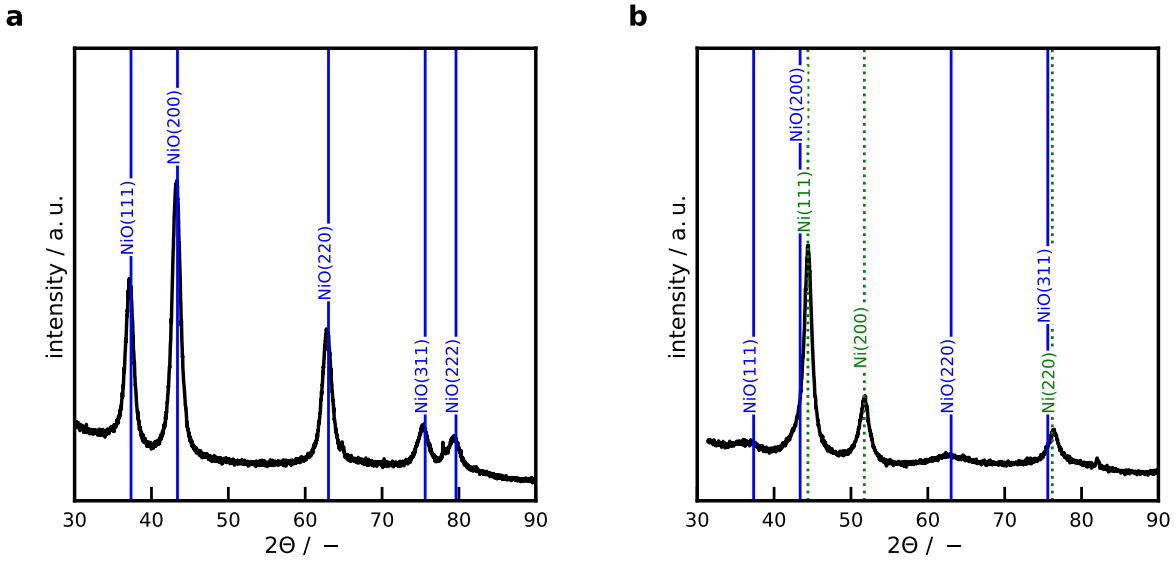

Figure B.5.: (a) XRD patterns for the BB(20) catalyst with 20 wt% calcined at 673 K. (b) XRD pattern for the same catalyst after reduction and passivation.

7.0 nm corresponds to the Ni crystals. This agrees well with the XRD result of 6.8 nm. The peak with the maximum at 27 nm can be associated with the primary SiO_2 particles, which have a nominal particle size of 20 nm. Remaining peaks at higher diameters of 50 and 95 nm can either be an error from the fitting procedure of the SAXS evaluation due to a high signal-to-noise ratio or small Ni/SiO_2 agglomerates.

Chemisorption

Recorded adsorption isotherms are provided in Figure B.7. Figure B.7a shows the adsorption isotherms for the BB(8) and 20 wt% catalyst for different calcination temperatures. With increasing calcination temperature, the adsorbed amount of H_2 decreases because the Ni crystal sinter and the *DOR* is lower. Double CO_2 adsorption isotherms are shown in Figure B.7b for BB(8), 20 wt%, without heat treatment.

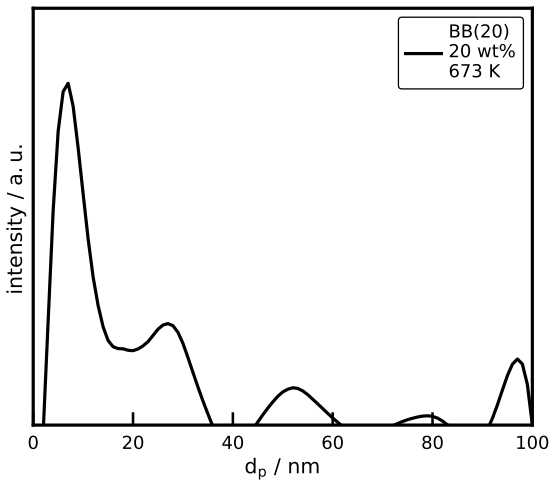

Figure B.6.: SAXS measurement of BB(20) with 20 wt% calcined at 673 K.

Between the isotherms, the sample is evacuated for 1 h at adsorption temperature. The catalyst shows a high initial CO_2 uptake at low pressures, followed by a linear increase. The initial uptake is a result of adsorption on the Ni crystal. As shown by the measurement of the pure support, the SiO_2 surface does not provide basic surface sites. The second isotherm further proves this for the catalyst, which shows only a CO_2 uptake at high pressures indicating basic sites with a weak binding strength on the support.

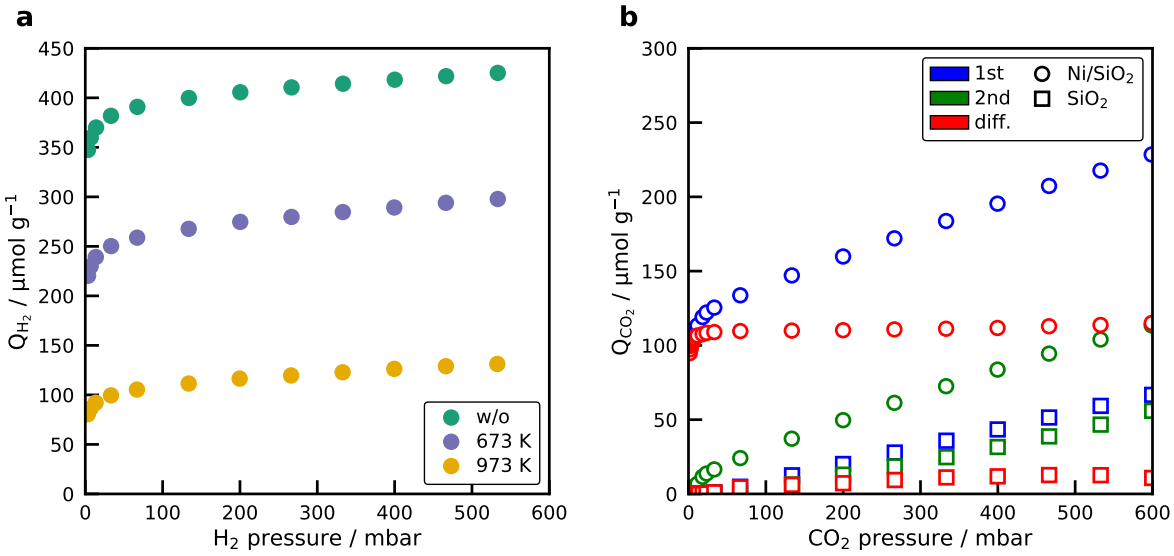

Figure B.7.: (a) Volumetric adsorption isotherms for H_2 adsorption on BB(8), 20 wt% at different calcination temperatures. (b) CO_2 adsorption isotherm for the Ni/SiO_2 catalyst with BB(8), 20 wt%, without calcination and the pure SiO_2 support.

Temperature-programmed reduction

Figure B.8 shows the recorded ion currents during the TPR of the BB(8) catalyst with 10 wt% Ni and without heat treatment. At low temperatures a desorption of CO_2 and at higher temperatures CO (CO^+) is observed. The catalyst is exposed to air and adsorbs CO_2, which is not entirely removed during the degassing. Due to the adsorbed CO_2, a small methane formation (CH_3^+) is recorded. The decomposition peak of the nitrates and the release of NO and NO_2 (NO^+) has the same position and shape as the

recorded TCD signal. It cannot be differentiated between NO and NO_2, since both components form a fragment on the m/z-ratio of 30.

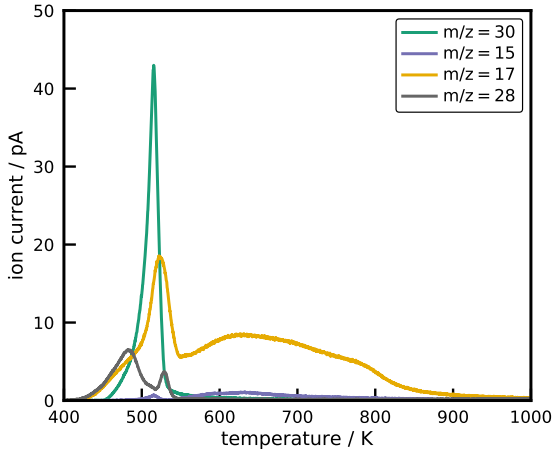

Figure B.8.: TPR profile of the Ni/SiO_2 (BB(8), 10 wt%, without calcination) recorded with the MS. Mass-to-charge (m/z) ratios of 30 (NO^+), 15 (CH_3^+), 17 (OH^+), and 28 (CO^+) are displayed.

Activation energies

Figure B.9 shows the Arrhenius diagram for some selected samples. The activation energies determined for the catalysts are in a narrow range.

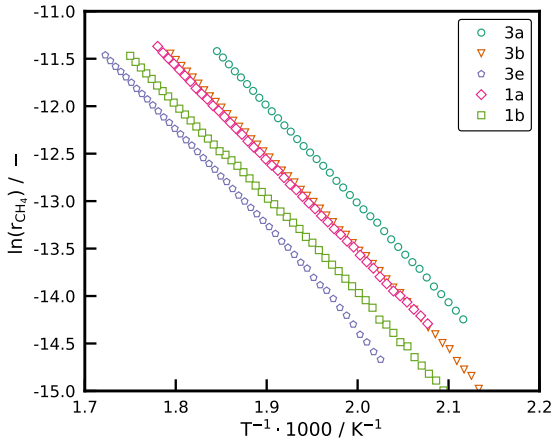

Figure B.9.: Arrhenius diagram for selected Ni/SiO_2 catalysts. The reaction rate was calculated with the differential fixed-bed assumption for conversions smaller than 10 %. *Conditions:* $m_{cat} = 30\,mg$, $\beta = 20\,K\,min^{-1}$, $\dot{V}_{H_2/CO_2/Ar} = 50\,mL_N\,min^{-1}$.

References

[1] R.-S. Zhou, R. L. Snyder. *Acta Crystallogr., Sect. B: Struct. Sci.* **1991**, 47 (5), 617–630. DOI: 10.1107/S0108768191002719.

[2] H. C. St. O'Neill, W. A. Dollase, C. R. Ross. *Phys. Chem. Miner.* **1991**, 18 (5), 302–319. DOI: 10.1007/BF00200188.

APPENDIX C

Supporting Information for Chapter 5

Chemicals

The gases used in this study were obtained from Linde AG with a quality of 5.0 for N_2, H_2, Ar, He, O_2, and 4.5 for CO_2. Gases were further purified with gas purifiers (ZPure^{TM} O_2/H_2O Filters) to remove oxygen and water contaminates. $Ni(NO_3)_2 \cdot 6\,H_2O$ was used from Alfa Aesar with a purity of 99.9985 % and Puralox SCCa 150/200 γ-Al_2O_3 particles were obtained from Sasol Germany GmbH. The spray-dried catalyst was produced from an aqueous colloidal silica suspension with a SiO_2 particle size of 20 nm (Köstrosol 0830AS, 30 wt%), which was stabilized by ammonia and provided by CWK Chemiewerk Bad Köstritz GmbH.

TPR

Figure C.1 shows the recorded TPR profiles for the Ni/γ-Al_2O_3, the Ni/SiO_2 catalysts, and a NiO reference (Puratronic, Alfa Aesar 99.998 %). The TPR profile of the Ni/γ-Al_2O_3 catalyst compares to the profile reported by Beierlein et al. [1] for the samples prepared with dry impregnation. The TPR shows one single broad peak consisting of three overlapping peaks, ranging from 600 to 1,100 K with a maximum around 543 K. The shoulder at 733 K corresponds to NiO, whereas the peak at 833 K is the reduction of Ni^{2+} in octahedral voids on the alumina and the peak at 1,033 K can be associated with either Ni^{2+} in tetrahedral voids or nickel aluminate [1].

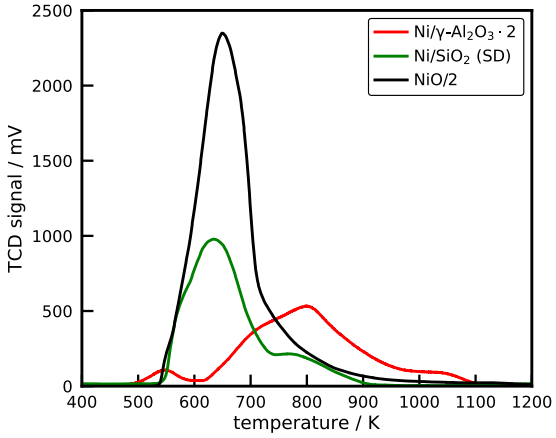

Figure C.1.: TPR profiles for the Ni/γ-Al_2O_3 and Ni/SiO_2 catalyst along with a NiO reference. *Conditions:* $m_{cat} = 20\,mg$, $x_{H_2} = 10.1\,\%$, $\beta = 10\,K\,min^{-1}$, $\dot{V}_{H_2/Ar} = 30\,mL_N\,min^{-1}$.

The TPR profile of the Ni/SiO_2 catalyst is a decomposed of two overlapping peaks. In addition to the peak of free NiO, a broad shoulder at higher temperatures is obtained, indicating that some NiO species are persistent to reduce for this catalyst. According to Mile et al. [2] this peak can be attributed to small nickel crystals, nickel silicate, or hydroxysilicate.

Degree of reduction

The degree of reduction was determined by a volumetric O_2 adsorption at 673 K. The required amount of Ni atoms in the catalyst sample were calculated from the integration of the TCD signal of the TPR. The TCD signal was calibrated with a NiO reference and the calibration factor $f_{\text{Calibration}}$ was determined according to

$$f_{\text{calibration}} = \frac{m_{\text{NiO}}}{M_{\text{NiO}} a_{\text{NiO}}} \tag{C.1}$$

where m_{NiO} is the mass of NiO in the TPR, M_{NiO} is the molar mass and a_{NiO} is the area under the recorded TPR profile. The degree of reduction (DOR) of the catalyst was calculated with

$$DOR = \frac{a_{\text{cat}} f_{\text{calibration}}}{2 m_{\text{cat}} Q_{\text{O}_2}} \tag{C.2}$$

where a_{cat} is the area under the TPR profile of the catalyst, m_{cat} is the catalyst weight and Q_{O_2} is the measured O_2 uptake during the volumetric adsorption experiment.

Static chemisorption

Before the experiment, the catalyst was reduced in the volumetric adsorption apparatus, and the sample was cooled in a vacuum to the desired experiment temperature. At this temperature, the sample was evacuated to below 1.33×10^{-4} mbar, and a leak test was performed with a maximum accepted leakage rate of 1×10^{-2} mbar min^{-1}. The adsorption isotherm was recorded at 30 points in the pressure range of 0 to 900 mbar with an equilibration interval of 60 s, where especially the low pressure range ($p < 100$ mbar) was sampled with a high resolution (20 increments). After the experiment, the free space was measured, and the sample was, therefore, evacuated for 1 h. The nickel surface area s_{Ni} was determined from the hydrogen uptake Q_{H_2} with the Equation (C.3) and corrected by the DOR.

$$s_{\text{Ni}} = Q_{\text{H}_2} z N_{\text{A}} \sigma_{\text{Ni}} \frac{1}{DOR} \tag{C.3}$$

where z is the adsorption stoichiometry, which is two for the dissociative adsorption of H_2, N_{A} is the Avogadro constant and σ_{Ni} is the surface area of one Ni atom (6.51 Å^2). Equation (C.4) was used for the determination of the size of the Ni crystals d_{Ni}, with a Ni density ρ_{Ni} of 8.9 g cm^{-3} and assuming a spherical shape [3].

$$d_{\text{Ni}} = \frac{6000 \omega_{\text{Ni}}}{\rho_{\text{Ni}} s_{\text{Ni}}} \tag{C.4}$$

The fraction of exposed surface atoms, the dispersion D_{Ni}, is derived from Equation (C.5) based on the measured Ni loading ω_{Ni}

$$D_{\text{Ni}} = z s_{\text{Ni}} W_{\text{Ni}} \frac{100}{\omega_{\text{Ni}}} \tag{C.5}$$

where W_{Ni} is the molar mass of Ni (58.69 g mol^{-1}). A reference material (0.5 wt% Pt/Al_2O_3 (Micromeritics Instrument Corp.)) was tested to evaluate the proper functionality of the chemisorption apparatus, and the required specifications were met.

TEM

Figure C.2 shows the TEM images from the different catalysts. Figure C.2a is the image of the Ni/γ-Al_2O_3 catalyst and Figure C.2b is the Ni/SiO_2 catalyst.

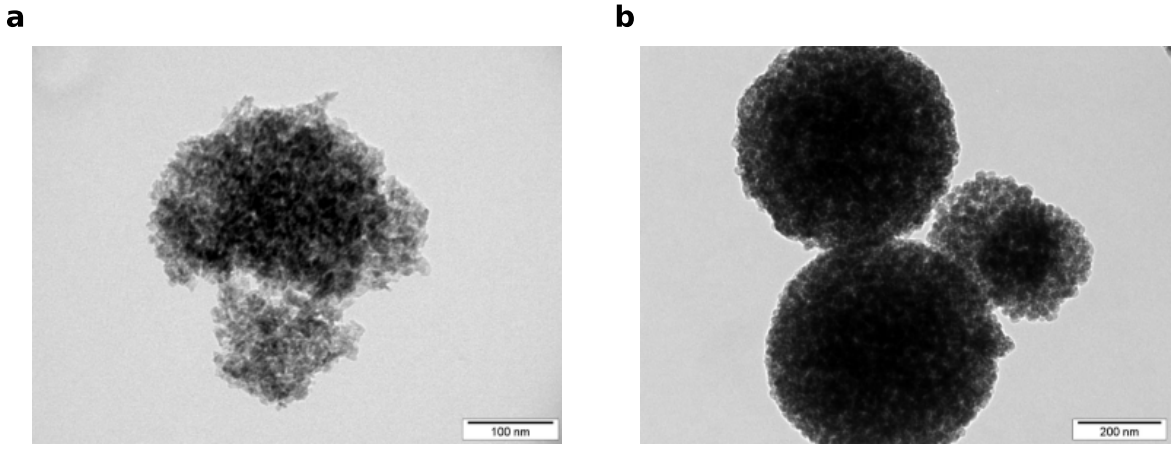

Figure C.2.: TEM images of the (a) Ni/γ-Al_2O_3 and (b) Ni/SiO_2 catalyst.

XRD

Figure C.3 shows the obtained diffractograms of the calcinated catalysts (Figure C.3a and b) and the catalysts after reduction and passivation (Figure C.3c to d). The XRD pattern of the calcinated Ni/γ-Al_2O_3 catalyst (Figure C.3a) shows reflections for NiO and γ-Al_2O_3. The reflection for γ-Al_2O_3 (440) is slightly shifted to higher angles, which indicates the existence of crystalline nickel aluminate ($NiAl_2O_4$) (see Figure C.3a) [1], which can also be seen in the TPR profile (see. Figure C.1). A more detailed discussion of the Ni/γ-Al_2O_3 XRD patterns is omitted because it is extensively provided in the work of Beierlein et al. [1] and Ewald et al. [4]. The XRD diffractogram of the passivated Ni/γ-Al_2O_3 (Figure C.3c) shows a similar pattern as the catalyst after calcination with additional reflections of Ni. A clear Ni(200) reflection is visible, but the other reflections overlap with NiO. The diffractogram of the silica catalyst (Figure C.3b) reveals reflections in the exact same position as the NiO reference. The passivated Ni/SiO_2 catalyst shows large Ni reflections and low-intensity broad NiO patterns. Figure C.4 shows the comparison of the Rietveld fit with the recorded XRD pattern.

BET

The BET measurements were always run with a reference sample (Silica-Alumina, Micromeritics Instrument Corp). In each measurement, it was checked that the specifications of the reference sample were met. Before the BET measurement, the sample was evacuated (SmartVacPrep, Micromeritics Instrument Corp) at 673 K for 4 h. Figure C.5a and b display the recorded N_2 adsorption isotherms and Figure C.5c and d displays the pore distribution obtained from the BJH-method for the passivated catalysts. The alumina catalyst and support show an adsorption isotherm, which can be classified as a type IV isotherm [5]. The passivated catalyst and support show a narrow pore size distribution with the most frequent pore diameters in the range of 9.5 to 11 nm. The desorption isotherm was used for the BJH analysis to determine the pore size distribution. The Ni/SiO_2 catalyst and the support show a completely different isotherm, which is a result of the production method. Spray-drying with Ni affects the surface structure of the catalyst particle.

Sintering of the Ni/γ-Al_2O_3 catalyst

The Ni/γ-Al_2O_3 catalyst was sintered to vary the Ni crystal size in order to evaluate the influence of the metal/support interface on the CO_2 adsorption. Initially, a H_2 chemisorption was performed to determine the Ni crystal size. Afterward, the sample was evacuated for 60 min at 733 K and cooled

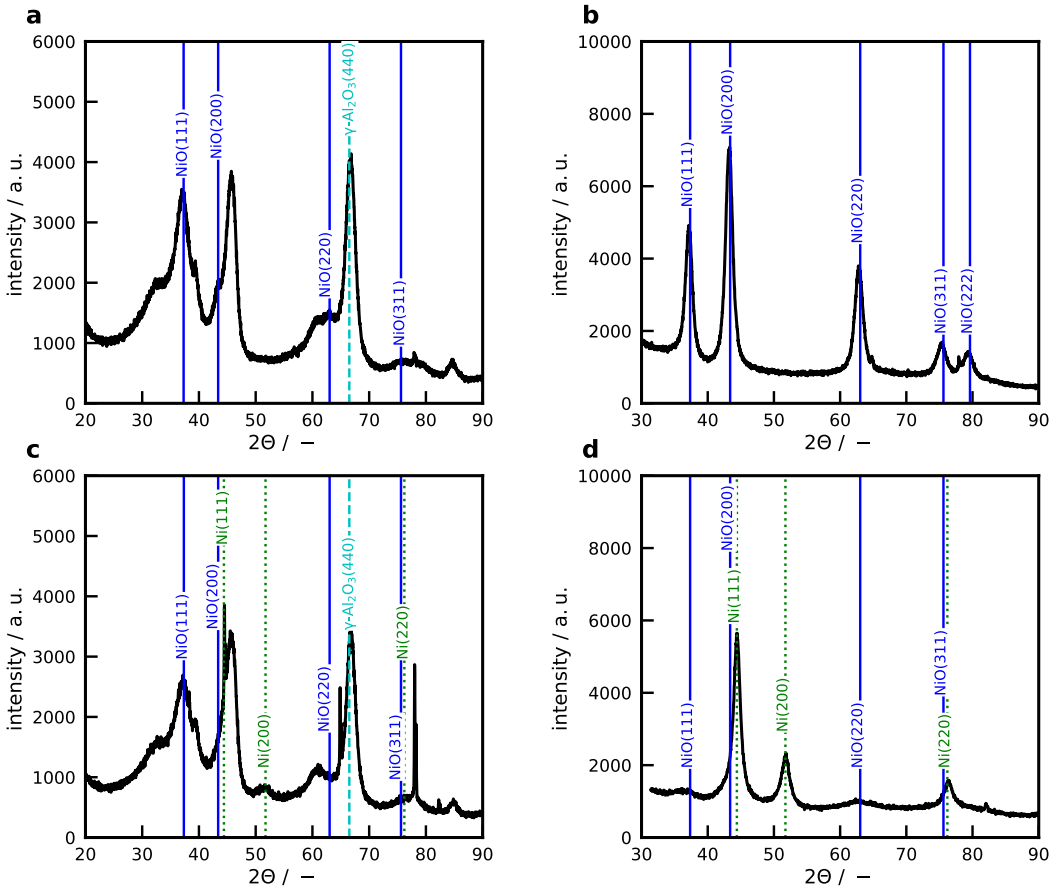

Figure C.3.: X-ray diffractograms of the calcinated (a) Ni/γ-Al_2O_3 and (b) Ni/SiO_2, passivated (c) Ni/γ-Al_2O_3 and (d) Ni/SiO_2.

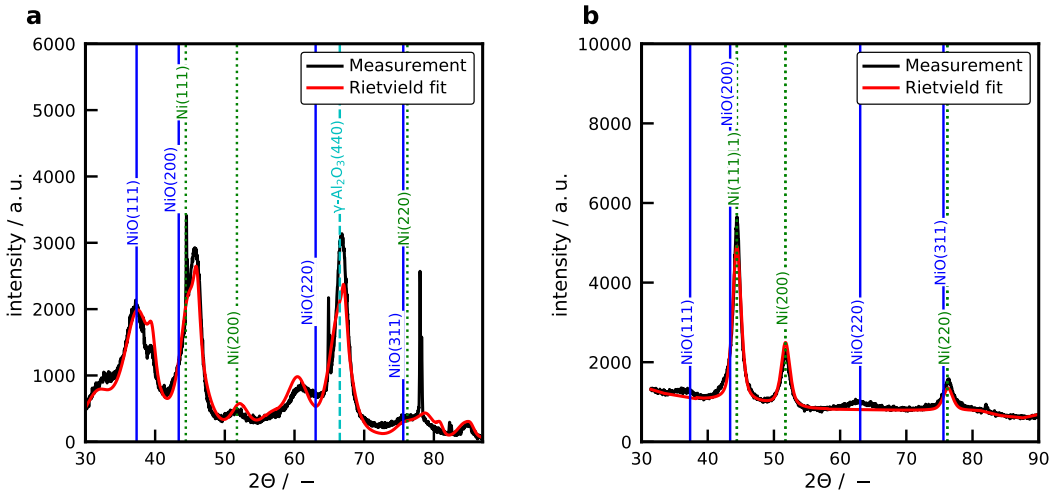

Figure C.4.: Comparison of the measured XRD pattern to the Rietveld fit for (a) Ni/γ-Al_2O_3 and (b) Ni/SiO_2.

to 323 K for the CO_2 chemisorption. After the CO_2 chemisorption, the catalyst is first degassed, and then heated in H_2 to 973 K and kept there for 120 min. Then the H_2 adsorption follows. This cycle was repeated three times. Since the change in diameter between the second and third run is small, the sintering temperature was increased to 1,023 K.

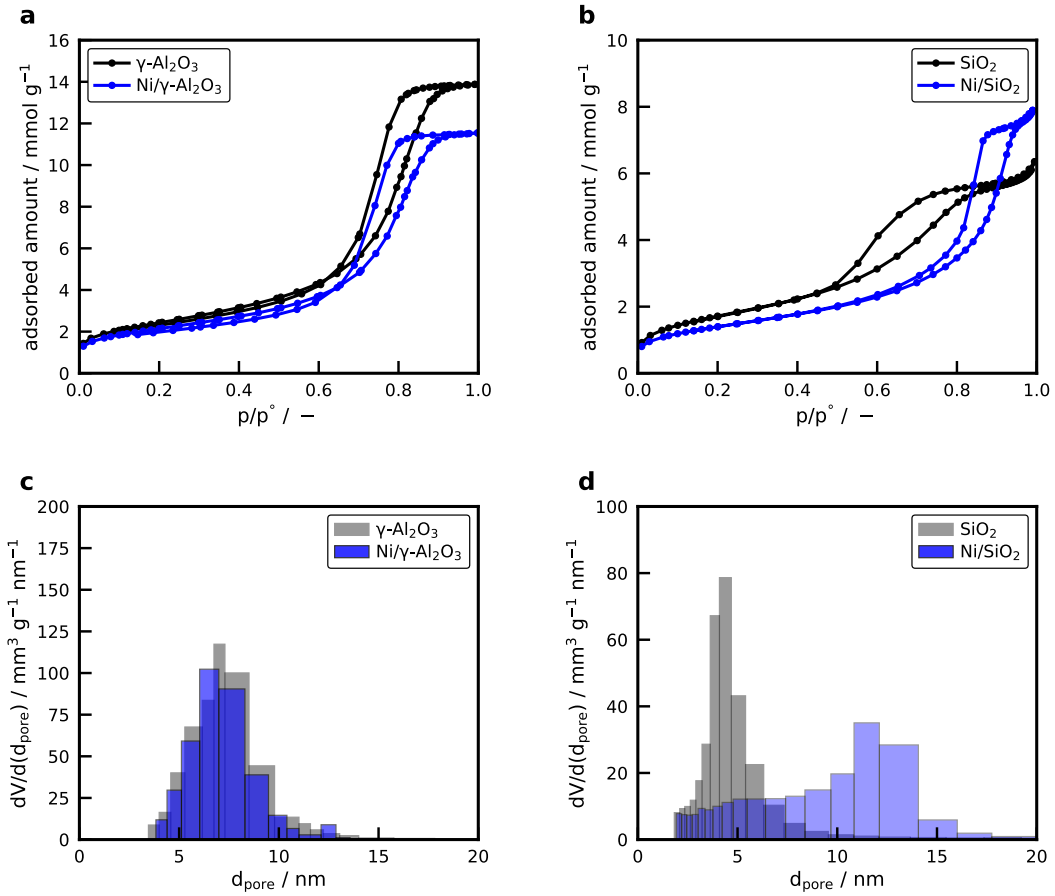

Figure C.5.: BET adsorption isotherms for (a) $Ni/\gamma\text{-}Al_2O_3$ and $\gamma\text{-}Al_2O_3$ and (b) for the Ni/SiO_2 catalyst and the used SiO_2 support. The histogram of the pore distribution for the catalysts is displayed in (c) and (d).

TPD

The ion currents were recorded for the mass-to-charge (m/z) ratios of 2 (H_2), 4 (He), 17 (H_2O), and 40 (Ar) for the H_2-TPD and 4 (He), 17 (H_2O), 28 (CO, CO_2), 40 (Ar), and 44 (CO_2) for the CO_2-TPD in upwind direction with a dwell time of 0.05 s per m/z-ratio, resulting in a measurement time for one cycle of 0.64 s. For the validation of the microkinetic model, the H_2 desorption was used. The H_2 adsorption before the TPD was conducted with a new pulse method described in previous work [6]. 20 consecutive pulses were injected into the carrier gas stream with a pulse frequency of $1\,\mathrm{min}^{-1}$. After the pulse series, the sample was kept at the adsorption temperature for 15 min to record the tailing of the adsorbate, which was caused by the desorption of weakly bound species. The initial coverage was varied by changing the temperature of the adsorption experiment. This method ensures a homogeneous saturation coverage of the differential fixed-bed because of the exposure to a large excess of adsorbate [7]. For the estimation of limiting effects during the temperature-programmed desorption experiments, the criteria of Gorte [8] and Demmin and Gorte [9] are used. With Equation (C.6), it is possible to estimate the influence of the lag time in the sample cell.

$$\frac{V\beta}{\dot{V}\,(T_\mathrm{f} - T_0)} < 0.01 \tag{C.6}$$

V is the volume of the catalyst zone (approx. 1 mL) , β the temperature ramp ($20\,\mathrm{K\,min}^{-1}$), $\dot{V}$ the volumetric flow rate ($30\,\mathrm{mL_N\,min}^{-1}$), T_f the final temperature (800 K) and T_0 the initial temperature

(323 K). It is also necessary to check if diffusion in the catalyst needs to be considered, which is formulated by Equation (C.7):

$$\frac{\beta r^2 \epsilon}{D\,(T_\mathrm{f} - T_0)} < 0.01 \tag{C.7}$$

where r is the radius of the pellets (125 µm), ϵ the porosity (0.4), and D the diffusion coefficient. This criterion is evaluated for CO_2, since it is the largest molecule in this study. The diffusion coefficient is calculated with the method of Fuller-Schettler-Giddings [10]. An effective diffusion coefficient for CO_2 at 323 K of $7.2\times10^{-7}\,\mathrm{m^2\,s^{-1}}$ is obtained from the Bosanquet equation when accounting for the effect of Knudsen diffusion. A value of 1.6×10^{-6} is calculated which satisfies the criterion:

$$\frac{\dot{V} r}{D A} < 0.1 \tag{C.8}$$

The effect of readsorption on the TPD profile is estimated with Equation (C.9):

$$\frac{\alpha \rho s F r^2}{\pi^2 D} > 1 \tag{C.9}$$

$\alpha\rho$ is the active surface area ($9.46\,\mathrm{m^2\,g^{-1}}$), s the sticking coefficient (assumed as 1), and $F = (RT/\pi W)^{0.5}$, with the ideal gas constant R ($8.314\,\mathrm{J\,K^{-1}\,mol^{-1}}$) and molar mass W. This criterion is satisfied, which means that it is necessary to account for readsorption and that the evaluation of the desorption rate isotherms results in the heat of adsorption. Transport limitation of the catalyst, as well as time lags during the TPD, can be excluded. Figure C.6 shows recorded TPD profiles after H_2 adsorption on the $Ni/\gamma\text{-}Al_2O_3$ catalyst for various initial surface coverages. The catalyst is saturated with a pulse method, described in previous work [6] where the initial surface coverage is adjusted with the temperature at which the adsorption experiment is performed to ensure a homogeneous concentration throughout the entire catalyst bed [7]. TPD profiles are cut off at 730 K because, after that temperature, the slope of the temperature ramp is no longer linear and H_2 desorbs at a constant temperature. The desorption of H_2 from the $Ni/\gamma\text{-}Al_2O_3$ catalyst has been extensively studied in the literature and the peaks of the TPD profile agree well with literature results [11–14]. Three overlapping peaks are observed after an adsorption at 323 K, which can be classified as β (weakly bound), α_2 and α_1 (two different types of strongly bound H^*) [11, 12]. The β-peak diminishes after adsorption at higher temperatures and the amount of strongly adsorbed H^* increases, which shows that the adsorption on Ni/Al_2O_3 is an activated process [11, 13]. For adsorption temperatures higher than 423 K, only the α_1-peak remains, the height of which decreases and peak temperature shifts to higher values with increasing adsorption temperature.

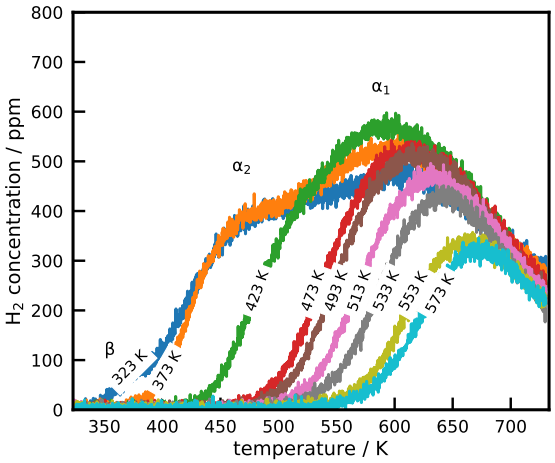

Figure C.6.: H_2-TPD with a temperature ramp of $20\,\mathrm{K\,min^{-1}}$ from the $Ni/\gamma\text{-}Al_2O_3$ catalyst with varying initial surface coverages by adjusting the adsorption temperature. *Conditions:* $m_\mathrm{cat} = 80\,\mathrm{mg}$, $\dot{V}_\mathrm{He} = 30\,\mathrm{mL_N\,min^{-1}}$, $\beta = 20\,\mathrm{K\,min^{-1}}$

Summary of the DFT results

Table C.1 shows the calculated single-point energies (SPE), zero-point energies (ZPE), and the vibrational frequencies for the adsorbates on the Ni facets. Vibrational frequencies below 56 cm^{-1} as well as imaginary values were set to 56 cm^{-1}. Figures C.7 to C.10 show the most stable adsorption geometries on the investigated facets.

Table C.1.: Summary of the results from the DFT calculation with VASP for the Ni(111) and Ni(211) slab as well as the gas-phase molecules. The single-point energies (SPE) and zero-point energies (ZPE), as well as the vibrational frequencies for the most stable position, are provided.

Species	Position	SPE / eV	ZPE / eV	Frequencies / cm^{-1}
Ni(111) (3×3)		-182.698	-	-
H^*	fcc	-186.706	0.171	816.1, 822.3, 1109.0
C^*	hcp	-190.546	0.098	504.1, 514.7, 562.6
O^*	fcc	-189.647	0.076	355.9, 385.2, 482.9
CO^*	hcp	-199.010	0.182	138.7, 144.2, 281.0, 281.6, 335.2, 1754.8
CO_2^*	atop	-205.241	0.323	56, 60.4, 72.0, 82.1, 94.3, 600.7, 619.0, 1302.8, 2325.2
Ni(100) (3×3)		-178.798	-	-
H^*	hollow	-182.760	0.103	465.2, 467.7, 733.2
C^*	hollow	-187.950	0.101	295.7, 662.6, 662.9
O^*	hollow	-186.054	0.06	304.6, 304.6, 355.3
CO^*	hollow	-195.081	0.165	131.8, 131.9, 251.2, 251.3, 274.7, 1618.3
CO_2^*	hollow	-201.339	0.312	56, 56, 56, 56.3, 59.2, 587.7, 609.6, 1300.3, 2323.6
Ni(110) (3×3)		-169.913	-	-
H^*	short-bridge	-173.751	0.162	220.5, 1134.5, 1263.3
C^*	hollow	-178.465	0.085	371.6, 472.6, 521.1
O^*	short-bridge	-176.762	0.069	120.8, 455.5, 539.0
CO^*	short-bridge	-186.276	0.183	56, 152.1, 278.9, 344.6, 349.5, 1820.8
CO_2^*	short-bridge	-192.607	0.277	56, 56, 56, 169.2, 231.5, 501.2, 639.3, 1133.6, 1730.0
Ni(211) (1×3)		-181.868	-	-
H^*	3-fold hollow	-185.871	0.167	678.0, 867.1, 1152.6
C^*	B5	-190.608	0.101	292.8, 664.3, 672.4
O^*	3-fold hollow	-188.988	0.069	231.1, 408.8, 473.8
CO^*	bridge	-198.176	0.182	56, 109.2, 266.8, 341.3, 350.9, 1838.1
CO_2^*	bridge	-204.515	0.287	56, 56, 65.7, 175.7, 251.7, 503.5, 646.4, 1140.3, 1747.8
Gas phase				
H_2		-6.970	0.338	4316.6
O_2		-9.578	0.116	1544.7
C		-1.305	0	-
CO		-14.447	0.138	2117.3
CO_2		-22.323	0.309	633.4, 1310.2, 2346.1

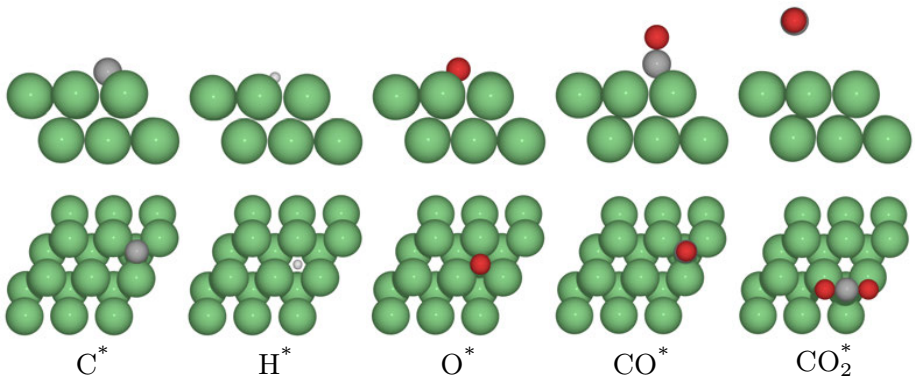

Figure C.7.: Side and top view of the stable adsorption geometries on the Ni(111) facet.

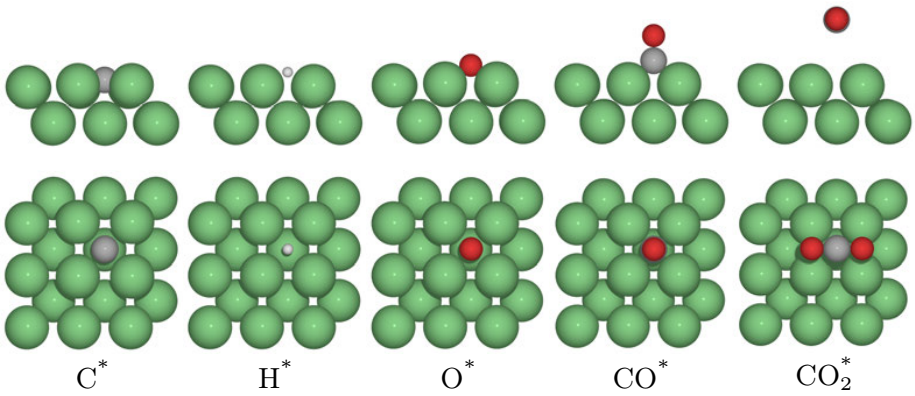

Figure C.8.: Side and top view of the stable adsorption geometries on the Ni(100) facet.

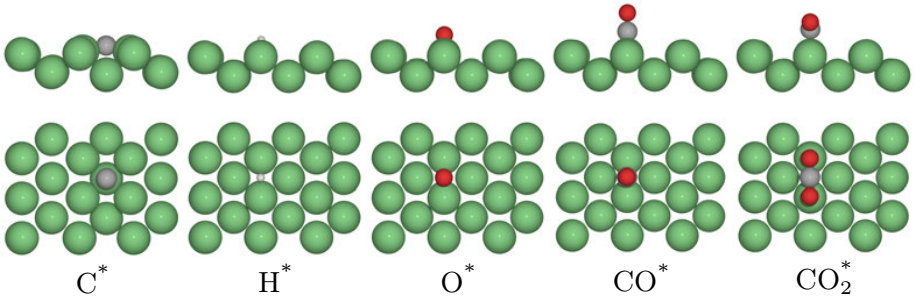

Figure C.9.: Side and top view of the stable adsorption geometries on the Ni(110) facet.

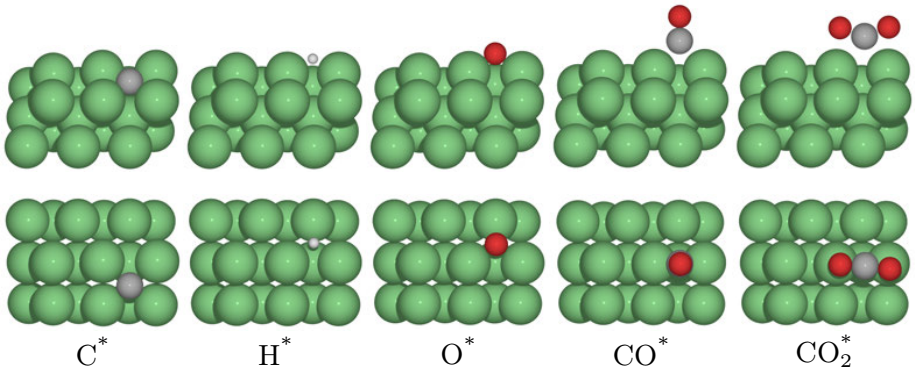

Figure C.10.: Side and top view of the stable adsorption geometries on the Ni(211) facet.

Microkinetic modeling

The comparison of the microkinetic model to the H_2 desorption experiments without any adjustments to the kinetic parameters is displayed in Figure C.11. Without adjusting any parameters, it is not possible to describe the recorded desorption patterns because of a higher binding strengths of H^* on Ni supported on Al_2O_3 and coverage effects.

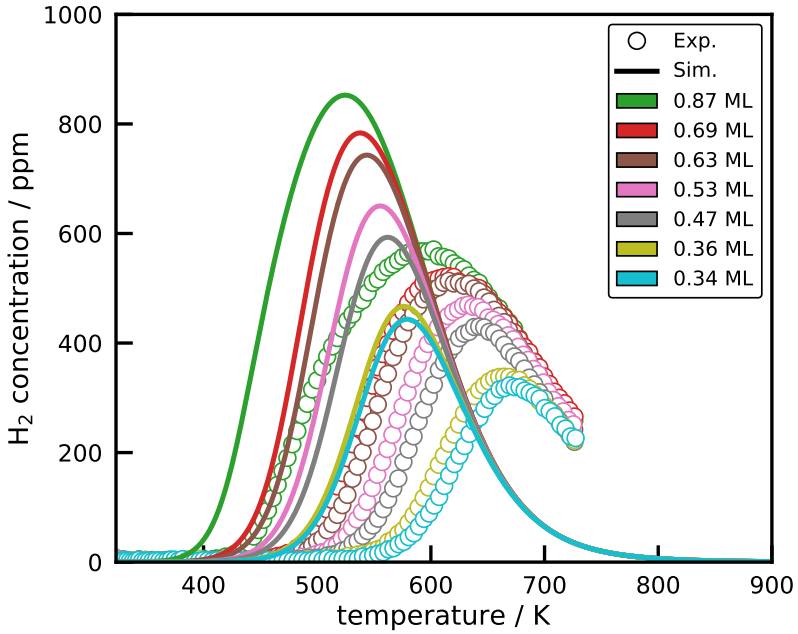

Figure C.11.: H_2 desorption profiles with varying initial coverage expressed in terms of mono-layers (ML) from the Ni/γ-Al_2O_3 catalyst compared to the microkinetic simulation of the multi-faceted Ni catalyst. The mono-layer coverage is defined by the uptake of H_2 from the static adsorption at 323 K with 121 µmol g^{-1}. *Conditions:* $\dot{V}_{carrier} = 30\,mL_N\,min^{-1}$, $\beta = 20\,K\,min^{-1}$

For the local sensitivity analysis in Figure C.12, the heat of formation or the activation energy is tweaked by $-1\,kJ\,mol^{-1}$ opposed to the figure reported in the manuscript, where the change is in the positive direction. Adjusting the values in the negative direction leads to a nearly symmetrical change compared to the adjustment in a positive direction.

The TPD simulations with the multi-faceted model show a sharp peak between 440 and 460 K. It is necessary to look at the surface coverages of the facets to explain the simulation, which is shown in Figure C.13. First of all, it becomes obvious that the initial coverages differ from the single facet simulation. Due to the decomposition of the total area in the facet distribution, the gas-phase concentrations during the adsorption change. The (100) facet is nearly entirely covered with O^* because all the CO^* desorbs due to the low CO pressure in the gas-phase. This CO adsorbs on the Ni(111) and Ni(110) facet and leads to the formation of CO_2. That is why these two facets are O^* deficient. The sharp peak can be seen in the surface coverages as well. This peak comes from a contribution from different facets. CO_2^* desorbs from the (211), and the (111) and (110) form CO_2^*, which immediately desorbs. On the (100) facet, CO adsorbs and starts to form CO_2 at a temperature of 450 K. An even more pronounced peak is obtained for some combination of parameters during the GUA.

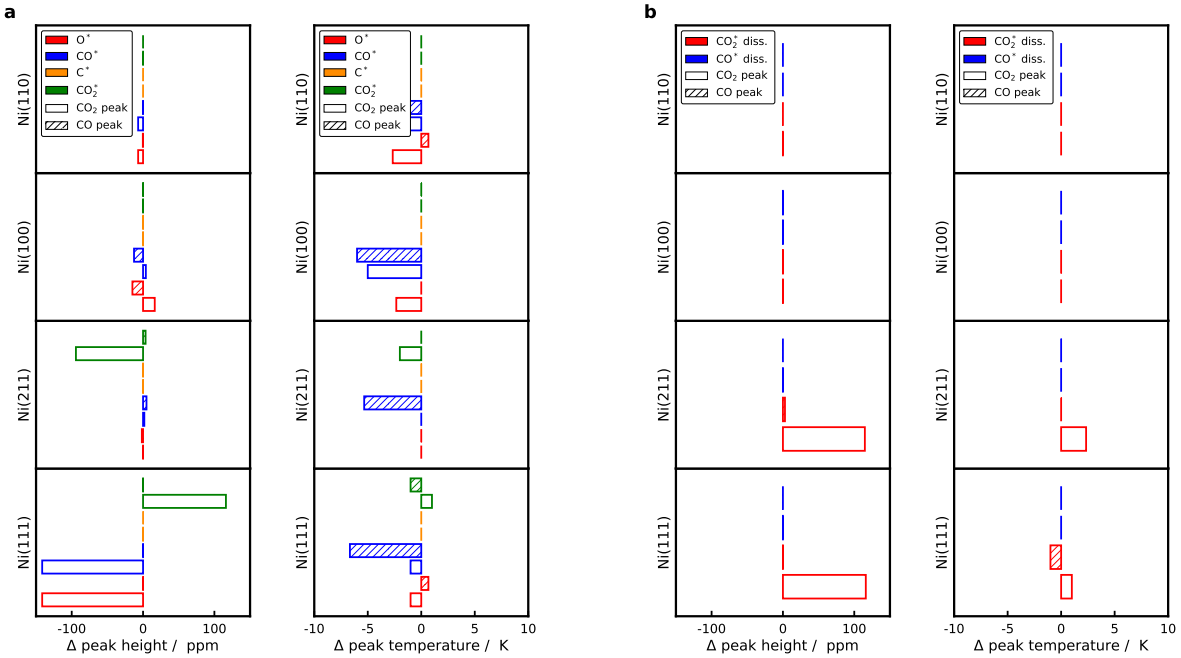

Figure C.12.: (a) Thermochemistry sensitivity analysis on the peak height (left) and the position of the peak maximum (right) of the CO and CO_2 peak. (b) Sensitivity analysis of the activation energy on the height and position of the desorption peak. The heat of formation of the adsorbates and the activation energy is tweaked by $-1\,\mathrm{kJ\,mol^{-1}}$ for the local sensitivity analysis.

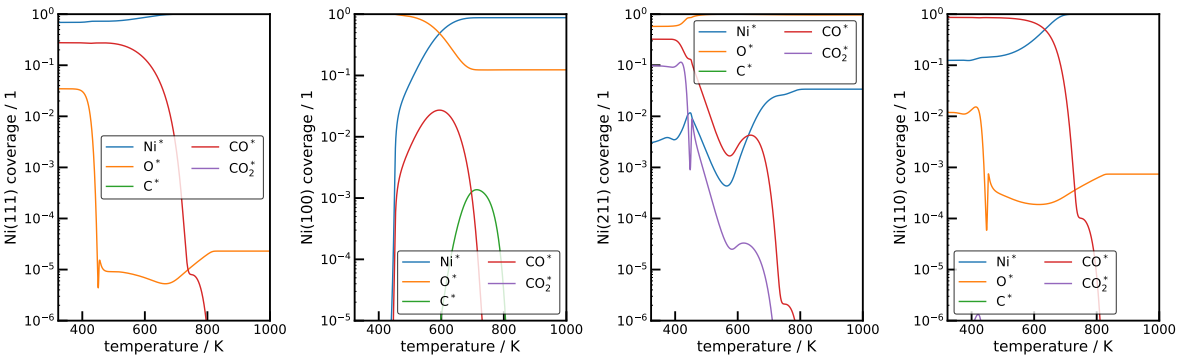

Figure C.13.: Simulated surface coverages of the four Ni facets during the TPD with the multi-facet model. The parameters for the Ni/SiO_2 catalyst were used.

References

[1] D. Beierlein, D. Häussermann, M. Pfeifer, T. Schwarz, K. Stöwe, Y. Traa, E. Klemm. *Appl. Catal., B* **2019**, 247, 200–219. DOI: 10.1016/j.apcatb.2018.12.064.

[2] Brynmor Mile, Diane Stirling, Michael A. Zammitt, Antony Lovell, Maurice Webb. *J. Catal.* **1988**, 114 (2), 217–229. DOI: 10.1016/0021-9517(88)90026-7.

[3] G. Ertl, H. Knözinger, F. Schüth, J. Weitkamp. Weinheim, Germany: Wiley-VCH Verlag GmbH & Co. KGaA, **2008**. DOI: 10.1002/9783527610044.

[4] S. Ewald, O. Hinrichsen. *Appl. Catal., A* **2019**, 580, 71–80. DOI: 10.1016/j.apcata.2019.04.005.

[5] J. M. Thomas, W. J. Thomas. 2 Aufl. Weinheim, Germany: Wiley-VCH Verlag GmbH, **2014**.

[6] J. Friedland, B. Kreitz, H. Grimm, T. Turek, R. Güttel. *ChemCatChem* **2020**, 12 (17), 4373–4386. DOI: 10.1002/cctc.202000278.

[7] J. L. Falconer, A. E. Zağli. *J. Catal.* **1980**, 62 (2), 280–285. DOI: 10.1016/0021-9517(80)90456-X.

[8] R. J. Gorte. *J. Catal.* **1982**, 75 (1), 164–174. DOI: 10.1016/0021-9517(82)90131-2.

[9] R. Demmin, R. J. Gorte. *J. Catal.* **1984**, 90 (1), 32–39. DOI: 10.1016/0021-9517(84)90081-2.

[10] E. N. Fuller, P. D. Schettler, J. C. Giddings. *Ind. Eng. Chem.* **1966**, 58 (5), 18–27. DOI: 10.1021/ie50677a007.

[11] L. Znak, J. Zieliński. *Appl. Catal., A* **2008**, 334 (1-2), 268–276. DOI: 10.1016/j.apcata.2007.10.015.

[12] S. Ewald, S. Standl, O. Hinrichsen. *Appl. Catal., A* **2018**, 549, 93–101. DOI: 10.1016/j.apcata.2017.09.023.

[13] G. Weatherbee, C. H. Bartholomew. *J. Catal.* **1984**, 87 (1), 55–65. DOI: 10.1016/0021-9517(84)90167-2.

[14] C. H. Bartholomew. *Catal. Lett.* **1990**, 7, 27–51. DOI: 10.1007/BF00764490.

APPENDIX D

Supporting Information for Chapter 6

Methods

DFT Calculations

DFT calculations were performed with the Vienna Ab-initio Simulation Package (VASP) [1, 2] using the plane-wave pseudopotential method. A generalized gradient approximation was applied with the RPBE functional [3]. All Ni electronic structure calculations were spin-polarized because of the magnetic properties and van der Waals interaction was accounted for with the DFT-D3 method [4]. The cutoff energy was set to 400 eV and a first-order Methfessel-Paxton smearing of 0.2 eV was used. The close-packed Ni(111) surface was modeled by four layers in a (3×3) supercell with a vacuum of 10 Å above the surface. The lattice constant was optimized for the applied DFT settings and results in a value of 3.48 Å for Ni(111) and 3.94 Å for Pt(111), which agrees with the experimental value of 3.52 Å and 3.94 Å [5], respectively. A Monkhorst-Pack mesh of (3×3×1) was used. Only the two top layers were relaxed together with the adsorbate until all forces were below 0.02 eV Å^{-1}. Vibration frequencies were calculated with a fixed Ni slab within the Atomic Simulation Environment. DFT calculations for Pt(111) were performed with the same settings for an optimized slab without spin-polarization. The binding energy of the adsorbate $\Delta E_b^{C_aO_bH_c^*}$ was referenced to the energy of the gas-phase molecule $E^{C_aO_bH_c(g)}$ and the Ni slab E^{Ni} with

$$\Delta E_b^{C_aO_bH_c^*} = E^{C_aO_bH_c^*} - E^{C_aO_bH_c(g)} - E^{Ni} \tag{D.1}$$

All energies were corrected for the zero-point energy. Thermodynamic properties of the adsorbates were calculated from the partition functions of the adsorbates with standard statistical methods via the same routines, which were used in the work of Blondal et al. [6]. For adsorbates with two frequencies below 100 cm^{-1}, the two lowest frequencies were replaced with a 2D gas partition function to account for free translation of the adsorbate over the metal surface. The surface area was estimated from the Ni(111) unit cell and amounts to 5.25 Å^2 atom^{-1} and to 6.72 Å^2 atom^{-1} for Pt(111). Heats of formation of the adsorbates were calculated with the method discussed in the work of Blondal et al. [6]. Briefly, a reference heat of formation for the gas-phase precursor $\Delta_f H_0^{C_aO_bH_c(g)}$ was calculated with a hypothetical gas-phase reaction of CH_4, H_2O and H_2. The binding energy $\Delta E_b^{C_aO_bH_c^*}$ from Equation (D.1) is also the heat of adsorption $\Delta H_{0,ads}^{C_aO_bH_c^*}$ at 0 K. Finally, the heat of formation of the adsorbate $\Delta_f H_0^{C_aO_bH_c^*}$ at 0 K was calculated with equation Equation (D.2), which was then corrected to 298 K with a group-additivity method via the difference in heat of formation from 0 K to 298 K of C (1.051 kJ mol^{-1}), H (4.234 kJ mol^{-1}), and O (4.430 kJ mol^{-1}) [7].

$$\Delta_f H_0^{C_aO_bH_c^*} = \Delta_f H_0^{C_aO_bH_c(g)} + \Delta_f H_0^{Ni} + \Delta H_{0,ads}^{C_aO_bH_c^*} \tag{D.2}$$

For a more detailed description of the method, the reader is referred to the paper of Blondal et al. [6] and the references therein. Transition states were accessed with the climbing-image nudged-elastic-band method (CINEB) [8]. The reaction coordinate was interpolated with five images between the initial and final state with a spring constant of 0.1 eV Å^{-1}. Each image was relaxed until the forces were below

$0.05\,\mathrm{eV\,Å^{-1}}$. Kinetic parameters were derived from transition state theory [9]. The rate constant is related to the free energy of the transition state $\Delta G_i^{\ddagger}$ via

$$k_\mathrm{i} = \frac{k_\mathrm{B}T}{h}\exp\left(\frac{-\Delta G_\mathrm{i}^{\ddagger}}{k_\mathrm{B}T}\right) = \frac{k_\mathrm{B}T}{h}\exp\left(\frac{-\Delta S_\mathrm{i}^{\ddagger}}{k_\mathrm{B}}\right)\exp\left(\frac{-\Delta H_\mathrm{i}^{\ddagger}}{k_\mathrm{B}T}\right) \tag{D.3}$$

where k_B is the Boltzmann constant and h is Planck's constant. The heat of formation of the transition state can not be calculated directly. However, the difference in enthalpy between the initial and transition state $\Delta H_\mathrm{i}^{\ddagger}$ corresponds to the difference in potential energy

$$\Delta H_\mathrm{i}^{\ddagger} = E_\mathrm{TST} + E_\mathrm{TST}^0 - \left(E_\mathrm{initial} + E_\mathrm{initial}^0\right) \tag{D.4}$$

where E_i is the potential energy and E_i^0 is the zero-point energy. The zero-point energy is calculated from the N vibration frequencies ν_i with

$$E_\mathrm{ZPE} = \frac{1}{2}\sum_{i=1}^{N} hc\nu_\mathrm{i} \tag{D.5}$$

where c is the speed of light. $\Delta S_i^{\ddagger}$ is the difference in entropy between the initial S_initial and transition state S_TST

$$\Delta S_\mathrm{i}^{\ddagger} = S_\mathrm{TST} - S_\mathrm{initial} \tag{D.6}$$

The vibrational contribution to entropy of the transition or initial state is determined from the partition functions of the adsorbates with Equation (D.7). While the initial or final state has $3N-6$ vibrational frequencies, the transition state has $3N-7$. All calculated transition states within this study have only one imaginary vibrational frequency. The entropy is calculated from the frequencies with

$$S^\mathrm{vib} = R\sum_{i}^{\mathrm{N}} - \ln\left(1-e^{-x_\mathrm{i}}\right) + \frac{x_\mathrm{i}e^{-x_\mathrm{i}}}{\left(1-e^{-x_\mathrm{i}}\right)} \tag{D.7}$$

where

$$x_\mathrm{i} = \frac{hc\nu_\mathrm{i}}{k_\mathrm{B}T} \tag{D.8}$$

The rate calculated with Equation (D.3) is regressed via the Arrhenius equation

$$k = A\exp\left(\frac{-E_\mathrm{a}}{RT}\right) \tag{D.9}$$

to determine the pre-exponential coefficient A and the activation energy E_a.

Reaction Mechanism Generation

The selection process in the rate-based algorithm is based upon the rates of formation for each species. Specifically, RMG evaluates the characteristic rate of the core species via Equation (D.10)

$$R_\mathrm{char} = \sqrt{\sum_{i}^{N_\mathrm{core}} R_\mathrm{i}^2} \tag{D.10}$$

where R_i is the rate of formation of species i in the core. If the rate of formation of edge-species j exceeds some fraction of the characteristic rate, $R_\mathrm{j} > \epsilon_\mathrm{core}R_\mathrm{char}$, where $\epsilon_\mathrm{core} \in (0,1]$ is a user-defined tolerance, that species is moved to the core, and the process starts over. This procedure is repeated until a specified termination criterion is reached. In the present work, we used the `terminationRateRatio`, which is defined as the ratio between the initial characteristic rate R_char^0 and the characteristic rate at

the present time step. If this ratio drops below a value of ϵ_{rate}, the mechanism expansion process is terminated.

$$\frac{R_{\text{char}}}{R^0_{\text{char}}} \leq \epsilon_{\text{rate}} \tag{D.11}$$

Figure D.1 to Figure D.10 shows the reaction families (templates) used for the generation of the methanation mechanisms in RMG.

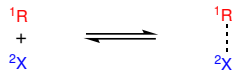

Figure D.1.: Adsorption of physisorbed species.

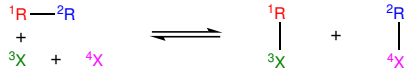

Figure D.2.: Dissociative adsorption.

Figure D.3.: Abstraction in α position.

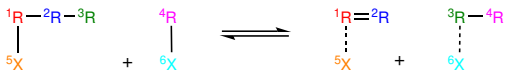

Figure D.4.: Abstraction in the β-position forming two physisorbed species.

Figure D.5.: Abstraction in the β-position forming one physisorbed species.

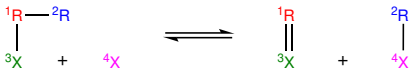

Figure D.6.: Dissociation in the α position.

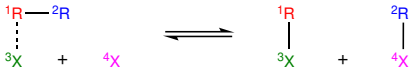

Figure D.7.: Dissociation of a physisorbed species.

Figure D.8.: Dissociation of a double bond in α position.

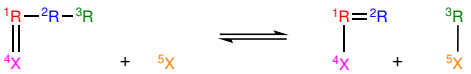

Figure D.9.: Dissociation in the β-position.

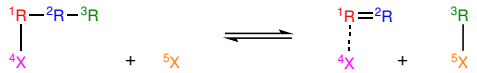

Figure D.10.: Dissociation in the β-position forming a physisorbed species

The parameters for the BEP relations for these reaction families are summarized in Table D.1. For surface reactions, the pre-exponential factor is typically set to $A = 1\times10^{13}\,\mathrm{s}^{-1}$ and then divided by the surface site density of $3.19\times10^{-9}\,\mathrm{mol\,cm}^{-2}$ for the Ni(111) facet [10].

Table D.1.: Brønsted-Evans-Polanyi relations for the reaction families with an exemplary reaction and the literature source of the relation.

Reaction family	A / $\mathrm{m^2\,mol^{-1}\,s^{-1}}$ or s / 1	α / –	E_0 / $\mathrm{kJ\,mol^{-1}}$	Reference
Dissociation of double bonds in α position		$CO^* + {}^* \rightleftharpoons C^* + O^*$		
R=R	3.2×10^{17}	0.84	185.1	Wang et al. [11]
C=O	3.2×10^{17}	1.05	116.7	This study + Vogt et al. [12]
Dissociation in α position		$CH^* + {}^* \rightleftharpoons C^* + H^*$		
R-R	3.2×10^{17}	0.84	185.1	Wang et al. [11]
C-C	3.2×10^{17}	0.7106	125.7	Sutton and Vlachos [13]
C-O	3.2×10^{17}	0.8125	141.6	Sutton and Vlachos [14]
C-H	3.2×10^{17}	1.15	62.8	This study
O-H	3.2×10^{17}	0.2815	72.8	Sutton and Vlachos [14]
C-OH	3.2×10^{17}	1.04	124.7	This study + Vogt et al. [12]
Dissociation in β position		$COH^* + {}^* \rightleftharpoons CO^* + H^*$		
R-R	3.2×10^{17}	0.84	185.1	Wang et al.[11]
C-H	3.2×10^{17}	1.105	102.4	Sutton and Vlachos [13]
O-H	3.2×10^{17}	0.2352	72.1	Sutton and Vlachos [14]
Dissociation in β position forming physisorbed species		$COOH^* + {}^* \rightleftharpoons CO_2^* + H^*$		
R-R	3.2×10^{17}	1.08	110.56	This study + Vogt et al. [12]
Dissociation of physisorbed species		$H_2O^* + {}^* \rightleftharpoons OH^* + H^*$		
R-R	3.2×10^{17}	0.2815	72.8	
H_2O	3.2×10^{17}	0.51	97.45	Wang et al. [15]
Adsorption of physisorbed species		$CO_2 + {}^* \rightleftharpoons CO_2^*$		
R	0.1	0.0	0	
CO_2	7×10^{-3}	0.0	0	Benziger and Madix [16]
Dissociative adsorption		$CH_4 + 2\,{}^* \rightleftharpoons CH_3^* + H^*$		
R	0.01	0.0	41.8	
H_2	0.1	0.0	3.8	Carvalho et al. [17]
CH_4	0.1	0.72	92.6	Wang et al. [15]
Abstraction in α position		$CH_3^* + O^* \rightleftharpoons CH_2^* + OH^*$		
R-R,R	3.2×10^{17}	0.37	99.3	This study
R-H,R	3.2×10^{17}	0.37	99.3	This study
C-H,O	3.2×10^{17}	0.94	129.3	Sutton et al. [18]
O-H,O	3.2×10^{17}	0.65	15.4	Sutton et al. [18]
C-H,C	3.2×10^{17}	0.37	99.3	This study
Abstraction in β position forming one physisorbed species		$COOH^* + O^* \rightleftharpoons CO_2^* + OH^*$		
R-R,R	3.2×10^{17}	0.94	129.3	Sutton et al. [18]
C-H,O	3.2×10^{17}	0.94	129.3	Sutton et al. [18]
O-H,O	3.2×10^{17}	0.65	15.4	Sutton et al. [18]
Abstraction in β position forming two physisorbed species		$COOH^* + OH^* \rightleftharpoons CO_2^* + H_2O^*$		
R-R,R	3.2×10^{17}	0.68	106.1	Sutton et al. [18]
C-H,OH	3.2×10^{17}	0.68	106.1	Sutton et al. [18]
O-H,OH	3.2×10^{17}	0.02	1.9	Sutton et al. [18]
CO_2 dissociation		$CO_2^* + {}^* \rightleftharpoons CO^* + O^*$		
	4.2×10^{15}		50	Kreitz et al. [10]

Parameters and settings used for the generation procedure are summarized in Table Table D.2 and parameters for the experimental procedure are listed in Table D.3.

Table D.2.: RMG settings used for the mechanism generation procedure. Parameters adapted during the constrained mechanism generation are reported in parenthesis.

Property	Value
Temperatures	573 K and 673 K
Pressure	1 bar
Surface site density	3.16×10^{-9} mol cm^{-2}
Specific surface area	1×10^{5} m^2 m^{-3}
H_2/CO_2	4/1
`toleranceMoveToCore`, ϵ_{core}	1×10^{-2} (1×10^{-1})
`terminationRateRatio`, ϵ_{rate}	1×10^{-13} (1×10^{-10})
Initial coverage	vacant site fraction = 1.0
Max. oxygen atoms	2
Max. carbon atoms	- (3)
No. RMG runs	500 (5,000)
$\Delta E_{\text{Ni}}^{\text{C}}$	-6.45 eV
$\Delta E_{\text{Ni}}^{\text{O}}$	-4.70 eV
$\Delta E_{\text{Ni}}^{\text{H}}$	-2.76 eV
$\delta E_{\text{Pt}}^{\text{HX}}$, $\delta E_{\text{Pt}}^{\text{CX}}$, $\delta E_{\text{Pt}}^{\text{OX}}$, δE_{a}^{0}	± 0.3 eV (each)
$\delta E_{\text{Pt}}^{\text{phys}}$	± 0.2 eV
$\delta\alpha$	± 0.15

Table D.3.: Summary of the conditions for the temperature-scanning experiment and the parameters used for the microkinetic model.

Property	Value
Initial temperature	323 K
Pressure	1 bar
Surface site density	3.16×10^{-9} mol cm^{-2}
Ni surface area	0.514 m^2
Reactor volume	1×10^{-6} m^3
Temperature ramp	20 K min^{-1}
Volumetric flow rate	50 mL$_N$ min^{-1}
H_2 mole fraction	0.197
CO_2 mole fraction	0.0502
Ar mole fraction	0.7528
No. of CSTRs	100
Inner diameter	5×10^{-6} mm
Porosity	0.4
Bed length	4×10^{-6} mm

Considering Uncertainties in RMG

There are two ways to account for uncertainty in the heat of formation of the adsorbates in RMG. The first method is to vary the binding energy for the descriptor (C, H, and O) on Ni(111) in RMGs' input file, which is described in (D.12).

$$\Delta E_{\mathrm{Ni}}^{\mathrm{AX}} = \Delta E_{\mathrm{Pt}}^{\mathrm{AX}} + \gamma \left((\Delta E_{\mathrm{Ni}}^{\mathrm{A}} + \delta E_{\mathrm{Ni}}^{\mathrm{A}}) - \Delta E_{\mathrm{Pt}}^{\mathrm{A}} \right) \tag{D.12}$$

The second approach is to assume that the DFT derived binding energy for the descriptor is correct and the heat of formation of the adsorbate in the Pt(111) database is varied, resulting in

$$\Delta E_{\mathrm{Ni}}^{\mathrm{AX}} = (\Delta E_{\mathrm{Pt}}^{\mathrm{AX}} + \delta E_{\mathrm{Pt}}^{\mathrm{AX}}) + \gamma \left(\Delta E_{\mathrm{Ni}}^{\mathrm{A}} - \Delta E_{\mathrm{Pt}}^{\mathrm{A}} \right) \tag{D.13}$$

The first method would automatically account for the correlation between the heats of formation, which means that e.g., if the binding energy of C^* is increased, the resulting values for CO^* and HCO^* are increased, which agrees with the d-band model [19]. Whereas the first method is easy to implement and accounts for correlation, it has a severe drawback because the uncertainty is scaled with the LS relation. If we perturbed the binding energy with $\pm 0.3\,\mathrm{eV}$, C^* would have an uncertainty of $\pm 0.3\,\mathrm{eV}$ because $\gamma = 1$ but the physisorbed species would not be uncertain at all since $\gamma = 0$. This premise is not valid. When we decrease the binding energy of C by $30\,\mathrm{kJ\,mol^{-1}}$, the CO binding energy will be decreased by the same amount. On top of that, there can be a small uncertainty but this will describe the general trend. Therefore, we choose the latter method within this work. Figure D.11 illustrates the quasi-random sampling and the correlation between the adsorbates according to the LS relations. The three descriptor species H^*, C^*, and O^* are uncorrelated and the quasi-random numbers fill the entire uncertainty range. The uncertainty domain for the C-O parameter space is illustrated in Figure D.11a, which shows the uniform distribution inside the boundaries of [-0.3 eV, 0.3 eV]

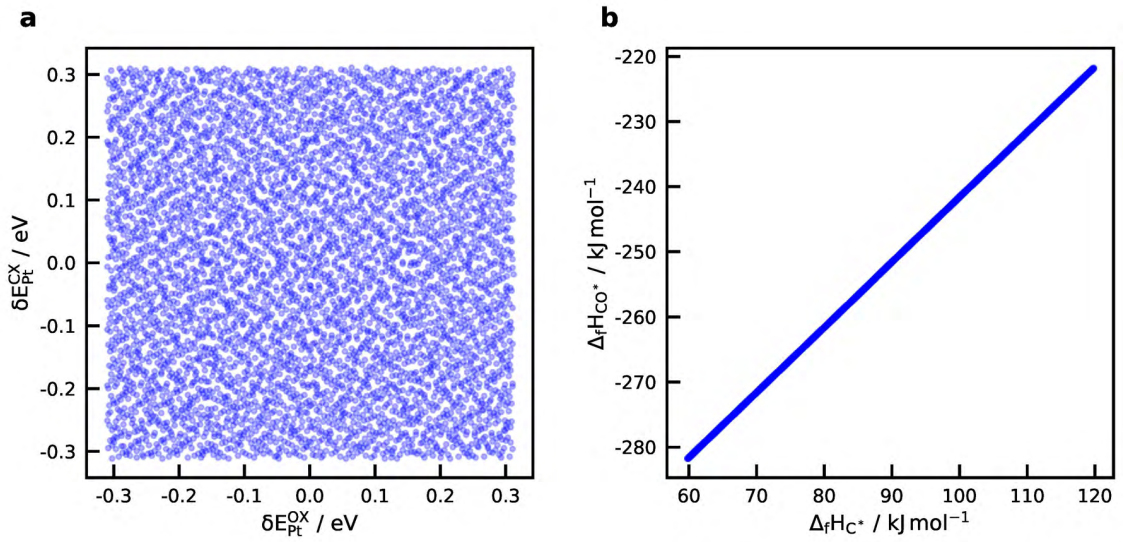

Figure D.11.: (a) Uncorrelated uncertainty space in the binding energies of CX (all species that bind through C) and OX (all species that bind through O) sampled with 5,000 quasi-random numbers. (b) Correlated uncertainty of the heat of formation of CO^* and C^*. All species that bind through carbon are linearly correlated according to the LS relation, which results in the linear behavior of the correlation.

The linear correlation between the binding energy of all adsorbates that bind through one of these descriptors and the descriptor should be valid for the uncertainty as well. When dealing with correlated uncertainty, this means that if we perturb e.g. the C binding energy by $+0.1\,\mathrm{eV}$, we have to perturb the

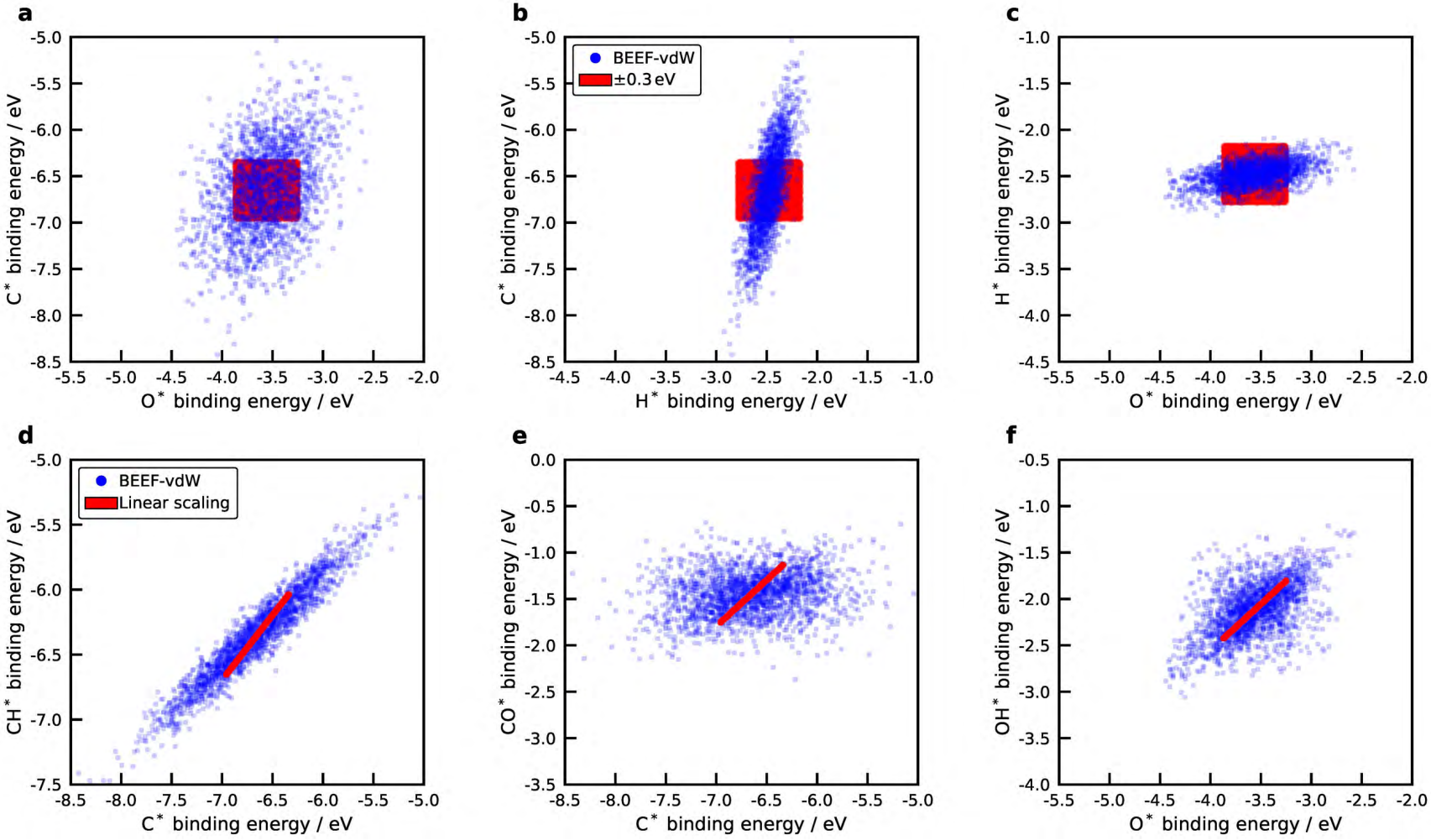

Figure D.12.: Probability distribution of (a) C^* and O^*, (b) C^* and H^*, (c) H^* and O^*, (d) C^* and CH^*, (e) C^* and CO^*, and (f) O^* and OH^* binding energies. Ensemble of 2000 binding energies calculated with the BEEF-vdW functional. The red area describes the uniform sampling of the data points within $\pm 0.3\,\mathrm{eV}$ around the mean value, which was applied in this work. The red line in d-f indicates the uncertainty estimate with the linear scaling approach.

binding energy of all species that bind through C, e.g. CO^* by $+0.1\,eV$. This is the strong correlation between the parameters according to the linear scaling (LS) relations, which is illustrated in Figure D.11b.

The uniform uncertainty distribution in the boundaries of [-0.3 eV, 0.3 eV] is a simplification of the true probability distribution of the uncertainty. A more accurate uncertainty distribution can be determined with the BEEF-vdW functional [20] and the usage of the Bayesian error estimate [21, 22]. We performed additional DFT calculations with the BEEF-vdW functional to check whether the more complex BEE distribution can be approximated with the uniform distribution. Electronic structure calculations were performed for the 3 descriptor species on Pt(111) using the projector augmented wave method in GPAW [23, 24]. The Pt(111) lattice constant was optimized for the BEEF-vdW functional and amounts to 4.02 Å. Adsorbates were relaxed on a (3×3) slab with 4 layers, where the top 2 were relaxed together with the adsorbate and the 2 bottom layers were fixed with 10 Å of vacuum above the slab until all forces were below $0.02\,eV\,Å^{-1}$. Geometry optimization was performed on a $(5\times5\times1)$ kpoints at 50 Ry and the single point was calculated for a $(7\times7\times1)$ mesh at 63 Ry. An ensemble of 2000 exchange-correlation functionals was created around the BEEF-vdW model parameters using the `BEEFensemble` command to calculate the uncertainty distribution of the species binding energy self-consistently. The results are displayed in Figure D.12.

Figure D.12a shows a scatter plot of the probability distribution of the C^* and O^* pair of binding energies. The uncertainty in C^* binding energies is significant with values from $-8.5\,eV$ to $-5\,eV$. The red box inside Figure D.12a-c shows the uniform [-0.3 eV, 0.3 eV] boundary around the average, which was used within this work. This comparison clearly shows that the applied uniform sampling distribution of this narrow uncertainty range stands to reason. We even underestimate the uncertainty in the DFT-derived binding energies for C^* and O^*. There is a correlation between the C^* and H^* binding energy [19, 25]. Figure D.12d-f displays the uncertainty correlation of C^*/CH^*, C^*/CO^*, and O^*/OH^*. In agreement with the results from a-c, the binding energies of the adsorbed molecules shows considerable scatter, in the range of up to 2 eV for CH^*. As expected from the linear scaling relations, there is a strong correlation between C^* and CH^* as well as O^* and OH^*. Interestingly, the uncertainty in CH^* is significant and in the same order as the uncertainty in C^*. The correlation between C^* and CO^* is not that strong, which is related to the unique structure of CO^*. The red line in each Figure D.12d-f shows the estimated uncertainty correlation of the binding energy in these molecules based on the LS relations. Figure D.12d-f shows clearly that the assumed uncertainty in these species as well as the uncertainty correlation (consequently the usage of the LS relations) stands to reason. It can be clearly seen, that the assumed uncertainty of our simplified approach is quite optimistic and the uncertainty that should be considered is considerably larger. Overall, based on these additional DFT data, we think that our method of including correlated uncertainty into the mechanism generation procedure is reasonable. Figure D.13 shows an example for the uncertainty range of the BEP relation in comparison to the DFT derived parameters.

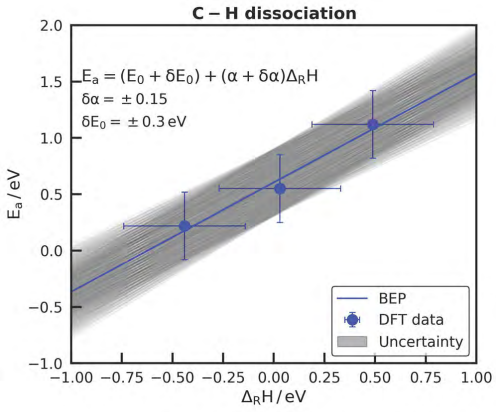

Figure D.13.: Example of the uncertainty in DFT derived BEP relationships for the C-H dissociation family.

Results and Discussion

DFT results

DFT calculations were performed for several important methanation intermediates and the raw data is summarized in Table D.4 and the data for the adsorbate in the gas-phase in Table D.6. The results for CO_2^*, $COOH^*$, and $HCOO^*$ on Pt(111), which were added to the thermochemistry library in RMG are reported in Table D.5.

Table D.4.: Summary of the results from the DFT calculation with VASP for the Ni(111) slab. The single-point energies (SPE) and zero-point energies (ZPE), as well as the vibrational frequencies for the most stable position, are provided.

Species	Pos	ML	SPE / eV	ZPE / eV	Frequencies / cm^{-1}	E_B / eV	$\Delta_f H$ / $kJ\,mol^{-1}$
Ni(111)	(3×3)		-182.698	-	-	-	-
H^*	fcc	1/9	-186.706	0.171	816.1, 822.3, 1109.0	-2.760	-50.26
C^*	hcp	1/9	-190.546	0.098	504.1, 514.7, 562.6	-6.445	154.30
O^*	fcc	1/9	-189.647	0.076	355.9, 385.2, 482.9	-4.700	-235.51
CO^*	hcp	1/9	-199.010	0.182	138.7, 144.2, 281.0, 281.6, 335.2, 1754.8	-1.821	-226.63
CO_2^*	atop	1/9	-205.241	0.323	56, 60.4, 72.0, 82.1, 94.3, 600.7, 619.0, 1302.8, 2325.2	-0.219	-387.78
OH^*	fcc	1/9	-193.490	0.343	248.3, 249.2, 436.2, 438.5, 439.6, 3721.3	-3.147	-260.63
H_2O^*	atop	1/9	-197.093	0.594	56, 56, 59.3, 78.4, 181.0, 297.6, 1503.9, 3653.4, 3802.9	-0.260	-264.06
CH^*	fcc	1/9	-195.138	0.359	416.7, 417.6, 622.8, 648.7, 650.2, 3042.2	-6.144	56.38
CH_2^*	fcc	1/9	-198.780	0.588	267.4, 274.9, 373.5, 506.0, 570.8, 665.4, 1380.6, 2450.1, 2996.6	-3.842	47.04
CH_3^*	fcc	1/9	-202.950	0.878	197.8, 204.8, 330.9, 347.8, 452.9, 453.7, 1145.0, 1286.5, 1287.1, 2765.3, 2842.8, 2847.1	-1.950	-7.40
CH_4^*	atop	1/9	-207.008	1.198	56, 56, 56, 81.4, 170.3, 319.5, 1253.0, 1275.3, 1297.1, 1483.3, 1494.8, 2896.1, 2967.7, 3029.6, 3062.8	0.192	-48.05
COH^*	fcc	1/9	-201.931	0.469	92.5, 146.0, 152.0, 395.3, 415.2, 445.3, 1087.5, 1244.0, 3581.1	-4.161	-160.83
HCO^*	bridge	1/9	-201.730	0.457	143.3, 154.5, 235.5, 284.1, 483.8, 622.3, 1166.6, 1281.2, 2889.6	-2.150	-142.62
$COOH^*$	bridge	1/9	-208.895	0.599	56, 56.6, 116.1, 205.4, 227.8, 444.4, 608.1, 664.6, 1093.7, 1247.8, 1489.1, 3513	-2.325	-392.51
$HCOO^*$	atop	1/9	-209.132	0.614	68.9, 104.6, 120.2, 276.8, 287.2, 308.1, 736.0, 961.6, 1288.5, 1318.5, 1490.6, 2944.4	-2.847	-413.94

The results for the transition state calculations are summarized in Table D.7 for the initial state (*e.g.* C−H) and the transition state (*e.g.* $C{-}H^{\ddagger}$). Table D.8 reports the calculated activation barriers and pre-exponential coefficients derived from the transition state calculations. Some activation barriers for Ni(111) were taken from Vogt et al [12]. BEP relations derived for the C−H dissociation and the CH−C abstraction are illustrated in Figure D.14.

Table D.5.: Summary of the results from the DFT calculation with VASP for the Pt(111) slab. The single-point energies (SPE) and zero-point energies (ZPE), as well as the vibrational frequencies for the most stable position, are provided.

Species	Pos	ML	SPE / eV	ZPE / eV	Frequencies / cm^{-1}	E_B / eV	$\Delta_f H$ / $kJ\,mol^{-1}$
Pt(111)	(3×3)		-215.626	-	-	-	-
CO_2^*	atop	1/9	-238.220	0.321	56, 56, 58.4, 87.7, 96.6, 596.4, 622.7, 1302.9, 2328.5	-0.260	-388.11
$COOH^*$	bridge	1/9	-242.183	0.620	56, 56, 64.9, 291.3, 295.8, 502.8, 594.7, 661.0, 1071.3, 1231.8, 1683.3, 3363.2	-2.677	-423.00
$HCOO^*$	atop	1/9	-241.641	0.607	85.3, 111.1, 122.0, 298.5, 332.8, 345.9, 780.4, 950.4, 1229.7, 1312.2, 1482.2, 2946.5	-2.421	-369.47

Table D.6.: Summary of the results from the DFT calculation with VASP for the gas-phase molecules. The single-point energies (SPE) and zero-point energies (ZPE), as well as the vibrational frequencies for the most stable position, are provided.

Species	SPE / eV	ZPE / eV	Frequencies / cm^{-1}
H_2	-6.970	0.338	4316.6
O_2	-9.578	0.116	1544.7
C	-1.305	0	-
CO	-14.447	0.138	2117.3
CO_2	-22.323	0.309	630, 633.4, 1310.2, 2346.1
OH	-0.7548	0.245	3579.3
H_2O	-14.152	0.611	150.9, 216.4, 3579.3
CH	-6.119	0.182	2724.4
CH_2	-12.124	0.472	1025.7, 3090.7, 3304.5
CH_3	-18.214	0.789	525.8, 1354.7, 1365.3, 3041.2, 3213.6, 3216.5
CH_4	-24.039	0.735	30.9, 58.4, 121.5, 225.8, 356.7, 2630.9, 2709.7, 2743.3, 2957.1
HCO	-16.776	0.35	1073.6, 1853.6, 2568.6
COH	-14.944	0.341	114.5, 1035.9, 1319.6, 2925.1
COOH	-23.841	0.568	574.5, 596.2, 1033.6, 1195.4, 1824.3, 3665.5
HCOO	-23.519	0.546	684.6, 972.9, 1214.3, 1298.4, 1445.6, 2980.5
HCOH	-19.554	0.71	1042.1, 1165.7, 1257.9, 1473.5, 2735.4, 3563.6
H_2CO	-21.866	0.707	1152.9, 1221.9, 1497.5, 1741.3, 2800.2, 2831.0

Table D.7.: Summary of the data from the TST calculation with VASP for Ni(111). The single-point energies (SPE) and zero-point energies (ZPE), as well as the vibrational frequencies are provided for the initial state (e.g. C−H) and the transition state (e.g. C−H‡).

Species	Pos	ML	SPE / eV	ZPE / eV	Frequencies / cm^{-1}
CH*		1/9	-195.140	0.359	416.7, 417.6, 622.8, 648.7, 650.2, 3042.2
C−H‡		1/9	-193.754	0.206	299.8,454.1,482.0,573.5,1509.4
CH−H*		1/9	-198.780	0.588	267.4, 274.9, 373.5, 506.0, 570.8, 665.4, 1380.6, 2450.1, 2996.6
CH−H‡		1/9	-198.522	0.504	124.5, 399.4, 418.1, 621.7, 658.3, 919.1, 1935.5, 3055.1
CH$_2$−H*		1/9	-202.944	0.878	197.8, 204.8, 330.9, 347.8, 452.9, 453.7, 1145.0, 1286.5, 1287.1, 2765.3, 2842.8, 2847.1
CH$_2$−H‡		1/9	-202.269	0.742	155.0,205.8, 295.0, 412.6, 538.6, 718.2, 869.0, 1327.8,1802.4, 2657.0, 2990.8
CH−H*,C*		1/9	-206.577	0.698	279.7, 299.6, 383.6, 504, 512.7, 548.3, 581.0, 584.3, 695.6, 1395.7, 2448.0, 3025.6
CH−H−C‡		1/9	-205.830	0.605	374.5, 414, 460.2, 463.1, 532.5, 557.7, 607.0, 631.7, 850.6, 1814.5, 3050.2
CH$_2$−H*,C*		1/9	-210.664	0.993	179.5, 200.7, 270.3, 334.0, 489.7, 489.9, 552.6, 556.8, 587.0, 1154.9, 1284.2, 1330.3, 2766.1, 2817.3, 2999.6
CH$_2$−H−C‡		1/9	-209.691	0.834	147.9, 259.8, 323.3, 417.9, 477, 493.9, 532.3, 561.6, 792.3, 861.5, 1267.0, 1523.7, 2853.7, 2937.4

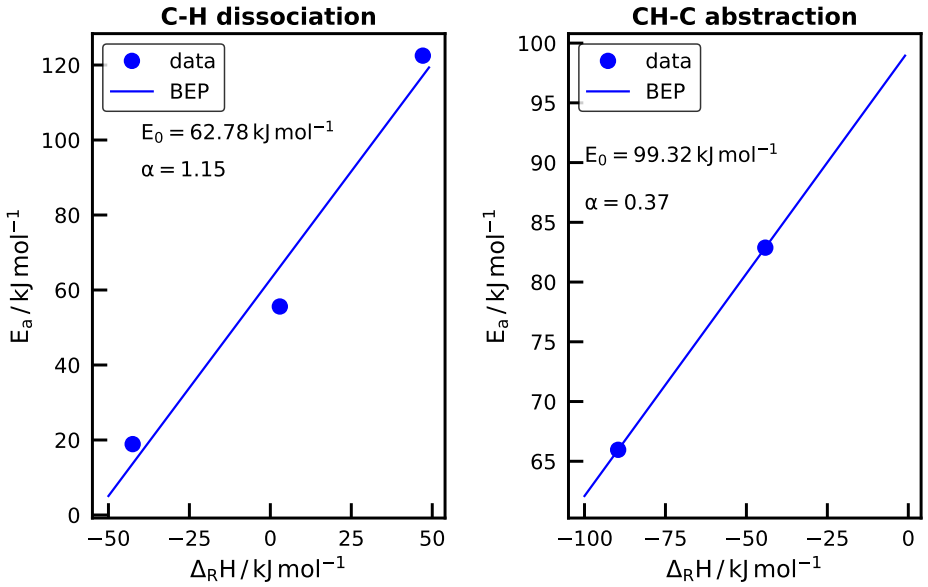

Figure D.14.: Brønsted-Evans-Polanyi (BEP) relations for the C-H dissociation (left) and the CH-C abstraction (right) reactions developed from the electronic structure calculations in this study.

Table D.8.: Summary of the results from the transition state calculations. Activation energies and pre-exponential coefficients were derived according to the described theory (see Transition State Theory).

Reaction	A / $cm^2\,mol^{-1}\,s^{-1}$	E_a / $kJ\,mol^{-1}$	ΔH_{rxn} / $kJ\,mol^{-1}$
C-H dissociation in α position			
$CH^* + {}^* \rightleftharpoons C^* + H^*$	8.75×10^{21}	122.5	47.1
$CH_2^* + {}^* \rightleftharpoons CH^* + H^*$	4.26×10^{21}	18.9	-42.5
$CH_3^* + {}^* \rightleftharpoons CH_2^* + H^*$	6.10×10^{21}	55.6	2.9
C-H, C abstraction in α position			
$CH_2^* + C^* \rightleftharpoons CH^* + CH^*$	2.33×10^{21}	66.0	-89.6
$CH_3^* + C^* \rightleftharpoons CH_2^* + CH^*$	6.13×10^{21}	82.9	-44.2
C=O dissociation in α position			
$CO^* + {}^* \rightleftharpoons C^* + O^*$		274.0 [12]	142.7
$HCO^* + {}^* \rightleftharpoons CH^* + O^*$		89.0 [12]	-37.8
$COOH^* + {}^* \rightleftharpoons COH^* + O^*$		112.0 [12]	-2.4
$HCOO^* + {}^* \rightleftharpoons CHO^* + O^*$		136.0 [12]	34.8
C-OH dissociation in α position			
$COOH^* + {}^* \rightleftharpoons CO^* + OH^*$		29.0 [12]	-91.9
$COH^* + {}^* \rightleftharpoons C^* + OH^*$		180.0 [12]	53.1
dissociation in β position forming physisorbed species			
$COOH^* + {}^* \rightleftharpoons H^* + CO_2^*$		63.0 [12]	-44.2
$HCOO^* + {}^* \rightleftharpoons H^* + CO_2^*$		85.0 [12]	-23.8

Mechanism Generation

Figure D.15 displays the number of species and reactions discovered by RMG in all 500 runs with the coarse settings. The mechanism size varies considerably. The number of unique species and reactions discovered by RMG for the coarse and fine generation stage is summarized in Table D.9. When the Ni surface was dominated by a single adsorbate (*e.g.* CO^*, O^*, or H^*), then the availability of vacant sites was reduced, and the overall rate of reaction on the surface is low, resulting in a small value for R_{char}. Consequently, many edge reactions, which for more reactive surfaces might otherwise be negligible, will have net rates that are greater than $\epsilon_{core} R_{char}$ and thus will be moved to the core.

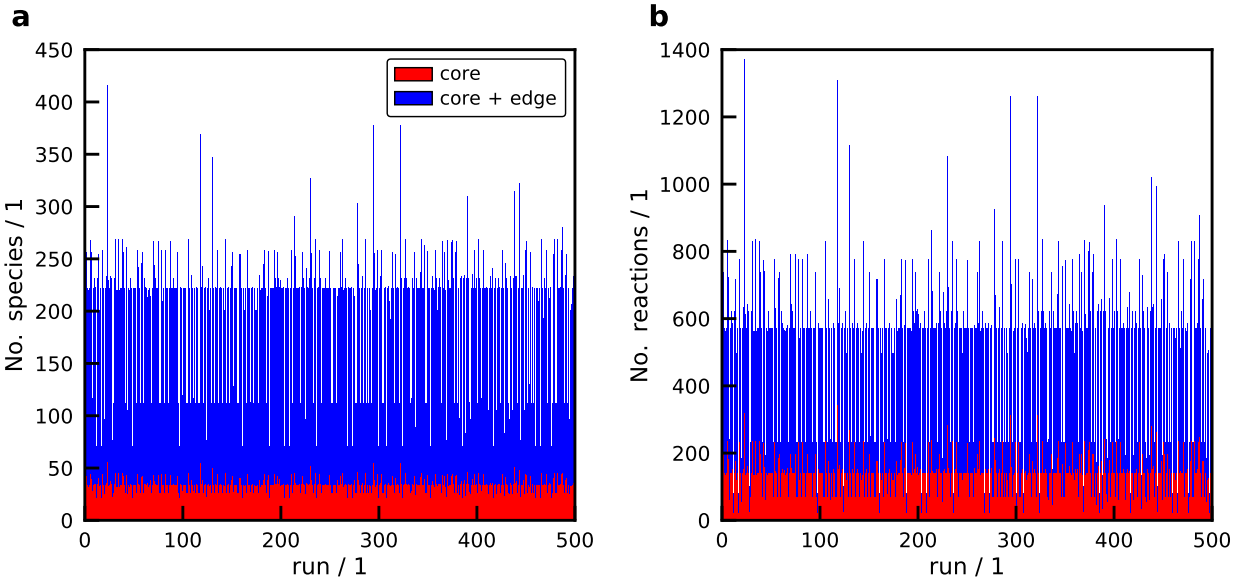

Figure D.15.: Number of species (a) and reactions (b) in the core (red) as well as the combined core and edge (blue) mechanism discovered by RMG under consideration of uncertainties for the coarse run.

Table D.9.: Results for the discovered species (spcs) and reactions (rxns) from the mechanism generation procedure with RMG under consideration of uncertainty in the model parameters.

	Run	Coarse	Fine
Core	Dissociation	84 rxns	36 rxns
	Abstraction	327 rxns	105 rxns
	Adsorption/Desorption	39 rxns	9 rxns
	$\sum$	64 spcs/450 rxns	35 spcs/150 rxns
Edge	Dissociation	369 rxns	118 rxns
	Abstraction	718 rxns	150 rxns
	Adsorption/Desorption	118 rxns	33 rxns
	$\sum$	426 spcs/1205 rxns	135 spcs/301 rxns

Microkinetic Modeling

Figure D.16 displays the simulation results with the full microkinetic models for all gas-phase products. Only CH_4, H_2O and CO are produced in significant quantities.

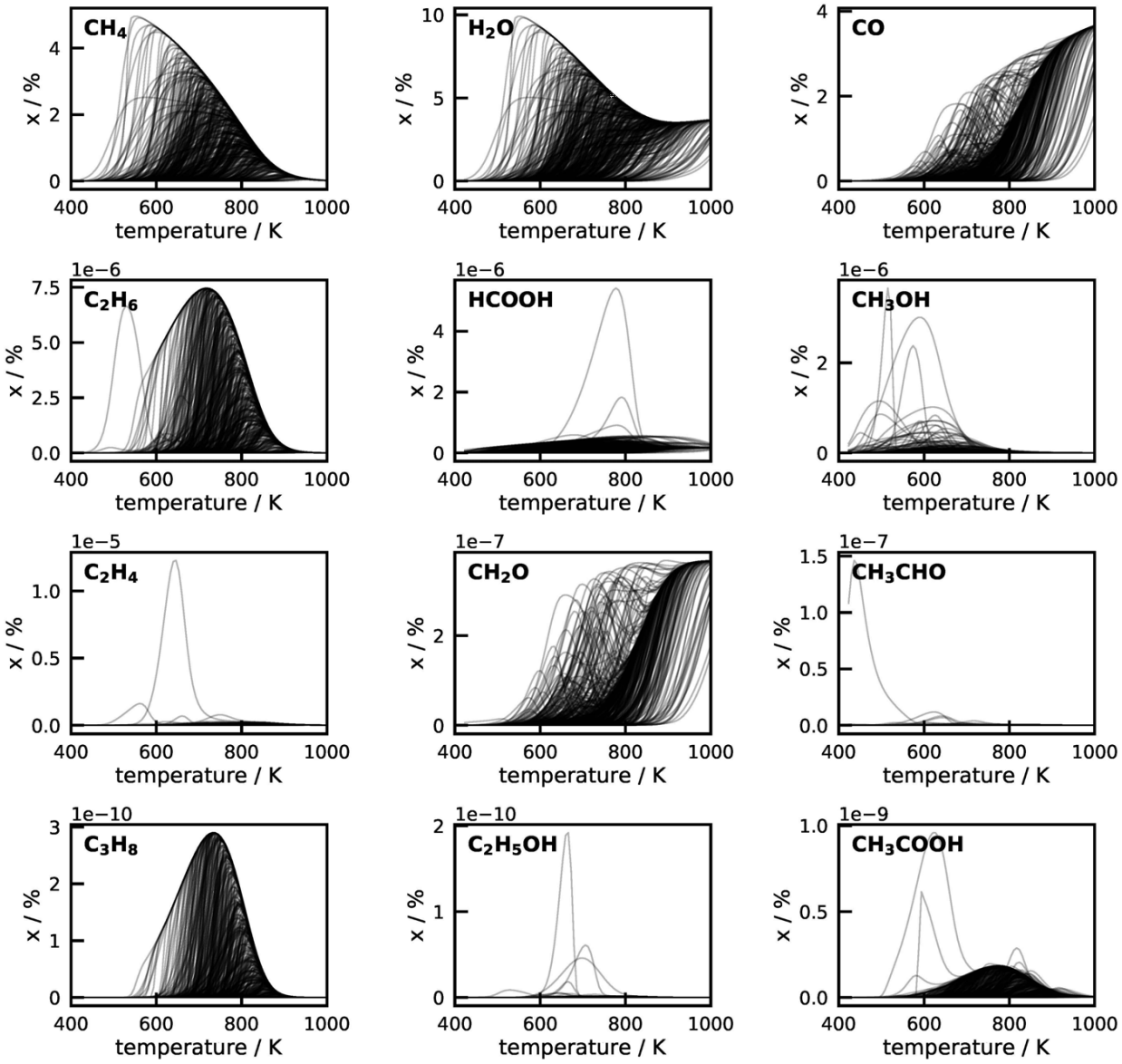

Figure D.16.: Gas-phase products concentration predicted by the full microkinetic model in simulation of the temperature-scanning experiment with the entire reaction network.

The model predictions for the coverage of the Ni(111) facet using the 5000 generated methanation mechanisms are shown in Figure D.17. Ample variations are obtained in the coverage and the most abundant intermediates are H^*, CO^* and O^*.

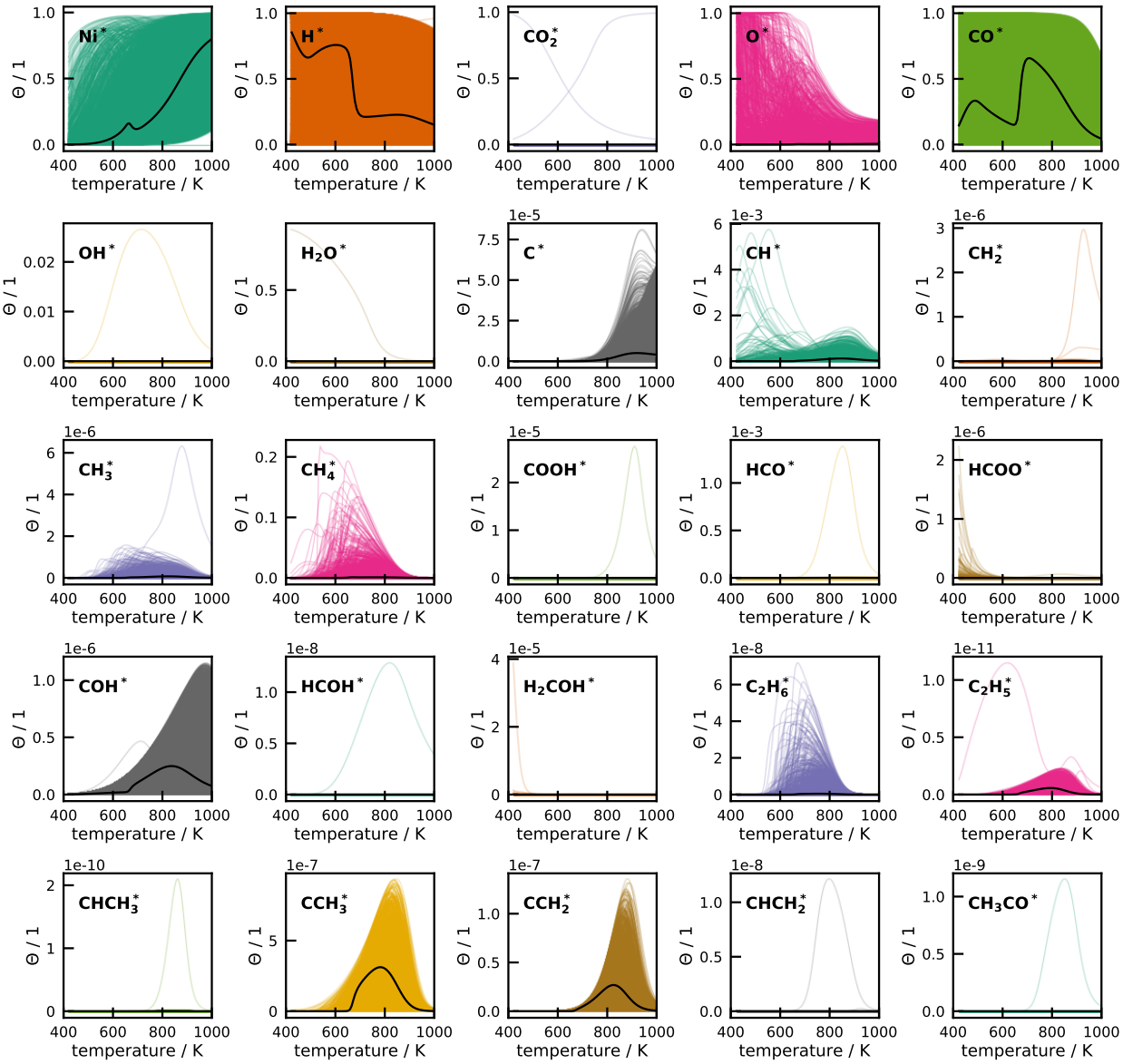

Figure D.17.: Simulation results for the coverages (Θ) over temperature on the Ni(111) facet with the reduced microkinetic model. The black line is the result with the nominal RMG settings.

Figure D.18 compares the model predictions from the GUA with the experimentally determined CO_2 conversion, CH_4 selectivity, and CH_4 yield. The coverage profiles for the best match and the mechanisms that are in good agreement with the data are provided in Figure D.19. CO_2 conversion and CH_4 yield can be predicted from the microkinetic model with a high accuracy, but the CH_4 selectivity can currently not be predicted.

Table D.10 contains the reduced microkinetic model with all the relevant chemistry for the mechanism that is in best agreement with data. The full microkinetic model for the best case is provided in Table D.11. A cti file with this mechanism is provided as well.

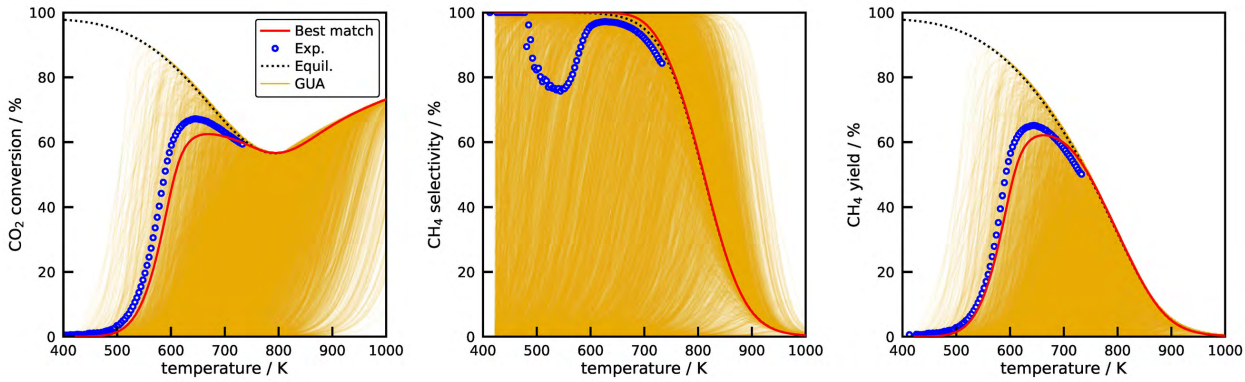

Figure D.18.: Comparison of the predictions from the microkinetic model with the experimental results for the CO_2 conversion, CH_4 selectivity, and CH_4 yield.

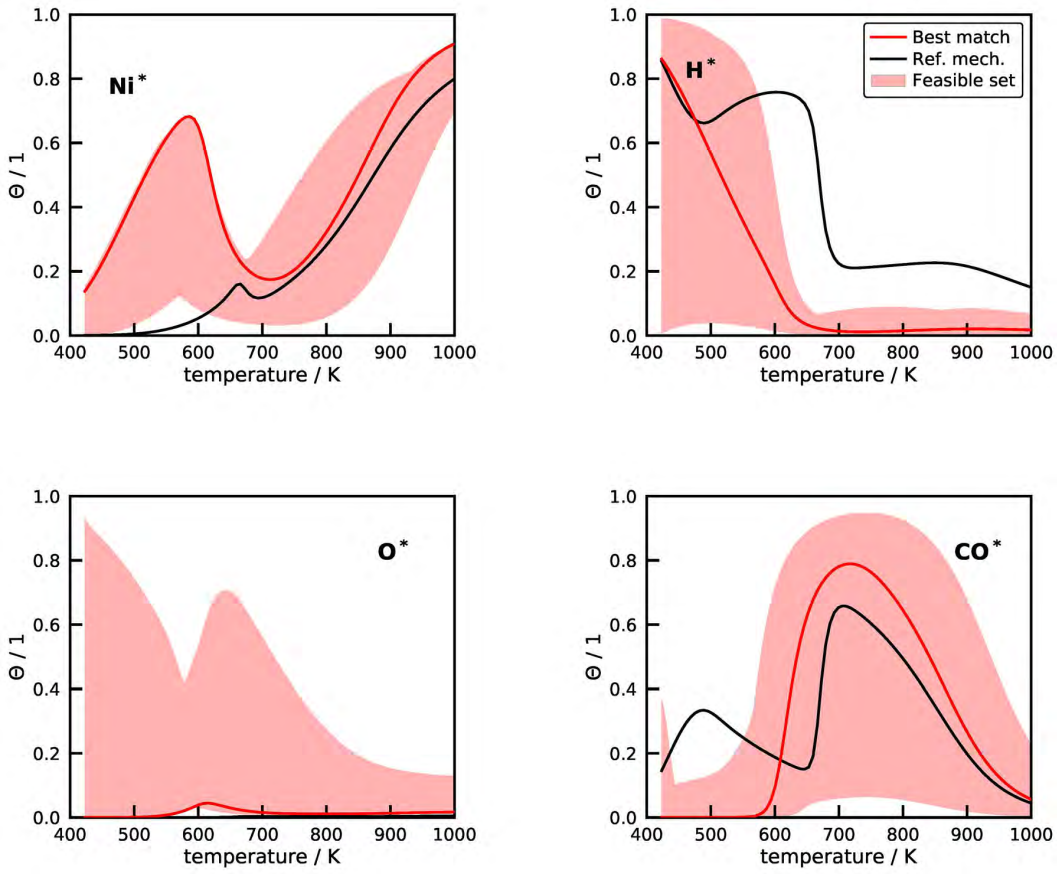

Figure D.19.: Coverage profiles of vacant sites (Ni^*), H^*, O^*, and CO^* for the mechanisms with best agreement to the data. The red line is the best case, the black line is the reference case and the reddish area contains the profiles from the mechanisms which are within 30 % of the lowest MAPE.

Table D.10.: Subset of the mechanism with the best agreement to the experimental data. The full mechanism is available in the SI.

rxn	reaction	A / $\mathrm{cm^2\,mol^{-1}\,s^{-1}}$ or s / $1^\dagger$	E_a / $\mathrm{kJ\,mol^{-1}}$
1	$CO + {}^* \rightleftharpoons CO^*$	$0.8^\dagger$	0.0
2	$CO_2^* + {}^* \rightleftharpoons CO^* + O^*$	4.20×10^{19}	74.5
3	$CH_4 + {}^* \rightleftharpoons CH_4^*$	$0.1^\dagger$	0.0
4	$CO_2 + {}^* \rightleftharpoons CO_2^*$	$7.00\times10^{-3\dagger}$	0
5	$H_2O + {}^* \rightleftharpoons H_2O^*$	$0.1^\dagger$	0.0
6	$H_2 + 2\,{}^* \rightleftharpoons 2\,H^*$	$0.1^\dagger$	17.8
7	$OH^* + {}^* \rightleftharpoons H^* + O^*$	3.20×10^{21}	22.2
8	$H_2O^* + {}^* \rightleftharpoons OH^* + H^*$	6.40×10^{21}	97.1
9	$CH_2^* + {}^* \rightleftharpoons CH^* + H^*$	6.40×10^{21}	0.0
10	$CH_3^* + {}^* \rightleftharpoons CH_2^* + H^*$	9.60×10^{21}	67.0
11	$CH_4^* + {}^* \rightleftharpoons CH_3^* + H^*$	1.28×10^{22}	102.4
12	$COOH^* + {}^* \rightleftharpoons OH^* + CO^*$	3.20×10^{21}	77.5
13	$COOH^* + {}^* \rightleftharpoons CO_2^* + H^*$	3.20×10^{21}	74.0
14	$COOH^* + {}^* \rightleftharpoons COH^* + O^*$	3.20×10^{21}	21.5
15	$HCO^* + {}^* \rightleftharpoons H^* + CO^*$	3.20×10^{21}	0.0
16	$HCO^* + {}^* \rightleftharpoons CH^* + O^*$	3.20×10^{21}	43.7
17	$COH^* + {}^* \rightleftharpoons H^* + CO^*$	3.20×10^{21}	61.5
18	$COH^* + O^* \rightleftharpoons OH^* + CO^*$	3.20×10^{21}	28.8
19	$COOH^* + O^* \rightleftharpoons CO_2^* + OH^*$	3.20×10^{21}	57.0
20	$COOH^* + OH^* \rightleftharpoons CO_2^* + H_2O^*$	3.20×10^{21}	0.0

Table D.11.: Full microkinetic model of the mechanism that is in best agreement with the experimental data.

rxn	reaction	A / cm^2 mol^{-1} s^{-1} or s / 1†	E_a / kJ mol^{-1}
1	$CO + {}^* \rightleftharpoons CO^*$	0.8†	0.00
2	$CO_2^* + {}^* \rightleftharpoons CO^* + O^*$	4.2e+19	74.47
3	$CH_4 + 2\,{}^* \rightleftharpoons CH_3^* + H^*$	0.4†	112.20
4	$CH_4 + {}^* \rightleftharpoons CH_4^*$	0.1†	0.00
5	$CO_2 + {}^* \rightleftharpoons CO_2^*$	0.007†	0.00
6	$H_2O + {}^* \rightleftharpoons H_2O^*$	0.1†	0.00
7	$H_2 + 2\,{}^* \rightleftharpoons 2\,H^*$	0.1†	17.79
8	$C_2H_6 + 2\,{}^* \rightleftharpoons 2\,CH_3^*$	0.01†	41.10
9	$C_2H_6 + 2\,{}^* \rightleftharpoons C_2H_5^* + H^*$	0.06†	41.10
10	$C_2H_6 + {}^* \rightleftharpoons C_2H_6^*$	0.1†	0.00
11	$CO^* + {}^* \rightleftharpoons C^* + O^*$	3.2e+21	197.54
12	$OH^* + {}^* \rightleftharpoons H^* + O^*$	3.2e+21	22.20
13	$H_2O^* + {}^* \rightleftharpoons OH^* + H^*$	6.4e+21	97.13
14	$CH^* + {}^* \rightleftharpoons C^* + H^*$	3.2e+21	101.91
15	$CH_2^* + {}^* \rightleftharpoons CH^* + H^*$	6.4e+21	0.00
16	$CH_3^* + {}^* \rightleftharpoons CH_2^* + H^*$	9.6e+21	67.03
17	$CH_4^* + {}^* \rightleftharpoons CH_3^* + H^*$	1.28e+22	102.36
18	$COOH^* + {}^* \rightleftharpoons OH^* + CO^*$	3.2e+21	77.46
19	$COOH^* + {}^* \rightleftharpoons CO_2^* + H^*$	3.2e+21	73.95
20	$COOH^* + {}^* \rightleftharpoons COH^* + O^*$	3.2e+21	21.51
21	$HCO^* + {}^* \rightleftharpoons H^* + CO^*$	3.2e+21	0.00
22	$HCO^* + {}^* \rightleftharpoons CH^* + O^*$	3.2e+21	43.72
23	$HCOO^* + {}^* \rightleftharpoons HCO^* + O^*$	3.2e+21	178.35
24	$HCOO^* + {}^* \rightleftharpoons CO_2^* + H^*$	3.2e+21	90.22
25	$COH^* + {}^* \rightleftharpoons C^* + OH^*$	3.2e+21	253.49
26	$COH^* + {}^* \rightleftharpoons H^* + CO^*$	3.2e+21	61.54
27	$HCOH^* + {}^* \rightleftharpoons CH^* + OH^*$	3.2e+21	120.82
28	$HCOH^* + {}^* \rightleftharpoons COH^* + H^*$	3.2e+21	0.00
29	$HCOH^* + {}^* \rightleftharpoons HCO^* + H^*$	3.2e+21	66.22
30	$H_2COH^* + {}^* \rightleftharpoons CH_2^* + OH^*$	3.2e+21	234.13
31	$H_2COH^* + {}^* \rightleftharpoons HCOH^* + H^*$	6.4e+21	96.72
32	$C_2H_6^* + {}^* \rightleftharpoons 2\,CH_3^*$	6.4e+21	106.05
33	$C_2H_6^* + {}^* \rightleftharpoons C_2H_5^* + H^*$	1.92e+22	101.30
34	$C_2H_5^* + {}^* \rightleftharpoons CH_2^* + CH_3^*$	3.2e+21	178.97
35	$C_2H_5^* + {}^* \rightleftharpoons CHCH_3^* + H^*$	6.4e+21	57.87
36	$CHCH_3^* + {}^* \rightleftharpoons CH_3^* + CH^*$	3.2e+21	129.08
37	$CHCH_3^* + {}^* \rightleftharpoons CCH_3^* + H^*$	3.2e+21	0.00
38	$CHCH_3^* + {}^* \rightleftharpoons CHCH_2^* + H^*$	9.6e+21	130.72
39	$CCH_3^* + {}^* \rightleftharpoons CH_3^* + C^*$	3.2e+21	227.60
40	$CCH_3^* + {}^* \rightleftharpoons CCH_2^* + H^*$	9.6e+21	140.24
41	$CCH_2^* + {}^* \rightleftharpoons CH_2^* + C^*$	3.2e+21	288.91
42	$CHCH_2^* + {}^* \rightleftharpoons CCH_2^* + H^*$	3.2e+21	0.00
43	$CHCH_2^* + {}^* \rightleftharpoons CH_2^* + CH^*$	3.2e+21	197.92
44	$COCH_3^* + {}^* \rightleftharpoons CH_3^* + CO^*$	3.2e+21	36.71
45	$COCH_3^* + {}^* \rightleftharpoons CCH_3^* + O^*$	3.2e+21	0.00
46	$C^* + OH^* \rightleftharpoons CH^* + O^*$	3.2e+21	74.08
47	$CH^* + OH^* \rightleftharpoons CH_2^* + O^*$	3.2e+21	117.19
48	$CH_2^* + OH^* \rightleftharpoons CH_3^* + O^*$	3.2e+21	87.45
49	$COOH^* + O^* \rightleftharpoons CO_2^* + OH^*$	3.2e+21	56.97
50	$HCO^* + O^* \rightleftharpoons OH^* + CO^*$	3.2e+21	119.75
51	$HCOO^* + O^* \rightleftharpoons CO_2^* + OH^*$	3.2e+21	192.83
52	$COH^* + O^* \rightleftharpoons OH^* + CO^*$	3.2e+21	28.75
53	$COH^* + OH^* \rightleftharpoons HCOH^* + O^*$	3.2e+21	122.22
54	$HCOH^* + O^* \rightleftharpoons HCO^* + OH^*$	3.2e+21	38.48
55	$HCOH^* + OH^* \rightleftharpoons H_2COH^* + O^*$	3.2e+21	76.07
56	$CHCH_3^* + OH^* \rightleftharpoons C_2H_5^* + O^*$	3.2e+21	90.96
57	$CHCH_3^* + O^* \rightleftharpoons CCH_3^* + OH^*$	3.2e+21	127.89
58	$CHCH_3^* + O^* \rightleftharpoons CHCH_2^* + OH^*$	9.6e+21	202.97
59	$CCH_3^* + O^* \rightleftharpoons CCH_2^* + OH^*$	9.6e+21	209.64
60	$CCH_2^* + OH^* \rightleftharpoons CHCH_2^* + O^*$	3.2e+21	122.54
61	$C^* + HCO^* \rightleftharpoons CH^* + CO^*$	3.2e+21	57.81
62	$CH^* + HCO^* \rightleftharpoons CH_2^* + CO^*$	3.2e+21	98.81
63	$CH_2^* + HCO^* \rightleftharpoons CH_3^* + CO^*$	3.2e+21	70.53
64	$CH_2^* + COH^* \rightleftharpoons CH_3^* + CO^*$	3.2e+21	88.16
65	$COOH^* + CO^* \rightleftharpoons CO_2^* + HCO^*$	3.2e+21	134.95
66	$COH^* + CO^* \rightleftharpoons HCO^* + CO^*$	3.2e+21	115.07
67	$HCOO^* + CO^* \rightleftharpoons CO_2^* + HCO^*$	3.2e+21	139.52
68	$C^* + COOH^* \rightleftharpoons COH^* + CO^*$	3.2e+21	61.44
69	$CH^* + COOH^* \rightleftharpoons HCOH^* + CO^*$	3.2e+21	93.14
70	$HCO^* + COH^* \rightleftharpoons HCOH^* + CO^*$	3.2e+21	103.60
71	$HCOH^* + CO^* \rightleftharpoons 2\,HCO^*$	3.2e+21	119.94
72	$CH_2^* + COOH^* \rightleftharpoons H_2COH^* + CO^*$	3.2e+21	66.07
73	$HCO^* + HCOH^* \rightleftharpoons H_2COH^* + CO^*$	3.2e+21	59.70
74	$COH^* + HCOH^* \rightleftharpoons H_2COH^* + CO^*$	3.2e+21	80.94
75	$CH_2^* + COCH_3^* \rightleftharpoons C_2H_5^* + CO^*$	3.2e+21	54.26

rxn	reaction	A / cm^2 mol^{-1} s^{-1}	E_a / kJ mol^{-1}
76	$CHCH_3^* + HCO^* \rightleftharpoons C_2H_5^* + CO^*$	3.2e+21	73.86
77	$CHCH_3^* + COH^* \rightleftharpoons C_2H_5^* + CO^*$	3.2e+21	90.38
78	$COCH_3^* + CH^* \rightleftharpoons CHCH_3^* + CO^*$	3.2e+21	71.53
79	$CCH_3^* + HCO^* \rightleftharpoons CHCH_3^* + CO^*$	3.2e+21	107.08
80	$CHCH_3^* + CO^* \rightleftharpoons CHCH_2^* + HCO^*$	9.6e+21	139.82
81	$COCH_3^* + C^* \rightleftharpoons CCH_3^* + CO^*$	3.2e+21	37.42
82	$CCH_3^* + CO^* \rightleftharpoons CCH_2^* + HCO^*$	9.6e+21	141.93
83	$CCH_2^* + HCO^* \rightleftharpoons CHCH_2^* + CO^*$	3.2e+21	103.91
84	$CCH_2^* + COH^* \rightleftharpoons CHCH_2^* + CO^*$	3.2e+21	110.41
85	$COOH^* + OH^* \rightleftharpoons CO_2^* + H_2O^*$	3.2e+21	0.00
86	$HCOO^* + OH^* \rightleftharpoons CO_2^* + H_2O^*$	3.2e+21	73.39
87	$CH_2^* + C^* \rightleftharpoons 2\,CH^*$	6.4e+21	69.90
88	$CH_3^* + C^* \rightleftharpoons CH_2^* + CH^*$	9.6e+21	98.19
89	$C^* + HCOH^* \rightleftharpoons CH^* + COH^*$	3.2e+21	71.80
90	$C^* + HCOH^* \rightleftharpoons CH^* + COH^*$	3.2e+21	65.11
91	$C^* + H_2COH^* \rightleftharpoons CH_2^* + COH^*$	3.2e+21	98.87
92	$C^* + H_2COH^* \rightleftharpoons CH^* + HCOH^*$	6.4e+21	109.01
93	$C_2H_5^* + C^* \rightleftharpoons CH_2^* + CCH_3^*$	3.2e+21	86.67
94	$C_2H_5^* + C^* \rightleftharpoons CHCH_3^* + CH^*$	6.4e+21	94.85
95	$CHCH_3^* + C^* \rightleftharpoons CH^* + CCH_3^*$	3.2e+21	69.40
96	$CHCH_3^* + C^* \rightleftharpoons CH^* + CCH_3^*$	3.2e+21	61.64
97	$C^* + CHCH_2^* \rightleftharpoons CH^* + CCH_2^*$	3.2e+21	64.81
98	$2\,CH_2^* \rightleftharpoons CH_3^* + CH^*$	6.4e+21	82.62
99	$C^* + HCOH^* \rightleftharpoons CH^* + COH^*$	3.2e+21	71.80
100	$C^* + HCOH^* \rightleftharpoons CH^* + COH^*$	3.2e+21	71.80
101	$CH^* + HCOH^* \rightleftharpoons CH_2^* + COH^*$	3.2e+21	106.11
102	$CH_2^* + HCOH^* \rightleftharpoons CH^* + H_2COH^*$	6.4e+21	71.79
103	$CH_2^* + HCOH^* \rightleftharpoons CH^* + H_2COH^*$	3.2e+21	76.42
104	$CH_2^* + CHCH_3^* \rightleftharpoons C_2H_5^* + CH^*$	6.4e+21	85.95
105	$CH_2^* + CHCH_3^* \rightleftharpoons C_2H_5^* + CH^*$	3.2e+21	86.23
106	$CHCH_3^* + CH^* \rightleftharpoons CH_2^* + CCH_3^*$	3.2e+21	102.63
107	$CHCH_3^* + C^* \rightleftharpoons CH^* + CCH_3^*$	3.2e+21	69.40
108	$CHCH_3^* + C^* \rightleftharpoons CH^* + CCH_3^*$	3.2e+21	69.40
109	$CH^* + CHCH_2^* \rightleftharpoons CH_2^* + CCH_2^*$	3.2e+21	105.80
110	$CH_2^* + COOH^* \rightleftharpoons CH_3^* + CO_2^*$	3.2e+21	101.83
111	$CH_2^* + HCOO^* \rightleftharpoons CH_3^* + CO_2^*$	3.2e+21	106.39
112	$CH_2^* + HCOH^* \rightleftharpoons CH^* + H_2COH^*$	3.2e+21	76.42
113	$CH_2^* + HCOH^* \rightleftharpoons CH_3^* + COH^*$	3.2e+21	77.82
114	$CH_2^* + HCOH^* \rightleftharpoons CH^* + H_2COH^*$	6.4e+21	71.79
115	$CH_2^* + HCOH^* \rightleftharpoons CH_3^* + HCO^*$	3.2e+21	93.02
116	$CH_3^* + HCOH^* \rightleftharpoons CH_2^* + H_2COH^*$	9.6e+21	100.08
117	$C_2H_5^* + CH_2^* \rightleftharpoons CH_3^* + CHCH_3^*$	6.4e+21	107.56
118	$CH_2^* + CHCH_3^* \rightleftharpoons C_2H_5^* + CH^*$	3.2e+21	86.23
119	$CH_2^* + CHCH_3^* \rightleftharpoons CH_3^* + CCH_3^*$	3.2e+21	74.35
120	$CH_2^* + CHCH_3^* \rightleftharpoons C_2H_5^* + CH^*$	6.4e+21	85.95
121	$CH_2^* + CHCH_3^* \rightleftharpoons CH_3^* + CHCH_2^*$	9.6e+21	112.90
122	$CH_2^* + CCH_3^* \rightleftharpoons CH_3^* + CCH_2^*$	9.6e+21	115.01
123	$CH_2^* + CHCH_2^* \rightleftharpoons CH_3^* + CCH_2^*$	3.2e+21	77.52
124	$HCOH^* + COOH^* \rightleftharpoons CO_2^* + H_2COH^*$	3.2e+21	92.95
125	$C_2H_5^* + COOH^* \rightleftharpoons C_2H_6^* + CO_2^*$	3.2e+21	67.02
126	$CHCH_3^* + COOH^* \rightleftharpoons C_2H_5^* + CO_2^*$	3.2e+21	104.56
127	$CCH_2^* + COOH^* \rightleftharpoons CO_2^* + CHCH_2^*$	3.2e+21	129.21
128	$2\,HCOH^* \rightleftharpoons HCO^* + H_2COH^*$	3.2e+21	85.81
129	$CHCH_3^* + HCOH^* \rightleftharpoons C_2H_5^* + HCO^*$	3.2e+21	95.25
130	$CCH_2^* + HCOH^* \rightleftharpoons CHCH_2^* + HCO^*$	3.2e+21	115.27
131	$HCOO^* + HCOH^* \rightleftharpoons CO_2^* + H_2COH^*$	3.2e+21	97.51
132	$C_2H_5^* + HCOO^* \rightleftharpoons C_2H_6^* + CO_2^*$	3.2e+21	78.58
133	$CHCH_3^* + HCOO^* \rightleftharpoons C_2H_5^* + CO_2^*$	3.2e+21	109.13
134	$CCH_2^* + HCOO^* \rightleftharpoons CO_2^* + CHCH_2^*$	3.2e+21	133.78
135	$2\,HCOH^* \rightleftharpoons COH^* + H_2COH^*$	3.2e+21	67.00
136	$CHCH_3^* + HCOH^* \rightleftharpoons C_2H_5^* + COH^*$	3.2e+21	81.16
137	$CHCH_3^* + COH^* \rightleftharpoons CCH_3^* + HCOH^*$	3.2e+21	107.43
138	$CHCH_2^* + COH^* \rightleftharpoons CCH_2^* + HCOH^*$	3.2e+21	110.60
139	$C_2H_5^* + HCOH^* \rightleftharpoons CHCH_3^* + H_2COH^*$	6.4e+21	96.74
140	$CHCH_3^* + HCOH^* \rightleftharpoons CCH_3^* + H_2COH^*$	3.2e+21	63.53
141	$CHCH_3^* + HCOH^* \rightleftharpoons CHCH_2^* + H_2COH^*$	9.6e+21	105.68
142	$CCH_3^* + HCOH^* \rightleftharpoons CCH_2^* + H_2COH^*$	9.6e+21	107.80
143	$CHCH_2^* + HCOH^* \rightleftharpoons CCH_2^* + H_2COH^*$	3.2e+21	66.70
144	$2\,CHCH_3^* \rightleftharpoons C_2H_5^* + CCH_3^*$	3.2e+21	77.69
145	$CHCH_3^* + CHCH_2^* \rightleftharpoons C_2H_5^* + CCH_2^*$	3.2e+21	80.86
146	$CHCH_3^* + CCH_3^* \rightleftharpoons C_2H_5^* + CCH_2^*$	9.6e+21	117.24
147	$2\,CHCH_3^* \rightleftharpoons C_2H_5^* + CHCH_2^*$	9.6e+21	115.12
148	$CHCH_3^* + CCH_2^* \rightleftharpoons CCH_3^* + CHCH_2^*$	3.2e+21	107.73
149	$CHCH_3^* + CCH_2^* \rightleftharpoons 2\,CHCH_2^*$	9.6e+21	135.15
150	$CCH_2^* + CCH_3^* \rightleftharpoons CCH_2^* + CHCH_2^*$	9.6e+21	137.26

Thermodynamic consistency

When developing microkinetic models, it is necessary that the entire reaction network is thermodynamically consistent. It is not only important that the entire mechanism conserves the thermochemistry, but each possible pathway to form methane (or any other product) is subjected to the constraints from the corresponding gas-phase reaction [26]. This means that any possible path should reproduce the change in the heat of formation and entropy to match the equilibrium constant calculated from the respective gas-phase reaction. Thereby, it ensures that the overall equilibrium constant of all surface reactions and the gas-phase reaction are identical. In the SI, this is exemplarily demonstrated for one path of the CO_2 methanation ($CO_2 + 4\,H_2 \rightleftharpoons CH_4 + 2\,H_2O$) and one path of the RWGS ($CO_2 + H_2 \rightleftharpoons CO + H_2O$). Since both paths sum up to the same reaction enthalpy and entropy as the methanation or reverse water-gas shift reaction, all of the 5,000 mechanisms are thermodynamically consistent. Thermodynamic consistency is ensured since the reverse rate is always calculated from the equilibrium constant [27, 28]. Thermodynamic consistency demands that the overall equilibrium constant must be equal to the equilibrium constant calculated with the gas-phase thermochemistry. Therefore, the model must conserve enthalpy as well as entropy over a wide temperature range. Mechanisms generated by RMG are thermodynamically consistent, because the reverse reaction rate is calculated from the forward rate and the equilibrium constant

$$k_r = \frac{k_f}{K_c} \tag{D.14}$$

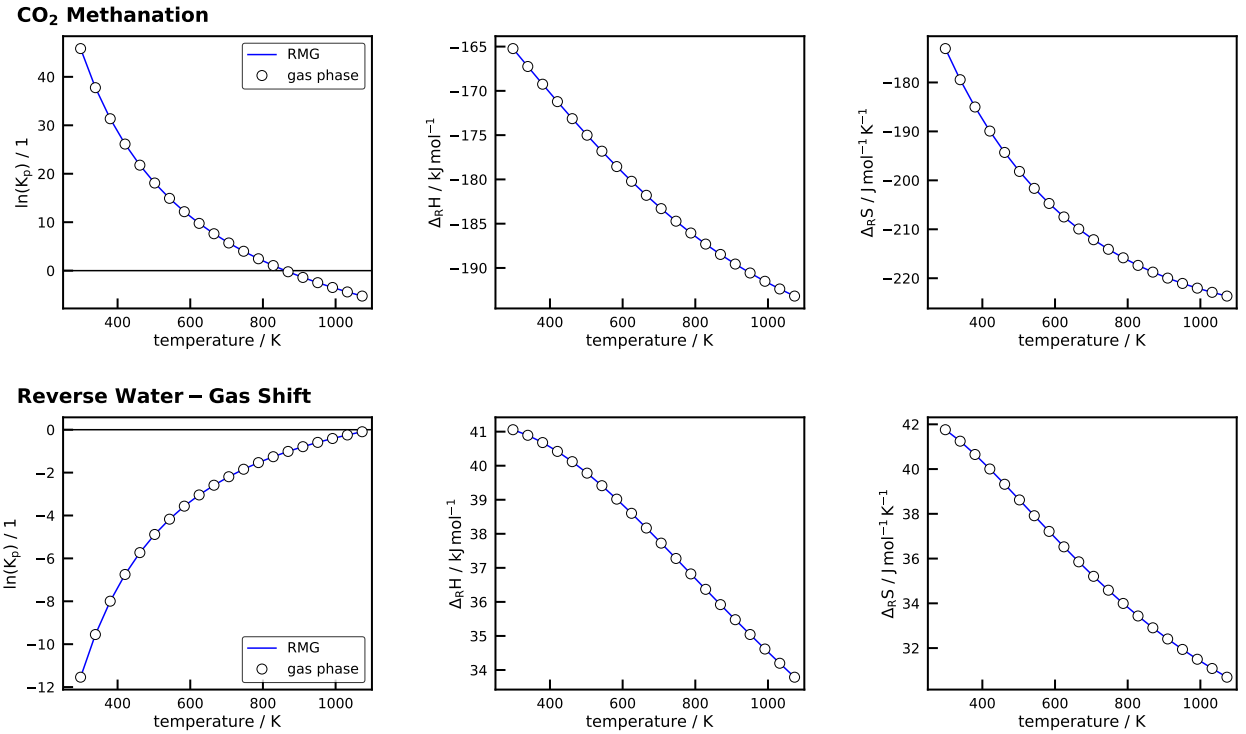

Figure D.20.: Test for thermodynamic consistency for the CO_2 methanation (top) and the RWGS reaction (bottom).

Additionally, we rely on BEP relations, which connects the adsorbate thermochemistry with the activation barriers. In order to check the thermodynamic consistency, we picked one possible path from the reference mechanism generated by RMG and tested a linear set of elementary reactions for the CO_2 methanation and the reverse water-gas shift illustrated in Figure D.20. Gas-phase thermochemistry was taken from the active thermochemical tables [29, 30]. Figure D.20 shows that thermodynamic properties calculated from one possible pathway of the microkinetic model agree with the values from the corresponding gas-phase reaction for the equilibrium constant K_p, the heat of reaction $\Delta_R H$, and the

change in entropy $\Delta_R S$. Therefore, the generated microkinetic models are always thermodynamically consistent.

CO_2 activation on Ni(111)

Several routes are responsible for the activation of CO_2^* in the carboxyl pathway, which are compared in the free energy diagram (see Figure D.21) at a temperature of 573 K. Free energy barriers were calculated from the rate constants. The rate constant for adsorption reactions is calculated via Equation (D.15), where n is the number of reactants on the surface. For example for the dissociative adsorption of H_2 n is 2. The resulting unit for k_f is then $mol^5\,mol^{-2}\,s^{-1}$, whereas for a non-dissociative adsorption the unit is $m^3\,mol^{-1}\,s^{-1}$. The reverse rate constant can be calculated from the concentration equilibrium constant. For the desorption of $2\,H^*$ the unit of the reverse rate constant is $m^2\,mol^{-1}\,s^{-1}$, whereas for the desorption of CO_2^* it is s^{-1}.

$$k_f = \frac{s}{\Gamma^n}\sqrt{\frac{RT}{2\pi W}}\exp\left(\frac{-E_a}{RT}\right) \tag{D.15}$$

$$K_p = \exp\left(\frac{-\Delta G_{rxn}}{RT}\right) \tag{D.16}$$

$$K_c = K_p\left(\frac{p}{RT}\right)^{\sum n_{gas}} \tag{D.17}$$

$$k_r = \frac{k_f}{K_c} \tag{D.18}$$

For the conversion of the rate constant to a free energy barrier, we need to recall transition state theory

$$k_{TST} = \frac{k_B T}{h}\exp\left(\frac{-\Delta G^\ddagger}{RT}\right)$$

$$\Delta G^\ddagger = -RT\ln\left(\frac{k_{TST}\,h}{k_B T}\right)$$

The unit of k_{TST} is s^{-1}, which means that we need to convert the units for the forward or reverse rate constant to a unit of s^{-1}. For all adsorption reactions, we need to multiply the forward rate constant by (p/RT), which has the unit $mol\,m^{-3}$. If the adsorption is dissociative, we have to account for the surface site density Γ with the units $mol\,m^{-2}$. For the reverse of the adsorption or any surface reaction we use Equation (D.20).

$$k_{TST} = k_f\Gamma^{n-1}\left(\frac{p}{RT}\right) \tag{D.19}$$

$$k_{TST} = k_r\Gamma^{n-1} \tag{D.20}$$

The free energy surface for the direct dissociation is displayed in Figure D.21a. The hydrogenation of CO_2^* to $COOH^*$ occurs via H^* (Figure D.21b), OH^* (Figure D.21c), and H_2O^* (Figure D.21d). The free energy barrier for the direct dissociation of CO_2^* is lower than the reaction of CO_2^* with H^* and the subsequent dissociation. However, the hydrogenation of CO_2^* via OH^* and H_2O^* provide pathways with lower free energy barriers. The colored area gives the boundaries from the best matches. Drastic variations in the free energy barriers in the range of $50\,kJ\,mol^{-1}$ are obtained for the different $COOH^*$ formation steps. Consequently, there is no clear domination of one route and it is very sensitive to the parameters. Figure D.21f illustrates the free energy surface via the carbide pathway, which possesses a significantly higher free energy barrier than formation of HCO^* and its dissociation to CH^* [12]. That is why this pathway does not contribute to the methane formation.

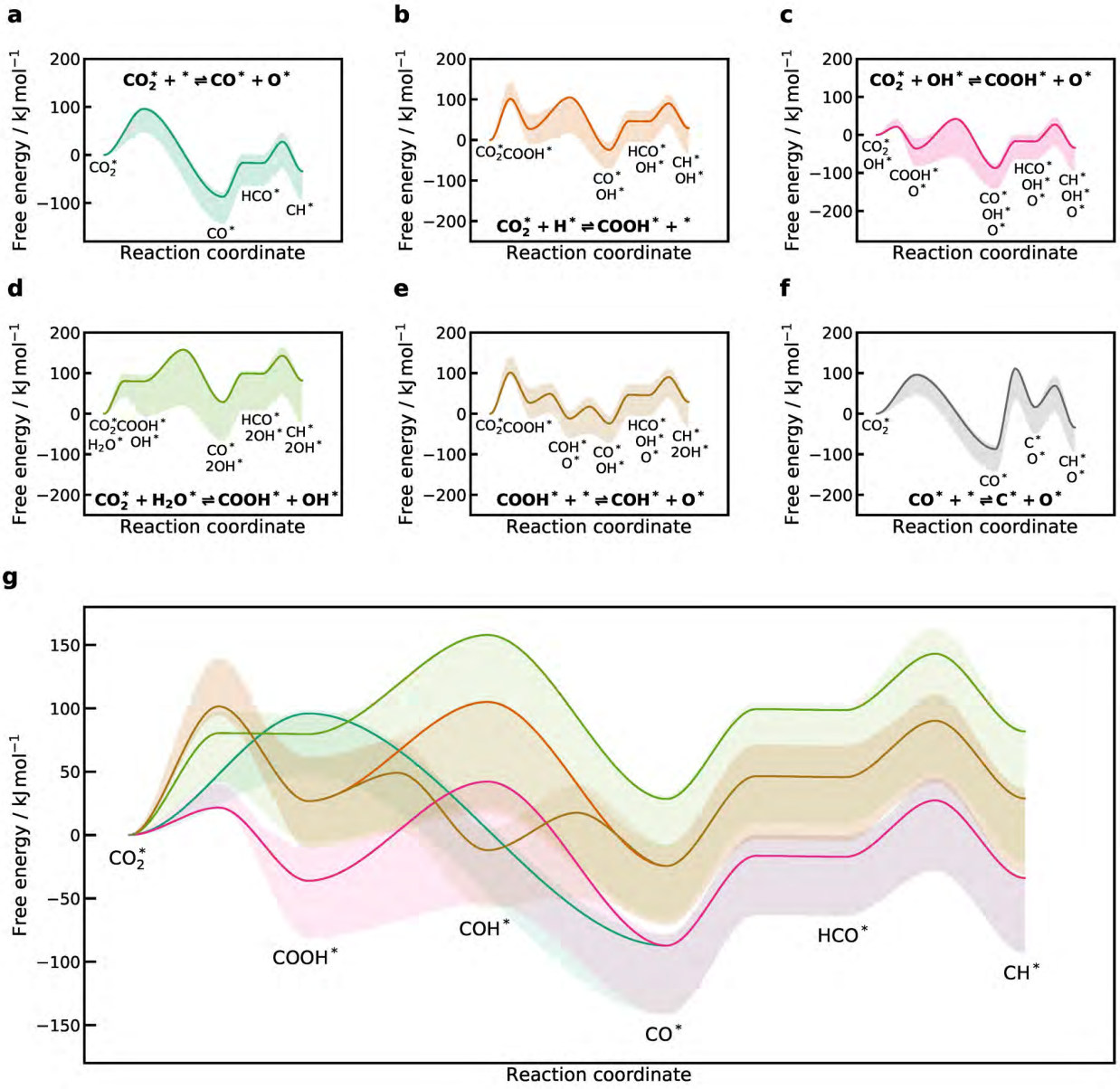

Figure D.21.: Free energy diagrams of the competing CO_2 dissociation and CH^* formation pathways at a temperature of 573 K. a) Direct dissociation route ($CO_2^* \longrightarrow CO^* + O^*$), b) Carboxyl formation via H^* ($CO_2^* + H^* \longrightarrow COOH^*$) and dissociation of $COOH^* \longrightarrow CO^* + OH^*$, c) Carboxyl formation via OH^* ($CO_2^* + OH^* \longrightarrow COOH^* + O^*$), d) Carboxyl formation via H_2O^* ($CO_2^* + H_2O^* \longrightarrow COOH^* + OH^*$). e) Carboxyl dissociation to COH^* ($COOH^* \longrightarrow COH^* + O^*$) and O-H bond fission in COH^* via H abstraction to O^* ($COH^* + O^* \longrightarrow CO^* + OH^*$). f) Direct dissociation with carbide pathway ($CO^* \longrightarrow C^* + O^*$). g) Comparison of the free energy diagrams of all possible pathways for CO_2^* activation and dissociation. All free energies are reference to the standard state free energy of CO_2 and 4 H_2. Figure c) includes OH^* and d) H_2O^* in the reference. The shaded area in the all figures contains the feasible set of mechanisms.

Sensitivity analysis

Figure D.22 shows a test for the convergence of the average values for the degree of rate control for important reactions. The average sensitivity coefficients and the standard deviation stabilize quickly and are constant if more than 1,000 mechanisms are evaluated.

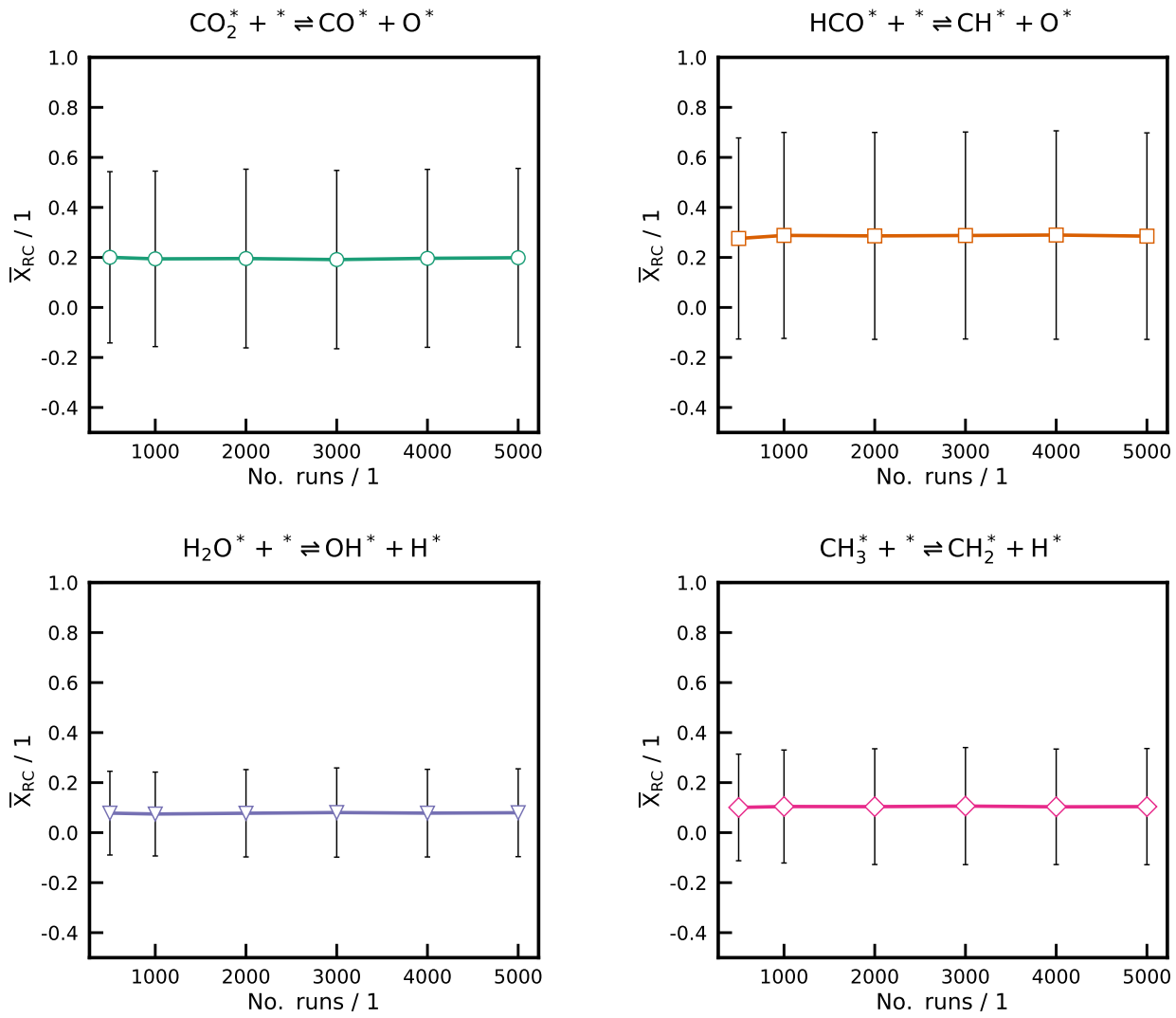

Figure D.22.: Convergence of the average values of the degree of rate control for the four most important reactions over the number of evaluated mechanisms. The error bars are the standard deviation.

Using 5,000 samples for a global sensitivity analysis in a 65 dimensional parameter space is usually at the lower end of required samples. With more samples, or in this case mechanisms, the derived sensitivity coefficients will be more accurate. Therefore, it is necessary to check for the accuracy, especially of the joint sensitivity coefficients, which is illustrated in Figure D.23. 4,500 samples were used for the construction of the surrogate model and 500 for the validation. In this accuracy check, we scrambled all 5,000 samples to always pick different 4,500/500 samples for surrogate construction/validation. The results show some deviation in the joint sensitivity coefficients, but most important we can still determine what are the most important interactions among the parameters. This is definitely good enough for a first screening method. For the derivation of more accurate sensitivity coefficients it is necessary to increase the number of samples (generated mechanisms) significantly.

Figure D.24 displays the result for the DRC analysis for the 50 reactions with the highest absolute average DRC. It can clearly be seen that only a handful of reactions are rate-controlling over within the uncertainty range, but the majority of the complex reaction network is never controlling the CH_4 formation rate. The thermodynamic DRC for all species is shown in Figure D.25 and shows the same behavior. Figure D.26 and Figure D.27 show the scatter plots for the (thermodynamic) DRC over the change in activation energy or the binding strength. Figure D.28 shows a scatter plot for the CH_4 mole fraction as a function of important intermediates and reactions.

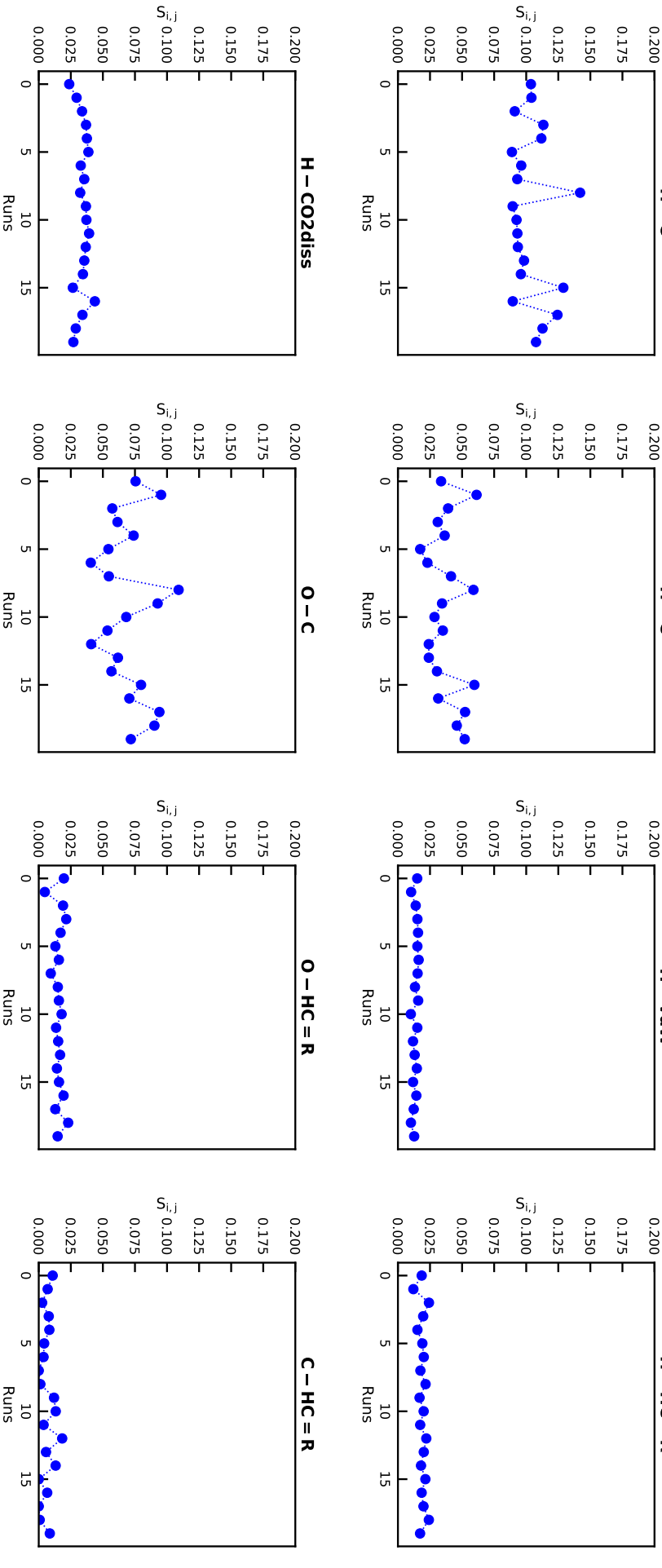

Figure D.23.: Joint sensitivity coefficients for several important pairs of parameters. In each run, different 4,500/500 samples were used for the surrogate construction/validation.

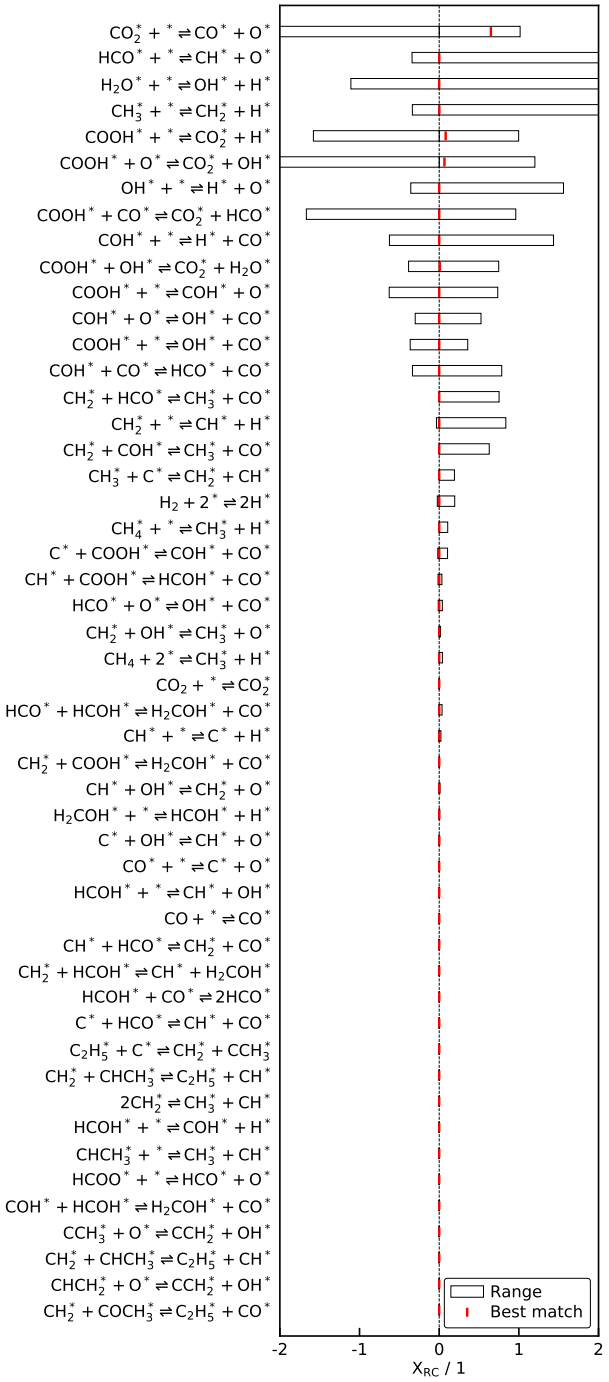

Figure D.24.: DRC of the elementary reactions at a temperature of 573 K. Only the 50 reactions with the highest DRC are displayed from all 150 reactions.

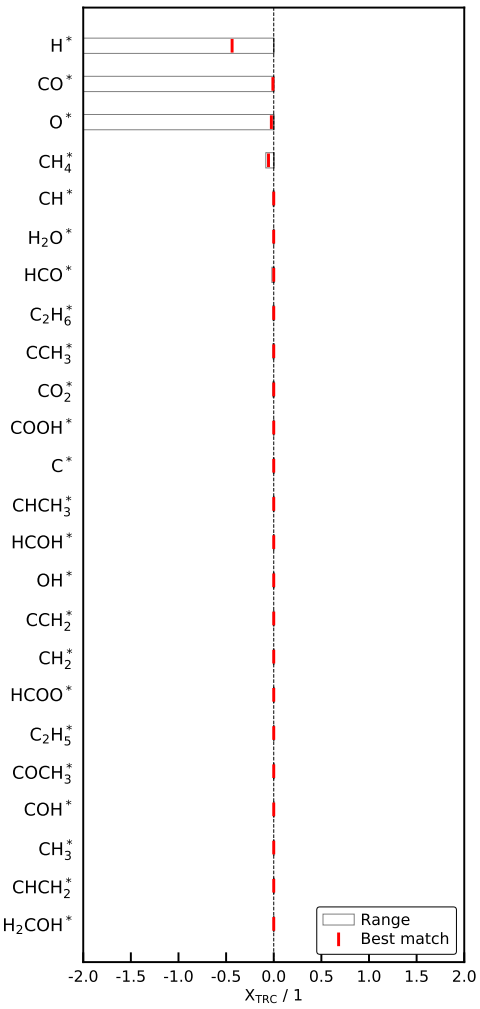

Figure D.25.: Thermodynamic DRC of all adsorbates at a temperature of 573 K.

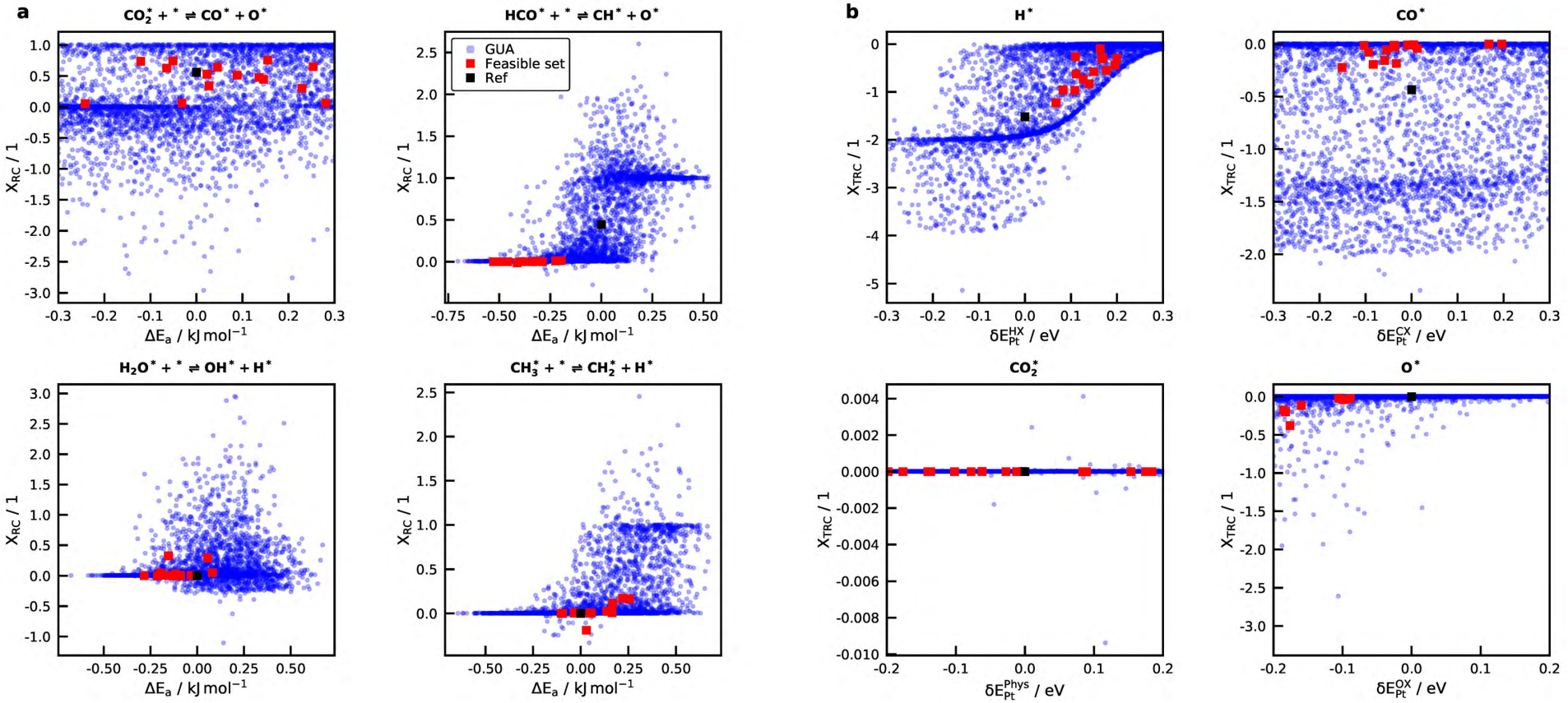

Figure D.26.: Scatter plots for the (a) degree of rate control versus the activation energy and (b) thermodynamic degree of rate control versus the change in binding strength at a temperature of 573 K.

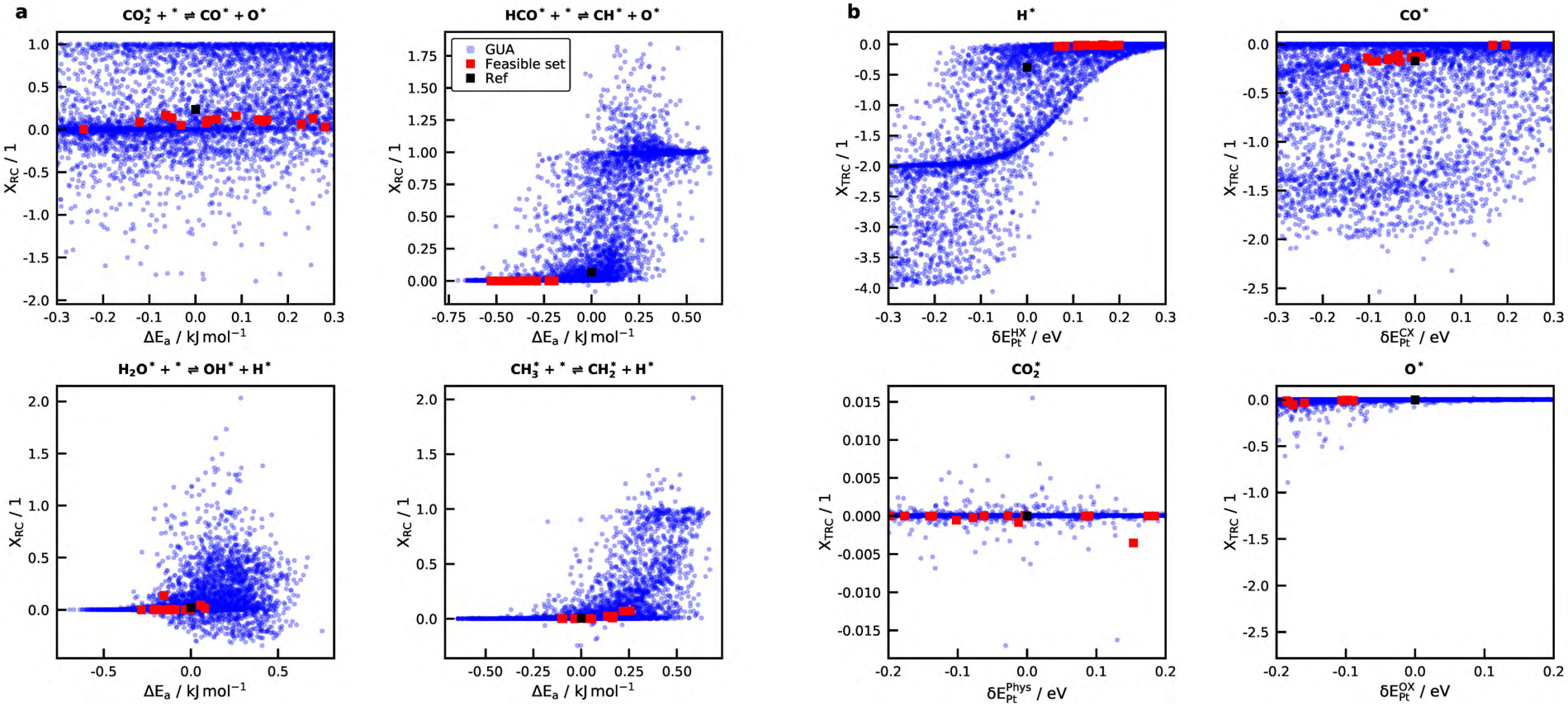

Figure D.27.: Scatter plots for the (a) degree of rate control versus the activation energy and (b) thermodynamic degree of rate control versus the change in binding strength at a temperature of 673 K.

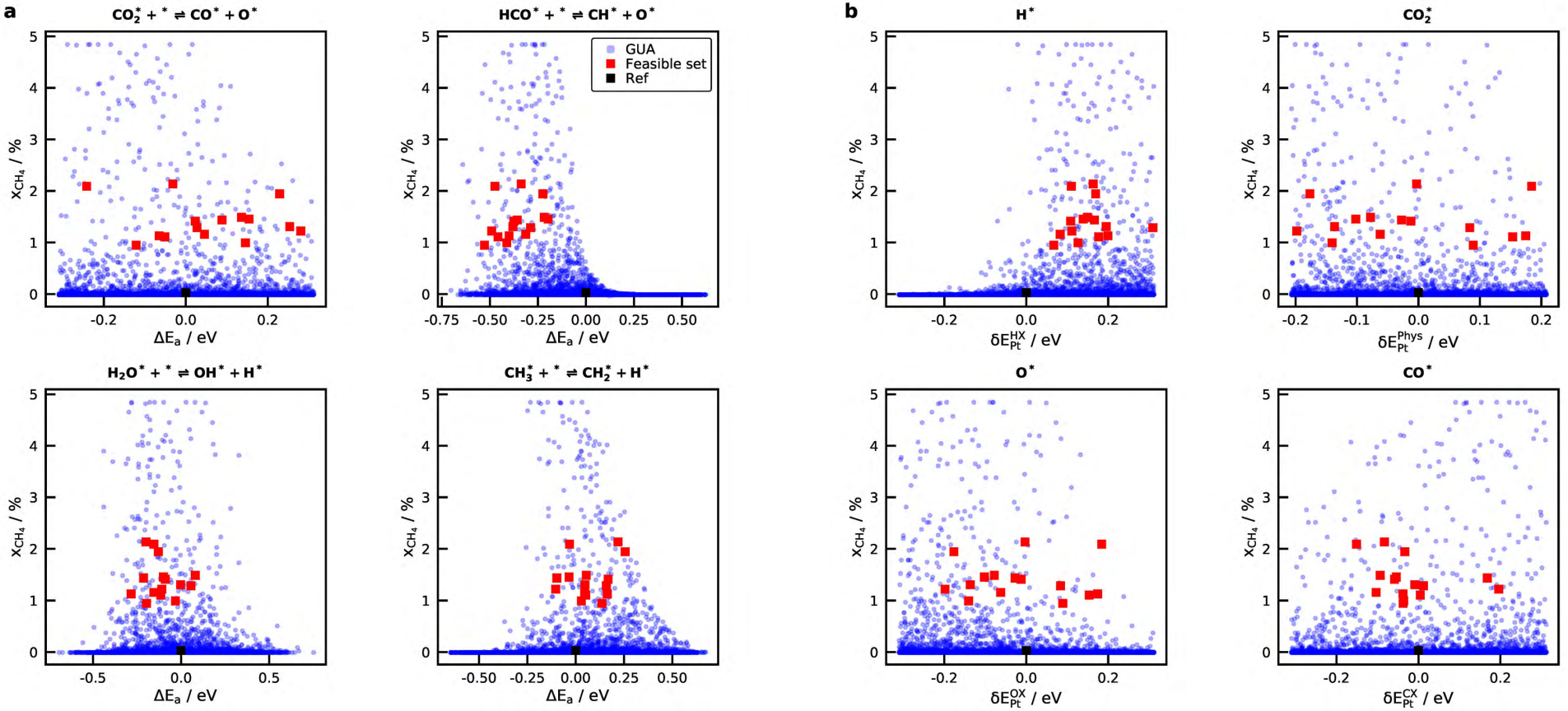

Figure D.28.: Scatter plots of the CH_4 mole fraction as a function of (a) activation barriers of important reactions and (b) heat of formation of important intermediates at a temperature of 573 K.

DRC maps

The DRC heatmaps and the gas-phase concentrations or coverages are created by spanning a 30×30 grid over the 2-dimensional space. All values that are within one point of the grid were averaged using the binned statistics function in Python. While there is some white space in the DRC heatmaps (see Figure D.29 and Figure D.30) due to the filtering of nonreactive mechanisms, we can also clearly see the correlation between thermochemistry and BEP relations. A band is obtained for the H_2O^* dissociation or CH_3^* dissociation with low barriers when H^* is stabilized and high barriers when H^* is destabilized. A destabilization of H^* increases the heat of formation for all reactions where it is on the side of the products. That is why the dissociation of H_2O^* and CH_3^* have high barriers when H^* is destabilized. For all the mechanisms in agreement with the experiments, we saw that the binding strength of H^* needed to be decreased. That is why the dissociation of H_2O^* and CH_3^* are rate-controlling for the good matches to the data. Heatmaps are displayed for the CH_4 (Figure D.31) and CO mole fraction (Figure D.35) concentration as well as all coverages (see Figure S30 to S33)

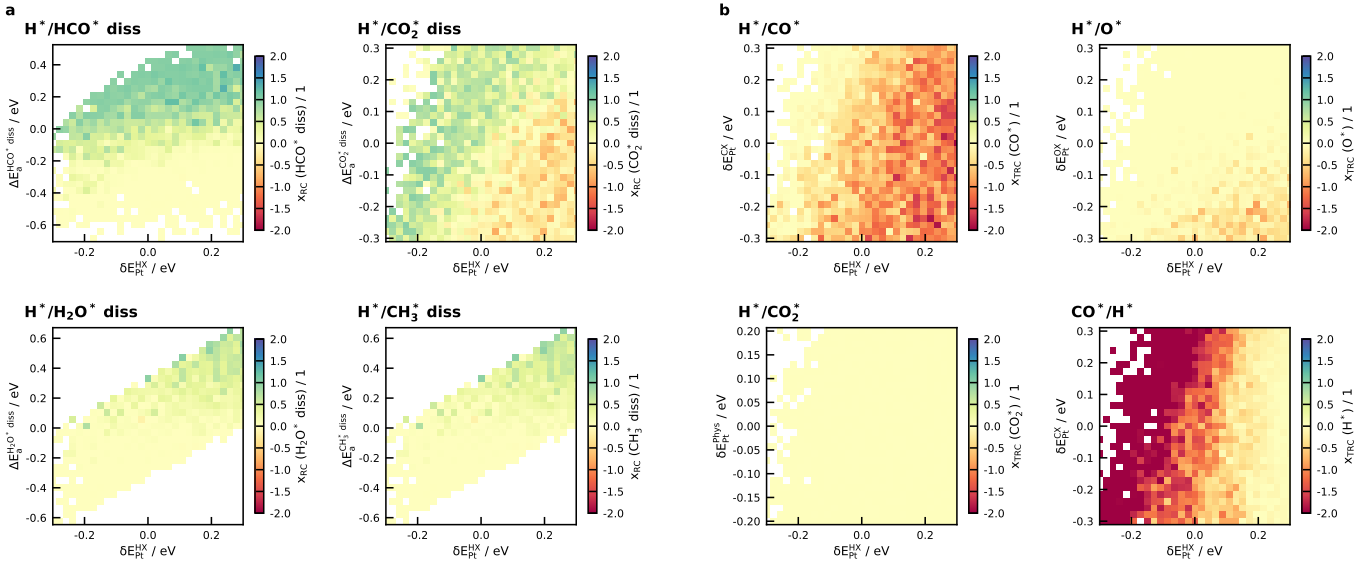

Figure D.29.: Map for the (a) degree of rate control and (b) thermodynamic degree of rate control versus versus H^* binding energy at a temperature of 573 K.

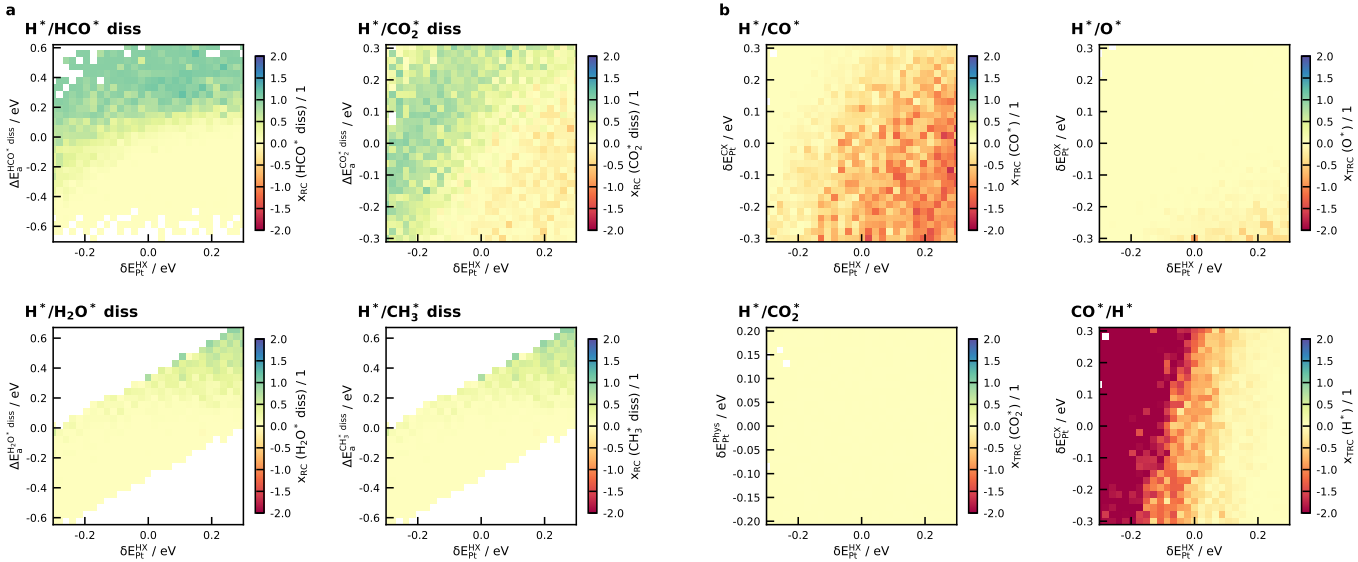

Figure D.30.: Map for the (a) degree of rate control and (b) thermodynamic degree of rate control versus versus H^* binding energy at a temperature of 673 K.

Maps for the Model Predictions

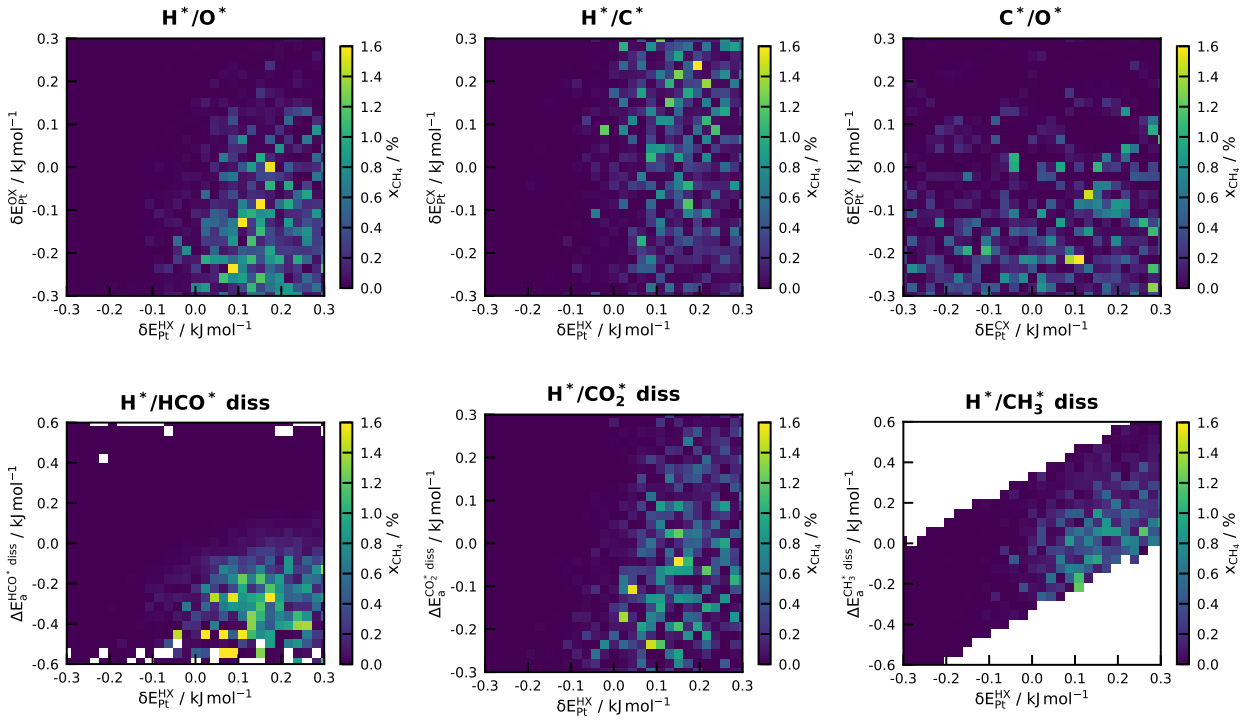

Figure D.31.: Heatmaps for the methane concentration at a temperature of 573 K versus the change in the hydrogen binding energy.

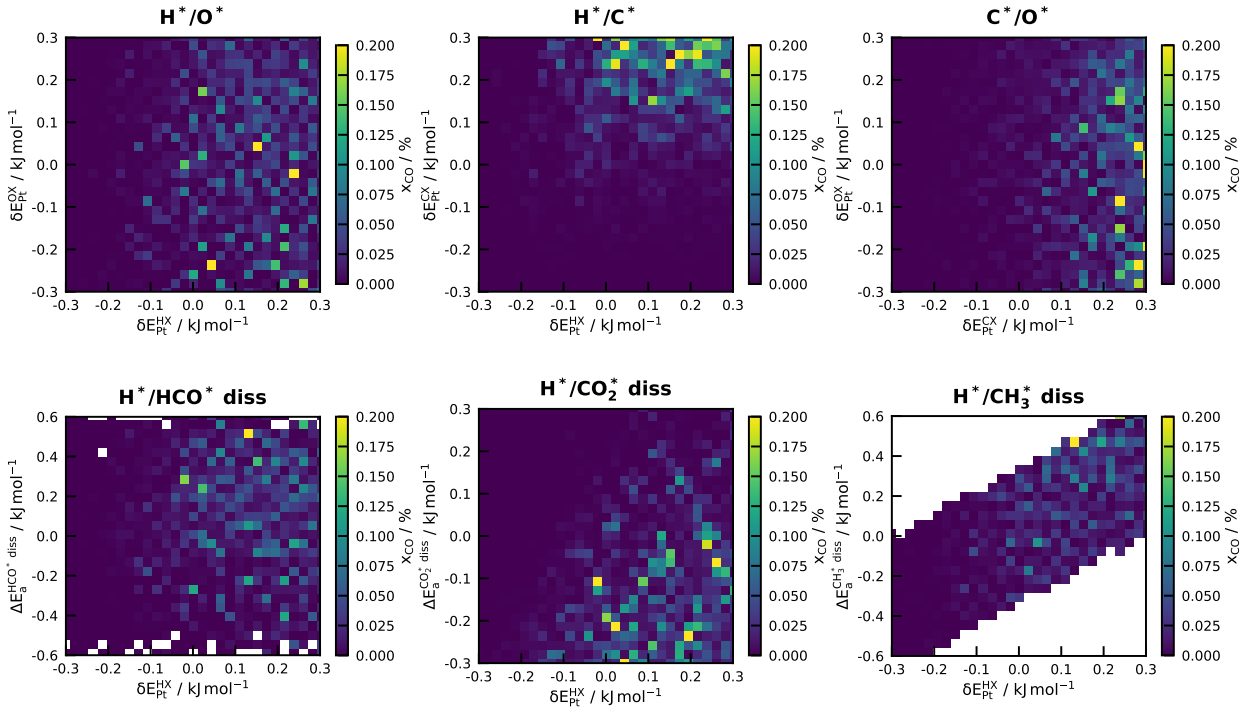

Figure D.32.: Heatmaps for the carbon monoxide concentration at a temperature of 573 K versus the change in the hydrogen binding energy.

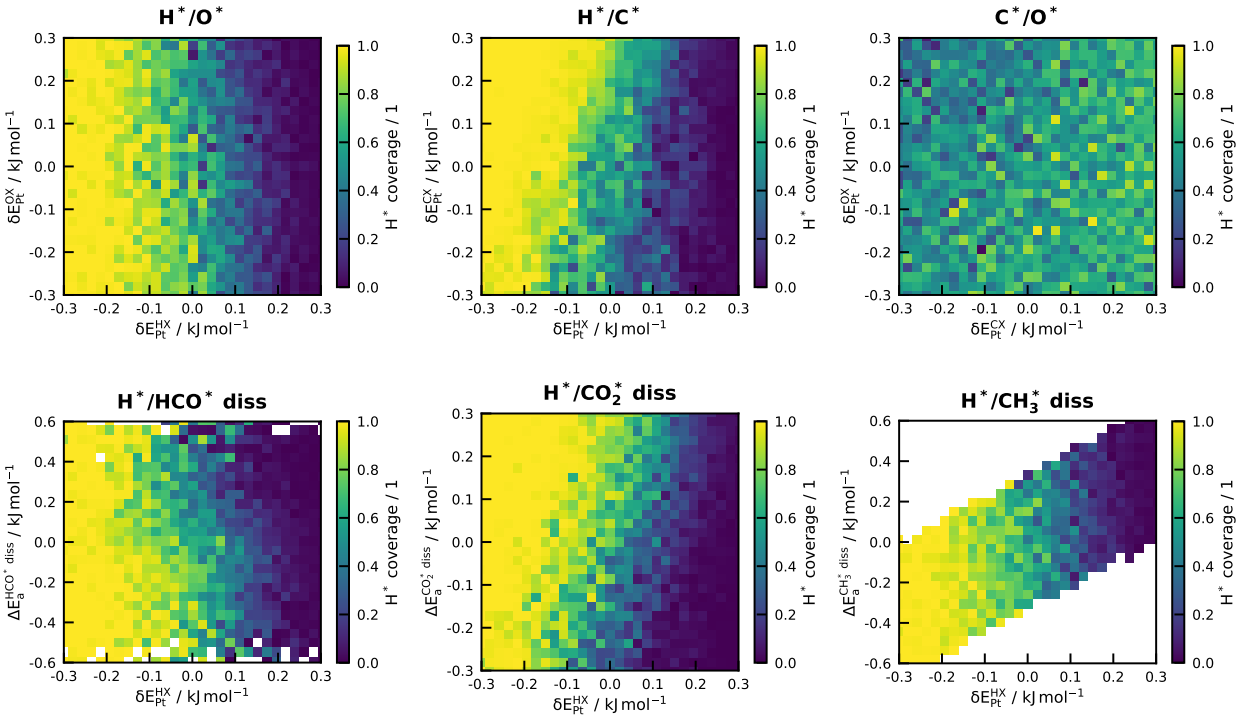

Figure D.33.: Heatmaps for the H^* coverage at a temperature of 573 K versus the change in the hydrogen binding energy.

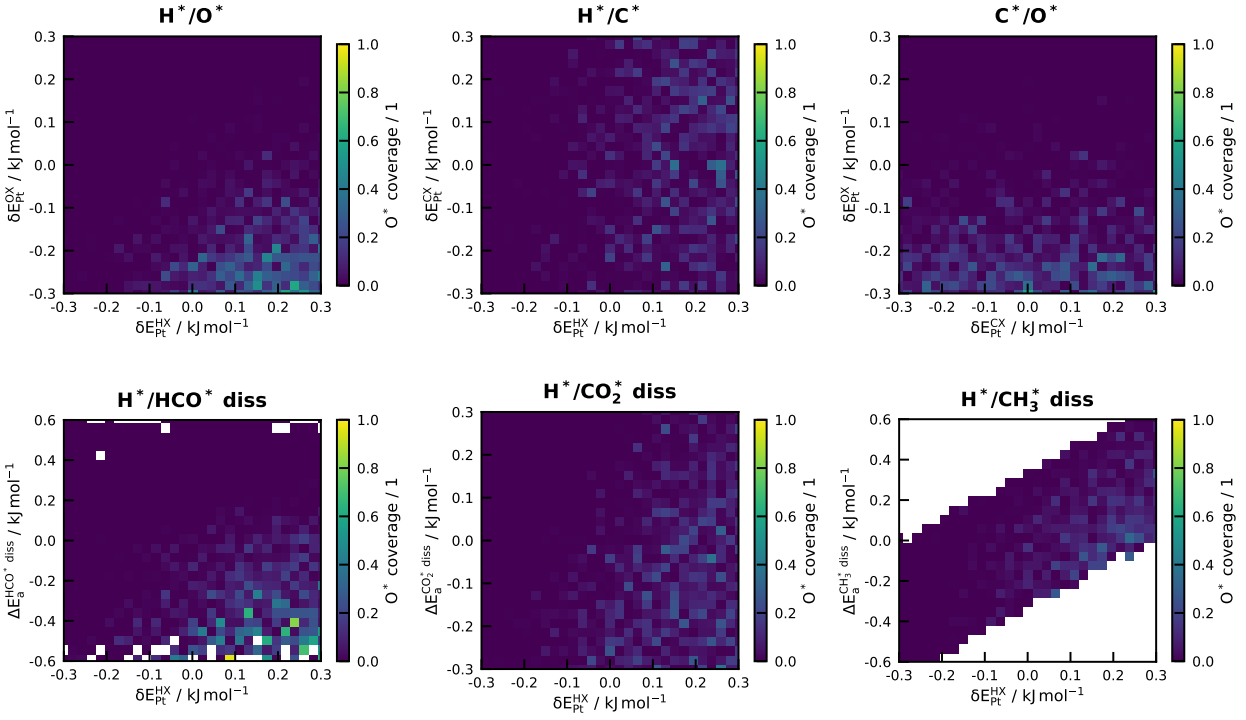

Figure D.34.: Heatmaps for the O^* coverage at a temperature of 573 K versus the change in the hydrogen binding energy.

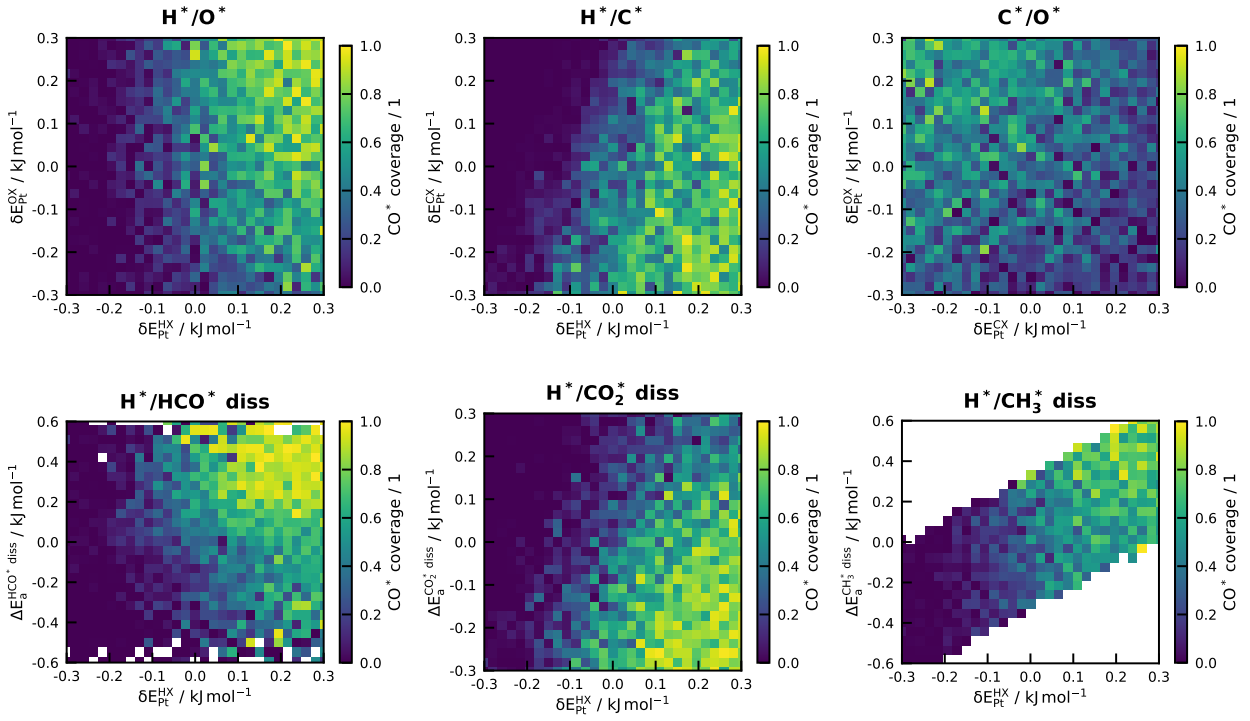

Figure D.35.: Heatmaps for the CO^* coverage at a temperature of 573 K versus the change in the hydrogen binding energy.

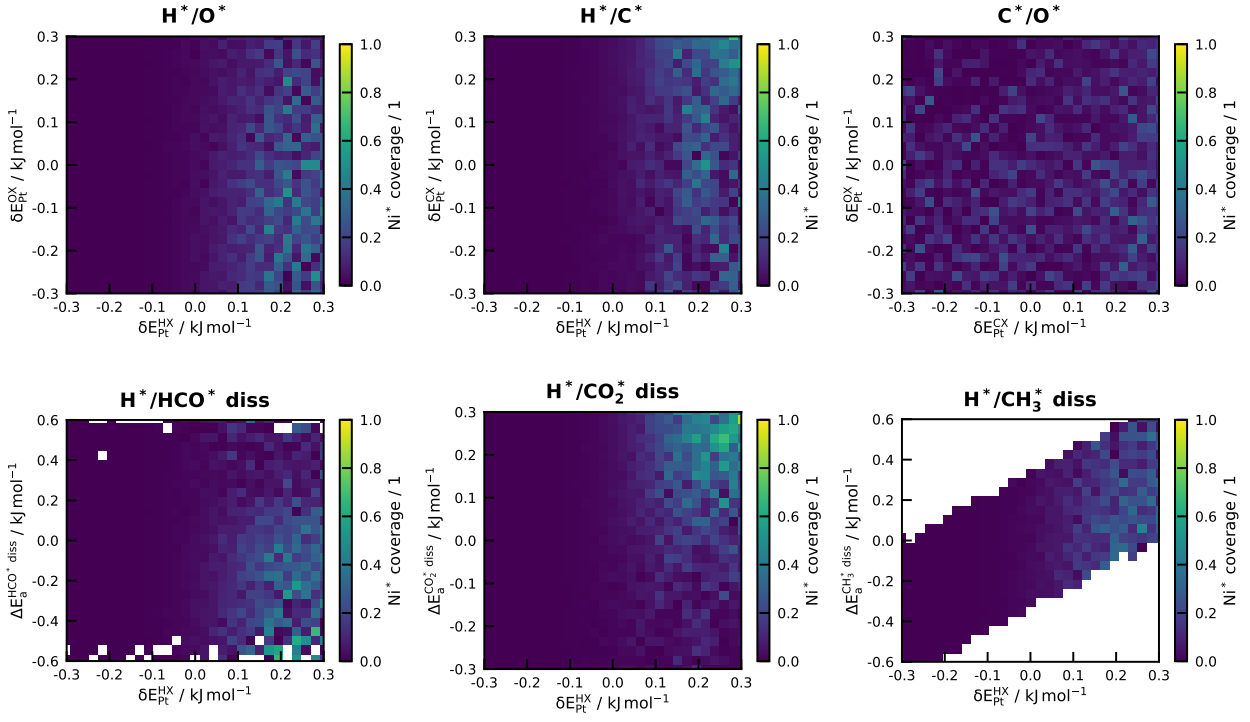

Figure D.36.: Heatmaps for the free Ni^* sites at a temperature of 573 K versus the change in the hydrogen binding energy.

Catalyst screening

The study shows that the mechanism can change considerably when the parameters are perturbed within the uncertainty range of ±0.3 eV. However, catalyst screening studies exploiting the LS and BEP relations vary the binding energies of the descriptor species over several eV to investigate all possible metals. A simple microkinetic model with just one formation pathway to the products of interest and a single rate-determining step is often assumed in this procedure. This assumption is not justified, as clearly demonstrated in the manuscript. Therefore, incorporating the automated mechanism generation procedure in the catalyst screening study is necessary to truly consider all the possible chemistry for a combination of binding energies of the descriptor species. Consequently, we tested whether the approach outlined in this manuscript can be used for catalyst screening. Five hundred distinct mechanisms were generated for the Pt(111) facet within the same method and uncertainty range as described in the manuscript. Binding energies for the Pt(111) facet were taken from the reference values in the current RMG version [31, 32].

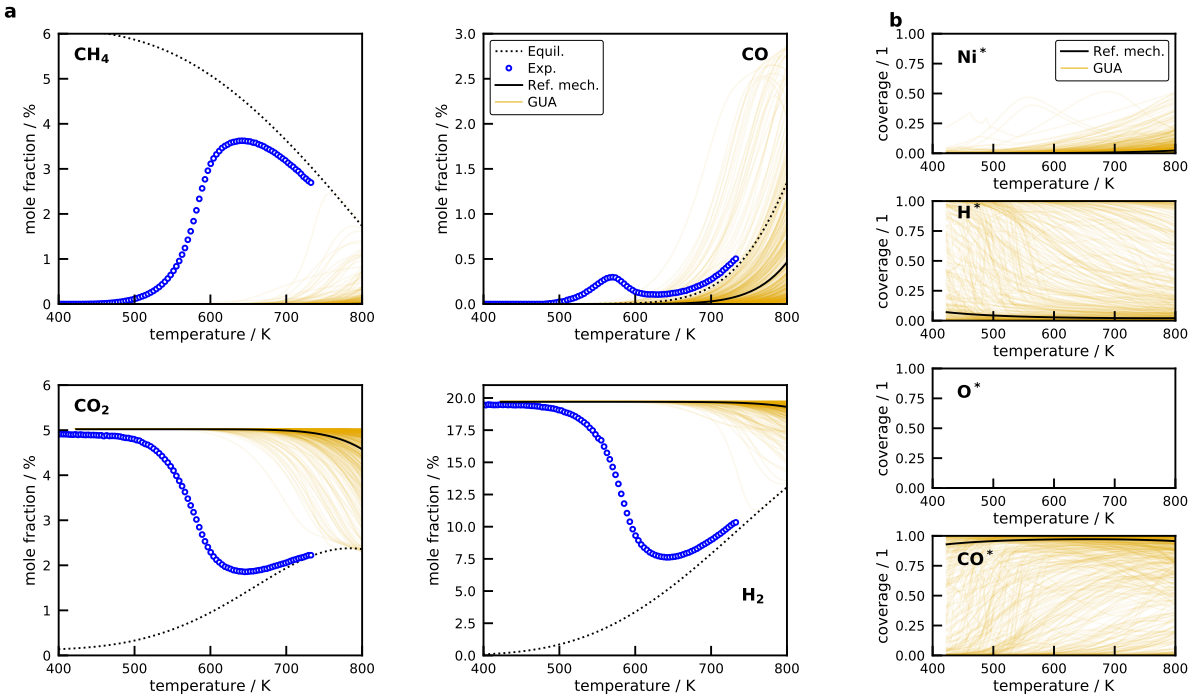

Figure D.37.: (a) Comparison of measured (open blue circle) and simulated (lines) mole fractions (on dry basis) for the temperature-scanning experiment using the microkinetic models generated by RMG for a Pt(111) facet. The dotted black line corresponds to the thermodynamic equilibrium, the solid black line to the generated reference mechanism. The gold colored area contains the model solutions of all generated mechanisms, where each mechanism is represented by a solid line. (b) Simulation results for the four species with highest coverage. The black line is the reference mechanism.

The binding energies are: $C^* = -7.025\,\text{eV}$, $O^* = -3.812\,\text{eV}$, and $H^* = -2.754\,\text{eV}$. All generated microkinetics were compared to the experimental methanation results from the Ni/SiO_2 catalyst using the plug-flow reactor simulation. The comparison of the gas-phase concentration is illustrated in Figure D.37a and the predicted coverages in Figure D.37b. Pt(111) is not an active methanation catalyst, as can be clearly seen in Figure D.37. Only at temperatures beyond 700 K does some methane formation occur, but primarily the facet converts the CO_2 to CO in the reverse water-gas-shift reaction. The surface coverage profiles show a vast range of solutions from a complete CO^* to H^* coverage again. In contrast to Ni(111), however, the surface is never covered in O^*. Finally, these results correctly quantify Pt(111) as an inactive methanation catalyst, showing that the proposed procedure can be used for catalyst screening, indeed.

References

[1] G. Kresse, J. Furthmüller. *Phys. Rev. B* **1996**, 54 (16), 11169–11186. DOI: 10.1103/physrevb.54.11169.

[2] G. Kresse, J. Furthmüller. *Comput. Mater. Sci.* **1996**, 6 (1), 15–50. DOI: 10.1016/0927-0256(96)00008-0.

[3] B. Hammer, L. B. Hansen, J. K. Nørskov. *Phys. Rev. B* **1999**, 59 (11), 7413–7421. DOI: 10.1103/PhysRevB.59.7413.

[4] S. Grimme. *J. Comput. Chem.* **2006**, 27 (15), 1787–1799. DOI: 10.1002/jcc.20495.

[5] C. Kittel. 8th ed. Hoboken, NJ: Wiley, **2005**.

[6] K. Blondal, J. Jelic, E. Mazeau, F. Studt, R. H. West, C. F. Goldsmith. *Ind. Eng. Chem. Res.* **2019**, 58 (38), 17682–17691. DOI: 10.1021/acs.iecr.9b01464.

[7] B. Ruscic, D. H. Bross. *Computer-Aided Chemical Engineering* **2019**, 45, 3–114. DOI: 10.1016/B978-0-444-64087-1.00001-2.

[8] G. Henkelman, B. P. Uberuaga, H. Jónsson. *J. Chem. Phys.* **2000**, 113 (22), 9901–9904. DOI: 10.1063/1.1329672.

[9] M. Salciccioli, M. Stamatakis, S. Caratzoulas, D. G. Vlachos. *Chem. Eng. Sci.* **2011**, 66 (19), 4319–4355. DOI: 10.1016/j.ces.2011.05.050.

[10] B. Kreitz, G. D. Wehinger, C. F. Goldsmith, T. Turek. *J. Phys. Chem. C* **2021**, 125 (5), 2984–3000. DOI: 10.1021/acs.jpcc.0c09985.

[11] S. Wang, B. Temel, J. Shen, G. Jones, L. C. Grabow, F. Studt, T. Bligaard, F. Abild-Pedersen, C. H. Christensen, J. K. Nørskov. *Catal. Lett.* **2011**, 141 (3), 370–373. DOI: 10.1007/s10562-010-0477-y.

[12] C. Vogt et al. *Nat. Commun.* **2019**, 10 (1), 5330. DOI: 10.1038/s41467-019-12858-3.

[13] J. E. Sutton, W. Guo, M. A. Katsoulakis, D. G. Vlachos. *Nat. Chem.* **2016**, 8 (4), 331–337. DOI: 10.1038/nchem.2454.

[14] J. E. Sutton, D. G. Vlachos. *Ind. Eng. Chem. Res.* **2015**, 54 (16), 4213–4225. DOI: 10.1021/ie5043374.

[15] S. Wang et al. *Phys. Chem. Chem. Phys.* **2011**, 13 (46), 20760–20765. DOI: 10.1039/c1cp20547a.

[16] J. B. Benziger, R. J. Madix. *Surf. Sci.* **1979**, 79 (2), 394–412. DOI: 10.1016/0039-6028(79)90297-8.

[17] T. P. de Carvalho, R. C. Catapan, A. A. M. Oliveira, D. G. Vlachos. *Ind. Eng. Chem. Res.* **2018**, 57 (31), 10269–10280. DOI: 10.1021/acs.iecr.8b01957.

[18] J. E. Sutton, P. Panagiotopoulou, X. E. Verykios, D. G. Vlachos. *J. Phys. Chem. C* **2013**, 117 (9), 4691–4706. DOI: 10.1021/jp312593u.

[19] A. J. Medford, A. Vojvodic, J. S. Hummelshøj, J. Voss, F. Abild-Pedersen, F. Studt, T. Bligaard, A. Nilsson, J. K. Nørskov. *J. Catal.* **2015**, 328, 36–42. DOI: 10.1016/j.jcat.2014.12.033.

[20] J. Wellendorff, K. T. Lundgaard, A. Møgelhøj, V. Petzold, D. D. Landis, J. K. Nørskov, T. Bligaard, K. W. Jacobsen. *Phys. Rev. B* **2012**, 85 (23), 316. DOI: 10.1103/PhysRevB.85.235149.

[21] J. E. Sutton, W. Guo, M. A. Katsoulakis, D. G. Vlachos. *Nat. Chem.* **2016**, 8 (4), 331–337. DOI: 10.1038/nchem.2454.

[22] S. Döpking, C. P. Plaisance, D. Strobusch, K. Reuter, C. Scheurer, S. Matera. *J. Chem. Phys.* **2018**, 148 (3), 034102. DOI: 10.1063/1.5004770.

[23] J. J. Mortensen, L. B. Hansen, K. W. Jacobsen. *Phys. Rev. B* **2005**, 71 (3), 4351. DOI: 10.1103/PhysRevB.71.035109.

[24] J. Enkovaara et al. *J. Phys.: Condens. Matter* **2010**, 22 (25), 253202. DOI: 10.1088/0953-8984/22/25/253202.

[25] F. Studt, F. Abild-Pedersen, Q. Wu, A. D. Jensen, B. Temel, J.-D. Grunwaldt, J. K. Nørskov. *J. Catal.* **2012**, 293, 51–60. DOI: 10.1016/j.jcat.2012.06.004.

[26] A. B. Mhadeshwar, H. Wang, D. G. Vlachos. *J. Phys. Chem. B* **2003**, 107 (46), 12721–12733. DOI: 10.1021/jp034954y.

[27] C. W. Gao, J. W. Allen, W. H. Green, R. H. West. *Comput. Phys. Commun.* **2016**, 203, 212–225. DOI: 10.1016/j.cpc.2016.02.013.

[28] C. F. Goldsmith, R. H. West. *J. Phys. Chem. C* **2017**, 121 (18), 9970–9981. DOI: 10.1021/acs.jpcc.7b02133.

[29] B. Ruscic, D. H. Bross. Active Thermochemical Tables (ATcT) Values Based on ver. 1.122g of the Thermochemical Network. **2019**.

[30] B. Ruscic, R. E. Pinzon, M. L. Morton, G. von Laszevski, S. J. Bittner, S. G. Nijsure, K. A. Amin, M. Minkoff, A. F. Wagner. *J. Phys. Chem. A* **2004**, 108 (45), 9979–9997. DOI: 10.1021/jp047912y.

[31] W. H. Green, R. H. West. https://rmg.mit.edu/. Version 3.0. **2021**.

[32] M. Liu et al. *J. Chem. Inf. Model.* **2021**, 61 (6), 2686–2696. DOI: 10.1021/acs.jcim.0c01480.

APPENDIX E

Supporting Information for Chapter 7

Additional Figures

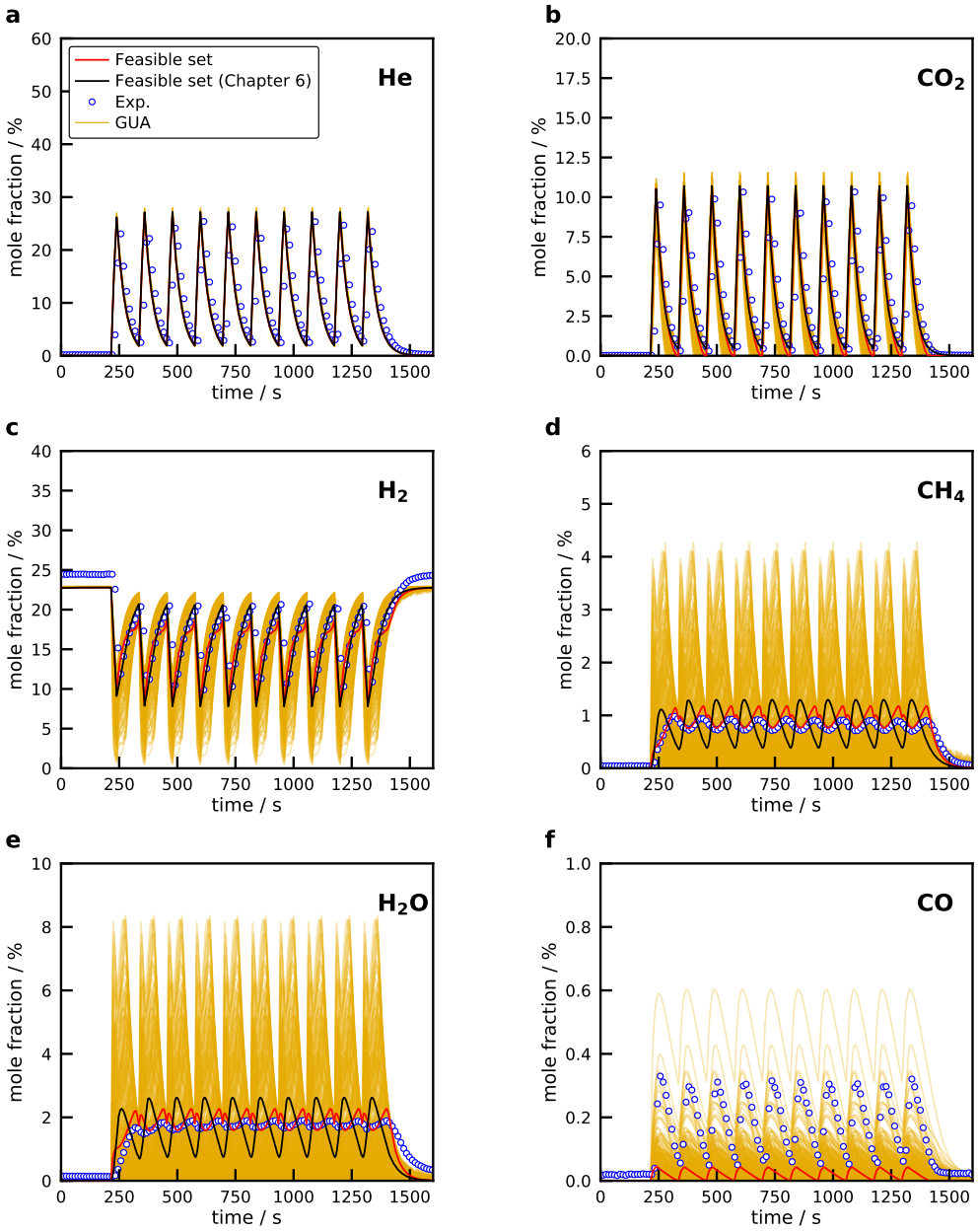

Figure E.1.: Comparison of transient experiments for (a) He, (b) CO_2, (c) H_2, (d) CH_4, (e) H_2O, and (f) CO with the simulations using all 5,000 generated microkinetic models derived in Chapter 6 for a cycle split ratio of $\gamma = 0.2$. The black line is the feasible set from Chapter 6, and the red line is the feasible set determined for the transient experiments.

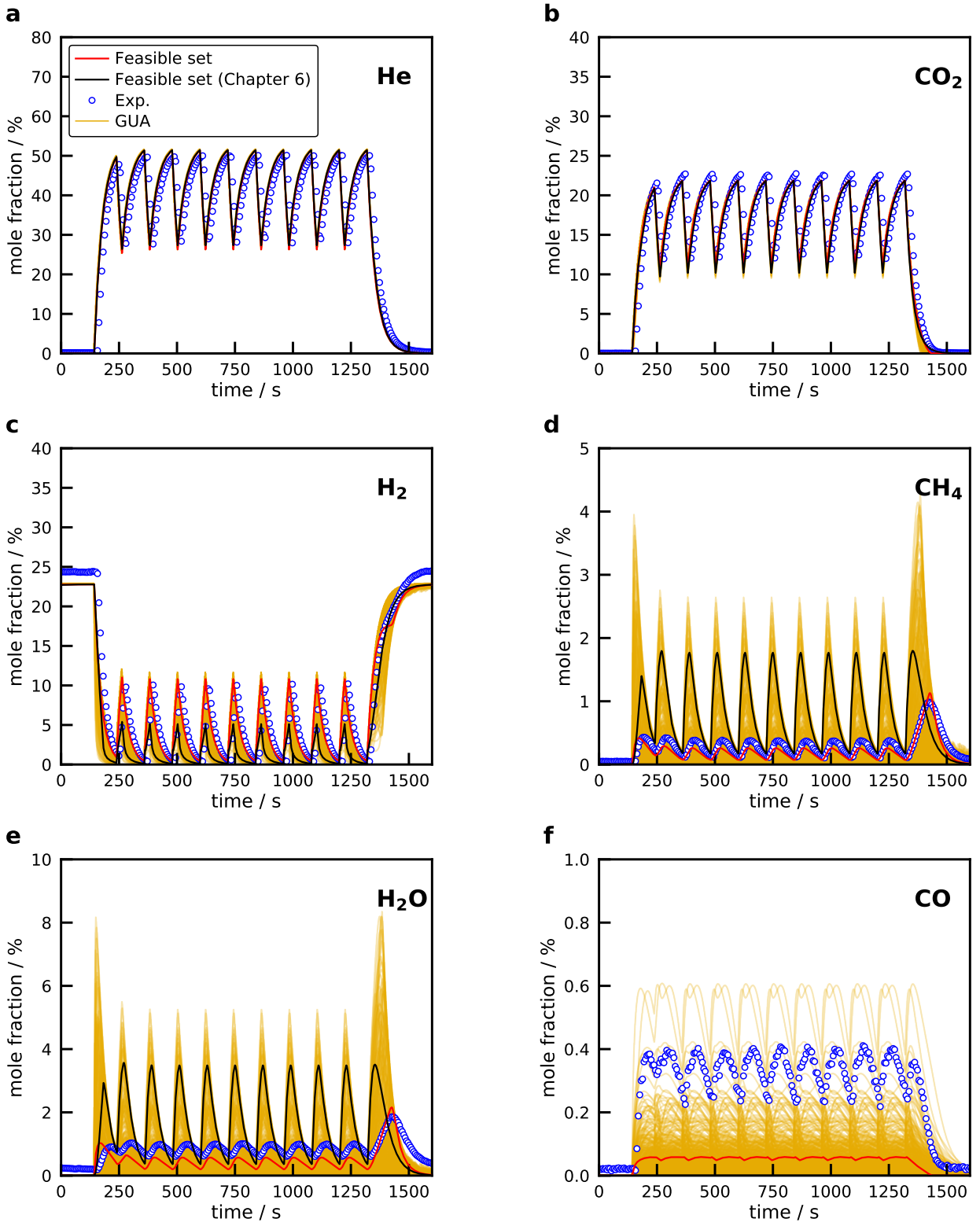

Figure E.2.: Comparison of transient experiments for (a) He, (b) CO_2, (c) H_2, (d) CH_4, (e) H_2O, and (f) CO with the simulations using all 5,000 generated microkinetic models derived in Chapter 6 for a cycle split ratio of $\gamma = 0.8$. The black line is the feasible set from Chapter 6, and the red line is the feasible set determined for the transient experiments.

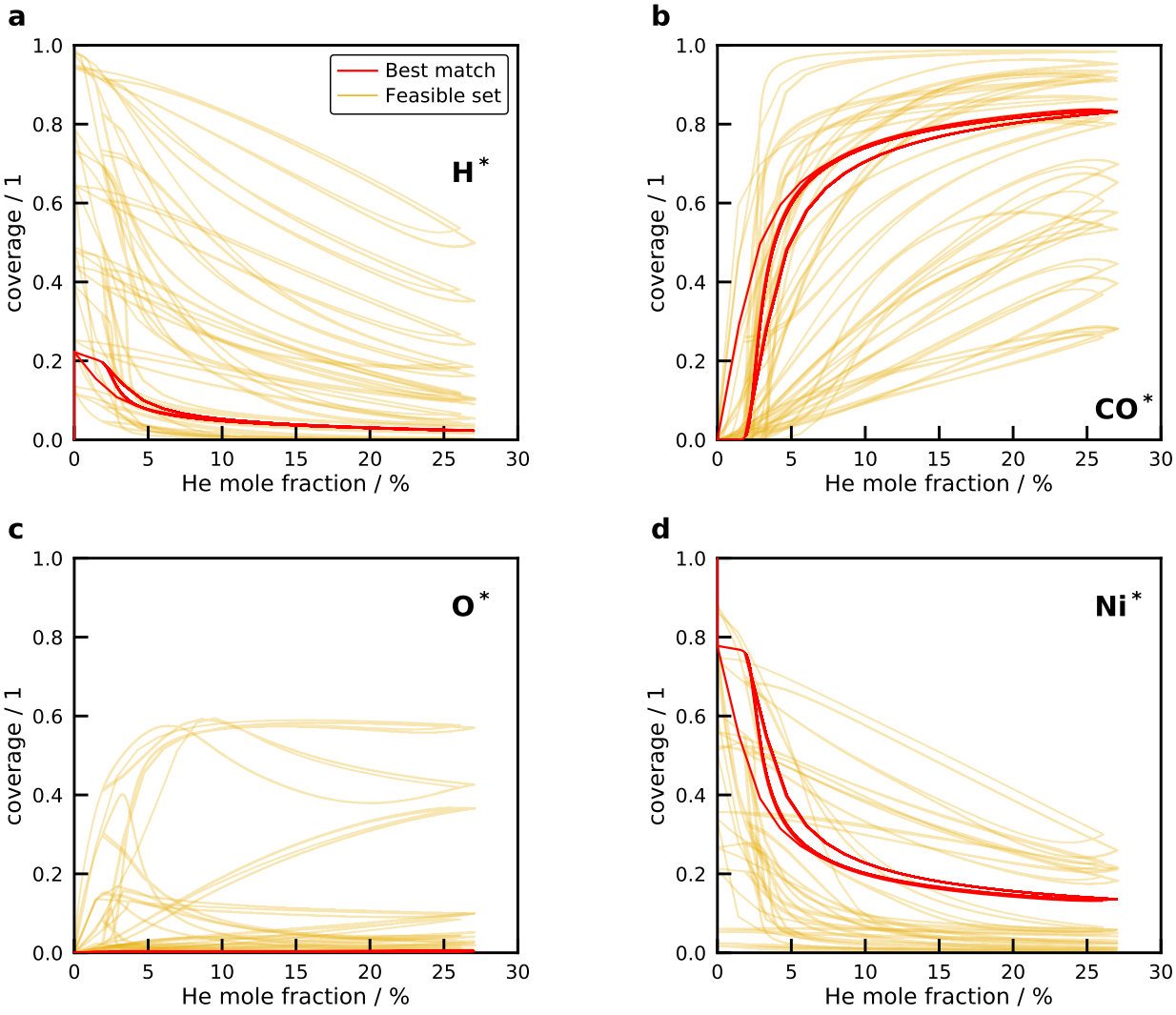

Figure E.3.: Phase plane diagrams of the surface coverage of (a) H^*, (b) CO^*, (c) O^*, and (d) vacant sites (Ni^*) for a cycle split ratio of $\gamma = 0.2$. The red line shows the best match and the yellow lines illustrate all mechanisms from the feasible set.

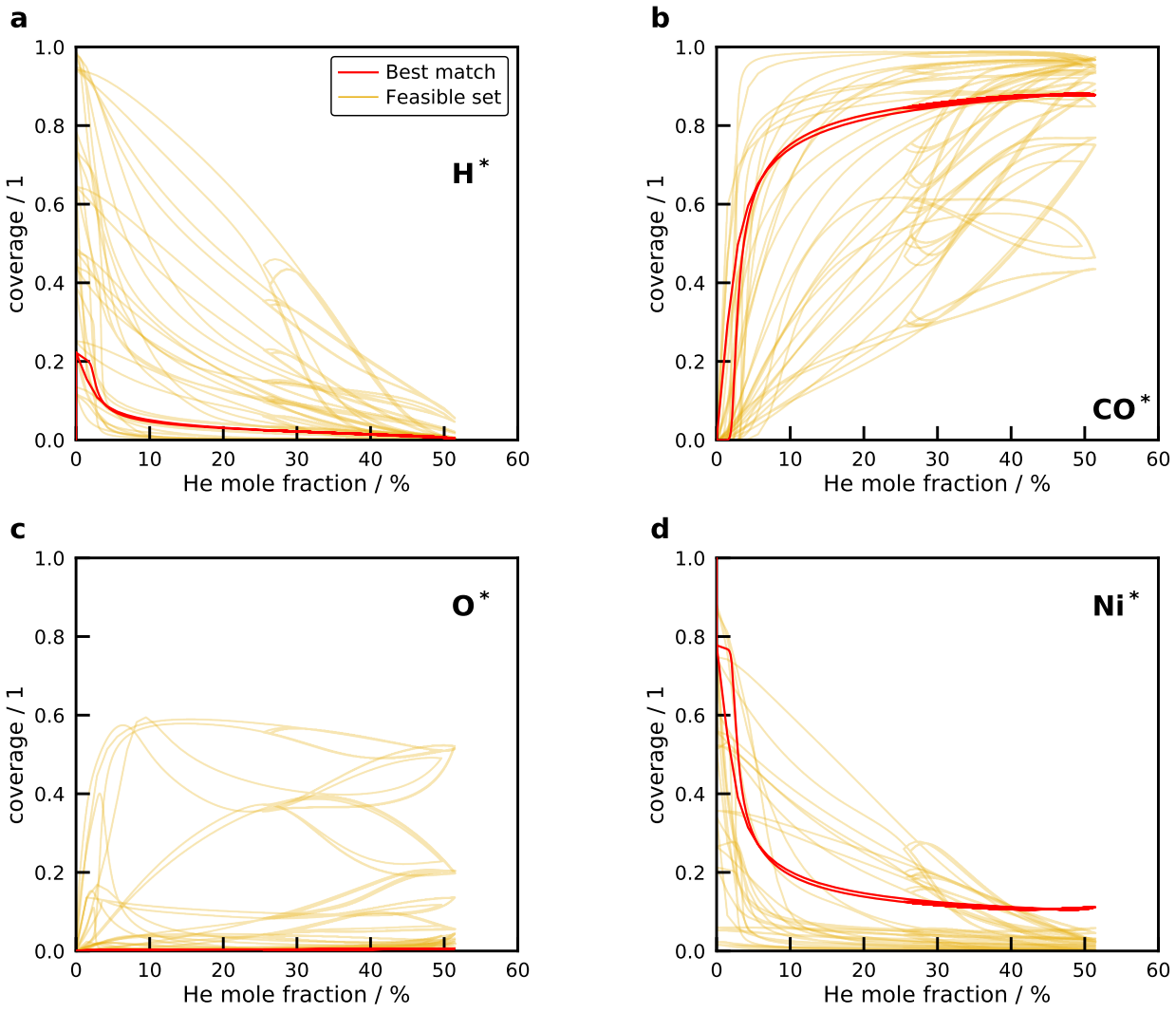

Figure E.4.: Phase plane diagrams of the surface coverage of (a) H^*, (b) CO^*, (c) O^*, and (d) vacant sites (Ni^*) for a cycle split ratio of $\gamma = 0.8$. The red line shows the best match and the yellow lines illustrate all mechanisms from the feasible set.

The Python code of the microkinetic model to simulate the transient CO_2 methanation experiments in the Berty reactor is provided in the following section with comments.

```
import cantera as ct
import numpy as np
import concurrent.futures
import pandas as pd

t=295 #temperature of the CSTR
T=t+273.15
pressure=5e5 #pressure of the CSTR
vol=98e-6
cat_area_per_vol = 1.121/vol  # Catalyst particle surface area (measured with H2 chemisorption) per
     unit volume
cat_area = cat_area_per_vol * vol
sccm = 395*1e-6/60

#Constant flows
V_purge=95
```

```
#Calculate the H2/Ar stream
V_Ar=210
V_H2=90

V1_ges=V_purge+V_H2+V_Ar
x_Ar_1=(V_Ar+V_purge)/V1_ges
x_H2_1=V_H2/V1_ges
#x_Ne=V_Ne/V1_ges

#Calculate the H2/Ar stream
V_He=210
V_CO2=90
V2_ges=V_purge+V_He+V_CO2
x_Ar_2=V_purge/V2_ges
x_He_2=V_He/V2_ges
x_CO2_2=V_CO2/V2_ges

n_runs=5001
offset=0


def TPR(k):
  try:
    file="".join(('/home/bjarne/Mechanism/20210401_RMG_Methanation/Fine/Data/File_',str(k+offset),'
    /cantera/chem.cti'))
    cti_file = file

    gas = ct.Solution(cti_file, 'gas')
    gas.TPX = T, pressure, 'Ar:0.7722, He:0, Ne:0.0, CO2(2):0,  H2(4):0.2278'
    #print(gas.density)
    # import the surface model
    surf = ct.Interface(cti_file,'surface1', [gas])
    surf.TP = T, pressure
    surf.coverages = {'site(7)':1}

    upstream = ct.Reservoir(gas, name='upstream')
    downstream = ct.Reservoir(gas, name='downstream')
    r=ct.IdealGasReactor(gas, energy='off')

    r.volume = vol
    rsurf=ct.ReactorSurface(surf, r, A=cat_area)

    mass_flow=sccm* gas.mean_molecular_weight*1e5/ct.gas_constant/273.15

    mflow = ct.MassFlowController(upstream, r, mdot=mass_flow)
    v = ct.PressureController(r, downstream, master=mflow, K=1e-9)
    sim=ct.ReactorNet([r])

    output_filename="".join(('/home/bjarne/Mechanism/20210428_Berty_Methanation/Data/File_',str(k+
    offset),'/Bang_bang_120_02.csv.gz'))

    ##set relative and absolute tolerances on the simulation
    sim.rtol = 1.0e-14
    sim.atol = 1.0e-20
    sim.max_err_test_fails = 100

    rxn_time=np.linspace(0,1700,1701)

    gas_mole_fracs=np.zeros([gas.n_species, len(rxn_time)])
    surf_fracs=np.zeros([surf.n_species, len(rxn_time)])

    sim.set_max_time_step(5e-3)

    #print(mflow.mdot(t))
    for i in range(len(rxn_time)):
```

```
        time=rxn_time[i]
        if time < 216:
            upstream.thermo.TPX=T,pressure, 'Ar:0.7722, He:0, Ne:0.0, CO2(2):0,  H2(4):0.2278'
        elif (time >= 216) and (time < 240):
            upstream.thermo.TPX=T,pressure, 'Ar:0.2405, He:0.5316, Ne:0.0, CO2(2):0.2278,  H2(4):0'
        elif (time >= 240) and (time < 336):
            upstream.thermo.TPX=T,pressure, 'Ar:0.7722, He:0, Ne:0.0, CO2(2):0,  H2(4):0.2278'
        elif (time >= 336) and (time < 360):
            upstream.thermo.TPX=T,pressure, 'Ar:0.2405, He:0.5316, Ne:0.0, CO2(2):0.2278,  H2(4):0'
        elif (time >= 360) and (time < 456):
            upstream.thermo.TPX=T,pressure, 'Ar:0.7722, He:0, Ne:0.0, CO2(2):0,  H2(4):0.2278'
        elif (time >= 456) and (time < 480):
            upstream.thermo.TPX=T,pressure, 'Ar:0.2405, He:0.5316, Ne:0.0, CO2(2):0.2278,  H2(4):0'
        elif (time >= 480) and (time < 576):
            upstream.thermo.TPX=T,pressure, 'Ar:0.7722, He:0, Ne:0.0, CO2(2):0,  H2(4):0.2278'
        elif (time >= 576) and (time < 600):
            upstream.thermo.TPX=T,pressure, 'Ar:0.2405, He:0.5316, Ne:0.0, CO2(2):0.2278,  H2(4):0'
        elif (time >= 600) and (time < 696):
            upstream.thermo.TPX=T,pressure, 'Ar:0.7722, He:0, Ne:0.0, CO2(2):0,  H2(4):0.2278'
        elif (time >= 696) and (time < 720):
            upstream.thermo.TPX=T,pressure, 'Ar:0.2405, He:0.5316, Ne:0.0, CO2(2):0.2278,  H2(4):0'
        elif (time >= 720) and (time < 816):
            upstream.thermo.TPX=T,pressure, 'Ar:0.7722, He:0, Ne:0.0, CO2(2):0,  H2(4):0.2278'
        elif (time >= 816) and (time < 840):
            upstream.thermo.TPX=T,pressure, 'Ar:0.2405, He:0.5316, Ne:0.0, CO2(2):0.2278,  H2(4):0'
        elif (time >= 840) and (time < 936):
            upstream.thermo.TPX=T,pressure, 'Ar:0.7722, He:0, Ne:0.0, CO2(2):0,  H2(4):0.2278'
        elif (time >= 936) and (time < 960):
            upstream.thermo.TPX=T,pressure, 'Ar:0.2405, He:0.5316, Ne:0.0, CO2(2):0.2278,  H2(4):0'
        elif (time >= 960) and (time < 1056):
            upstream.thermo.TPX=T,pressure, 'Ar:0.7722, He:0, Ne:0.0, CO2(2):0,  H2(4):0.2278'
        elif (time >= 1056) and (time < 1080):
            upstream.thermo.TPX=T,pressure, 'Ar:0.2405, He:0.5316, Ne:0.0, CO2(2):0.2278,  H2(4):0'
        elif (time >= 1080) and (time < 1176):
            upstream.thermo.TPX=T,pressure, 'Ar:0.7722, He:0, Ne:0.0, CO2(2):0,  H2(4):0.2278'
        elif (time >= 1176) and (time < 1200):
            upstream.thermo.TPX=T,pressure, 'Ar:0.2405, He:0.5316, Ne:0.0, CO2(2):0.2278,  H2(4):0'
        elif (time >= 1200) and (time < 1296):
            upstream.thermo.TPX=T,pressure, 'Ar:0.7722, He:0, Ne:0.0, CO2(2):0,  H2(4):0.2278'
        elif (time >= 1296) and (time < 1320):
            upstream.thermo.TPX=T,pressure, 'Ar:0.2405, He:0.5316, Ne:0.0, CO2(2):0.2278,  H2(4):0'
        else:
            upstream.thermo.TPX=T,pressure, 'Ar:0.7722, He:0, Ne:0.0, CO2(2):0,  H2(4):0.2278'

        upstream.syncState()
        mass_flow=sccm* upstream.thermo.mean_molecular_weight*1e5/ct.gas_constant/273.15
        mflow.set_mass_flow_rate(mass_flow)
        sim.reinitialize
        sim.advance(time)
        gas_mole_fracs[:,i]=gas.X
        surf_fracs[:,i]=surf.X

    data=np.c_[rxn_time,gas_mole_fracs.T]
    names=list(['Time'] + gas.species_names)
    df=pd.DataFrame(data, columns=[names])
    df.to_csv(output_filename, index=False, compression="gzip")
    print(k+offset)

  except:
    print('Something is wrong for ' + str(k+offset)+'!')


with concurrent.futures.ProcessPoolExecutor() as executor:
    f=[executor.submit(TPR,i) for i in range(n_runs)]
```

Publications and Conference Contributions

Further publications were prepared within this doctoral studies, which are listed below:

1. **B. Kreitz**, G. D. Wehinger, C. F. Goldsmith, T. Turek. *30th European Symposium on Computer Aided Process Engineering*. Ed. by S. Pierucci, F. Manenti, G. L. Bozzano, D. Manca. Vol. 48. Computer Aided Chemical Engineering. Elsevier, **2020**, 529–534. DOI: 10.1016/B978-0-12-823377-1.50089-6
2. S. Flaischlen, J. Martin, **B. Kreitz**, T. Turek, G. D. Wehinger. *30th European Symposium on Computer Aided Process Engineering*. Ed. by S. Pierucci, F. Manenti, G. L. Bozzano, D. Manca. Vol. 48. Computer Aided Chemical Engineering. Elsevier, **2020**, 499–504. DOI: 10.1016/B978-0-12-823377-1.50084-7
3. J. Friedland, **B. Kreitz**, H. Grimm, T. Turek, R. Güttel. *ChemCatChem* **2020**, 12 (17), 4373–4386. DOI: 10.1002/cctc.202000278
4. **B. Kreitz**, J. Brauns, G. D. Wehinger, T. Turek. *Chemie Ingenieur Technik* **2020**, 92 (12), 1992–1997. DOI: 10.1002/cite.202000019
5. G. D. Wehinger, **B. Kreitz**, A. Nagy, T. Turek. *Chemical Engineering Journal* **2020**, 389, 124342. DOI: 10.1016/j.cej.2020.124342
6. **B. Kreitz**, J. Friedland, R. Güttel, G. D. Wehinger, T. Turek. *Chemie Ingenieur Technik* **2019**, 91 (5), 576–582. DOI: 10.1002/cite.201800191
7. P. Haug, **B. Kreitz**, M. Koj, T. Turek. *International Journal of Hydrogen Energy* **2017**, 42 (24), 15689–15707. DOI: 10.1016/j.ijhydene.2017.05.031

Within the PhD studies, the following lectures were presented at conferences. The presenting author is underlined.

1. B. Kreitz, G. D. Wehinger, C. F. Goldsmith, T. Turek. "Microkinetic development for the methanation of CO_2 on Ni catalysts with RMG-Cat", *ChemReactor 24*, **2021**, virtual
2. B. Kreitz, G. D. Wehinger, C. F. Goldsmith, T. Turek. "Microkinetic modeling of the CO_2 methanation on Ni catalysts with automatically generated mechanisms", *Catalysis Talks*, **2021**, virtual
3. B. Kreitz, G. D. Wehinger, C. F. Goldsmith, T. Turek. "Microkinetic modeling of the CO_2 methanation on Ni catalysts with an automatically generated mechanism", *Annual Meeting on Reaction Engineering 2021*, **2021**, virtual
4. B. Kreitz, G. D. Wehinger, C. F. Goldsmith, T. Turek. "Development of a microkinetic model for the CO_2 methanation with an automated reaction mechanism generator", *ESCAPE 30 - European Symposium in Computer Aided Process Engineering*, 2020, virtual
5. B. Kreitz, J. Martin, S. Flaischlen, G. D. Wehinger, T. Turek. "Are steady-state kinetics sufficient for the simulation of the transient CO_2 methanation?", *ECCE 12*, **2019**, Florence, Italy
6. B. Kreitz, J. Martin, S. Flaischlen, G. D. Wehinger, T. Turek. "Transient kinetic study of the CO_2 methanation on Ni catalysts", *Europacat 2019*, **2019**, Aachen, Germany
7. B. Kreitz, J. Martin, S. Flaischlen, G. D. Wehinger, T. Turek. "Transient methanation of CO_2 on Ni catalysts", *52. Annual German Catalysis Meeting*, **2019**, Weimar, Germany
8. B. Kreitz, J. Brauns, G. D. Wehinger, T. Turek. "Dynamic operation of a lab-scale Power-to-Gas system", *Annual meeting on Energy Process Engineering 2019*, **2019**, Frankfurt, Germany
9. B. Kreitz, G. D. Wehinger, T. Turek. "Studies on the dynamic methanation of CO_2, *ProcessNet-Annual meeting 2018*", **2018**, Aachen, Germany
10. B. Kreitz, G. D. Wehinger, T. Turek. "Dynamic methanation of CO_2 - Effects of concentration forcing", *Annual Meeting on Reaction Engineering 2018*, **2018**, Würzburg, Germany